AN ABSTRACT OF THE DISSERTATION OF

Aaron K. Goodwin for the degree of Doctor of Philosophy in Chemical Engineering presented on August 26, 2010.

Title: Conversion of Biomass Constituents to Hydrogen-rich Gas by Supercritical Water in a Microchannel Reactor.

Abstract approved:

_____

Gregory L. Rorrer

Microreactors offer high rates of heat transfer able to intensify highly endothermic biomass reforming reactions in supercritical water. In this study, two continuous flow microreactor configurations were used to gasify biomass constituents in supercritical water. The first reactor configuration was a micro diameter stainless steel or Hastelloy tube (508 μm – 762 μm) imbedded into a reactor block. The reactor provided high rates of heat transfer to the reacting fluid to sustain an isothermal reaction temperature and was used to elucidate interactions between phenol, a lignin model compound, and xylose, a hemicellulose model compound, during co-gasification. In addition, a reaction mechanism and kinetics for phenol and xylose gasification by supercritical were estimated.

The second microreactor configuration studied was a parallel channel Hastelloy microreactor. The reactor consisted of 14 parallel rectangular microchannels (1000 μm by 127 μm) integrated into a single contiguous reactor block by diffusion bonding a series of shims between two header plates. Fabrication of the reactor from Hastelloy C-276, a high nickel content alloy, substantially intensified biomass gasification reactions and promoted the water gas shift and methanation reactions due to its high catalytic

activity and the large surface area to volume ratio in the microchannel. The dispersion and channel flow distribution in the microchannel reactor was characterized experimentally and modeled using computational fluid dynamics by a tracer pulse study. Furthermore, computational fluid dynamics were used to investigate the effect of endothermic biomass reforming reactions and the average fluid Reynolds number on the reaction temperature. Lastly, xylose was completely gasified to H_2 and CO_2 in the parallel channel microreactor at 650°C and 250 bar within a 1.4 second residence time.

Conversion of Biomass Constituents to Hydrogen-rich Gas by Supercritical Water in a Microchannel Reactor

by

Aaron K. Goodwin

A DISSERTATION

submitted to

Oregon State University

In partial fulfillment of

the requirements for the

degree of

Doctor of Philosophy

Presented August 26, 2010

Commencement June 2011

Doctor of Philosophy dissertation of Aaron K. Goodwin presented on August 26, 2010

APPROVED:

Major Professor, representing Chemical Engineering

Head of the School of Chemical, Biological and Environmental Engineering

---

Dean of the Graduate School

I understand that my dissertation will become part of the permanent collection of Oregon State University libraries. My signature below authorizes release of my dissertation to any reader upon request.

Aaron K. Goodwin, Author

ACKNOWLEDGMENTS

The author graciously acknowledges the funding support for this research from Bend Research and the U.S. Army under the Tactical Energy Systems program administered through the Oregon Nanoscience and Microtechnology Institute. The author thanks Todd Miller, Jack Rundel, and Anna Garrison of the Micro/Nanofabrication Facility of the Oregon State University Microproducts Breakthrough Institute at Oregon State University for assistance with the design and fabrication of the microchannel reactor, and computational fluid dynamic modeling. Additionally, the author would like to acknowledge and thank possibly the greatest machinist in the world, Manfred Dittrich. Manfred was an integral part of the fabrication of the Hastelloy microchannel reactor. He continuously put in countless hours machining and fabricating reactor parts out of exotic material and to incredibly tight tolerances.

The author expresses sincere gratitude to advisor Dr. Gregory L. Rorrer for his patients and advising. He helped me develop a sense of how to think critically about engineering problems, in addition to learning how to implement a solution. His mentoring is an invaluable tool I will use for the rest of my life. The author would also like to thank Clayton Jeffryes, Jermey Campbell, and Tavi Cruz-Uribe for their support, help, and encouragement. Most importantly the author would like to acknowledge my wife and best friend, Johannah Goodwin, who has given me unyielding support and patients throughout graduate school.

TABLE OF CONTENTS

LIST OF FIGURES

LIST OF FIGURES (Continued)

LIST OF FIGURES (Continued)

LIST OF FIGURES (Continued)

LIST OF FIGURES (Continued)

LIST OF FIGURES (Continued)

LIST OF FIGURES (Continued)

LIST OF TABLES

Conversion of Biomass Constituents to Hydrogen-rich Gas by Supercritical Water in a Microchannel Reactor

Chapter 1: Comprehensive Introduction

1.1 Research rationale

Concerns about declining fossil fuel reserves and increasing atmospheric CO_2 concentration from the combustion of fossil fuels has motivated a considerable body of research in the field of alternative energy. Biomass is a renewable, CO_2 neutral and readily available potential feedstock that can be thermochemically converted to energy and transportation fuels which may significantly contribute to the worlds energy supply. Currently, there are four main contenders for thermochemical conversion of biomass; combustion, pyrolysis, gasification and liquefaction [1]. Combustion is a process in which biomass, with a moisture content of 50% or less, is burned in air to convert chemical energy stored in the biomass to thermal energy, which can be used to generate mechanical or electrical energy. Pyrolysis is the chemical decomposition of biomass in the absence of oxygen to a liquid fraction termed bio-oil, char, and gas. Pyrolysis derived bio-oil can be used directly as a fuel, refined to synthetic diesel fuel, or used as a feedstock to produce commodity chemicals. Gasification partially combusts biomass with a controlled amount of oxidant to H_2 and CO. The product gas can be directly combusted for heat generation, fed to a PEM fuel cell for electricity generation, or used as a feedstock for the Fischer-Tropsch synthesis to produce fuels and chemicals. Liquifaction is a low temperature high pressure catalytic process used to break down biomass into small molecules that polymerize and form a bio-oil similar to pyrolysis. Although liquefaction and pyrolysis share similar end products, liquefaction takes place at a much lower temperature and unlike pyrolysis, liquefaction does not require an energy intensive drying step. Of these thermochemical conversion technologies gasification is particularly attractive for biomass conversion due to its numerous end product uses and capacity to process a wide range of biomass feedstocks.

Traditionally petroleum based feedstocks, such as coal, were gasified in the presence of steam at temperatures greater than 600°C and atmospheric pressure. However, the

conversion of lignocellulosic based biomass feedstocks to gas is severely limited by steam reforming, due to the formation of pyrolytic char and tar which limits gasification efficiency and decreases the H_2 yield [2]. Nevertheless, the problem was overcome when Modell [3] replaced steam with supercritical water as a reaction medium and converted Maplewood sawdust to tar and gas without char formation. Since then, supercritical water has been used to gasify a wide variety of biomass including glucose, cellulose, and starch [4-22], hemicellulose [7, 18], lignin [6-8, 18-20, 22-28], and waste biomass feeedstocks including black liquor [29], cassava waste [14], corn cob and corn silage [15, 20, 30], fruit shells [7, 15], sawdust [4, 9, 13, 15, 22], rice straw [15, 22], algae [31], and sewage sludge [5]. Of the candidate thermochemical conversion technologies considered for electricity generation, supercritical water gasification was concluded to be the most efficient process based on energy conversion for biomass feedstock containing a moisture content of 40% or more [32].

1.2 Supercritical water

Supercritical water is an attractive reaction medium to reform biomass due to its solubilization and transport properties, as well as its ability to suppress tar and coke formation [33]. Furthermore, water is a benign and environmental friendly solvent and naturally present to various extents in all types of biomass. As water is heated past its critical temperature, 374°C, at pressures greater than 221 bar, its physical properties undergo significant change. Its ionic character and ability to hydrogen bond is lessened due to a significant decrease in its dielectric constant which results in enhanced solubility of non-polar organic molecules and higher reactivity. From a microscopic point of view, an increase in reactivity can be attributed to a decrease in hydrogen bonding. A breakdown in the hydrogen bonding network, as well as a decrease in the hydrogen bonding lifetime, leads to an increase in mobility for single water molecules, and results in increased collision frequencies between reactant and solvent, thus resulting in greater reactivity [34]. A decrease in coke and tar formation is due to a reduced chance that a reactant or intermediate will react with one another and polymerize. Moreover, at

temperatures greater than 600°C, supercritical water is a strong oxidizer and will react with carbon to produce CO and CO_2 which, for biomass gasification, produces H_2 yields in excess of the feedstock. For biomass gasification supercritical water provides a homogeneous reaction medium eliminating mass transport limitations characteristic in multiphase reactions. Conversely, because of the significant decrease in its dielectric constant, supercritical water is a poor solvent for inorganic salts. However, depending on the desired application the physical properties of supercritical water including solubility and reactivity can be tuned by adjusting its temperature and pressure [35]. Transport properties in supercritical water benefit from an increase in species diffusion rates and a decrease in fluid viscosity compared to liquid water, and an increase in heat transfer compared to steam [36]. Several characteristics of supercritical water including miscibility with non-polar compounds and gas, enhanced transport properties, and ability to suppress coking reactions, make it an ideal reaction medium to reform biomass.

1.3 Biomass feedstocks

Plant biomass is a complex mixture of organic materials derived from CO_2, water, and sunlight. The three main constituents that comprise lignocellulosic plant biomass are 50% cellulose, 20% hemicellulose, and 30% lignin. The chemical structure for the most abundant monomer in each biomass constituent is presented in Figure 1.1. However, several other types of biomass considered a potential feedstock for thermochemical conversion to energy and fuels such as potatoes, rice, and cassava, contain up to 50% starch, and 10% protein. Cellulose is a crystalline polysaccharide carbohydrate that forms the primary structural elements of green plants. It is made from glucose monomers that are linked together through a β-1,4 glycosidic bond [37]. When glucose or cellulose is reformed with water, H_2 and CO_2 are the major products. The overall reaction for glucose is

$$C_6H_{12}O_6 + 6H_2O \rightarrow 6CO_2 + 12H_2 \qquad (1.1)$$

where stoichiometrically it is possible to produce 12 moles of H_2 for every one mole of glucose reacted.

In contrast to cellulose, hemicellulose is an amorphous heterogeneous biopolymer made up of several monosaccharides including xylose, mannose, galactose, rhamnose, and arabinose and is found in primary and secondary lignocellulosic biomass cell walls. Xylose, an aldopentose, is a five carbon sugar that makes up the biomass based polymer xylan, the backbone of hemicellulose. Xylose is typically the most abundant monomer that makes up hemicellulose, and thus is commonly used as a hemicellulose model compound. The xylose reforming reaction in water is

$$C_5H_{10}O_5 + 5H_2O \rightarrow 5CO_2 + 10H_2 \quad (1.2)$$

The theoretical hydrogen yield based on reforming is 10 moles of H_2 per mole of xylose reacted.

Lignin present in cellulosic based biomass is a highly complex three dimensional polymer comprised of phenyl propane units connected by carbon or ether linkages. It is an integral part of the cell wall in biomass and gives lignocellulosic biomass its mechanical strength. Although, lignin is very complex, the three main monomers that comprise lignin are coumaryl alcohol, coniferyl alcohol, and sinapyl alcohol. Typical model compounds for lignin include common monolignols such as phenol, guaiacol, p-cresol, or any alkyl phenol. Lignin is also available in pretreated forms such as organosolv lignin which is derived from native biomass.

1.4 Catalytic supercritical water gasification

Supercritical water gasification of biomass has several advantages compared to traditional gasification including the direct use of wet biomass feedstocks, a single reactor for biomass hydrolysis and gasification, additional H_2 generation through reforming, and a compressed gas product, convenient for storage and transportation. Recently there have been several reviews for biomass gasification by supercritical water

[10, 39-49]. Two strategies for supercritical water biomass gasification have emerged, a low temperature (350°C to 500°C) catalytic route that generally produces CH_4 as its major gas product, and a high temperature (500°C to 750°C) route that produces H_2 as its major gas product.

Catalytic gasification by supercritical water is an attractive alternative to high temperature biomass reforming because it reduces the minimum reaction temperature necessary for gasification. This substantial reduces the overall process cost since the majority of the energy input into supercritical water gasification goes into heating up a large excess of water in relation to biomass in the feed. As a result of the harsh reaction environment, the catalyst system must be highly active and stable in supercritical water. Furthermore, the catalyst system should be able to suppress coke and char formation to avoid catalyst deactivation. Catalysts considered for biomass gasification by supercritical water include carbon catalysts, alkaline catalysts, and transition metal catalysts.

1.4.1 Carbon catalysts

Activated carbon has great potential as an effective catalyst for biomass gasification in supercritical water as it has been shown to improve gas yields and H_2 selectivity. Antal et al. [4] and Xu et al. [5] catalytically gasified glucose with an activated carbon catalyst, and were able to achieve greater than 90% carbon gasification efficiency (CGE), or carbon recovered in the gas, for a 22 wt% glucose feed solution at temperatures ranging from 600°C to 750°C. Furthermore, Antal et al [4] gasified real biomass feedstocks including cornstarch, potato starch, sawdust, and potato waste, and were able to achieve greater than 70 % CGE for feed concentrations ranging from 8.9 wt% to 13.7 wt % at temperatures greater than 700°C. Both groups concluded that gas composition and gas yield were a strong function of reactor temperature and increased H_2 yields were due to the promotion of the water gas shift reaction.

Although carbon catalysts have shown to improve CGE and the H_2 yield for biomass gasification, two technical issues need to be addressed. The first is reactor plugging. Antal et al. [4] reported that all feed solutions with greater than 15 wt% organic material plugged the reactor within 1 - 2 hours of on stream time. For feed concentrations less than 15 wt % they observed a prolonged time on stream, but eventually the reactor would plug due to a buildup of ash and char in the heating zone. The second issue needed to be addressed is catalyst deactivation. Xu et al. [5] observed a decrease in catalytic activity after 4 hours of operation, but noted that catalyst deactivation was prolonged when swirl flow was initiated in the entrance of the reactor, essentially increasing the rate of heat transfer to the fluid.

1.4.2 Alkaline catalysts

Alkaline catalysts benefit biomass gasification in supercritical water by increasing gasification yields and H_2 selectivity [6-7, 50], and are used in alkaline lignocellulosic biomass pretreatment processes for bioconversion of cellulose to ethanol [51-52]. Sinag et al. [50] observed a nearly 2-fold increase in the H_2 yield and significant decrease in the CO concentration for glucose gasification at 500°C with a K_2CO_3 catalyst. They attributed the improved H_2 yield to an increase in the kinetics of the forward water gas shift reaction via formate formation. They also determined that the addition of K_2CO_3 led to an increase in acid formation, and a decrease in furfural formation. This is important because the polymerization of furfurals with other liquid intermediates is thought to be one of the cause of char and coke [53-54]. Ultimately, less furfural formation will improve the CGE since furfural is more difficult to gasify than small organic acids. Guo et al. [7] used $Ca(OH)_2$ to gasify glucose to H_2 and CH_4, both which had increased yields compared to experiments with no catalyst. However, due to the formation of $CaCO_3$ from CO_2 and $Ca(OH)_2$, there was little to no CO_2 or CO in the product gas. Kruse et al. (2000) showed that KOH could enhance the gasification of lignin. The group gasified pyrocatechol, a lignin model compound, at 600°C and 400 MPa with KOH and achieved a 99% carbon gasification efficiency for a 6.6 wt % feed solution.

Generally, alkaline catalysts have improved biomass gasification in supercritical water by catalyzing biomass gasification reactions and promoting the water gas shift reaction, however, Kruse et al. [53] and Sinag et al. [50] observed a solid residue accumulate in batch and continuous flow reactors during gasification experiments. In one case the solid residue accounted for up to 8% of the carbon fed to the reactor. Additionally, alkaline catalysts are thought to increase corrosion to the reactor material. Energy dispersive X-ray (EDX) analysis performed by Sinag et al. [50] on solid particles filtered from the liquid products indicated the presence of Ni, Mo, and Cr, all of which are primary constituents of their Inconel reactor.

1.4.3 Metal and metal oxide catalysts

Metal and metal oxides are a third class of catalyst used for biomass gasification by supercritical water. Metal catalysts and catalyst supports are limited to materials that are stable in the strongly oxidizing environment of supercritical water. Currently, metal catalysts investigated for biomass gasification in supercritical water include Ru, Rh, Pd, Pt, and Ni. Catalyst supports include CeO_2 γ-Al_2O_3, γ – Al_2O_3, TiO_2, carbon, and MnO. Typically, biomass gasification over metal catalysts at temperatures ranging from 350°C to 500°C produces gas rich in CH_4, CO_2, and H_2, with small amounts of CO and C_{2+} hydrocarbons. A significant difference between low temperature gasification with a metallic catalyst and high temperature gasification is the amount of CH_4 present in the gas products. Osada et al. [6] produced gas containing up to 41 mole % CH_4 from lignin gasification at 400°C with a Ru / TiO_2 catalyst, compared to Guo et al. [7] who measured around 10 mole % CH_4 for non-catalytic continuous gasification of lignin in Hastelloy tubular reactor at temperatures ranging from 500°C – 775°C.

High biomass carbon gasification efficiency can be achieved with metallic catalysts for long reaction times, but generally depends on the activity of the catalyst system, water density, temperature, and feedstock. Sato et al. [55] was able to gasify lignin with a 20 wt

% Ni / MgO catalyst at 400°C in a batch reactor, however, a 360 min reaction time was necessary for 78% carbon gasification efficiency. Sato et al. [24] ranked several transition metal catalysts and supports in order of catalytic activity for supercritical water gasification of alkylphenols at 400°C as: Ru / γ- Al_2O_3 > Ru / Carbon > Rh / Carbon, > Pt / γ-Al_2O_3 > Pd / Carbon > Pd / γ-Al_2O_3. However, carbon gasification efficiencies were low, and ranged from 0.2% - 15%. Hao et al. [9] observed a similar trend for the gasification of cellulose and sawdust at 500°C and ranked catalytic systems based on catalytic activity as: Ru / Carbon > Pd / Carbon > CeO_2 particles > CeO_2 nano particles > $(CeZr)_xO_2$. They observed carbon gasification efficiencies as high as 94% for cellulose, and 77% for sawdust with a Ru / carbon catalyst. Yamaguchi et al. [56] investigated several metal catalysts on titania and activated carbon supports and, similar to the previous reports, concluded Ru had the highest catalytic activity followed by Rh > Pt > Pd > Ni. Furthermore, for Ru / carbon catalysts Osada et al. [57] determined that gasification efficiency was a function of reactor pressure, and were able to increase carbon gasification efficiencies for lignin gasified at 400°C up to 47% by optimizing the water density.

Although metallic catalysts designed for low temperature biomass gasification by supercritical water have demonstrated potential to lower the activation energy for gasification reactions and increase selectivity in the gas products, the stability of these catalyst systems need to be addressed before this technology can come to fruition [58-64]. Metal catalysts are typically expensive, thus the lifetime of a catalyst and support becomes an important factor when optimizing a catalytic process. Osada et al. [60] investigated the stability of several supports for Ru catalysts including γ-Al_2O_3 , TiO_2, and carbon. They concluded that γ-Al_2O_3 and carbon supports demonstrated poor stability due to a change in morphology in γ-Al_2O_3, and a decrease in surface area for the carbon support. TiO_2 was the most stable support, but carbon gasification efficiency decreased after the third subsequent use. Additional studies by Byrd and Gupta [63] and Lu et al. [65] investigated the stability of adding CeO_2 to γ-Al_2O_3 as a catalysts support. Although CeO_2 was found to stabilize the γ-Al_2O_3 support by inhibiting carbon formation on the catalyst, the improvement was only incremental and the catalyst eventually became

deactivated due to the formation of carbon on the catalyst surface and sintering. Catalyst stability is a critical issue that needs to be improved before low temperature catalytic gasification by supercritical water can be considered as a viable themochemical conversion technology for biomass.

1.5 High temperature supercritical water gasification

Above 600°C biomass can be completely non-catalytically and stoichiometrically gasified to H_2 and CO_2 by supercritical water and is generally referred to as the "high temperature route". At these conditions gasification efficiency is highly dependent on the type of biomass processed, heat transfer to the reacting fluid, reaction time, and reactor material. Major gas products are H_2, CO_2, CH_4, and CO and minor gas products include C_2 and C_3 saturated and unsaturated hydrocarbons. Once the gas products have been produced from the feed substrate gas composition is determined by the extent of the water gas shift and the methanation reactions.

Due to the complex structure and wide variety of lignocellulosic biomass it is difficult to clearly establish the effect of reaction condition on gasification yields. For that reason glucose has been extensively studied as a biomass model compound to investigate the effects of reaction condition on gasification rates and product selectivity [4, 11-16, 53, 66-73]. In addition, cellulose and starch, polymers of glucose, have been investigated to isolate any effects from hydrolysis on gasification [4, 14, 17-19, 74]. Given that supercritical water gasification of glucose has been studied in greater detail than any other biomass constituent and is the most abundant biomass moiety, this review will focus on the effect of reaction conditions on glucose and cellulose gasification as a representative biomass model compound. Furthermore, since hemicellulose and cellulose moieties shares a similar chemical structure the trends observed for glucose gasification is likely similar for hemicellulose gasification.

1.5.1 Reaction mechanism for glucose decomposition in supercritical water

Liquid intermediate formation from the decomposition of glucose by supercritical water has been the subject of several studies, and recently been reviewed [43]. Holgate et al. [66] continuously gasified a 0.001 M aqueous glucose solution in a Hastelloy reactor at 600°C and 246 bar, and determined the major recalcitrant liquid intermediates to be acetic acid, acrylic acid, acetonylacetone, and acetaldehyde. Goodwin and Rorrer [16] gasified glucose at 650°C and 250 bar in a stainless steel microreactor, and determined major liquid intermediates to be acetic acid, propenoic acid, 5-HMF, and phenol. They established a residence time dependence on liquid intermediate formation and reactivity, and concluded that phenol was the most difficult liquid intermediate to gasify. Williams and Onwudili [75] proposed the formation of phenol was a product of the Diels Alder reaction between 3-hydrofuranone and a diene intermediate. The difference in liquid intermediate formation between Holgate et al. [66] and Goodwin and Rorrer [16] can be attributed to differences in feed concentration and reactor material. In order to gain insight into how feed concentration affects liquid product formation, a closer examination of the glucose decomposition reaction mechanism near the critical temperature of water is necessary.

Several studies have investigated the decomposition of glucose and cellulose near the critical temperature of water to determine a reaction mechanism and how the fluid heating rate affects glucose decomposition selectivity [53, 68, 71, 74-75]. A general reaction schematic proposed by Kruse and Gawlik [53] is presented in Figure 1.2. The fluid heating period has the most significant impact on liquid product formation and therefore also affects gas yields. A slow heating period will promote the formation of refractory liquid intermediates, as well as coke precursors, while a fast heating period will lead to the formation of organic acids. In the subcritical region, glucose decomposition is dominated by an ionic reaction environment and favors the formation of furfurals and to a lesser extent aromatic compounds through dehydration [50, 53], whereas in the supercritical region glucose mainly decomposes to organic acids through a free radical reaction mechanism [68]. Given that furfurals and other unsaturated

hydrocarbons will tend to react with other liquid intermediates and polymerize in a free radical environment [76-77], rapid heating in the entrance of the reactor will reduce coke precursor formation and increase gasification kinetics due to a decrease in furfural formation.

1.5.2 Effect of pressure on supercritical water gasification

Carbon gasification efficiency, gas composition, and biomass decomposition kinetics is a weak function of reactor pressure. Lu et al [15] and Kabyemela et al [67] observed a small decrease in the carbon gasification efficiency with increasing pressure for glucose gasification. Additionally, Lu et al. [15] observed an increase in the total organic carbon (TOC) in the liquid products with increasing pressure. They explained the influence of pressure on the gasification products by examining the role of water in the gasification process. They noted that water properties such as density and dielectric constant increase as a function of increasing pressure. The result is an increase in reaction rates caused by ionic mechanisms, which in turn increased the rate of glucose hydrolysis to 5-HMF. Ogihara et al. [78] studied the effect of reaction density on cellulose dissolution in supercritical water in a batch reactor, and concluded that water density substantially affects cellulose dissolution due to the change in the dielectric constant which impacts waters ability to disrupt H_2 bonding. Specifically, they reported the lowest dissolution temperature occurred at a water density of 800 kg m^{-3}, however, regardless of pressure the highest dissolution temperature was 355°C, well below reaction temperatures need to promote complete biomass gasification.

1.5.3 Effect of temperature on supercritical water gasification

The effect of temperature on glucose gasification by supercritical water can be divided into two specific aspects: reaction temperature and fluid heating rate. As previously stated increasing the fluid heating rate improves biomass gasification efficiency and decreases the formation of coke due to a decrease in furfural formation [50, 71]. In regard

to reaction temperature, Kersten et al. [13] concluded carbon gasification efficiency and H_2 yield were strong functions of reaction temperature below 650°C, and a function of feed concentration thereafter for glucose gasification in quartz batch reactors. An increase in H_2 yield with increasing temperature can be explained by an increase in the gasification efficiency and an increase in the forward water gas shift reaction. As the reaction temperature approaches 700°C a dramatic decrease in the concentration of CO and the disappearance of C_2 and C_3 hydrocarbons are observed. The decrease in CO is due to increased activity in the water gas shift reaction. Several thermodynamic studies have predicted the effect of reaction temperature on gas composition and gas yields based on minimization of Gibbs energy [79-81]. From these studies it is evident that gas composition is a strong function of temperature below 600°C due to a change in the equilibrium constant for the water gas shift and methanation reactions in addition to incomplete gasification of the feed substrate. Above 600°C the gas products mainly consist of CO_2 and H_2 with small amounts of CO and CH_4 due to the large excess of water in the feed which drive the forward water gas shift and reverse methanation reactions by the law of mass action. Lee et al. [12] estimated reaction kinetics for glucose gasification by supercritical water as pseudo first order and derived an Arrhenius temperature dependence on the rate constant.

1.5.4 Effect of feed concentration on supercritical water gasification

Supercritical water gasification of biomass becomes increasingly difficult at high feed concentrations due to heat transfer limitations in traditional continuous flow tubular reactors. Specifically, as feed concentration increases, carbon gasification efficiency and H_2 yield decrease and the formation of char and coke in the entrance region of the reactor is observed and eventually leads to reactor plugging [4, 13, 15]. An explanation proposed by Matsumura et al. [2] stated that increasing the biomass feedstock concentration will increase the concentration of furfurals and other unsaturated heterocyclic compounds produced in the fluid heating period. After the biomass is heated past the critical temperature of water, the high concentration of furfural type compounds react with other

liquid intermediates and polymerize to form coke and char [77]. Although reactor design is one way to address the issue of increased char and coke formation during continuous biomass gasification with concentrated feedstocks [82], an alternate solution is to minimize or eliminate char and coke formation by substantially increasing the rate of heat transfer to the reacting fluid and reduce the amount of furfural compounds formed.

1.5.5 Effect of reactor material on supercritical water gasification

In addition to a heat transfer, reactor material is an important design consideration for supercritical water gasification of biomass. Not only does the reactor material have to be corrosion resistant and able to withstand continual stresses imparted from working at 650°C and 250 bar, but certain metals that comprise steel and nickel alloys significantly affect gasification performance and gas and liquid product selectivity due to unintentional catalytic activity [4, 8, 11, 13, 25-26, 44]. Quartz capillary bath reactors have been used to avoid unintentional catalysis and establish a clear relationship between catalysis from metal in the reactor wall and biomass gasification [8, 23, 13, 17, 25-26]. Based on previous studies it was concluded that the high Ni content in both Inconel and Hastelloy reactors catalyze biomass gasification reactions and promote the water gas shift and methanation reactions. However, Yu et al. [11] observed much higher carbon gasification efficiency for the gasification of acetic acid, a major liquid intermediate for the decomposition of glucose, in a corroded Hastelloy reactor compared to a new Hastelloy reactor and Inconel reactor at the same reaction conditions. When Hastelloy C-276 is exposed to supercritical water, it develops an outer oxide layer at the surface consisting of nickel oxide and an inner layer rich in chromium, oxygen, and nickel clusters [83-84]. The change in surface chemistry after prolonged exposure to supercritical water might explain the difference in gasification performance between new and corroded Hastelloy reactors. Additionally, the amount of nickel in the reactor wall influences the extent of "unintentional catalysis." Resende and Savage [8] showed that increasing the catalyst surface area to biomass weight ratio improves gasification yields and H_2 selectivity for cellulose gasification with a nickel catalyst. Nickel alloys such as Hastelloy and Inconel

would be an excellent reactor material for biomass gasification by supercritical water due to the materials resistance to high temperatures and corrosion as well as its high catalytic activity in the reactor wall.

1.6 Hemicellulose gasification by supercritical water

Given that potential feedstocks may contain complex mixtures of solubilized biomass materials it is important to individually characterize the gasification of each biomass constituent. Currently, there are only a small number of investigations that report on gasification of hemicellulose. Apart from studies using real biomass, xylan has been catalytically gasified by supercritical water just above the critical temperature of water, 450°C – 500°C [7, 18, 85]. However, reported H_2 yields were less than 1 mol H_2 per mol of xylan, far below the theoretically yield of 9 moles of H_2 per mol of xylose. Additionally, previous kinetic studies for xylose decomposition in near critical water and supercritical water have shown that mechanistically xylose decomposes similarly to glucose. Below the critical temperature of water xylose is dehydrated to furfural and above the critical temperature of water xylose is reacted via a retro aldol condensation to glyceraldehyde and glycoaldehyde [86-87]. Therefore like glucose, gasification of hemicellulose will benefit from high rates of heat transfer by decreasing furfural formation.

1.7 Lignin gasification by supercritical water

Of the three major constituents that make up lignocellulosic biomass, lignin has a higher energy density than either cellulose or hemicellulose, however, it is the most recalcitrant to gasify in supercritical water due to its highly stabilized pi bonding network. For example, when cellulose was gasified at 500°C, 0.08 g cm^{-3} water density, and 5 minute reaction time a carbon gasification efficiency of 33% was achieved, whereas only a 22% carbon gasification efficiency was achieved when lignin was gasification at the same conditions [19]. Phenol and other mono and di-substituted phenolic compounds such as

guaiacol are excellent model compounds for lignin gasification by supercritical water [5, 25-26, 88-89]. Pretreated lignin derived from real biomass has also been investigated, although it is only sparingly soluble in an aqueous solution and therefore is limited to batch processing or being fed to the reactor as a slurry [17, 19, 20, 23]. Gas composition from lignin and phenol gasification consisted of H_2, CO_2, CH_4, and CO and similar to glucose, was influenced by the reactor material, temperature, and residence time. However, in contrast to carbohydrate gasification DiLeo et al. [26] observed that increasing the water density lowered phenol conversion, and increasing the phenol concentration in the feed accelerated the decomposition of phenol. Furthermore, when phenol was co-gasified with lignin a homogeneous phase is formed that promotes lignin hydrolysis and inhibits re-polymerization of the phenolics [88, 90]. Since carbohydrates decompose to various liquid intermediates, including phenol, at a much faster rate than lignin, interactions between biomass constituents will have a significant influence on gasification rates [18, 89].

Since phenol is also used as a model compound for pollutants, there have been several studies that investigate the kinetics and reaction mechanism for the oxidation of phenol and other lignin model compounds in supercritical water [25, 27, 91-97]. Phenol conversion was determined to be pseudo first order, and has a rate constant with an Arrhenius temperature dependency [25]. Liquid intermediate formation from phenol decomposition was studied by Gopalan and Savage [94]. They proposed that phenol is decomposed via two main reaction pathways, dimerization and ring opening. Typical intermediates for phenol decomposition include benzene, phenol dimers, organic acids, and single ring oxygenates.

1.8 Microchannel reactors

Microchannel reactors are an ideal platform to gasify biomass by supercritical water, as they provide rapid heat transfer to the reacting fluid that drive endothermic biomass reforming reactions and result in a very fast fluid heating period. Additionally,

microchannels have a large surface area to volume ratio that will exploit catalytic activity from the reactor wall.

1.8.1 Current uses and fabrication techniques

Microreactor technology, including current and state of the art applications and fabrication techniques, has been reviewed [98-103]. Microreactors gained popularity in the 1970s as a result of process intensification concepts and manufacturing methods derived from the electronic industry [102]. Thrusts towards the miniaturization of electronics led to novel manufacturing techniques allowing for micron sized complex geometries to be realized. Manufacturing techniques include chemical etching, vapor deposition, micromachining, and lithography. Specifically, techniques used for metal microreactor fabrication include mechanical and laser micromachining, wet etching, and laser ablation. Advances in manufacturing methods ultimately led to advances in microchannel reactor design. Microchannels have been integrated into several microstructure devices used in a wide variety of applications including micromixers, microreactors, MEMS devices, and microheat exchangers. Recently Trachsel et al. [104] constructed a silicon glass microreactor designed to operate at 80°C and 140 bar. The unique design and transparent reactor material allows for observation of flow profiles, catalyst packing, and temperature imaging. Coupled with new fabrication techniques, microreactor design will continue to evolve, offering many improvements over traditional processing in batch and flow reactors.

1.8.2 Advantages for microreactor processing

Microreactors offers several advantages compared to chemical processing in traditional continuous flow reactors or batch reactors as a result of dramatically smaller passages than conventional reactors. Chemical processing in traditional continuous flow reactors is typically limited by mass or heat transfer. Microchannels significantly intensify heat and mass transfer rates by using micron sized passages with high surface area to volume

ratios. For this reason microreactors can facilitate reaction pathways often difficult to control in continuous flow tube reactors, including highly endothermic and exothermic reactions. More precise temperature control increases product selectivity, resulting in increased yields, and offers an alternative approach to batch processing. Additionally, high heat transfer rates decrease the chance of reactor runaway during highly exothermic reactions. High mass transfer rates can reduce the amount of catalyst necessary for chemical reactions reducing costs and improving product yield and selectivity. Chemical processing in a microreactor also improves safety due to smaller holdup volumes and less waste. Furthermore, microreactor systems can be used for portable or on demand synthesis and destruction of hazardous chemicals, eliminating high transportations costs and safety risks. This is particularly attractive for biomass processing. Due its low energy density, high water content, and low ratio of biomass per unit land transportation costs become a significant issue for centralized processing [105]. Alternatively, microchannel reactor systems would allow for on farm processing eliminating transportation costs altogether.

1.8.3 Microreactor scale up

Processes scale up which involves taking a process from bench scale to pilot scale and finally to commercial scale is tedious and often requires new reactor design at each step. However, process scale up in a microreactor is often more straight forward compared to scaling up chemical reactions in traditional continuous flow reactors. A microreactor is scaled up by parallel processing. The feed stream is split into numerous sub streams by a header or distribution plate within the microreactor. Each sub stream is processed in an individual microchannel and recombined at the reactor outlet. The number of microchannels integrated into the device determines the target reactor volume. Therefore the same framework can be used for the bench scale and commercial scale reactors, the only difference being the number of channels in the device. A critical goal for microreactor scale up is to achieve identical physics in each microchannel within the reactor, as mal distributed flow between microchannels reduces the benefit of enhanced

transport properties. Microchannel flow distribution is often addressed through header design [106-107].

1.9 Rationale for current investigation thesis overview

Supercritical water has been proven to be an ideal reaction medium to reform biomass and biomass constituents in continuous flow reactors. However, one of the technical barriers that need to be addressed for continuous flow operation is low biomass gasification efficiency and reactor plugging due to the formation of coke and recalcitrant liquid intermediate formation during the fluid heating period. Increasing the heating rate has been shown to decrease coke formation and increase gasification efficiency. However, traditional continuous flow tube reactors do not have adequate heat transfer necessary to eliminate coke formation and drive highly endothermic biomass reforming reactions. Microreactors provide an ideal platform for supercritical water biomass gasification due to large surface area to volume ratios which provide high rates of heat transfer and enhanced catalytic activity from nickel in the reactor material, and have already been proven an ideal platform for catalytically steam reforming methanol and other hydrocarbons to produce H_2 gas [108-114]. This work is focused on the development of a supercritical water parallel channel Hastelloy microreactor for supercritical water gasification of biomass to H_2 rich gas. Several objectives detailed in the subsequent chapters were met to achieve this goal.

An isothermal microtubular reactor was designed to demonstrate the benefits of enhanced heat transfer on biomass gasification by supercritical water. The reactor tubes were interchangeable which allowed for the use of tubes constructed from several different alloys and tubes with various inner diameters. Chapter 2 focuses on isothermal gasification of xylose and phenol as model compounds for hemicellulose and lignin in the microtube reactor at conditions where gasification is dominant. Specifically, the effect of residence time and temperature on gas yield and H_2 selectivity is investigated for each

biomass constituent. The biomass constituents were then co-gasified to elucidate interactions between hemicellulose and lignin during gasification.

Chapter 3 focuses on the isothermal supercritical water gasification of xylose in the microtubular reactor. Unlike xylose gasification in Chapter 2 which used a stainless steel microtube, this investigation used a microtube constructed from a high nickel content alloy, Hastelloy C-276. Two kinetic models describing xylose gasification by supercritical water at reaction temperatures from 450°C to 650°C and 250 bar were developed. The decomposition kinetic model uses a more detailed reaction mechanism to predict liquid intermediate formation, whereas the gasification kinetic model uses a simplified reaction mechanism and an in depth thermodynamic analysis to better predict gasification rates and gas composition at condition where gasification is dominant.

Chapter 4 is focused on fabrication of a supercritical water parallel channel Hastelloy microreactor. Considering the intrinsic kinetics for xylose and phenol gasification described in the previous studies, an intricate high heat flux microreactor was designed and fabricated for biomass gasification by supercritical water. The reactor had 14 parallel microchannels integrated into a single contiguous device by microfabrication techniques.

Chapter 5 describes the fluid flow and dispersion in the parallel channel microreactor by a tracer pulse residence time distribution study. Computational fluid dynamics (CFD) was used to simulate experimental results and determine the effect of Reynolds number on the flow field through the reactor. Furthermore, the flow uniformity between the microchannels is discussed based on comparing CFD simulations for a single microchannel to experimental results.

Chapter 6 describes xylose gasification in the parallel channel Hastelloy microreactor at 650°C and 250 bar. CFD simulations of the microreactor and the kinetic model for xylose gasification developed in Chapter 3 were used to predict temperature and speciation in the reactor. Specifically, the effects of endothermic xylose reforming and residence time on the reaction temperature were investigated.

Chapter 7 sums up all of the results from the current research in a comprehensive conclusion.

1.10 Literature Cited

1. Zhang L, Xu C, Champagne P 2010 *Energy Conservation and Management* **51** 969-982
2. Matsumura Y, Minowa T, Potic B, Kersten S, Prins W, van Swaaij W, Beld B, Elliott D, Neuenschwander G, Kruse A, Antal J M J 2005 *Biomass and Bioenergy* **29** 269-292
3. Modell M 1985 Gasification and liquefaction of forest products in supercritical water (Elsevier Applied Publishers: London)
4. Antal J A J, Allen S G, Schulman D, Xu X 2000 *Ind Eng Chem Res* **39** 4040-4053
5. Xu X, Matsumura Y, Stenberg J, Antal J A J 1996 *Ind Eng Chem Res* **35** 2522-2530
6. Osada M, Sato T, Watanabe M, Adschiri T, Arai K 2004 *Energy and Fuels* **18** 327-333
7. Guo L, Lu Y, Zhang X, Ji C, Guan Y, Pei A 2007 *Catalysis Today* **129** 275-286
8. Resende F L P, Savage P E 2010 *Ind Eng Chem Res* **49** 2694-2700
9. Hao X, Guo L, Zhang X, Guan Y 2005 *Chemical Engineering Journal* **110** 57-65
10. Byrd A, Pant K, Gupta R 2007 *Ind Eng Chem* **46** 3574-3579
11. Yu D, Aihara M, Antal J A J 1993 *Energy and Fuels* **7** 574-577
12. Lee I G, Kim M S, Ihm S K, 2002 *Ind Eng Chem Res* **41** 1182-1188
13. Kersten S R A, Potic B, Prins W, Van Swaaij W P M 2006 *Ind Eng Chem Res* **45** 4169-4177
14. Williams P T, Onwudili J 2006 *Energy and Fuels* **20** 1259-1265
15. Lu Y J, Guo L J, Ji C M, Zhang X M, Hao X H, Yan Q H 2006 *International Journal of Hydrogen Energy* **31** 822-831
16. Goodwin A K, Rorrer G L 2008 *Ind Eng Chem* **47** 4106-4114
17. Resende F, Neff M, Savage P 2007 *Energy and Fuels* **21** 3637-3643
18. Yoshida T, Matsumura Y 2001 *Ind Eng Chem* **40** 5469-5474
19. Resende F L P, Savage P E 2009 *Energy & Fuels* **23** 6213-6221
20. Jin H, Lu Y, Guo L, Cao C, Zhang X 2010 *International Journal of Hydrogen Energy* **35** 3001-3010

21. Voll F A P, Rossi C C R S, Silva C, Guirardello R, Souza R O M A, Cabral V F, Cardozo-Filho L 2009 *International Journal of Hydrogen Energy* **34** 9737-9744

22. Yoshida T, Oshima Y, Matsumura Y 2004 *Biomass and Bioenergy* **26** 71-78

23. Resende F, Fraley S, Berger M, Savage P 2008 *Energy and Fuels* **22** 1328-1334

24. Sato T, Osada M, Watanabe M, Shirai M, Arai K 2003 *Ind Eng Chem* **42** 4277-4282

25. DiLeo G, Neff M, Savage P 2007 *Energy and Fuels* **21** 2340-2345

26. DiLeo G, Neff M, Kim S, Savage P 2008 *Energy and Fuels* **22** 871-877

27. Matsumura Y, Nunoura T, Urase T, Yamamoto K 2000 *Journal of Hazardous Materials* **B73** 245-254

28. Kruse A, Meier D, Rimbrecht P, Schacht M 2000 Ind Eng Chem Res 39 4842-4848

29. Sricharoenchaikul V 2009 *Bioresource Technology* **100** 638-643

30. D'Jesus P, Boukis N, Kraushaar-Czarnetzki B, Dinjus E 2006 *Ind Eng Chem* **45** 1622-1630

31. Stucki S, Vogel F, Ludwig C, Haiduc A G, Brandenberger M 2009 *Energy & Environmental Science* **2** 535-541

32. Yoshida Y, Dowaki K, Matsumura Y, Matsuhashi R, Li D, Ishitani H, Komiyama H 2003 *Biomass Bioenergy* **25** 257-272

33. Calzavara Y, Joussot-Dubien C, Boissonnet G, Sarrade S 2005 *Energy Conversion and Management* **46** 615-631

34. Kruse A, Dinjus E 2007 *Journal of Supercritical Fluids* **41** 361-379

35. Weingärtner H, Frank E U 2005 *Angew Chem Ed* **44** 2672-2692

36. Savage P 2000 *Catalysis Today* **62** 167-173

37. Berg J M, Tymoczko J L, Stryer L 2002 *Biochemistry* (W.H. Freeman and Co: New York)

38. Demirbas A 2010 *Energy Sources Part A* **32** 1342-1354

39. Calzavara Y, Joussot-Dubien C, Boissonnet G, Sarrade S 2005 *Energy Conversion and Management* **46** 615-31

40. Loppinet-Serani A, Aymonier C, Cansell F 2008 *ChemSusChem* **1** 486-503

41. Navarro R M, Sánchez-Sánchez M C, Alvarez-Galvan M C, del Valle F, Fierro J L G 2009 *Energy Environ Sci* **2** 35-54

42. Peterson A A, Vogel F, Lachance R P, Fröling M, Antal Jr M J, Tester J 2008 *Energy Environ Sci* **1** 32-65

43. Kruse A 2008 *Biofuels Bioproducts & Biorefining* **2** 415-37

44. Guo Y, Wang S Z, Xu D H, Gong Y M, Ma H H, Tang X Y 2010 *Renewable and Sustainable Energy Reviews* **14** 334-343

45. Kruse A, Vogel H 2008 *Chem Eng Technol* **31** 1241-1245

46. Savage P E 2009 *Journal of Supercritical Fluids* **47** 407-414

47. Vogel F 2009 *Handbook of Green Chemistry: Green Calalysis* vol 2, ed P T Anastas and R H Crabtree (Germany: Wiley-VCH Verlag GmbH & Co KGaA) pp 281-324

48. Ding Z Y, Frisch M A, Li L, Gloyna E F 1996 *Ind Eng Chem Res* **35** 3257-3279

49. Savage P E 2000 *Catalysis Today* **62** 167-173

50. Sinag A, Kruse A, Rathert J, 2004 *Ind Eng Chem* **43** 502-508

51. Mosier N, Wyman C, Dale B, Elander R, Lee Y, Holtzapple M, Ladisch M 2005 *Bioresource Technology* **96** 673-686

52. Hendriks A, Zeeman G, 2009 *Bioresource Technology* **100** 10-18

53. Kruse A, Gawlik A 2003 *Ind Eng Chem* **42** 267-279

54. Chuntanapum A, Matsumura Y 2010 *Ind Eng Chem Res* **49** 4055-4062

55. Sato T, Furusawa T, Ishiyama Y, Sugito H, Miura Y, Sato M, Suzuki M, Itoh N 2006 *Ind Eng Chem* **45** 615-622

56. Yamaguchi A, Hiyoshi N, Sato O, Bando K K, Osada M, Shirai M 2009 *Catalysis Today* **146** 192-195

57. Osada M, Sato O, Watanabe M, Arai K, Shirai M 2006 *Energy and Fuels* **20** 930-935

58. Byrd A J, Gupta, R B 2010 *Applied Catalysis A: General* **381** 177-182

59. Furusawa T, Sato T, Saito M, Ishiyama Y, Sato M, Itoh N, Suzuki N 2007 *Applied Catalysis A: General* **327** 300-310

60. Osada M, Sato O, Arai K, Shirai M 2006 *Energy & Fuels* **20** 2337-2343

61. Tomita K, Oshima Y 2004 *Ind Eng Chem Res* **43** 7740-7743

62. Yu J, Savage P E 2001 *Applied Catalysis B: Environmental* **31** 123-132

63. Aki S N V K, Ding Z, Abraham M A 1996 *AICHE Journal* **42** 1995-2004

64. Aki S N V K, Ding Z, Abraham M A 1996 *AICHE Journal* **42** 1195-2004

65. Lu Y, Li S, Guo L, Zhang X 2010 *International Journal of Hydrogen Energy* **35** 7161-7168.

66. Holgate R H, Meyer J C, Tester J W 1995 *AICHE Journal* **41** 637-647

67. Kabyemela B, Adschiri T, Malaluan R, Arai K 1997 *Ind Eng Chem* **36** 1552-1558

68. Kabyemela B, Adschiri T, Malaluan R, Arai K 1999 *Ind Eng Chem* **38** 2888-2895

69. Hao X H, Guo L J, Mao X, Zhang X M, Chen X J 2003 *International Journal of Hydrogen Energy* **28** 55-64

70. Watanabe M, Aizawa Y, Iida T, Levy C, Aida T M, Inomata H 2005 *Carbohydrate Research* **340** 1931-1939

71. Watanabe M, Aizawa Y, Iida T, Nishimura R, Inomata H 2005 *Applied Catalysis* **295** 150-156

72. Yoshida T, Matsumura Y 2009 *Ind Chem Res* **48** 8381-8386

73. Weiss-Hortala E, Kruse A, Ceccarelli C, Barna R 2010 *Journal of Supercritical Fluids* **53** 42-47

74. Ehara K, Saka S 2002 *Cellulose* **9** 301-311.

75. Williams P T, Onwudili J 2005 *Ind Eng Chem Res* **44** 8739-8749

76. Chuntanapum A, Yong T L, Miyake S, Matsumura Y 2008 *Ind Eng Chem Res* **47** 2956-2962

77. Chuntanapum A, Matsumura Y 2010 *Ind Eng Chem Res* **49** 4055-4062

78. Ogihara Y, Smith R, Inomata H, Arai K 2005 *Cellulose* **12** 595-606

79. Tang H, Kitagawa K 2005 *Chemical Engineering Journal* **106** 261-267

80. Yan Q, Guo L, Lu Y 2006 *Energy Conservation and Management* **47** 1515-1528

81. Lu Y, Guo L, Zhang X, Yan Q 2007 *Chemical Engineering Journal* **131** 233-244

82. Yoshida T, Matsumura Y 2009 *Ind Eng Chem Res* **48** 8381-8386

83. Zhang Q, Tang R, Yin K, Luo X, Zhang L 2009 *Corrosion Science* **51** 2090-2097

84. Boukis N, Habicht W, Franz G, Dinjus E 2003 *Materials and Corrosion* **54** 326-330

85. Yoshida K, Kusaki J, Ehara K, Saka S 2005 *Applied Biochemistry and Biotechnology* **121** 795-806

86. Qi J, Xiuyang L, *Chin J Chem Eng* **15** 666-669

87. Sasaki M, Hayakawa T, Arai K, Adschiri T, **2** 169-176

88. Saisu M, Sato T, Watanabe M, Adschiri T, Arai K 2003 *Energy and Fuels* **17** 922-928

89. Weiss-Hortala E, Kruse A, Ceccarelli C, Barna R 2010 *J of Supercritical Fluids* **53** 42-47

90. Fang Z, Sato T, Smith R L J, Inomata H, Arai K, Kozinski J A 2008 *Bioresource Technology* **99** 3424-3430

91. Henrikson J, Savage P 2003 *AICHE Journal* **49** 718-726

92. Yermakova A, Mikenin P, Anikeev V 2005 *Theoretical Foundations of Chemical Engineering* **40** 168-174

93. Portela E, Nebot E, Martinez de la Ossa E 2001 *Chemical Engineering Journal* **81** 287-299

94. Goplan S, Savage P 1994 *J Phys Chem* **98** 12646-12652

95. Sato T, Adschiri T, Arai K 2003 *J Anal Appl Pyrolysis* **70** 735-746

96. Savage P E, Gopalan S, Li R 1994 *Chemical Oxidation* **3** 34-41

97. Okuda K, Ohara S, Umetsu M, Takami S, Adschiri T 2008 *Bioresource Technology* **99** 1846-1852

98. Shah K, Ouyang X, and Besser R S 2005 *Chem Eng Technol* **28** 303-13

99. Hessler V, Loeb P, Loewe H, and Kolb G 2007 *Micro Instrumentation* **1** 85-129

100. Brandner J J 2008 *Microreactors in Organic Synthesis and Catalysis* **1** 1-17

101. Hessler V, Knobloch C, and Loewe H 2008 *Recent Patents on Chemical Engineering* **1** 1-16

102. Holladay J D, Wang Y, and Jones E 2004 *Chem Rev* **104** 4767-90

103. Lerou J J, Tonkovich A L, Silva L, Perry S, McDaniel P J 2010 *Chemical Engineering Science* **65** 380-385

104. Trachsel F, Hutter C, von Rohr P 2008 *Chemical Engineering Journal* **135S** 309-316

105. Searcy E, Flynn P 2009 *Appl Biochem Biotechnol* **154** 271-286

106. Commenge J M, Falk L, Corriou J P, and Matlosz M 2002 *AICHE Journal* **48** 345-58

107. Amador C, Gavriilidis A, and Angeli P 2004 *Che Eng J* **101** 379-90

108. Holladay J, Wang Y, Jones E 2004 *Chem Rev* **104** 4767-4790

109. Casanovas A, Saint-Gerons M, Griffon F, Llorca J 2008 *International Journal of Hydrogen Energy* **33** 1827-1833

110. Cao C, Wang Y, Rozmiarek R 2005 *Catalysis Today* **110** 92-97

111. Levent M, Gunn D, El-Bousiffi A 2003 *International Journal of Hydrogen Energy* **28** 945-959

112. O'Connell M, Kolb G, Schelhaas K P, Schuerer J, Tiemann D, Ziogas A, Hessel V 2009 *International Journal of Hydrogen Energy* **34** 6290-6303

113. Stefanidis G D, Vlachos D G 2009 *Chemical Engineering Science* **64** 4856-4865

114. Casanovas A, Dominguez M, Ledesma C, Lopez E, Llorca J 2009 *Catalysis Today* **143** 32-37

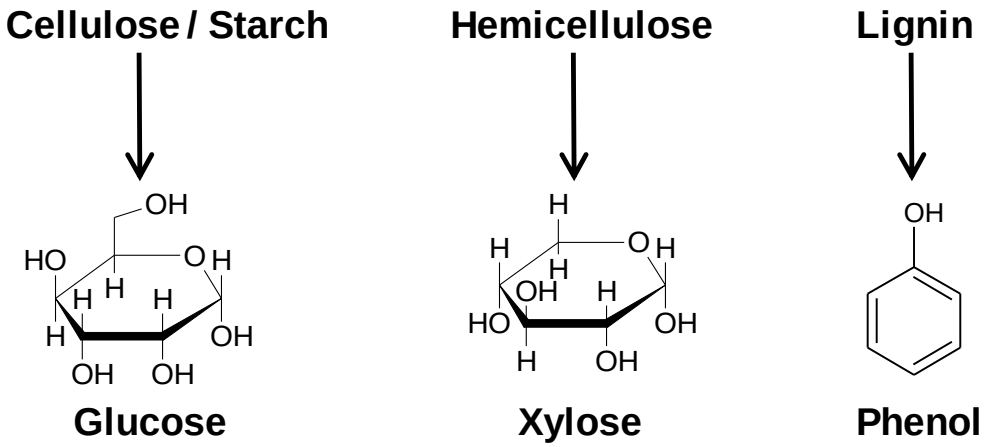

Figure 1.1. Lignocellulosic biomass constituent monomers.

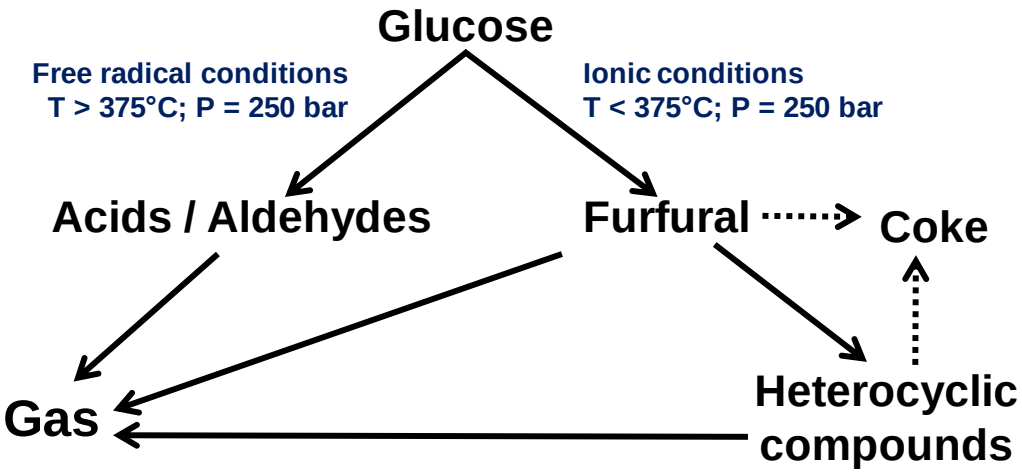

Figure 1.2. General Reaction pathway for the degradation of glucose in supercritical water adopted from Kruse and Gawlik [53].

Chapter 2: Conversion of Xylose and Xylose-Phenol Mixtures to Hydrogen-Rich Gas by Supercritical Water in an Isothermal Micro-tube Flow Reactor

2.1 Abstract

Microchannel reactors offer high rates of heat transfer to endothermic reforming reactions, particularly for the supercritical water gasification of biomass constituents such as hemicellulose and lignin, which are byproducts from cellulosic ethanol production. Xylose (the principal sugar in hemicellulose) and phenol (the principal moiety in lignin) served as model compounds. The carbon in xylose was completely reformed to H_2-rich gas (62% H_2, 34% CO_2) by supercritical water at 250 bar within a microtube flow reactor. Hydrogen gas yields of 8.2 ± 0.6 mol H_2 mol^{-1} xylose where achieved within a 1.0 s fluid residence time at 650°C using a Hastelloy C276 microtube reactor, versus 4.8 ± 0.4 mol H_2 mol^{-1} xylose 750°C using a 316 stainless steel microtube reactor. The short residence times were attributed to the high heat transfer rates and isothermal temperature profiles in the 508 μm inner diameter microtube reactor, which were confirmed by modeling studies. Phenol was difficult to gasify, and the activation energy for phenol conversion was 264 ± 20 kJ mol^{-1}. However, when a mixture of 1.6 mol phenol/mol xylose was gasified at 750°C and 250 bar, the apparent rate constant of phenol conversion increased from 0.66 ± 0.03 to 2.8 ± 0.3 s^{-1}. Although the H_2 gas yield was 2.9 mol H_2 mol^{-1} phenol + xylose (41% H_2 in product gas), if the 19% CH_4 in the product gas was also reformed, the yield increased to 8.5 ± 0.6 mol H_2 mol^{-1} mixture.

2.2 Introduction

Production of bioethanol from lignocellulosic biomass produce two product streams rich in hemicellulose or lignin. The first byproduct stream is generated as a result of biomass pretreatments aimed at making cellulose accessible to enzymatic hydrolysis. Typical chemical pretreatment processes strip the lignocellulosic biomass of the hemicellulose and a fraction of the lignin [1-2], creating an aqueous byproduct stream rich in these constituents. The second byproduct stream is a solid lignin rich residue, and comes from enzymatically hydrolyzing the cellulose in the biomass. Currently, the solid residue is dried and combusted to provide energy for boiler steam [3], and although, the hemicellulose can be hydrolyzed and fermented to biofuels such as ethanol [4], an alternative approach is to combine the solid lignin residue with the solubilized hemicellulose and lignin rich stream and gasify the mixture. However, conventional steam reforming of lignocellulosic biomass is severely limited due to the formation of pyrolytic char and tar [5], Nevertheless, supercritical water (374°C and 221 bar) has been proven an effective way to reform lignocellulosic biomass has to hydrogen rich gas with little to no char and tar formation. Attributes that make supercritical water reforming an attractive platform to reform lignocellulosic biomass compared to other reforming methods include direct processing of wet feedstocks, additional hydrogen generation through reforming, and the generation of a compressed product gas. Biomass gasification in near- and supercritical water has been recently reviewed [5-12].

Lignocellulosic biomass, such as herbaceous crops and forest and agriculture residues, are comprised of 20% to 30% lignin, 20% to 30% hemicellulose and about 40% to 60% cellulose. Of the three major constituents that make up lignocellulosic biomass, lignin has a higher energy density than either cellulose or hemicellulose, however, it is the most recalcitrant to gasify in supercritical water [13]. Lignin is a highly complex bio-polymer comprised of three phenyl propane monomers, trans-p-coumaryl, coniferyl, and sinapyl alcohol, connected by carbon or ether linkages. Gasification of lignocellulosic biomass in supercritical water to hydrogen rich gas containing little to no carbon monoxide has been demonstrated [14-18]. Previous studies for lignin model compounds, including

organosolv lignin, phenol, P-cresol, guaiacol, and pyrocatechol, have focused on the characterization of gas products at 400°C in the presence of Ni or Ru catalysts [19-24], homogeneous KOH or K_2CO_3 catalysts [14, 25], or non-catalytically at reaction temperatures between 365°C and 725°C [26-28, 29]. While these studies provide insight into gas yields and composition, they were all conducted in batch reactors, which does not allow for the analysis of transport processes under steady state, continuous flow conditions.

Phenol is an excellent model compound to study the kinetics and chemistry associated with supercritical water gasification of lignin [26]. Previous mechanistic studies on lignin suggest that supercritical water decomposes lignin to several monomers that share the phenol moiety as a common building block [29] as well as phenol itself as a decomposition product of those monomers [28,30]. The mechanism and kinetics for decomposition of phenol in supercritical water has previously been studied in the presence of an oxidation source, H_2O_2, and O_2 [31], however, there are very few investigations for supercritical water gasification of phenol in the absence of an external oxidation source at conditions where gasification is dominant [32].

Hemicellulose is an amorphous heterogeneous biopolymer made up of several monosaccharides including xylose, mannose, galactose, rhamnose, and arabinose. The most abundant polysaccharide and backbone of hemicellulose is xylan, a β-1,4-linked condensation polymer of the five carbon sugar xylose [4]. Contrary to lignin, there have been very few investigations for the supercritical water gasification of hemicellulose. Apart from studies utilizing real biomass, xylan has been catalytically gasified in supercritical water just above the critical point temperature of water (450°C – 500°C) [13-14, 33]. However, reported H_2 yields were 1 mol H_2 / mol xylan were far below the theoretically yield of 9 moles of H_2 / mol of xylose.

Given that potential feed-stocks may contain complex mixtures of solubilized biomass derived material, it is important to individually characterize biomass constituents as well mixtures of constituents to determine how interactions between substrates will affect gasification. Previous work has shown that the amount of lignin in the feed has a

significant effect on the gasification efficiency and H_2 yield [13, 34-35] for gasification of cellulose / xylan / lignin mixtures. Of particular interest is how interactions between hemicellulose and lignin in a mixture will affect gasification efficiency and gas product composition under isothermal, continuous flow conditions. Given that supercritical water gasification of hemicellulose is much faster than lignin, rapid gasification of hemicellulose to H_2 and CO_2 may promote the hydrogenation of lignin [36], and increase gasification efficiency and influence the gas composition. An aqueous mixture of xylose and phenol will serve as model compounds for hemicellulose and lignin and will be used to emulate a biomass pretreatment stream.

In our previous work, we demonstrated a significant enhancement for supercritical water gasification of glucose by using a microchannel reactor [37]. The reactor architecture consisted of 28 parallel rectangular microchannels (500 μm by 76 μm) that were integrated into a single contiguous block by micro-lamination techniques. The micron sized channel dimensions provided high rates of heat transfer to the reacting fluid that resulted in complete gasification of glucose in a two second residence time.

In the present study a microtube reactor is used to continuously and isothermally reform xylose phenol mixtures to H_2 rich gas. The present study has two objectives. The first objective is to characterize aqueous intermediate product formation, gas composition, and reaction kinetics for continuous, isothermal supercritical water reforming of phenol and xylose as a function of residence time and temperature. The second objective is to determine how the co-gasification of xylose and lignin will affect gasification kinetics and gas composition.

2.3 Experimental

2.3.1 Micro-tubular Reactor and Test Loop

The micro-tubular reactor is presented in Figure 2.1. It consisted of a 2 meter long, 1.6 mm (1/16 inch) outer diameter, 508 micron inner diameter, 316 stainless steel tube imbedded in a 316 stainless steel block. The stainless steel block had a 2 meter by 1.6

mm (1/16 inch) by 1.6 mm (1/16 inch) square channel cut into it by a computer numerical controlled mill. The channel was oriented in a serpentine array of eight passes. The tubing was fitted into the channel making the surface of the stainless steel block flush. A second 316 stainless steel block was screwed into the first block acting as a top cover. The dimensions of the reactor block including the top cover were 29.5 cm (11.6 inches) by 7.9 cm (3.1 inches) by 0.94 cm (0.37 inches).

A schematic of the continuous flow micro-tubular reactor test loop is presented in Figure 2.1. The feed was pumped to the reactor, at 25°C and 250 bar, by a Teledyne ISCO 260D syringe pump operating at constant flow. The feed was heated to the reaction temperature inside the reactor furnace by two 375 W flat plate ceramic heaters that sandwiched the reactor block. The primary mode of heat transfer to the reactor tubing was conduction from the ceramic heaters. The reactor temperature was controlled with a PID controller with a Type J thermocouple inserted approximately 1 inch into the bottom part reactor block halfway between the inlet and outlet tubing. The hot reactor effluent exiting the reactor was condensed by a shell and tube heat exchanger using water as the coolant. The pressure was decreased from 250 bar to 1.03 bar by an adjustable precision back-pressure regulator (KHB1WOA6C2P6000, Swagelok Inc., stainless steel). After the reactor effluent was at ambient temperature and pressure, the gas and liquid were separated in a gas liquid separator. The liquid was collected for further analysis. The gas products were dried and quantified with a gas mass flowmeter (Omega Inc. FMA 1800 series, 0-20 sccm, and 0-100 sccm, aluminum / brass body) and collected in a 2.0 liter Tedlar gas collection bag. The volumetric gas flowrate obtained from the gas mass flowmeter was corrected for gas composition.

Reactor conditions considered by this study are presented in Table 2.1. The reactor temperature was taken at the thermocouple in the reactor block used by the PID controller, and the pressure was taken at the pump head. The fluid residence time (τ) was estimated by

$$\tau = \frac{V_R \, \rho_R(T,P)}{\upsilon_o \, \rho_o} \qquad (2.1)$$

where V_R is the reactor volume (cm^3), υ_o is the volumetric flowrate of the liquid feed to the reactor (250 bar, 25°C), ρ_o is the density of the liquid feed (1.01 g/cm^3), and ρ_R is the density of the fluid at the reactor temperature and pressure. The reactor residence time is based on the fluid at the reactor set point temperature and pressure, and does not account for fluid density changes as the fluid heats up from the subcritical liquid state to the supercritical fluid state. The fluids physical properties were estimated from water at the reactor temperature and pressure. Therefore, density or heat effects from the formation of gas products in the reactor were not factored into the residence time calculation. Prior to reactor experiments, newly installed microtubes were conditioned by a three-step protocol: 1.0 g min^{-1} water at 750 °C and 250 bar for 24 h, 20 mL min^{-1} H^2 at 2 bar for 24 h, and 0.5 mL min^{-1} of 20 g L^{-1} xylose solution at 750°C and 250 bar for 24 h.

2.3.2 Analytical Procedures

Gas and liquid products were analyzed by gas chromatography (GC) and high performance liquid chromatography (HPLC). Gas products were quantitatively analyzed by a Hewlett-Packard HP 5890 GC equipped with a thermal conductivity detector (TCD), and Alltech Associates Carbosphere 80/100 1/8 inch by 6 ft packed column. Gas species CO_2, CO, and CH_4 were analyzed using He as the carrier gas at 28 ml/min, an oven temperature of 85°C, a injector temperature of 120°C, and a detector temperature of 120°C. A standard gas sample size of 50 µl was injected a total of three times. These gas compounds were identified by retention time and quantified by external calibration against a standard gas mixture (Alltech Associates Inc., gas standard #19792). Hydrogen gas present in the gas products was analyzed by a separate GC method. The Carrier gas was N_2 flowing at 34.0 ml/min an oven temperature of 85°C, a injector temperature of 120°C, and a detector temperature of 120°C. A standard gas sample size of 100 µl was injected a total of three times. Hydrogen was identified by retention time and quantified by external calibration.

The liquid products from supercritical water gasification of phenol were analyzed on a Hewlett-Packard HP 5890 GC equipped with a flame ionization detector (FID). Phenol and other liquid by-products were eluted on a Hewlett Packard HP-5 capillary GC column, 0.32 mm inner diameter by 30 m long. The carrier gas was He, and the on column flow rate was set to 1 ml/min. The inlet and detector temperature was 250°C, and the oven temperature was set to 45°C for 12 min then ramped to 200°C at 7.0°C/min finally the temperature was held for 5 min at 200°C. The injection volume was 1 µl.

Residual sugar present in the liquid products was analyzed on an Agilent 100 series HPLC equipped with a Hewlett Packard HP-1037 refractive index (RI) detector, and was eluted on a SupelcoGel PB column at 85°C with HPLC grade water flowing at 0.6 ml/min as the eluent. Organic acids and organic intermediates in the liquid products were analyzed by a Dionex DX-300 HPLC with UV detection at 210 nm and 290 nm. The acids and liquid intermediates were eluted on a BioRad HPX-87H column at 85°C. The eluent was 0.12 mM sulfuric acid flowing at 0.6 ml/min. Injection volumes for the sugars analysis and organic acids analysis was 20 µl. Sugars and acids were identified by retention time and quantified by external calibration. The organic acids were further identified by UV spectrum. Sugar and organic acid standards were obtained from Sigma-Aldrich.

2.3.3 Thermodynamic Calculations

Thermodynamic equilibrium calculations were performed on ChemCad 6.1 (Chemstations, Inc.). The enthalpy for reforming of phenol to H_2 and CO_2 in the gaseous state is 395 kJ mol^{-1} at 25 °C and 472 kJ mol^{-1} at 750 °C. The enthalpy for xylose reforming is 287 kJ mol^{-1} at 25 °C and 335 kJ mol^{-1} at 750 °C. Thermodynamic parameters for xylose are provided in the literature [38].

2.3.4 Simple Reactor Model

The material and energy balance for a differential volume of the microtube reactor are

$$\frac{dC_A}{dx} = -\frac{k_1(T)}{V_\infty} C_A \qquad (2.2)$$

$$\frac{dT}{dx} = \frac{1}{\rho(T,P) V_\infty f_H(T,P)} \left(\frac{4h}{d}(T_s - T) - k_1(T) C_A \Delta\hat{H}_R(T) \right) \qquad (2.3)$$

where C_A is the concentration of the feed stock (mol m^{-3}), k_1 is the first order rate constant for the reforming reaction of the feed substrate (s^{-1}), d is the inner diameter of the microtube (m), h is the convective heat transfer coefficient from the tube wall to the reacting fluid (W m^{-2} K^{-1}), ρ(T,P) is the density of the reacting fluid (kg m^{-3}), $\Delta\hat{H}_R$(T) is the enthalpy of the reforming reaction (J mol^{-1}), T is the reacting fluid temperature at position x (°C), T_s is the temperature of the wall of the reactor (°C), V_∞ is the average velocity at position x (m s^{-1}), x is the axial position of the microtube (m^{-1}), and f_H(T,P) is the derivative of the specific enthalpy of the mixture with respect to T at position x (J kg^{-1} K^{-1}).

The reacting fluid velocity was estimated from the continuity equation, $\dot{m} = \rho(T,P) V_\infty \pi d^2 / 4$, where $\dot{m}$ is the mass flow rate of the reacting fluid (kg s^{-1}). At the feed concentration considered by this study, 20 g L^{-1}, water was the dominant component in the reacting fluid representing 98 % of the reacting fluid by weight or 96.5 mol % when xylose was used as the feed or 92.6 mol % when phenol was used as the feed. For this reason the thermophysical properties reacting fluid were estimated by the properties of water at the local temperature of the reactor and the system pressure of 250 bar. Water above its critical point pressure (221 bar) has no phase change enthalpy per se. However, the specific heat capacity Cp (T,P) of the fluid is a highly nonlinear function of temperature T just before and after its critical point temperature (374 °C). Therefore, fH (T,P) was estimated by Cp (T,P). The heat transfer coefficient h (W $m^{-2}K^{-1}$) for laminar flow (Reynolds number, Re < 2100) at low Graetz numbers (Gr) was estimated by

Hausen's correlation for a microtube [39]. If *Re* was in the turbulent flow regime, then the Dittus-Boelter correlation was used to estimate *h*. The Graetz number was estimated from $Gr = Re\ Pr\ d/L$, where L is the tube length, Pr is the Prandtl number of the fluid, and Re is the Reynolds number. The Reynolds number was estimated by $Re = V_\infty\ d/v$, where v is the fluid kinematic viscosity ($m^2\ s^{-1}$). Differential Equations 2.2 and 2.3 were solved in MatLab (ver. 7.0), using the interpolation function for thermophysical data of water from the NIST database [40]. In the integration of Equation 2.3, to account for the fact that the convection heat transfer rate to the tube cannot exceed the maximum heat delivery rate provided by the ceramic heater ($\dot{Q}$), the convection heat transfer flux term $q = h(Ts - T)$ was replaced with $q = \dot{Q}/\pi dL$. For a 2.0 m length tube with d = 508 μm, q = 23.5 W/cm^2, whereas for d = 1.7 mm, q = 7.0 W/cm^2.

2.4 Results and Discussion

Isothermal supercritical water gasification of xylose, phenol, and a mixture of xylose and phenol to hydrogen rich gas in a continuous flow micro-tubular reactor is described. No increase in pressure drop or reactor plugging was observed for any of the xylose and phenol experiments at all conditions tested.

Previous supercritical water gasification studies focused on hemicellulose and lignin model compounds were performed in sealed batch reactors [13-14, 19, 21-24, 25, 27-29, 32], and thus do not represent gasification under steady state flow conditions. Additionally, previous work on supercritical water gasification of biomass in continuous flow reactors has focused on glucose as a substrate and used reactor inner diameters of 1.7 mm to 9.5 mm [41-46, 16, 35, 47], which are much larger than the tube diameters considered by this study (508 µm, 762µm). Given that supercritical water gasification of biomass has extremely fast gasification kinetics, in some cases less than 1.0 sec for complete gasification, it is necessary to gasify these substrates in a reactor designed to be isothermal at short residence times (~ 1.0 sec). In laminar flow at low Graetz numbers the heat transfer coefficient, *h*, is inversely proportional to tubing diameter, and thus

decreasing the reactor diameter to the micron range can provide rapid and intensified heat transfer to the reacting fluid, assuring an isothermal reaction temperature profile down the length of the reactor [48–53]. Recently, a review on supercritical water gasification of biomass emphasized the need for high rates of heat transfer to the reacting fluid [12], which the microtube reactor and the parallel channel microreactor in our previous study [37] were designed to meet.

Calculations from this study suggest that previous studies that gasified biomass in continuous flow reactors were not at isothermal conditions for short residence times. The calculated temperature and phenol concentration at the center of a 508 μm diameter, 2.0 m long stainless steel tube is presented in Figure 2.2. The model results are from supercritical water gasification of phenol at 750°C, 250 bar, and at 5.0 sec and 1.0 sec residence times based on the reactor pressure and temperature set point. The initial concentration of phenol was 216 mM, and the first order kinetics, specifically the activation energy and pre-exponential terms that account for the Arrhenius temperature dependence of the rate constant, were estimated from experimentally determined kinetic data from this study. The heat of reaction, 451 kj mol^{-1}, was based on phenol reforming at 25°C and 1 bar. For comparison, the temperature profile and phenol concentration at the center of a 1.7 mm, 2.0 m long stainless steel tube reactor is presented in Figure 2.2. Based on these calculations, it is evident that the microtube reactor maintains an isothermal temperature down the majority of the reactor length. At a fluid residence time of 1.0 sec, the 1.7 mm reactor tube does not even reach the reactor temperature set point, and thus the low fluid temperature was not sufficient to degrade phenol.

2.4.1 Xylose

This was the first reported investigation for supercritical water gasification in a continuous flow reactor. Although xylose gasification has previously been studied in catalytic batch reactors just above the critical temperature of water [13-14], the reported

H_2 yields were approximately 1.0 mol H_2 per mole of xylan reacted, significantly lower than the theoretical H_2 yield of 9 for xylan and 10 for xylose based on reforming

$$C_5H_{10}O_5\ (xylose) + 5\,H_2O \rightarrow 5\,CO_2 + 10\,H_2 \qquad (2.4)$$

Xylose decomposition by supercritical water resulted in gaseous and organic liquid products in the condensed reactor effluent. Gas composition, H_2 yield, and carbon gasification efficiency for xylose, phenol, and xylose phenol mixture can be found in Table 2.2. The values are representative of reactor residence times that gas composition and gas yields were nearly independent of residence time. Gas composition predicted by thermodynamic equilibrium is compared to experimental values. For supercritical water gasification of xylose at reaction temperatures of 650ºC and 750ºC in the stainless steel and Hastelloy reactors the major gas products were CO_2 and H_2, and the minor gas products were CH_4 and CO. At 750 °C the gas composition was independent of residence time ranging from 1.1 seconds – 8.9 seconds in the stainless steel reactor. For a reaction temperature of 650 ºC the gas composition vs. residence time for the stainless steel reactor and Hastelloy reactor is presented in Figure 2.3. At 650°C in the stainless steel reactor the concentration of CO_2 increased from 31.9% at a 0.8 second residence time to 39.7% at a 3.1 second residence time, and the concentration of CO decreased from 18.5% at a 0.8 second residence time to 6.4% at a 3.1 second residence time. In the Hastelloy reactor the concentration of CO_2 and CO were independent of residence time and averaged 34% and 1.1% respectively. The reason for the lower concentration of CO in the product gas from the Hastelloy reactor compared to the stainless steel reactor can be attributed to the difference in the amount of Ni in the reactor material. Hastelloy is composed greater than 50 wt % Ni [54], whereas stainless steel is composed of only 16 wt % Ni [55]. Ni has been shown to catalyze the water gas shift reaction and the reforming of CH_4 [56-57]. The lower CO concentration from the Hastelloy reactor is closer to equilibrium values suggesting that in the Hastelloy reactor the water gas shift reaction was approaching thermodynamic equilibrium, whereas in the stainless steel reactor the water gas shift reaction kinetics were sensitive to residence time.

The concentration of CH_4 in the product gas was independent of residence time for supercritical gasification of xylose regardless of the reaction temperature and reactor material. However, in the Hastelloy reactor the average CH_4 concentration was lower compared to the stainless steel reactor, and was comparable to values predicted by thermodynamic equilibrium. The high concentration of CH_4 (11%) in the stainless steel reactor was most likely due to the CH_4 being reformed to a lesser extent. In addition, the H_2 concentration in the stainless steel reactor was lower compared to the Hastelloy reactor, suggesting that the CH_4 in the Hastelloy was being reformed to H_2 gas.

Gasification performance of a feed stock is typically benchmarked by its carbon gasification efficiency. The carbon gasification efficiency, defined as the amount of carbon in the gas divided by the total amount of carbon fed to the reactor, was independent of residence time tested for reaction temperatures of 650ºC and 750ºC in the stainless steel and Hastelloy reactors. The carbon gasification efficiency and H_2 yield vs. reactor residence time for the stainless steel and Hastelloy microtube reactors are presented in Figure 2.4 for the Hastelloy reactor. Average values over the range of residence times tested are located in Table 2.2. Complete carbon gasification efficiency was achieved at 750°C in the stainless steel reactor within a residence time of 1.1 sec, and in less than 1.0 second residence time at 650°C in the Hastelloy reactor. However, the carbon gasification only averaged 81% at 650°C in the stainless steel reactor at 650°C. The complete conversion of carbon in less than 1.0 second residence time in the Hastelloy reactor is currently the shortest reported residence time for complete gasification of biomass constituents by supercritical water at comparable reaction conditions. The lower carbon gasification efficiency in the stainless steel reactor suggests that 650°C is an insufficient reaction temperature to gasify recalcitrant liquid intermediates from xylose degradation. Increased carbon recovery in the Hastelloy reactor is a result of increased decomposition and gasification kinetics due to the higher nickel content in the reactor wall [58, 45, 34]. Corrosion to the reactor wall, associated with supercritical water processing in stainless steel continuous flow reactors is known to expose Ni and Cr to the reactor surface [58].

The H_2 yield, defined as the moles of H_2 gas generated per mole of feed reacted was independent of residence times tested for the stainless steel and Hasteloy reactor. Average values over the range of residence times tested are located in Table 2.1. The theoretical H_2 yield for xylose decomposition is 5, and for xylose reforming in supercritical water, Equation 2.4, is 10. In the stainless steel reactor the H_2 yield was far below the theoretical yield for reforming, however, if the hydrogen in the CH_2 is accounted for, the H_2 yield for 750°C almost doubles from 4.8 to 9.0 moles of H_2 generated per mole of xylose fed. At 650°C the H_2 yield was much less than 750°C due to incomplete gasification of the feed substrate. In addition, the high CO concentration in the product gas suggests the low H_2 yield is also due to non-equilibrium conversion of the CO by the water gas shift reaction. In the Hastelloy reactor the H_2 yield, was 8.2 and 9.6 including the hydrogen in methane. These yields are close to the theoretical H_2 yield based on reforming. Given that the total H_2 yield, including CH_4, was greater than the theoretical H_2 yield based only on xylose in the stainless steel and Hastelloy reactor, it is evident that a portion of the hydrogen in the product gas is being liberated from water, and thus represents a significant increase in the amount of gas being produced per mole of feed. The difference in the theoretical H_2 yield based on xylose reforming and the H_2 yield in the stainless steel reactor at 750°C and the Hastelloy reactor at 650°C is due to the incomplete reforming of CH_4 in the product gas. If the CH_4 in the product gas was reformed to CO and H_2, and the CO was shifted to CO_2, a H_2 yield of 10 would be achieved.

The clear condensed liquid effluent from the reactor was analyzed for sugars and other dissolved organic compounds. A sugars analysis performed by HPLC equipped with a refractive index detector revealed no residual xylose in the liquid effluent for all residence times tested at 650ºC and 750ºC in the stainless steel reactor and Hastelloy reactor. From a kinetics standpoint, complete xylose conversion was achieved at 650°C in less than a 1.0 second residence time. However, organic intermediates were detected in the liquid products at a 650ºC reaction temperature. A representative HPLC chromatogram with UV detection at 210 nm is presented in Figure 2.5. The major liquid intermediate was acetic acid (1). There was also small amounts of propionic and

propenoic acid present (2), as well as phenol (3). The concentration of propionic / propenoic acid and phenol was insignificant and thus was not quantified. The amount of acetic acid present in the liquid products as a result of gasification at 650°C in the stainless steel reactor versus residence time is presented in Figure 2.6. The acetic acid concentration was highest, 52 mmol/L, at a 1.3 second residence time and decreased as a function of increasing residence time thereafter. There were no organic liquid intermediates detected in the liquid products for gasification experiments conducted at 750°C in the stainless steel reactor or 650°C in the Hastelloy reactor.

It is difficult to compare results obtained from isothermal supercritical water gasification of xylose since this is the first known study that uses a hemicellulose model compound in a continuous flow reactor. However, the gas products and reaction kinetics from supercritical water gasification of xylose are comparable to glucose, a hexose and model cellulose compound. Similar to xylose, the supercritical water gasification of glucose in a stainless steel flow reactor at 650°C produced gas with a H_2 concentration ranging from 33% - 47%, about 36% CO_2, and a about 10% CH_4 [15, 37]. Also similar to xylose, a carbon gasification efficiency greater than 80% is attainable at relatively short residence times, 2 second – 40 second, at reaction temperatures above 600°C in a continuous flow stainless steel reactor [41, 15, 37, 42, 43, 44]. One possible reason for the similar reaction kinetics and product selectivity for glucose and xylose is a comparable reaction mechanism. A simplified scheme showing how xylose is decomposed by supercritical water based on our liquid product analysis is presented in Figure 2.7. The scheme shows that xylose is broken down to acetic and propenoic acid which is gasified to CO and H_2. The gas phase products resulting from gasification of organic acids were subject to gas phase reactions including the water gas shift, methanation reaction, and methane reforming reaction. The presence of acetic acid and propenoic acid present in the liquid products suggest that like glucose, xylose is being broken down to organic acids that are being further gasified. Given that acetic acid was the principal intermediate liquid product, it is likely that acetic acid is more recalcitrant to gasify comparatively. The presence of phenol in the liquid products indicates the presence of furan type compounds that may have reacted with a diene via a Diels Alder cyclo-addition [59].

2.4.2 Phenol

The goals for the supercritical water gasification of phenol were to determine the effect of residence time on gasification performance and reaction kinetics at 750ºC and 250 bar in the stainless steel reactor, and determine the effect of residence time on major liquid intermediate formation and gasification. The theoretical H_2 based on gasification of the substrate is 3 moles of H_2 per mole of phenol reacted, however for phenol reforming

$$C_6H_5OH + 11\,H_2O \rightarrow 6\,CO_2 + 14\,H_2 \qquad (2.5)$$

the theoretical H_2 yield is 14 moles of H_2 produced per mole of phenol reacted, in which case 11 moles of H_2 are being liberated from water.

The resulting condensed reactor effluent from a 2.0 wt % aqueous phenol feed solution contained hydrogen rich gaseous and organic liquid products. Gas composition versus residence time is presented in Figure 2.8. At residence times greater than 5 seconds the gas composition was independent of residence time, and average values are reported in Table 2.2. At residence times less than 5 seconds, CO increased with decreasing residence time, 34.5% at a 1.3 second residence time, and CO_2 decreased with decreasing residence time, 15.5% at a 1.3 second residence time. This is likely due to non equilibrium conversion of CO by the water gas shift reaction as well as a consequence of incomplete gasification of the feed substrate. The concentration of H_2 and CH_4 in the product gas was relatively constant as a function of residence time, and comparable to gas composition from the gasification of xylose in the stainless steel reactor.

A GC-FID liquid analysis for the reactor effluent reveled residual phenol at very short residence times and the presence of benzene at all residence times tested. A detailed reaction mechanism for the degradation of phenol in supercritical water has been proposed by Gopalan and Savage [61]. A sample gas chromatogram comparing a 1.3 second residence time to a 27 second residence time is presented in Figure 2.9. Benzene (1) is present in both chromatograms, while phenol (3) is only present in the 1.3 second

residence time chromatogram. The concentration of phenol and benzene in the liquid products vs. residence time is presented in Figure 2.10. At 700°C, incomplete phenol conversion was observed for residence times up to 73 sec, whereas at 750°C and residence times greater than 7.4 seconds complete phenol conversion was achieved. An apparent first order rate constant of 0.66 ± 0.03 sec^{-1} was calculated for the supercritical water gasification of phenol at 750ºC, and 0.078 ± 0.007 sec^{-1}. The rate constants were calculated from the slope of a linear regression line of the equation ln $(1/(1-X_p))$, where X_p is phenol conversion. The apparent activation energy (E_a) for phenol conversion in supercritical water in the absence of an external oxidation source was 353 kJ mol^{-1}, and the Arrhenius constant (A_E) was 7.1 x 10^{13}, which was estimated from apparent rate constant versus temperature data from 700°C to 750°C. The concentration of benzene was constant with respect to residence time, and averaged 0.42 mg/ml ± 0.14 mg/ml or a 2.5% molar yield. Benzene molar yields as high as 7.5% and 5% have been reported for the supercritical water gasification of phenol [32, 46]. The relatively constant low concentration of benzene suggests that carbon gasification efficiency is not limited by the decomposition of benzene, rather is dependent on the decomposition of other, more recalcitrant liquid intermediates. Possible refractory intermediates include dimers formed by radical recombination reactions such as dibenzofuran and biphenyl [60].

Gasification of lignin model compounds such as phenol is generally slower than cellulose or hemicellulose model compounds due to high chemical stability provided by its aromatic network. The carbon gasification efficiency and H_2 yield for gasification of phenol at 750ºC by supercritical water is shown in Figure 2.11. The carbon recovery in the gas increased from 21% at a 1.3 second residence time to 68% at a 27 second residence time, and the H_2 yield increased from 0.8 moles of H_2 generated per mole of phenol fed to 3.7, which is greater than the theoretical H_2 yield based on the decomposition of phenol, but much less than the theoretical H_2 yield based on reforming. If the hydrogen atoms in the methane are accounted for, the H_2 yield increases to 5.2 at a 27 second residence time which indicates 2.2 moles or 42% of hydrogen in the product gas came from water. It has been shown that with the addition of a nickel catalyst, a H_2 yield of 9 is attainable [32], suggesting that supercritical water gasification of phenol may

significantly benefit from a reactor constructed from a high nickel content alloy such as Hastelloy. DiLeo et al. [26] determined the optimal equilibrium conditions for liberating hydrogen from water during supercritical water gasification was low reactant loading, low water density, and high temperature. Specifically, in this study they were able to liberate more than 70% of the hydrogen atoms in their product gas from water when they used Ni catalysts to gasify 2.0 wt % phenol at 600ºC and a 1 hour residence time. Although we are not using a Ni catalyst specifically, the reactor tube was fabricated from 304 stainless steel, which nominally contains 17 wt % Ni and 12 wt % Cr.

There have been many previous studies on the supercritical water gasification of phenol; however, there are few studies that report on supercritical water gasification of phenol above 600ºC in a continuous flow reactor, where gasification is dominant in the absence of an external oxidation source. It is difficult to compare results from the isothermal supercritical water gasification of phenol to previous studies due to different conditions and reactor setups used. For example Xu et al. [46] catalytically gasified phenol at 600ºC and 34.5 MPa in an Inconel 625 flow reactor with an inner diameter of 4.75mm and a carbon catalyst. The highest carbon gasification efficiency they achieved was 12% and 80% phenol conversion. Although Xu et al. [46] used a high nickel content reactor as well as a carbon catalyst, the heat transfer to the reacting fluid was most likely poor due to the large reactor tube diameter. We attribute our high percentage of carbon recovery in the gas and fast phenol decomposition kinetics to fast heating rates as well as rapid heat transfer to the reacting fluid characteristic of micron sized reactor passages.

2.4.3 Xylose / Phenol Mixture

The goal of supercritical water gasification experiments with a mixture of xylose and phenol was to determine if interactions exist between phenol and xylose that influence gasification performance. A 1:1 (w/w) aqueous solution of phenol / xylose was gasified at 750ºC and 250 bar. The resulting gas composition is presented in Figure 2.12. Similar to xylose and phenol the gas consisted of H_2, CO_2, CH_4, and CO. However, unlike the

individual substrates, the gas contained a high concentration of CH_4 (18 %), and every component of the gas products was residence time dependent. CH_4 and CO_2 increased with increasing residence time, whereas, CO and H_2 decreased with increasing residence time. The effect of residence time on gas composition suggests interactions between phenol and xylose during supercritical water gasification may influence the rate at which the phenol is being gasified.

The H_2 yield and carbon recovery for the supercritical water gasification of phenol / xylose mixture versus residence time is presented in Figure 2.11. The H_2 yield for the mixture had a maximum value of 3.1 mol of H_2 per mol of feed at a 10.6 second residence time and linearly decreased thereafter. The carbon gasification efficiency for the mixture increased as a function of increasing residence time similar to phenol. A maximum carbon recovery of 86.2% was achieved at a residence time of 27 seconds.

At 750 °C, the gasification of phenol in supercritical water was much slower than that of xylose, as shown in Figures 2.10 and 2.11. However, the addition of xylose to phenol accelerated the rate of phenol decomposition by a factor of 3, increasing the apparent first order rate constant to 2.0 ± 0.2 sec^{-1}. The concentration of phenol and benzene in the liquid products are presented in Figure 2.10. For the gasification of the xylose / phenol mixture by supercritical water, the H_2 produced by xylose decomposition and the water gas shift reaction promoted the hydrogenation of phenol to benzene and consequently accelerated the rate of phenol decomposition. Furthermore, the high concentration of H_2 provided by xylose reforming might have also promoted the continued hydrogenation of benzene to cyclohexane, which then was reformed by supercritical water to H_2 and CO. An increase in the rate of benzene hydrogenation would lower the accumulation of the benzene intermediate, which would account for the lower concentration of benzene measured in the liquid products.

The total volumetric gas production rate, referenced to 25°C and 1 atm, versus feed rate for xylose, phenol, and the xylose / phenol mixture are compared in Figure 2.13. The gas production rates for xylose were linear as a function of feed rate for reaction temperatures of 650ºC and 750ºC. Additionally, the gas production rate for xylose in the Hastelloy

reactor at 650°C was comparable to the gas production rate at 750°C in the stainless steel reactor due to a catalytic effect from high Ni content in the Hastelloy reactor. The higher gas production rate observed in the Hastelloy reactor was due to a higher percentage of methane in the product gas being reformed to H_2 and CO_2. A decrease in the gas production rate from the gasification xylose by supercritical water at 650°C in the stainless steel reactor was due to refractory liquid byproduct formation. Contrary to xylose the gas production rate for the supercritical water gasification of phenol leveled off as the phenol feed rate was increased due to incomplete gasification of the substrate. However, when xylose was added to phenol the volumetric gas production rate was linear, suggesting that interactions between H_2 from the rapid gasification of the xylose, and phenol were increasing the gasification rate of phenol.

Lignin is more recalcitrant to gasification in supercritical water than cellulose. The results of this study suggest that the gasification of a mixture of hemicellulose and lignin by supercritical water may accelerate the conversion of lignin by facilitating hydrogenation, using H_2 generated by rapid reforming of hemicellulose. Specifically, in cellulosic biorefinery operations, it is envisioned that a portion of the lignocellulosic pretreatment stream that contains solublized hemicellulose and lignin could be added to the residual lignin stream from enzymatic cellulose hydrolysis, as proposed in Figure 2.14. The combined byproduct streams, which already contain water, could be converted directly to a compressed H_2-rich gas at supercritical water conditions.

2.5 Conclusion

In conclusion, this study demonstrated that the microtube configuration used in this study ensured isothermal gasification of xylose, phenol, and xylose / phenol mixtures under continuous flow conditions at short residence times. Complete xylose gasification based on carbon was achieved in less than 1 second residence time at 650ºC and 250 bar in the Hastelloy microtube reactor. Complete conversion of phenol was achieved at 750°C, 250 bar and a 7.4 second residence time in the stainless steel reactor. It was determined that

the addition of xylose to phenol significantly increased the gasification rate of phenol in supercritical water at 750°C.

2.6 Acknowledgement

This research was supported by Bend Research, Inc., Bend, Oregon, and by the US Army under the Tactical Energy Systems program administered through the Oregon Nanoscience and Microtechnologies Breakthrough Institute.

2.7 Literature Cited

1. Mosier N, Wyman C, Dale B, Elander R, Lee Y, Holtzapple M, Ladisch M, 2005 *Bioresource Technology* **96** 673-686
2. Hendriks A, Zeeman G 20009 *Bioresource Technology* **100** 10-18
3. Wyman C E 1994 *Bioresource Technology* **50** 3-16
4. Saha B 2003 *Journal of Industrial Microbiology & Biotechnology* **30** 279-291
5. Matsumura Y, Minowa T, Potic B, Kersten S, Prins W, van Swaaij W, Beld B, Elliott D, Neuenschwander G, Kruse A, Antal M *Biomass and Bioenergy* **29** 269-292
6. Kruse A, Dinjus E 2007 *J of Supercritical Fluids* **41** 361-379
7. McKendry P 2002 *Bioresource Technology* **83** 55-63
8. Calzavara Y, Joussot-Dubien C, Boissonnet G, Sarrade S 2005 *Energy Conversion and Management* **46** 615-631
9. Loppinet-Serani A, Aymonier C, Cansell F 2008 *ChemSusChem* **1** 486-503
10. Navarro R M, Sánchez-Sánchez M C, Alvarez-Galvan M C, del Valle F, Fierro J L G 2009 *Energy Environ Sci* **2** 35-54
11. Peterson A A, Vogel F, Lachance R P, Fröling M, Antal J M J, Tester J 2008 *Energy Environ Sci* **1** 32-65
12. Kruse A 2008 *Biofuels Bioproducts & Biorefining* **2** 415-37
13. Yoshida T, Matsumura Y 2001 *Ind Eng Chem* **40** 5469-5474
14. Guo L, Lu Y, Zhang X, Ji C, Guan Y, Pei A 2007 *Catalysis Today* **129** 275-286
15. Lu Y J, Guo L J, Ji C M, Zhang X M, Hao X H, Yan Q H 2006 *International Journal of Hydrogen Energy* **31** 822-831
16. D'Jesus P, Boukis N, Kraushaar-Czarnetzki B, Dinjus E 2006 *Ind Eng Chem* **45** 1622-1630
17. Demirbas A 2010 *Energy Sources Part A* **32** 1342-1354
18. Hao X H, Guo L J, Mao X, Zhang X M, Chen X J 2003 *International Journal of Hydrogen Energy* **28** 55-64
19. Sato T, Osada M, Watanabe M, Shirai M, Arai K 2003 *Ind Eng Chem* **42** 4277-4282

20. Osada M, Sato T, Watanabe M, Adschiri T, Arai K 2004 *Energy and Fuels* **18** 327-333

21. Yoshida T, Oshima Y, Matsumura Y 2004 *Biomass and Bioenergy* **26** 71-78

22. Sato T, Furusawa T, Ishiyama Y, Sugito H, Miura Y, Sato M, Suzuki M, Itoh N *Ind Eng Chem* **45** 615-622

23. Osada M, Sato O, Arai K, Shirai M 2006 *Energy and Fuels* **20** 2337-2343

24. Osada M, Sato O, Watanabe M, Arai K, Shirai M 2006 *Energy and Fuels* **20** 930-935

25. Kruse A, Meier D, Rimbrecht P, Schacht M 2000 *Ind Eng Chem* **39** 4842-4848

26. DiLeo G, Neff M, Kim S, Savage P 2008 *Energy and Fuels* **22** 871-877

27. Resende F, Fraley S, Berger M, Savage P 2008 *Energy and Fuels* **22** 1328-1334

28. Okuda K, Ohara S, Umetsu M, Takami S, Adschiri T *Bioresource Technology* **99** 1846-1852

29. Saisu M, Sato T, Watanabe M, Adschiri T, Arai K 2003 *Energy and Fuels* **17** 922-928

30. Martino C J, Savage P E 1997 *Ind. Eng Chem Res* **36** 1385-1390

31. Portela E, Nebot E, Martinez de la Ossa E 2001 *Chemical Engineering Journal* **81** 287-299

32. DiLeo G, Neff M, Savage P 2007 *Energy and Fuels* **21** 2340-2345

33. Yoshida K, Kusaki J, Ehara K, Saka S 2005 *Applied Biochemistry and Biotechnology* **121** 795-806

34. Kersten S, Potic B, Prins W, Van Swaaij W 2006 *Ind. Eng Chem Res* **45** 4169-4177

35. Yoshida T, Oshima Y 2004 *Ind Eng Chem Res* **43** 4097-4104

36. Arai K, Adschiri T, Watanabe M 2000 *Ind Eng Chem Res* **39** 4697-4701

37. Goodwin A, Rorrer G 2008 *Ind Eng Chem* **47** 4106-4114

38. Goldberg R N, Tewari Y B 1989 *J Phys. Chem. Ref. Data* **18** 809-880

39. Celata G P, Cumo M, McPhail S J, Zummo G 2007 *Microfluid Nanofluid* **3** 697-707

40. National Institute for Standards and Technology (NIST) NIST Chemistry WebBook *http://webbook.nist.gov* accessed 2008

41. Holgate R, Meyer J, Tester J 1995 *AICHE Journal* **41** 637-647

42. Lee I, Kim M, Ihm S 2002 *Ind Eng Chem Res* **41** 1182-1188

43. Yu D, Aihara M, Antal J 1993 *Energy and Fuels* **7** 574-577

44. Hao X, Guo L, Mao X, Zhang X, Chen X 2003 *International Journal of Hydrogen Energy* **28** 55-64

45. Antal J, Allen S, Schulman D, Xu X 2000 *Ind Eng Chem Res* **39** 4040-4053

46. Xu X, Matsumura Y, Stenberg J, Antal J 1996 *Ind Eng Chem Res* **35** 2522-2530

47. Byrd A, Pant K, Gupta R 2007 *Ind Eng Chem* **46** 3574-3579

48. Holladay J, Wang Y, Jones E 2004 *Chem Rev* **104** 4767-4790

49. Gokhale S, Tayal R, JayaramanV, Kulkarni B 2005 *International Journal of Chemical Reactor Engineering* **3** 1542

50. Palo D, Stenkamp V, Dagle R, Jovanovic G 2006 *Advanced Micro and Nanosystems* **5**

51. Roberge D, Bieler N, Thalmann M 2006 *Pharma Chem* **5** 14-17

52. Hessler V, Loeb P, Loewe H, Gunther K 2007 *Micro Instrumentation* 85-129

53. Mills P, Quiram D, Ryley J 2007 *Chemical Engineering Science* **62** 6992-7010

54. American Society for Metals (ASM) *Metals Handbook. Properties and Selection: Iron Nonferrous Alloys and Special-Purpose Materials* 10th ed (ASM International: Materials Park, OH 1990 vol. 2)

55. American Society for Metals (ASM). *Metals Handbook. Properties and Selection: Iron Steels and High Performance Alloys*, 10th ed (ASM International: Materials Park, OH 1990 vol. 1)

56. Bustamante F, Enick R M, Killmeyer R P, Howard B H, Rothenberger K S, Cugini A V, Morreale B D, Ciocco M V 2005 *AICHE Journal* **51** 1440-1454

57. Kruse A, Dinjus E 2003 *Angew Chem Int Ed* **42** 909-911

58. Resende F, Neff M, Savage P 2007 *Energy and Fuels* **21** 3637-3643

59. Sinag A, Kruse A, Rathert J 2004 *Ind Eng Chem Res* **43** 502-8

60. Williams P, Onwudili J 2005 *Ind Eng Chem Res* **44** 8739-8749

61. Goplan S, Savage P 1994 *Phys Chem* **98** 12646-12652

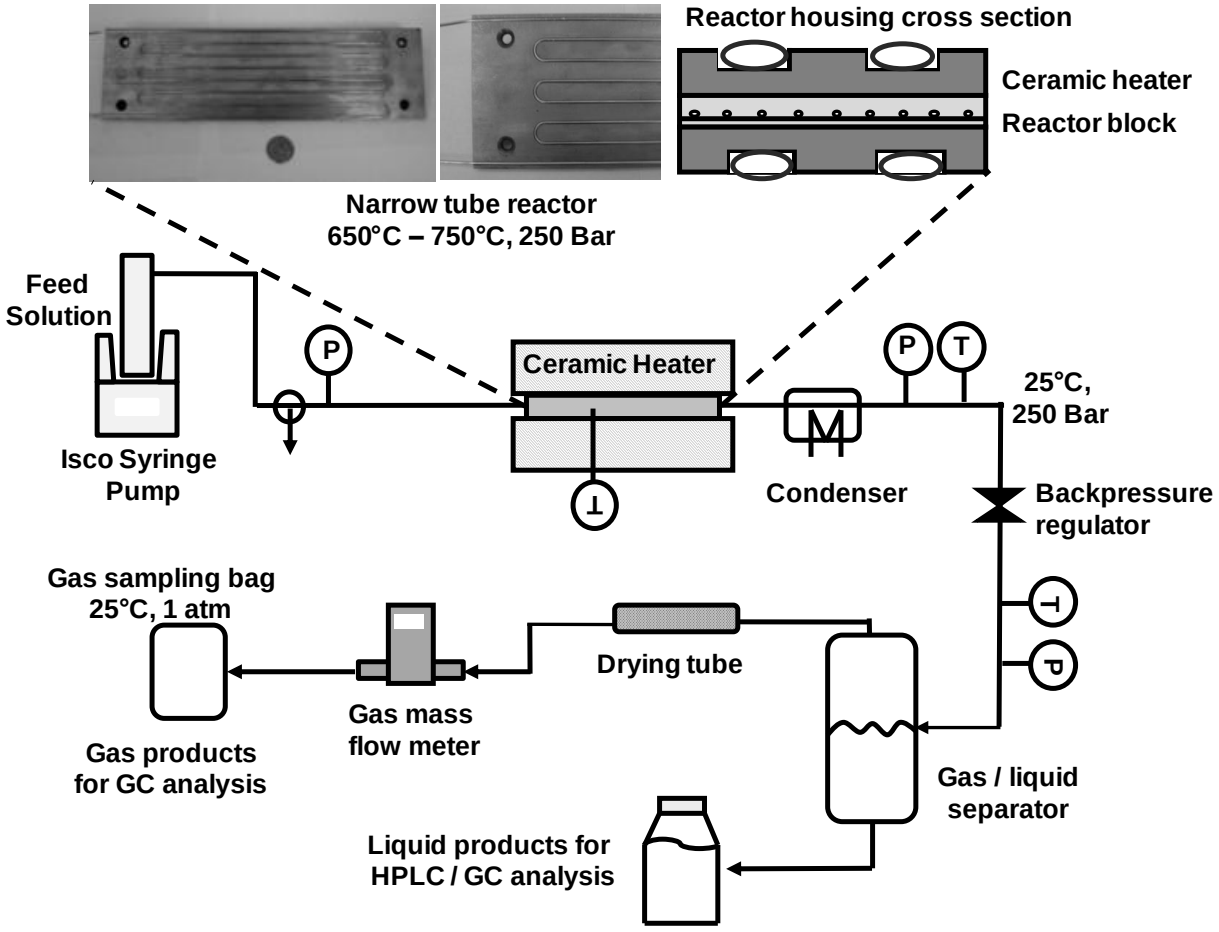

Figure 2.1. Microtubular reactor and continuous flow reactor test loop.

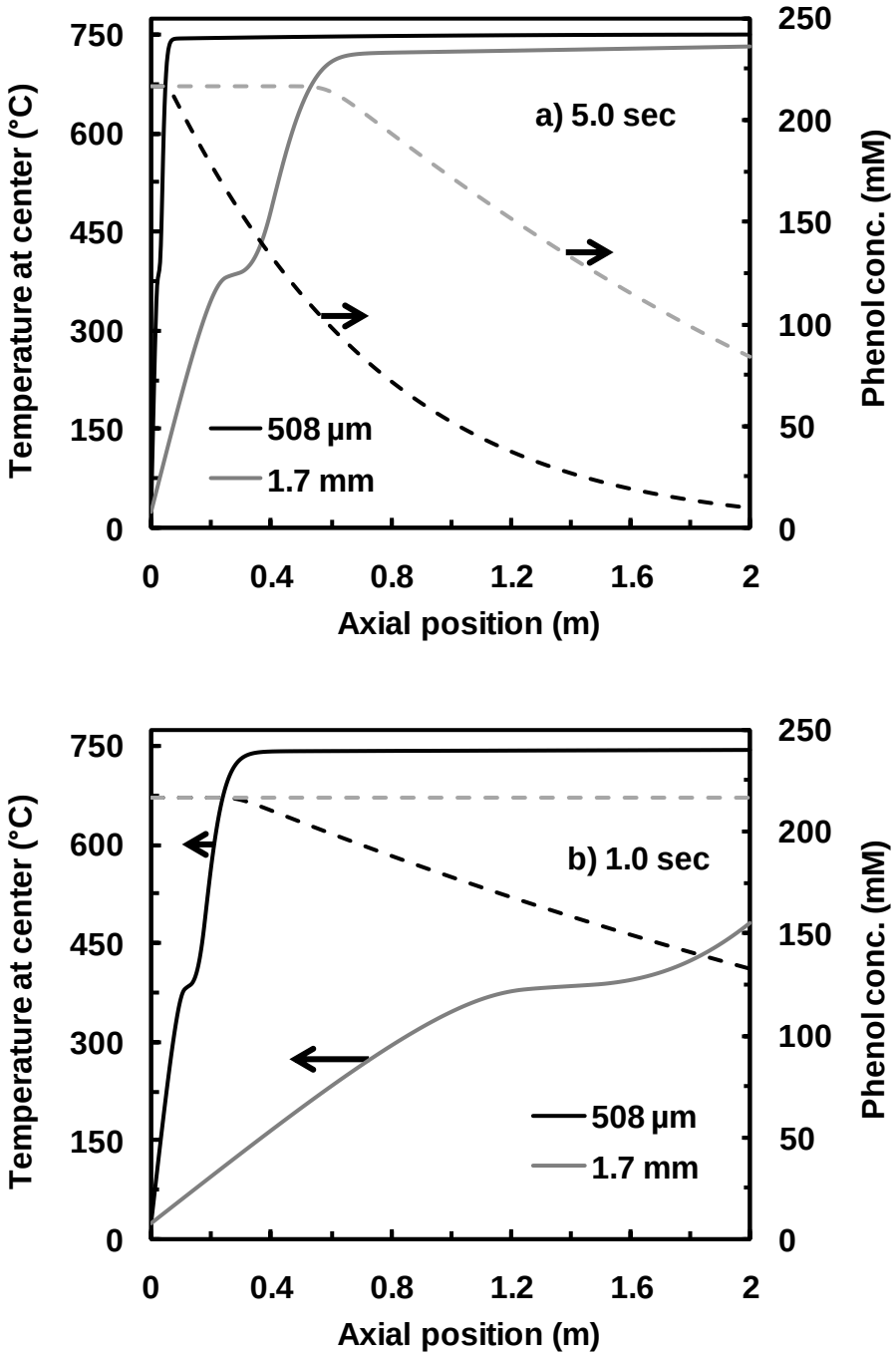

Figure 2.2. Prediction of temperature profiles in the microtube reactor. a) Comparison of temperature and phenol conversion profiles in the 508 µm diameter tube vs. 1.7 mm diameter tube at a heater block temperature of 750°C, fluid pressure of 250 bar and 5.0 sec reactor residence time. b) Comparison at 1.0 sec. reactor residence time.

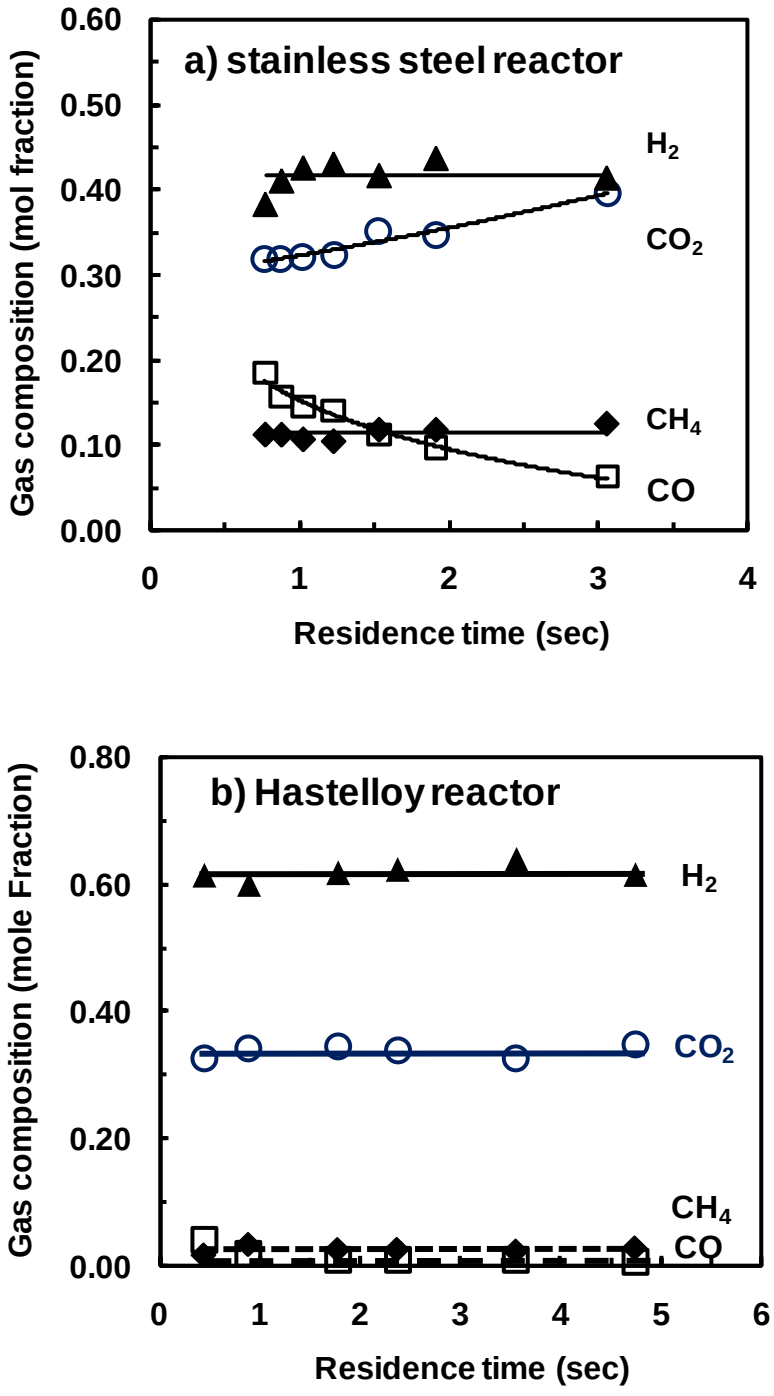

Figure 2.3. Gas composition from supercritical water gasification of xylose (42 g L^{-1}, 277 mM) verses residence time at 650°C and 250 bar. in the a) stainless steel micro tube reactor and b) Hastelloy microtube reactor.

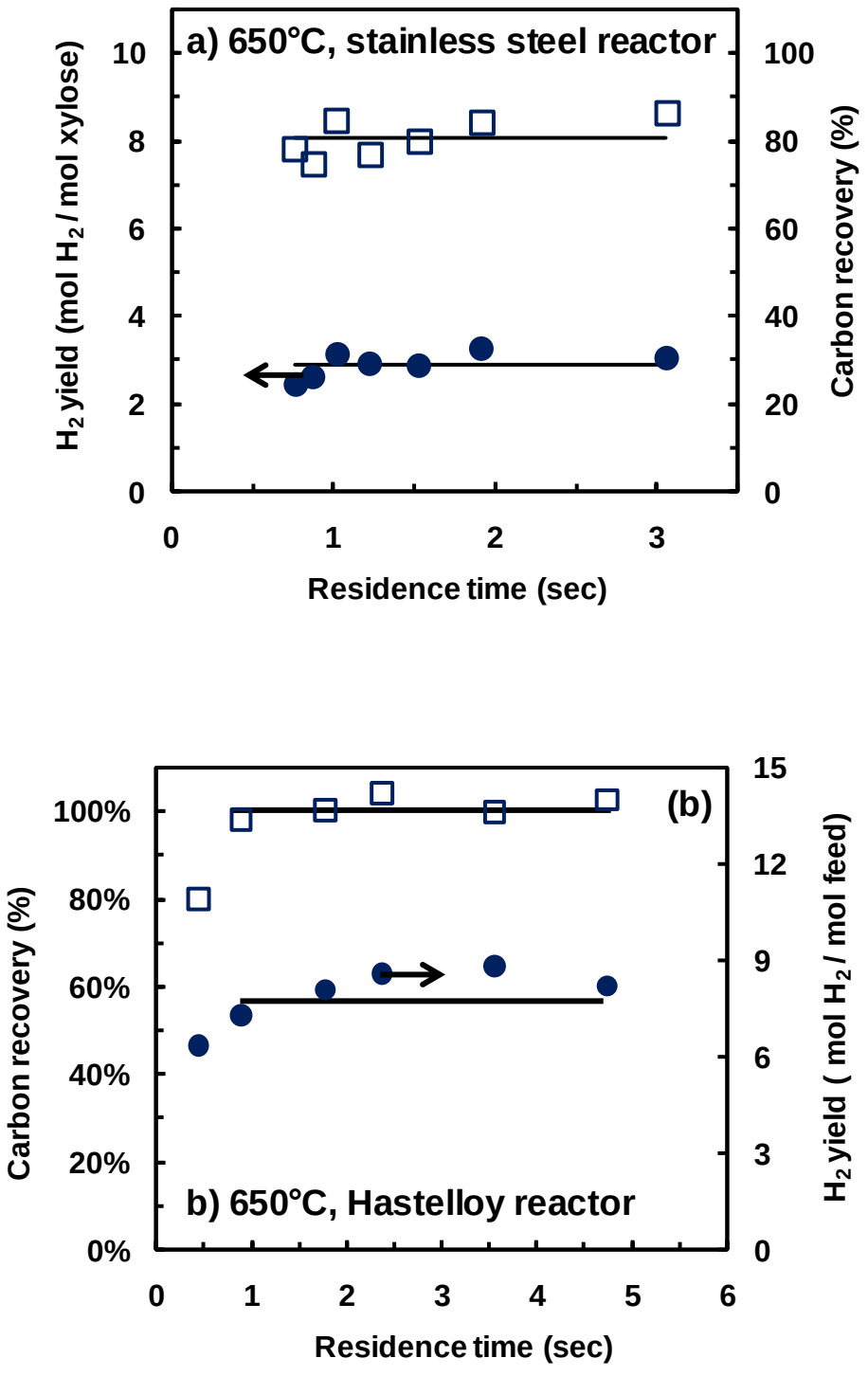
a) 650°C, stainless steel reactor
H2 yield (mol H2 / mol xylose)
Carbon recovery (%)
Residence time (sec)
0
2
4
6
8
10
0
20
40
60
80
100
0
1
2
3
(b)
b) 650°C, Hastelloy reactor
Carbon recovery (%)
H2 yield (mol H2 / mol feed)
Residence time (sec)
0%
20%
40%
60%
80%
100%
0
3
6
9
12
15
0
1
2
3
4
5
6

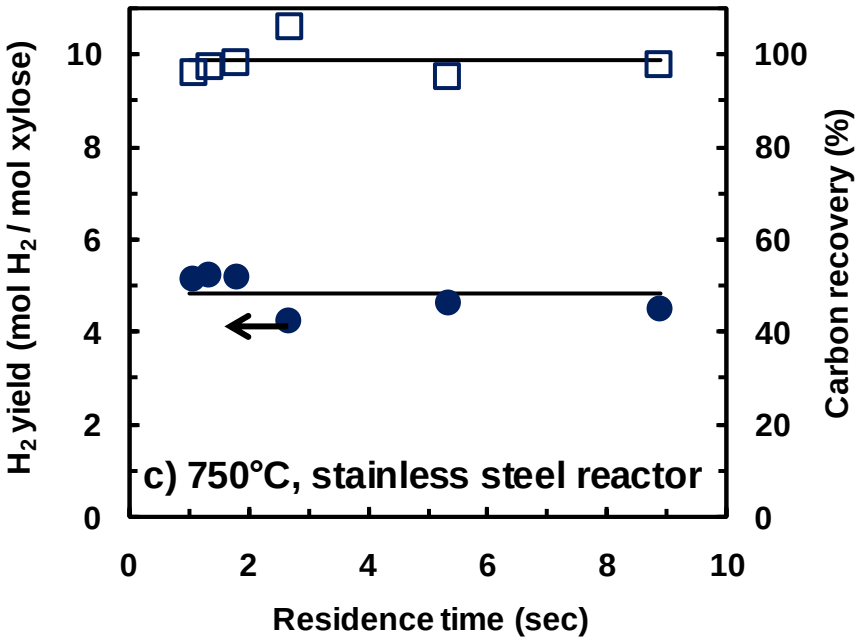

Figure 2.4. Carbon gasification efficiency and H_2 yield from the supercritical water gasification of xylose (20 g L^{-1}, 136 mM) verses residence time at 250 bar and a) 650°C in the stainless steel micro tube reactor, b) 650°C in the Hastelloy microtube reactor, and c) 750°C in the stainless steel micro tube reactor.

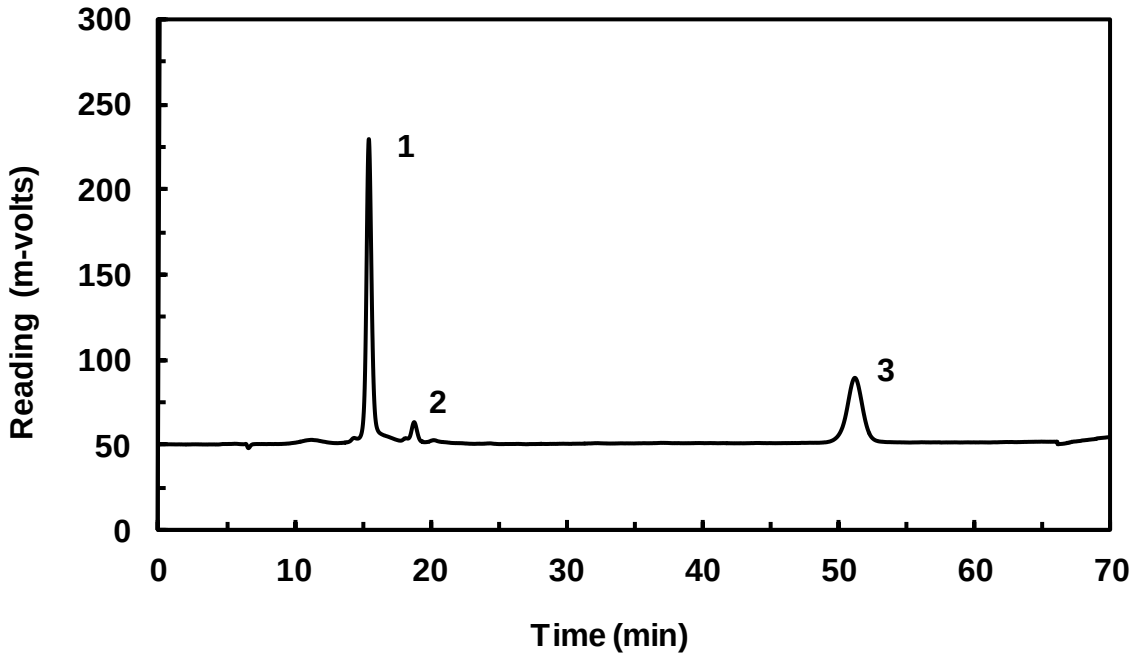

Figure 2.5. HPLC chromatogram of the liquid products from the supercritical water gasification of xylose (20 g L^{-1}, 136 mM) at 650ºC, 250 bar, and a 1.5 second residence time in the stainless steel reactor. Compound identification: acetic acid (1), propenoic / propionic acid (2), phenol (3).

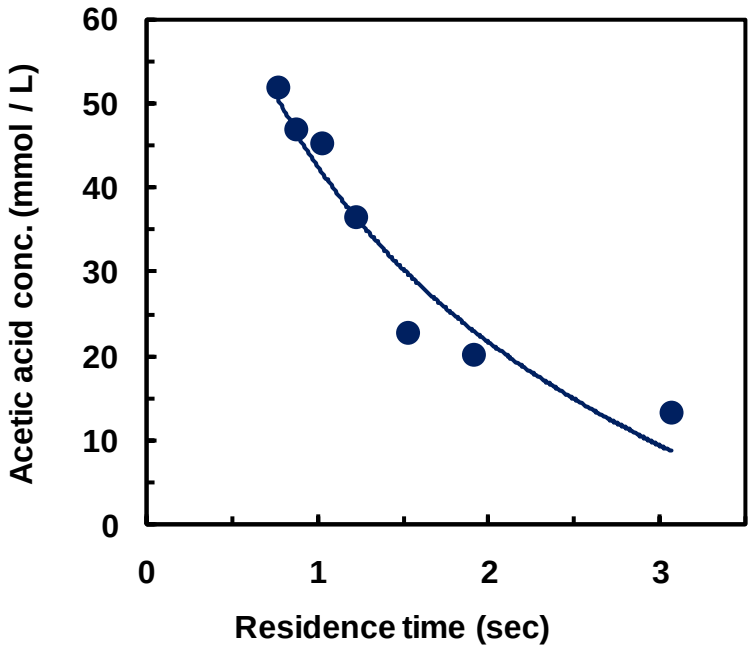

Figure 2.6. Acetic acid concentration in the liquid products from the supercritical water gasification of xylose (20 g L^{-1}, 136 mM) verses residence time at 250 bar and 650°C in the stainless steel micro tube reactor.

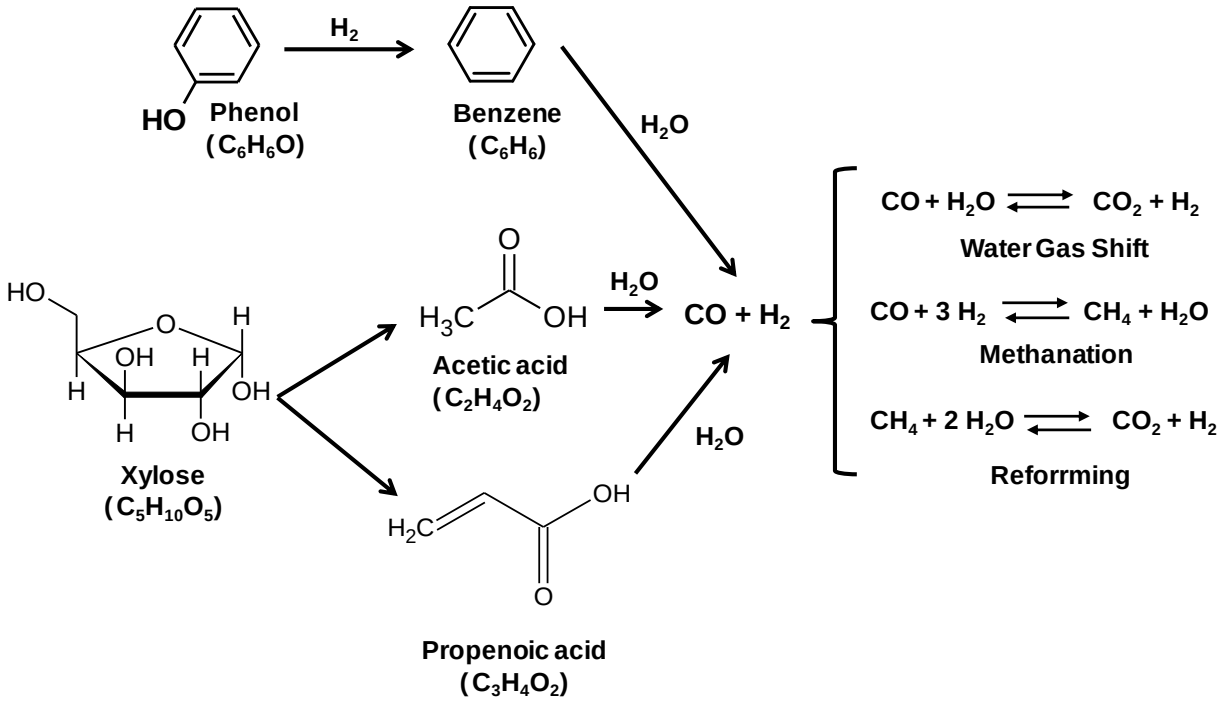

Figure 2.7. Scheme for supercritical water gasification of xylose and phenol.

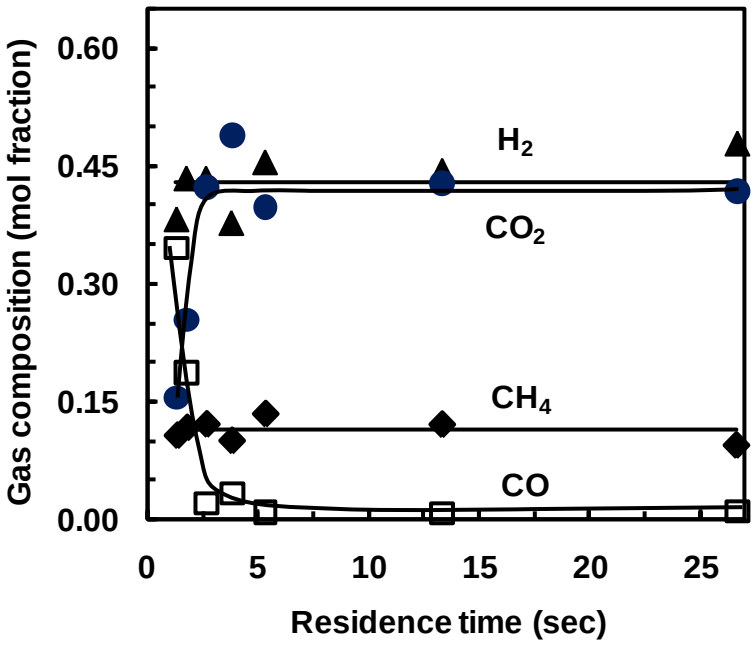

Figure 2.8. Gas composition from the supercritical water gasification of phenol (20 g L^{-1}, 216 mM) verses residence time at 750°C and 250 bar in the stainless steel reactor.

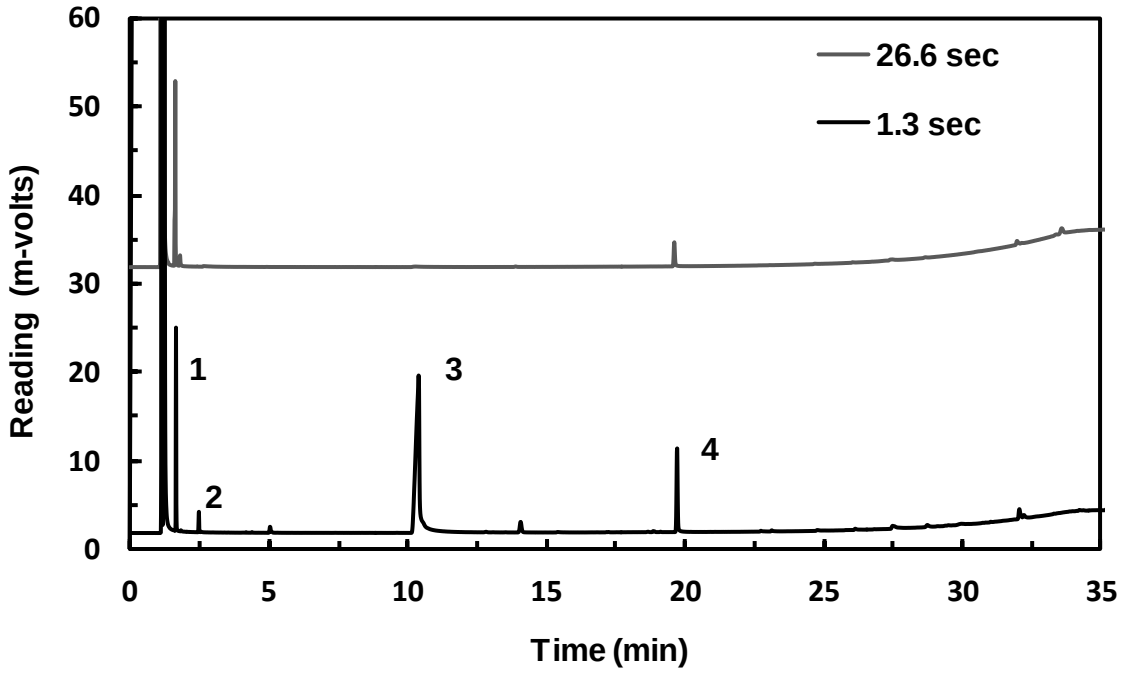

Figure 2.9. GC chromatograms of the liquid products from the supercritical water gasification of phenol (20 g L^{-1}, 216 mM) at two representative residence times from reactions at 750°C and 250 bar in the stainless steel reactor. Compound identification: benzene (1), phenol (3), peaks (2) and (4) are unknown.

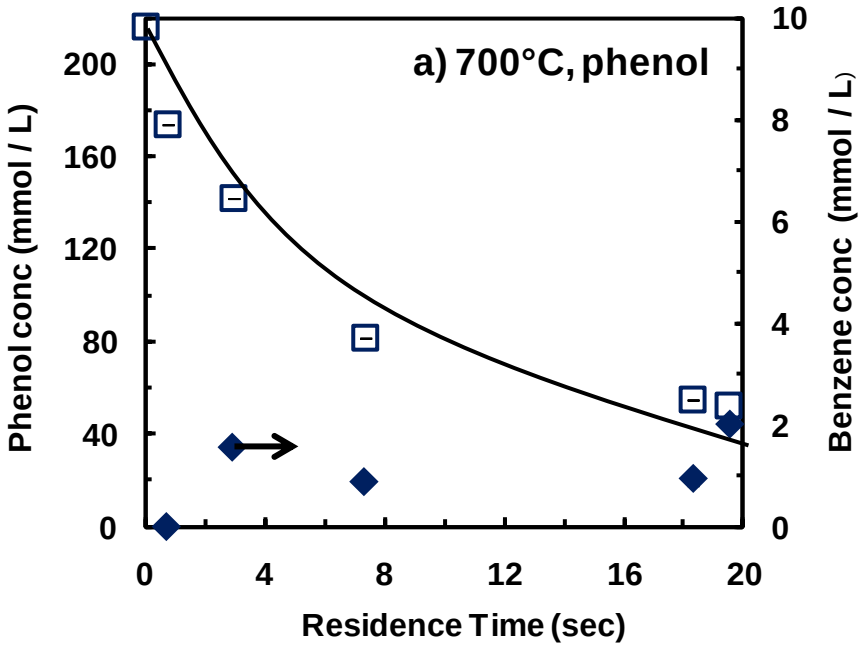
a) 700°C, phenol
Phenol conc (mmol / L)
Benzene conc (mmol / L)
Residence Time (sec)
0
40
80
120
160
200
0
2
4
6
8
10
0
4
8
12
16
20

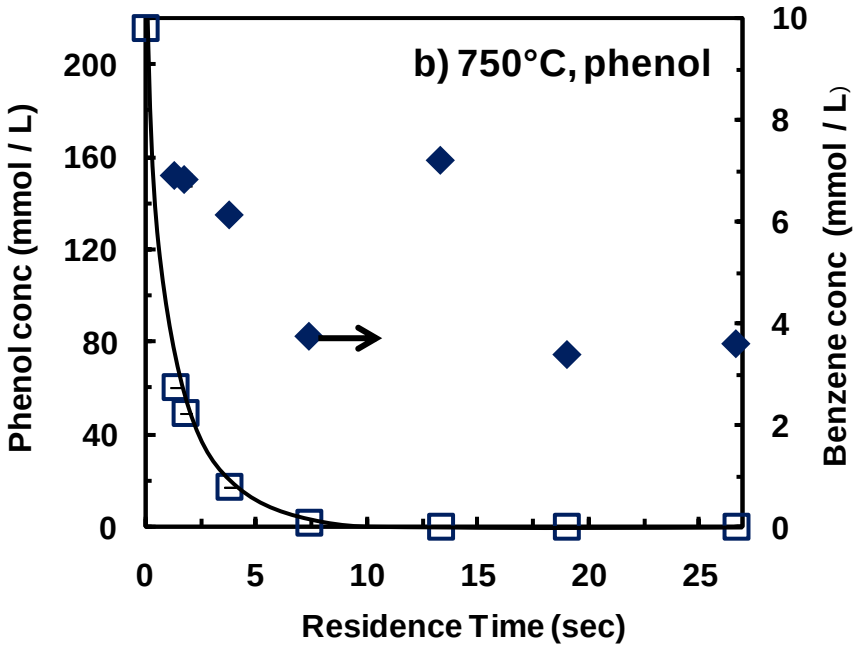
b) 750°C, phenol
Phenol conc (mmol / L)
Benzene conc (mmol / L)
Residence Time (sec)
0
40
80
120
160
200
0
2
4
6
8
10
0
5
10
15
20
25

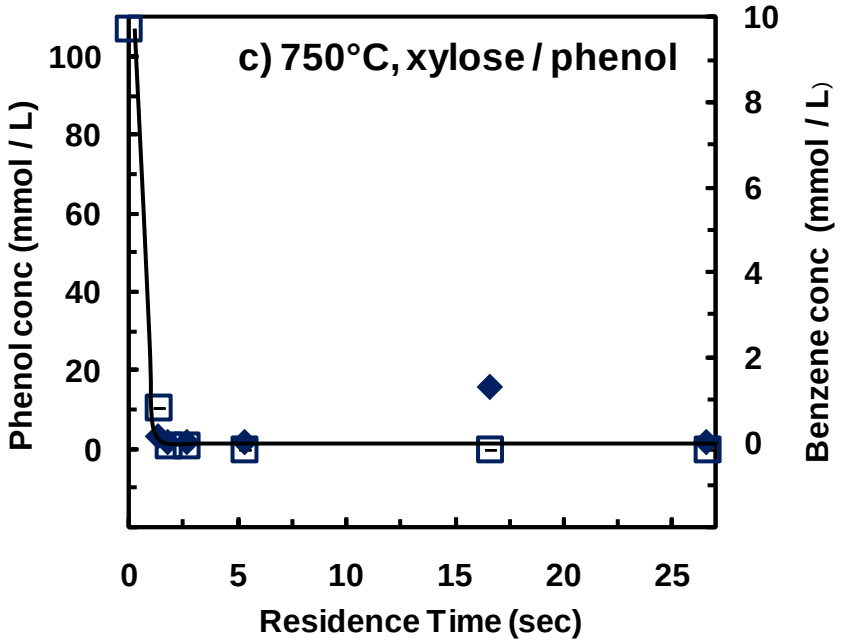

Figure 2.10. Liquid product concentration versus residence time for the supercritical water gasification of phenol and phenol / xylose mixture (10 g L^{-1} phenol, 10 g L^{-1} xylose) in the stainless steel reactor at a) phenol, 700°C; b) phenol, 750°C; c) xylose / phenol mixture 750°C.

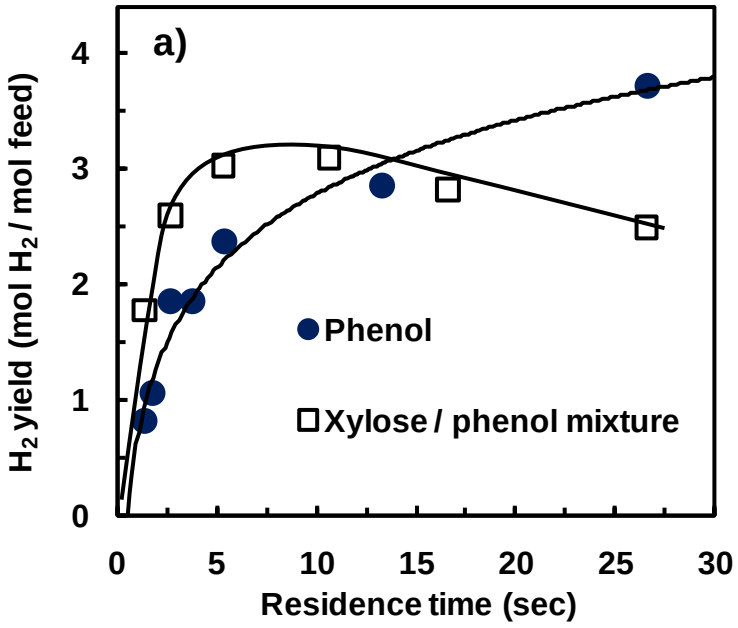

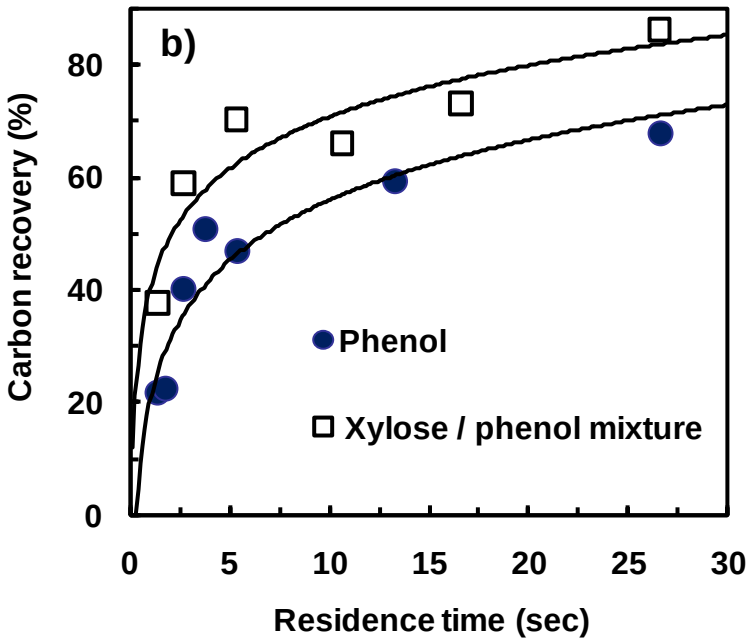

Figure 2.11. a) H_2 yield and b) recovered carbon in the gas from the supercritical water gasification of phenol (20 g L^{-1}, 216 mM) and a xylose phenol mixture (10 g L^{-1} xylose and 10 g L^{-1} phenol) versus residence time at 750°C and 250 bar in the stainless steel reactor.

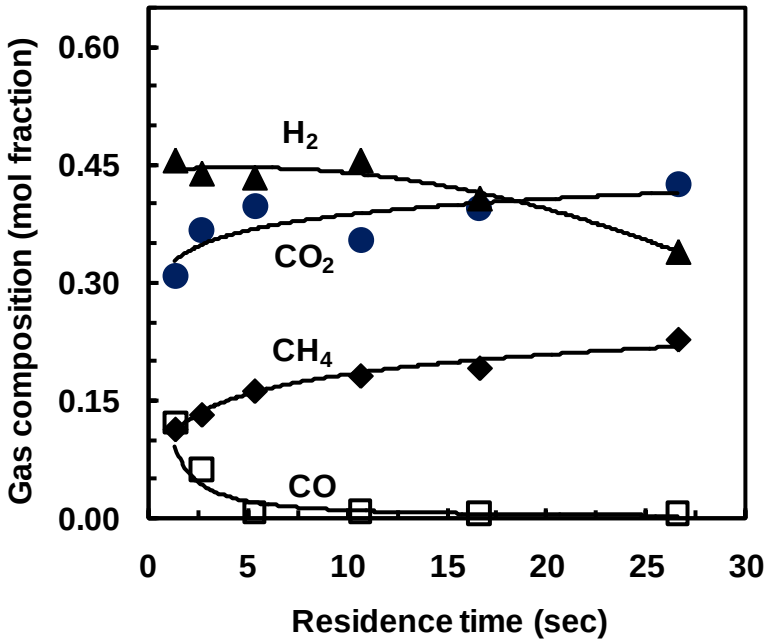

Figure 2.12. Gas composition from the supercritical water gasification of a xylose / phenol mixture (10 g L^{-1} xylose and 10 g L^{-1} phenol) versus residence time at 750°C and 250 bar in the stainless steel reactor.

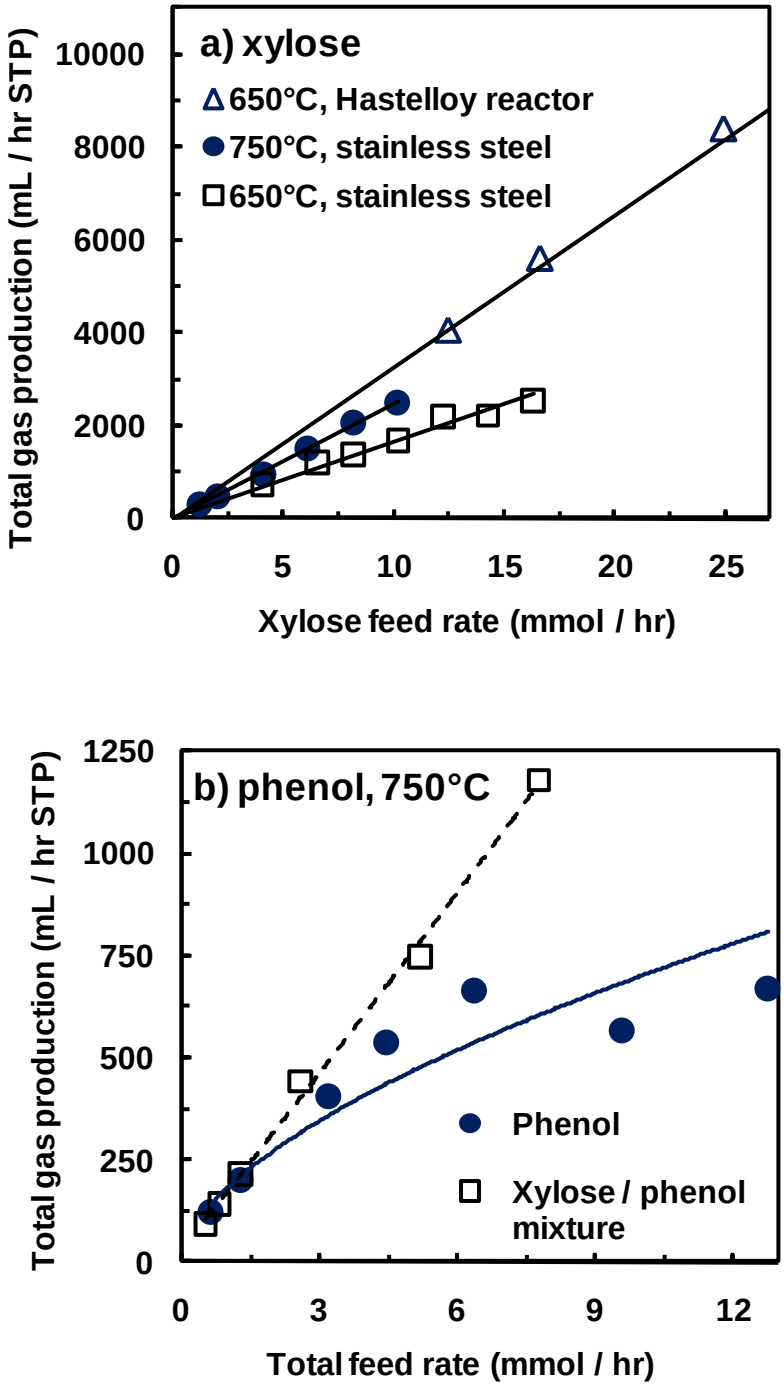

Figure 2.13. Gas production rate versus feed rate for the supercritical water gasification of a) xylose (20 g L^{-1}, 136 mM) in the stainless steel reactor and (42 g L^{-1}, 277 mM) in the Hastelloy reactor, b) phenol (20 g L^{-1}, 216 mM) (b), and a xylose phenol mixture (10 g L^{-1} xylose and 10 g L^{-1} phenol) in the stainless steel reactor at 750°C.

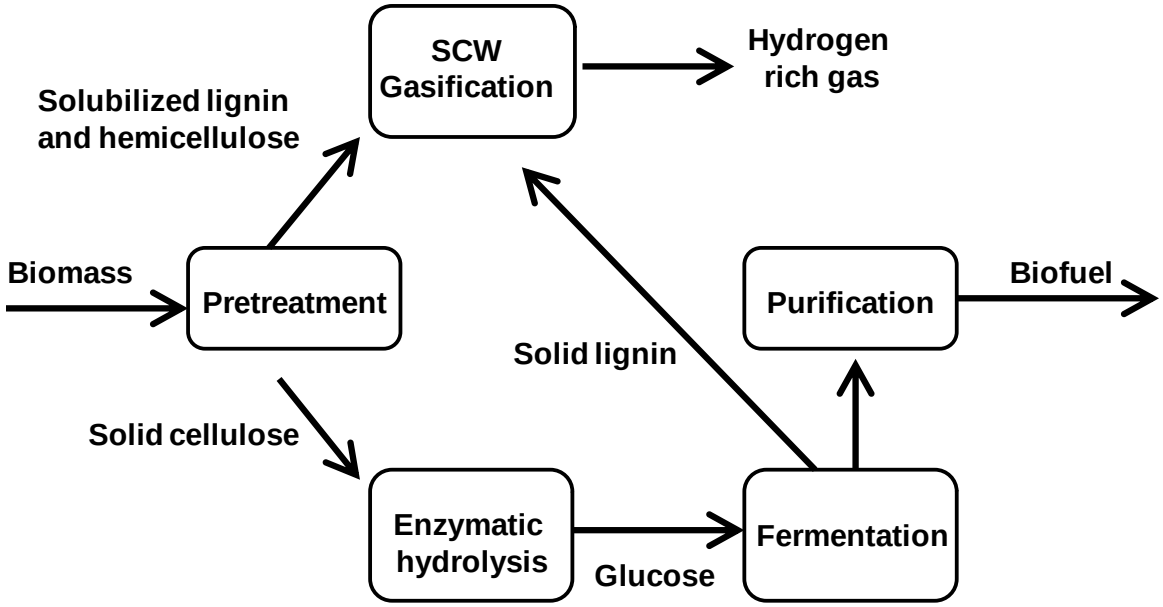

Figure 2.14. Concept for hydrogen gas production from biochemical conversion of lignocellulosic biomass byproduct streams.

Table 2.1. Microtube reactor conditions

Process parameter	Xylose	Phenol	Phenol / xylose
Temperature (°C)	650, 750	700, 750	750
Pressure (bar)	250	250	250
Density of water (g cm^{-3})		0.064 (650°C)	
		0.056 (750°C)	
Feed concentration (wt%)	2.0, 4.0	2.0	2.0
Liquid feed rate (cm^3 min^{-1})	0.15 - 8.0	0.05 - 1.0	0.05 - 1.0
Fluid residence time (sec)	0.44 - 8.9 sec	1.3 - 74 sec	1.3 - 26.6 sec

Table 2.2. Gas phase data for the supercritical water gasification of xylose, phenol, and xylose phenol mixture at 250 bar

Feed	Reaction Temperature (°C)	Residence time (sec)	Reactor material	Gas composition (mole %)				Gas yield		
				H_2	CO_2	CO	CH_4	CGE (%)	H_2 yield (H_2)	H_2 yield (H_2 + CH_4)
xylose	650	0.8 - 3.1	316 SS	42 ± 2	34 ± 3	13 ± 4	11 ± 1	81 ± 4	2.9 ± 0.3	6.1 ± 0.6
xylose	650	0.9 - 4.7	H-C276	62 ± 1	34 ± 1	1.1 ± 0.5	2.8 ± 0.4	101 ± 2	8.2 ± 0.6	9.6 ± 0.5
xylose	750	1.1 - 8.9	316 SS	49 ± 3	39 ± 3	0.8 ± 0.4	11 ± 2	99 ± 4	4.8 ± 0.4	9.0 ± 0.5
xylose / phenol	750	5.3 - 27	316 SS	41 ± 5	39 ± 3	0.7 ± 0.1	19 ± 1	74 ± 9	2.9 ± 0.3	8.5 ± 0.6
phenol	750	5.3 - 27	316 SS	46 ± 2	41 ± 2	0.9 ± 0.1	12 ± 2	58 ± 10	3.0 ± 0.7	4.4 ± 0.7
				Equilibrium values						
xylose	650			66	33	0.3	0.5			
xylose	750			66	33	0.02	0.7			
xylose / phenol	750			68	30	0.1	1.1			
phenol	750			69	29	0.4	1.4			

Chapter 3: Reaction Rates for Supercritical Water Gasification of Xylose in a Micro Tubular Reactor

3.1 Abstract

Two kinetic models describing supercritical water gasification of xylose at reaction temperatures from 450°C to 650°C and 250 bar were developed. Reaction rate constants were non-linearly estimated from product yield vs. residence time data by sum of the least squares method. The xylose decomposition kinetic model uses a detailed reaction mechanism to predict liquid intermediate production and gasification rates, whereas the xylose gasification kinetic model uses a simplified reaction mechanism to better predict gas yield and gas composition at conditions where gasification is dominant. Both models assume that gas phase reactions are in thermodynamic equilibrium, however, the gas phase reactions in the gasification kinetic model account for non-ideal interactions in the reacting fluid by accounting for the fugacity of each species in the mixture using the Peng-Robinson equation of state. Major gas products measured were CO_2, H_2, CH_4, CO, and C_2H_6. The highest measured concentrations of liquid intermediates were acetic acid and propanoic acid. Finally, an analysis of gas composition and gas yields for concentrated feed stocks is discussed based on the gasification kinetic model.

3.2 Notation

a_i	Peng Robinson attraction parameter (N m^4 mol^{-2})
A_i	Dimensionless form of a
A_E	Pre-exponential factor in the Arrhenius equation
b_i	Peng Robinson repulsion parameter (m^3 mol^{-1})
B_i	Dimensionless form of b
CGE	Carbon gasification efficiency (moles of carbon recovered in the gas per mole of carbon in the feed)
C_i	Concentration of component i at reaction T and P (mol m^{-3})
$C_{Xy,\,O}$	Initial concentration of xylose at reaction T and P (mol m^{-3})
$C_{H2O,\,O}$	Initial concentration of water at reaction T and P (mol m^{-3})
E_a	Activation energy (kJ mol^{-1})
Δh_{rxn}	Enthalpy of reaction (kJ mol^{-1})
$K_{eq,i}$	Equilibrium constant from reaction i
K_{ij}	Binary interaction coefficient between species i and j
k_j	Rate constant of reaction j (sec^{-1}) and (m^3 mol^{-1} sec^{-1})
P	Reactor pressure (bar)
P_{Ci}	Critical pressure of species i (bar)
R_g	Universal gas constant (J mol^{-1} K^{-1})
r_j	Rate of reaction j (mol m^{-3} sec^{-1})
T	Reactor temperature (°C)
T_{ci}	Critical temperature of species i (°C)
v_{ci}	Critical volume of species i (m^3 mol^{-1})
V_r	Reactor volume (cm^3)
v_o	Volumetric flow rate at reactor inlet (cm^3 min^{-1})
X_i	Mole fraction of species i
Z	Compressibility factor

Greek Symbols

α	function of the acentric factor
φ_i	Fugacity coefficient of species i
ρ_o	Fluid density at reactor inlet (g cm^{-3})
ρ_R	Fluid density at reactor T and P (g cm^{-3})
τ	Reactor residence time based on reactor T and P (sec)
ν	Specific volume (m^3 mol^{-1})
ω	Acentric factor

Species

Xy	Xylose
Gly	Glyceraldehyde
MF	Methyl formate
FF	Furfural
AA	Acetic acid
PA	Propanoic acid
Eth	Ethane
ML	Maple lactone
WSHS	Water soluble humic substances

3.3 Introduction

Hemicellulose is an amorphous biopolymer that typically makes up 25% – 35% of lignocellulosic biomass. Xylan, generally the most common polymer found in herbaceous crops and hardwood hemicellulose, is a hetero-polysaccharide that consists of a homopolymeric backbone of $\beta-(1,4)$ linked xylose residues [1]. Lignocellulosic biomass pretreatment processes aimed at making cellulose accessible to enzymatic hydrolysis for bio-ethanol production typically produce an aqueous stream of soluble hemicellulose and lignin as a byproduct [2-3]. The amounts of hemicellulose and lignin are dependent on the type of biomass, severity, and type of pretreatment [2,4]. However, solubilized C_5 sugars in the pretreatment stream, such as xylose, cannot be directly fermented to ethanol by yeast typically used in the cellulose to bio-ethanol process unless they are isomerized to xylulose [5]. In addition, chemicals used in the pretreatment process may produce toxins that inhibit fermentation or cause problems in downstream processing [5]. Alternatively, the hemicellulose rich aqueous stream can be directly reformed to H_2 and CO_2 or reacted to commodity chemicals by supercritical water (374°C and 221 bar) [4].

Biomass gasification to H_2 rich gas is an alternative, renewable, and CO_2 neutral energy source, and may contribute to the increasing world energy supply. Supercritical water reforming is an excellent platform to gasify biomass. Advantages include direct processing of wet feedstocks, short residence times for complete gasification, additional hydrogen generation through reforming, and generation of a compressed product gas. Recently there have been several reviews of supercritical water gasification [6-11]. Previous studies have shown that 6 carbon sugars in biomass, such as glucose, fructose, and cellulose, a polymer of glucose, can be completely gasified by supercritical water to H_2 and CO_2 [12-27]. Additionally, a reaction mechanism and kinetic parameter estimates for the non-catalytic gasification of glucose by supercritical water have been proposed [28-34]. However, there are very few studies on supercritical water gasification of xylose and xylan, model compounds for hemicellulose [4, 12, 35]. Although the reaction mechanism and kinetics for supercritical water gasification of xylose will likely be

similar to glucose, differences in decomposition chemistry may affect gasification rates due to the formation or absence of refractory liquid intermediates, and the formation or suppression of coke precursors. Previous kinetic studies for xylose degradation just above and below the critical temperature of water suggest that xylose is predominantly reacted via a retro-aldol condensation and to a much lesser extent dehydrated to furfural. The relative rates of these reactions are strongly influenced by reaction conditions [36-37]. These kinetic studies provide insight for initial xylose degradation in supercritical and near critical water, however, these studies are focused on feedstock conversion, and do not report gasification kinetics. Currently, there are no reported investigations that determine an overall gasification reaction mechanism and model the kinetic parameters for gasification of xylose in supercritical water at conditions where gasification is dominant.

In our previous work we showed that high rates of heat transfer, characteristic of micron sized reactor passages, may significantly intensify endothermic biomass gasification reactions in supercritical water [4, 13]. For example, xylose was stoichiometrically reformed to H_2 rich gas within a 1.0 sec residence time at 750°C under isothermal continuous flow conditions in a μ-tubular reactor. Furthermore, we demonstrated that the addition of xylose to phenol in the feed accelerated the gasification rate of phenol, most likely due to a hydrogen donor effect from the rapid gasification of xylose. In order to optimize any reactive process such as the co-gasification of solubilized hemicellulose and lignin in a biomass pretreatment stream, it is essential to determine intrinsic reaction kinetics and mechanistic data for each substrate.

In the present study a reaction mechanism for the supercritical water gasification of xylose is proposed and two kinetic models were developed. The decomposition kinetic model focuses on the kinetics describing the formation and gasification of major liquid intermediate products from the decomposition of xylose by supercritical water. The gasification kinetic model assumes a simplified reaction mechanism for xylose decomposition to liquid intermediates and is focused on better predicting gas yields and gas composition. Although real biomass feed streams will likely be more complex, the

two models offer different perspectives on how to approach supercritical water gasification of hemicellulose rich feed streams. The decomposition kinetic model provides greater insight for production of liquid chemicals from xylose by estimating reaction rates of several major liquid intermediates, while the gasification kinetic model better predicts gasification rates and gas composition at conditions where gasification is dominant. Kinetic parameters for both models were non-linearly estimated from product yield vs. residence time data by sum of the least squares method. An isothermal, continuous flow Hastelloy-C276 µ-tubular reactor was used to gasify xylose at 250 bar and reaction temperatures ranging from 450°C to 650°C.

3.4 Model Development

3.4.1 Reaction Mechanism

The decomposition kinetic model reaction mechanism for the supercritical water gasification of xylose is presented in Figure 3.1. The proposed reaction scheme does not account for all liquid intermediates and gas products generated, rather only includes intermediates and products comprising more than 1% of the total carbon in the feed, with the exception of H_2 and methyl formate. All of the identified and non-identified minor compounds were consolidated into a term called water soluble humic substances (WSHS). The identification and quantification of all the minor gas and liquid products are not practical and beyond the scope of this study.

In the proposed reaction mechanism xylose is either dehydrated to furfural, or reacted via a retro aldol condensation to glyceraldehyde and methyl formate. Glyceraldehyde is reacted to acrylic acid which is reduced, by H_2, to propanoic acid. Methyl formate, which was not present in the measured liquid products, is assumed to react rapidly to acetic acid. Propanoic and acetic acid are stoichiometrically gasified to H_2 and CO. Decomposition of propanoic acid may also proceed down a second pathway where it is gasified to ethane and CO_2. There are three proposed pathways for the decomposition of furfural. In the first pathway, furfural is gasified directly to CO, H_2, CH_4, and CO_2. In the

second pathway, furfural is reacted to maple lactone, which is gasified to CO, H_2, and CH_4. Lastly, furfural is broken down to WSHS, which is gasified to CO and H_2. Since WSHS include all of the minor liquid products, it is difficult to incorporate this term in the model. Nevertheless, the majority of the recalcitrant liquid intermediates are likely products of furfural reacted species. Finally, the water gas shift reaction and the methanation reaction were assumed to be at thermodynamic equilibrium based on the ideal gas law.

The gasification kinetic model reaction mechanism is a simplified version of the previous reaction mechanism, and is presented in Figure 3.2. This reaction mechanism assumes that xylose is either dehydrated to furfural or decomposed to WSHS. Additionally, furfural is reacted to WSHS, and WSHS is gasified to CO and H_2. The water gas shift and methanation reactions are assumed to be in thermodynamic equilibrium, as in the previous model however, the non-ideal behavior of each species in the reacting fluid is accounted for by incorporating the fugacity coefficient of each species based on the Peng Robinson equation of state into the model.

3.4.2 Rate Equations and Kinetic Parameter Estimates

The development of both kinetic models was governed by four major assumptions. The first assumption was an isothermal reacting fluid. This assumption was based on heat transfer calculations and reactor design described in our previous work [4]. Second, in the decomposition kinetic model the concentration of water is constant and calculated at the temperature and pressure of the reactor. The concentration of water was used to calculate equilibrium values for the water gas shift and methanation reaction. In all other reactions that consumed water, the concentration was included in the rate constant, and the reaction was assumed to be pseudo first order. The gasification kinetic model assumed a non-constant concentration of water, initially calculated at the temperature and pressure of the reaction. Third, all of the liquid decomposition and gasification reactions are irreversible and first order or pseudo first order with respect to the reactants. All of the gas phase

reactions were reversible and assumed to be at thermodynamic equilibrium. Equilibrium relationships for the water gas shift and methanation reactions in the vapor phase as a function of temperature were obtained from *Chemcad 6* (Chemstations inc.). Fourth, the temperature dependence of the rate constants can be described by the Arrhenius equation. Based on the previous assumptions the decomposition, gasification, and gas phase reactions and their rates for the decomposition kinetic model are as follows:

$$C_5H_{10}O_5\ (Xy) \xrightarrow{k_1} C_2H_4O_2(MF) + C_3H_6O_3(Gly) \qquad r_1 = k_1 C_{Xy} \qquad (3.1)$$

$$C_5H_{10}O_5(Xy) \xrightarrow{k_2} C_5H_4O_2(FF) + 3H_2O \qquad r_2 = k_2 C_{Xy} \qquad (3.2)$$

$$C_3H_6O_3(Gly) + H_2 \xrightarrow{k_3} C_3H_6O_2(PA) + H_2O \qquad r_3 = k_3 C_{Gly} C_{H_2} \qquad (3.3)$$

$$C_2H_4O_2(MF) \xrightarrow{k_4} C_2H_4O_2(AA) \qquad r_4 = k_4 C_{MF} \qquad (3.4)$$

$$C_5H_4O_2(FF) \xrightarrow{k_5} C_xH_yO_z(WSHS) \qquad r_5 = k_5 C_{WSHS} \qquad (3.5)$$

$$C_5H_4O_2(FF) + CH_4 \xrightarrow{k_6} C_6H_8O_2(ML) \qquad r_6 = k_6 C_{FF} C_{CH_4} \qquad (3.6)$$

$$C_3H_6O_3(PA) + H_2 \xrightarrow{k_7} C_2H_6 + H_2O + CO_2 \qquad r_7 = k_7 C_{PA} C_{H_2} \qquad (3.7)$$

$$C_2H_4O_2(AA) \xrightarrow{k_8} 2CO + 2H_2 \qquad r_8 = k_8 C_{Eth} \qquad (3.8)$$

$$C_3H_6O_2(PA) + H_2O \xrightarrow{k_9} 3CO + 4H_2 \qquad r_9 = k_9 C_{PA} \qquad (3.9)$$

$$C_5H_4O_2(FF) + 3H_2O \xrightarrow{k_{10}} CO_2 + CH_4 + 3CO + 3H_2 \qquad r_{10} = k_{10} C_{FF} \qquad (3.10)$$

$$C_xH_yO_z(WSHS) + z\ H_2O \xrightarrow{k_{11}} 5CO + 5H_2 \qquad r_{11} = k_{11} C_{WSHS} \qquad (3.11)$$

$$C_6H_8O_2(ML) + 3H_2O \xrightarrow{k_{12}} CH_4 + 5CO + 5H_2 \qquad r_{12} = k_{12} C_{ML} \qquad (3.12)$$

$$C_2H_6 + H_2O \xrightarrow{k_{13}} 2CO + 5H_2 \qquad r_{13} = k_{13} C_{Eth} \qquad (3.13)$$

$$CO + H_2O \underset{k_{15}}{\overset{k_{14}}{\rightleftharpoons}} H_2 + CO_2 \qquad r_{14} = k_{14} C_{CO} C_{H_2O} - k_{15} C_{H_2} C_{CO_2} \qquad (3.14)$$

$$CO + 3H_2 \underset{k_{17}}{\overset{k_{16}}{\rightleftharpoons}} CH_4 + H_2O \qquad r_{15} = k_{16} C_{CO} C_{H_2}^3 - k_{17} C_{CH_4} C_{H_2O} \qquad (3.15)$$

The concentration of each component '*i*' (C_i) as a function of time can be expressed in terms of the following differential equations for each of the 13 species:

$$\frac{dC_{Xy}}{dt} = -r_1 - r_2 \quad (3.16)$$

$$\frac{dC_{Gly}}{dt} = r_1 - r_3 \quad (3.17)$$

$$\frac{dC_{MF}}{dt} = r_1 - r_4 \quad (3.18)$$

$$\frac{dC_{AA}}{dt} = r_4 - r_8 \quad (3.19)$$

$$\frac{dC_{PA}}{dt} = r_3 - r_7 \quad (3.20)$$

$$\frac{dC_{FF}}{dt} = r_2 - r_5 - r_6 - r_{10} \quad (3.21)$$

$$\frac{dC_{ML}}{dt} = r_6 - r_{12} \quad (3.22)$$

$$\frac{dC_{WSHS}}{dt} = r_5 - r_{11} \quad (3.23)$$

$$\frac{dC_{Eth}}{dt} = r_7 - r_{13} \quad (3.24)$$

$$\frac{dC_{CO_2}}{dt} = r_7 + r_{10} + r_{14} \quad (3.25)$$

$$\frac{dC_{CO}}{dt} = 2r_8 + 3r_9 + 3r_{10} + 5r_{11} + 5r_{12} + 2r_{13} - r_{14} - r_{15} \quad (3.26)$$

$$\frac{dC_{CH_4}}{dt} = r_{12} + r_{15} + r_{11} - r_6 \quad (3.27)$$

$$\frac{dC_{H_2}}{dt} = 2r_8 + 4r_9 + 3r_{10} + 5r_{11} + 5r_{12} + 5r_{13} + r_{14} - 3r_{15} - r_7 - r_3 \quad (3.28)$$

Reaction and rate equations for the gasification kinetic model are:

$$C_5H_{10}O_5(Xy) \xrightarrow{k_{18}} C_5H_4O_2(FF) + 3H_2O \qquad r_{18} = k_{18}C_{Xy} \quad (3.29)$$

$$C_5H_{10}O_5(Xy) \xrightarrow{k_{19}} C_xH_yO_z\,(WSHS) \qquad r_{19} = k_{19}C_{Xy} \quad (3.30)$$

$$C_5H_4O_2(FF) \xrightarrow{k_{20}} C_xH_yO_z(WSHS) \qquad r_{20} = k_{20}C_{FF} \quad (3.31)$$

$$C_xH_yO_z(WSHS) \xrightarrow{k_{21}} 5CO + 5H_2 \qquad r_{21} = k_{21}C_{WSHS} \quad (3.32)$$

The water gas shift, Equation 3.14, and the methanation reaction, Equation 3.15, are included in the gasification model. The differential equations that describe the gasification kinetic model are

$$\frac{dC_{Xy}}{dt} = -r_{18} - r_{19} \quad (3.33)$$

$$\frac{dC_{FF}}{dt} = r_{18} - r_{20} \quad (3.34)$$

$$\frac{dC_{WSHS}}{dt} = r_{19} + r_{20} - r_{21} \quad (3.35)$$

$$\frac{dC_{CO}}{dt} = 5r_{21} - r_{14} - r_{15} \quad (3.36)$$

$$\frac{dC_{H_2}}{dt} = 5r_{21} + r_{14} - 3r_{15} \quad (3.37)$$

$$\frac{dC_{CO_2}}{dt} = r_{14} \quad (3.38)$$

$$\frac{dC_{CH_4}}{dt} = r_{15} \quad (3.39)$$

$$\frac{dC_{H_2O}}{dt} = r_{14} - r_{15} \quad (3.40)$$

The initial conditions at $t = 0$ for the differential equations for both models are $C_{Xy} = C_{Xy,O}$; $C_{H2O} = C_{H2O,O}$; $C_{Gly} = C_{MF} = C_{AA} = C_{PA} = C_{FF} = C_{ML} = C_{WSHS} = C_{Eth} = C_{CO2} = C_{CO} = C_{CH4} = C_{H2} = 0$. Concentration values for all species are in moles m^{-3} at the temperature and pressure of the reaction. Carbon gasification efficiency (CGE) was based on the percentage of recovered carbon in the gas from the feed

$$CGE = \frac{\sum_{i,g} n_i C_{i,g}(T,P)}{n_{Xy} C_{Xy,o}(T,P)} \quad (3.41)$$

where *n* is the moles of carbon per mole of species, and $C_{i,g}$ are the concentration of the gas phase species, CO_2, CO, CH_4, C_2H_6, C_2H_4, C_2H_2 at reactor temperature and pressure. Hydrogen yield was defined as the amount of H_2 produced per mole of xylose reacted. Product gas composition was calculated by

$$X_i = \frac{C_i(T,P)}{\sum_{i,g} C_{i,g}(T,P)} \qquad (3.42)$$

where X_i is the mole fraction of component *i*. Water was not included in the product gas composition. Thermodynamic equilibrium rate constants for gas phase reactions were calculated by the Van 't Hoff equation assuming a constant Δh^o_{rxn}

$$\ln \frac{K_{eq}}{K_{eq,298K}} = -\frac{\Delta h^o_{rxn}}{R_g}\left(\frac{1}{T} - \frac{1}{298}\right) \qquad (3.43)$$

Where $K_{eq,298K}$ is the equilibrium constant at standard state, and Δh^o_{rxn} is the enthalpy of reaction at standard state. Fugacity coefficients for each species in the mixture were calculated from the Peng Robinson equation of state to account for non-ideal gas behavior of each species in the reacting fluid.

$$P = \frac{R_g T}{v-b} - \frac{a\alpha}{v(v+b)+b(v-b)} \qquad (3.44)$$

where *a* and *b* are interaction parameters given by

$$a_i = \frac{0.457\, R_g^{\,2}\, T_c^2}{P_c} \qquad (3.45)$$

$$b_i = \frac{0.0778\, R_g\, T_c}{P_c} \qquad (3.46)$$

and α is a function of the acentric factor given by

$$\alpha = \left(1+\left(0.37464+1.54266\omega-0.266992\omega^2\right)\left(1-\left(T/T_c\right)^{0.5}\right)\right)^2 \qquad (3.47)$$

where ω is the acentric factor for each pure species i. This equation of state is appropriate for thermodynamic analysis of supercritical fluid applications including supercritical water gasification [38]. Van der Waals mixing rules were used to apply the Peng Robinson equation to a mixture

$$a = \sum_i^n \sum_j^n X_i X_j a_{ij} \qquad (3.48)$$

$$b = \sum_i^n \sum_j^n X_i X_j b_{ij} \qquad (3.49)$$

$$a_{ij} = \left(1-k_{ij}\right)\left(a_i - a_j\right)^{0.5} \qquad (3.50)$$

$$b_{ij} = \frac{\left(b_i + b_j\right)}{2} \qquad (3.51)$$

where k_{ij} is an additional interaction parameter estimated by

$$k_{ij} = 1-\frac{8\left(v_{ci}v_{cj}\right)^{0.5}}{\left(v_{ci}^{1/3}+v_{cj}^{1/3}\right)^3} \qquad (3.52)$$

Based on the Peng Robinson equation of state, the compressibility factor, Z, and the Van der Waals mixing rules the fugacity coefficient for each component in the mixture could be calculated by

$$\ln\phi_i = \frac{B_i}{B}\left(Z-1\right)-\ln\left(Z-B\right)-\frac{A}{2\left(2B\right)^{0.5}}\left(\frac{2\sum_j X_i A_{ij}}{A}-\frac{B_i}{B}\right)\ln\left(\frac{Z+\left(1+\sqrt{2}\right)B}{Z+\left(1-\sqrt{2}\right)B}\right) \qquad (3.53)$$

The dimensionless interaction and repulsion parameters A and B are given by

$$A_i = \frac{a_i P}{\left(R_g T\right)^2} \qquad (3.54)$$

$$B_i = \frac{b_i P}{RT} \qquad (3.55)$$

Fugacity coefficients were used in the gasification kinetic model to more accurately calculate equilibrium gas phase concentrations for CO, CO_2, CH_4, H_2, and H_2O in Equations 3.14 and 3.15. Easy Fit Model Design version 4.32 was used to non-linearly fit rate constants to the set of differential Equations 3.16-3.28 and 3.33-3.40 at 450°C, 500°C, and 550°C. Parameters for the rate constant estimation are presented in Table 3.1. All data points were equally weighted, and initial guesses for the rate constants were determined by trial and error method.

3.5 Experimental

3.5.1 Micro-tubular Reactor and Test Loop

A 2 meter long, 1.6 mm (1/16 in.) outer diameter, 762 µm (0.03 in.) inner diameter Hastelloy C-276 tube with a volume of 0.912 cm^3 (VICI THC-130) served as the µ-tubular reactor (Figure 3.1a). The tube was inserted into a milled stainless steel reactor block. Details of the reactor setup have been previously described [4].

The continuous flow reactor test loop is presented in Figure 3.3. The feed was pumped to the reactor, at 25°C and 250 bar, by a Teledyne Isco 260D syringe pump (266 ml capacity) operating at constant flow. The feed was heated and maintained at the reaction temperature by two 375 W flat plate ceramic heaters (Thermcraft Inc., 29.5 cm x 7.93 cm x 2.06cm with a Ni-Cr wire heating element) that were mounted to the top and bottom of the reactor heating block. The reactor temperature was maintained by a PID controller with a Type J thermocouple inserted into the center of the reactor heating block. All sides of the reactor heating block were insulated with 3.8 cm thick Fibercraft board (Thermcraft, Inc.). Due to the narrow bore of the tubing it was not possible to directly

measure the reacting fluid temperature, however previous calculations suggest the reactor temperature is isothermal [4].

The hot reactor effluent exiting the reactor was cooled to 20°C with a shell and tube heat exchanger using water as the coolant. The pressure was decreased from 250 bar to 1.03 bar by an adjustable precision back-pressure regulator (KHB1WOA6C2P6000, Swagelok Inc., stainless steel). The condensed liquid products were collected for further analysis. The gas products were dried and quantified with a gas mass flowmeter (Omega Inc. FMA 1800 series, 0-20 sccm, and 0-100 sccm, aluminum / brass body). Gas samples were collected in a 2.0 liter Tedlar gas collection bag and corrected for gas composition.

The feed solution consisted of 4.0 wt % α-D-xylose (Sigma-Aldrich X1500, >99% purity, CAS108-95-2, mol. Wt. 150.13) dissolved in 96 wt% de-ionized distilled water. All xylose feed solutions were degassed with helium prior to use. The liquid feed flow rate to the reactor ranged from 0.15 ml/min to 8.0 ml/min at 25°C and 250 bar. The fluid residence time (τ) was estimated by $\tau = V_R \rho_R / v_o \rho_o$. Where V_R is the reactor volume (cm^3), v_o is the volumetric flowrate ($cm^3\ min^{-1}$) of the liquid feed at the reactor inlet temperature T_o, and system pressure P, ρ_o is the density of the liquid feed at T_o and P ($g\ cm^{-3}$), and ρ_R is the density of the fluid at the reactor set point temperature T and P ($g\ cm^{-3}$). The reactor residence time is based on the fluids properties at the reactor set point temperature and pressure, and does not account for fluid density changes as the fluid heats up from the subcritical liquid state to the supercritical fluid state. The fluid physical properties were estimated from water at the reactor temperature and pressure. Therefore, density or heat effects from the formation of gas products in the reactor were not factored into the residence time calculation. Newly installed Hastelloy C-276 microtubes were conditioned as previously reported [4].

3.5.2 Analytical Procedures

Gas and liquid products were analyzed by gas chromatography (GC) and high performance liquid chromatography (HPLC). Gas products were quantitatively analyzed

by a SRI multiple gas analyzer #1 equipped with a thermal conductivity detector for H_2 analysis, and a FID detector with a methanizer for CO, CH_4, CO_2, C_2H_2, C_2H_4, and C_2H_6 analysis. The gas mixture was separated on two columns, a 2-meter Molecular Sieve 13X and a 2-meter Silica Gel. The GC oven temperature was held at 40°C for 3 min., then ramped to 135°c at a rate of 16°C/min, and finally held at 135°C for 2.67 min. A standard gas injection volume of 250 µl was injected three times for all gas samples. The concentration of the gas species was reported as an average of three injections, and the standard deviation was typically less than 2% of the reported value. Gas products were identified by retention time and quantified by external calibration against a standard gas mixture (Alltech Associates Inc., gas standard #19792). Calibration was performed with three 100 µL standard gas injections. Procedures for the analysis of residual sugar, organic acids, and other organic liquid intermediates present in the liquid products by high performance liquid chromatography (HPLC) were previously described [4]. For liquid products measured by HPLC an average peak area of two injections was reported, and the standard error was less typically than 10%.

3.6 Results and Discussion

Two kinetic models were developed to describe intrinsic reaction kinetics for supercritical water gasification of xylose. The decomposition model focuses on estimating kinetic parameters for major liquid intermediates governed by the reaction mechanism in Figure 3.1. The gasification kinetic model primarily focuses on predicting gas composition, H_2 yield, and gasification rates at conditions where gasification is dominant by using a simplified reaction mechanism, presented in Figure 3.2. Both models assume the water gas shift and methanation reactions are in thermodynamic equilibrium, however, the gasification kinetic model compensates for the non-ideal behavior of the gas species by accounting for the species fugacity in the mixture derived from the Peng Robinson equation of state and Van der Waals mixing rules. Additionally, water is incorporated into the model as a reacting species to better predict gas composition for high feed stock concentrations. For dilute feedstock concentrations these

reactions are dominated by the law of mass action due to the large concentration of water present in the reacting fluid.

The decomposition kinetic model is more appropriate for predicting and investigating the synthesis of commodity chemicals derived from supercritical water reforming of hemicellulose rich feed streams, whereas the gasification model is appropriate for modeling and optimization for gasification of hemicellulose rich feed streams. The natural log of the non-linearly estimated rate constants for the decomposition kinetic model and gasification kinetic model are plotted versus inverse temperature are presented in Figures 3.4(A) and 3.4(B) respectively. The estimated rate constants were fit by a linear regression line. The Activation energy and the pre-exponential factor for all of the first order and pseudo first order reactions were determined by the y-intercept and the slope of the linear regression line. Kinetic parameter estimations and their errors for Equations 3.1 – 3.13 and 3.29 – 3.32 are presented in Table 3.2. The somewhat large error associated with the estimated kinetic terms is most likely due to an incomplete reaction mechanism rather than poor data.

3.6.1 Liquid Phase Analysis

The decomposition kinetic model will primarily be used to analyze the liquid products for supercritical water gasification of xylose. Major decomposition intermediates from the supercritical water gasification of xylose are all water soluble and can be found in Figure 3.1. Given that complete conversion of xylose was achieved at all temperatures and residence times tested, it is useful to compare kinetic parameter estimates to published values. The activation energy and pre-exponential term for the dehydration of xylose to furfural in the decomposition model, Equation 3.2, were estimated to be 120 kJ mol^{-1}, and 1.2 x 10^{12} sec^{-1} respectively, and 147.5 kJ mol^{-1} and 1.3 x 10^{13} sec^{-1} for the gasification model, Equation 3.29. Both values are in good agreement with Qi and Xiuyang (2007) [36] who estimated the activation energy to be 111 kJ mol^{-1}, and pre-exponential of 1.4 x 10^{12} sec^{-1} for dehydration of xylose to furfural in near critical water. Activation energy

and pre-exponential for xylose degradation by retro aldol condensation to glyceraldehyde and methyl formate were estimated to be 134 kJ mol^{-1}, and 1.5 x 10^{13} sec^{-1} in the decomposition model, and were higher than previous published values of 102 kJ mol^{-1} and 6.9 x 10^{8} reported by Sasaki et al. [37]. The difference may be attributed to the reactor material. Whereas this study uses Hastelloy C-276, Sasaki et al. [37] used stainless steel reactor tubing. Nickel, which makes up a significant larger percentage of the Hastelloy C-276 than stainless steel, has been shown to catalyze gasification reactions of glucose and cellulose [19, 26]. It is likely that nickel in the reactor wall will have a similar catalytic effect for xylose decomposition in supercritical water. The calculated ratio of the rate constants (k_2 / k_1) for the decomposition model is plotted versus temperature and is presented in Figure 3.5. The ratio of the rate constants is unity just above the critical temperature for water, which suggests that xylose dehydration to furfural is favored below the critical temperature of water in an ionic reaction environment, while retro aldol condensation to pyruvaldehyde and methyl formate is favored above the critical point of water in a free radical dominated reaction environment. This is consistent with previous mechanistic studies for xylose and glucose in near and supercritical water [31, 34, 37]. Given that the mechanism for xylose decomposition changes from ionic to free radical at the critical temperature of water, rate constants for xylose dehydration to furfural and retro aldol condensation to pyruvaldehyde and methyl formate can significantly affect gas and liquid product yield prediction at temperatures just above the critical temperature of water. Of the two reaction mechanisms described, the decomposition reaction mechanism can more accurately predict gas and liquid product yields for xylose gasification just above the critical temperature of water.

Since the term WSHS in the decomposition model is based on the formation and gasification of minor liquid products derived from furfural, it is useful to compare the estimated kinetic parameters to literature values. Consequently, Qi and Xiuyang (2007) [36] estimated the rate constant for the reaction of furfural to “decomposition products” just below the critical point of water. Although the reaction mechanisms for both models differ slightly and Qi and Xiuyang (2007) [36] study was focused on feedstock

conversion and not gasification, estimates for the activation energy and pre-exponential term, 58.8 kJ mol^{-1} and 2.0 x 10^3 sec^{-1}, were in good agreement with our estimates of 55.6 kJ mol^{-1} and 5.7 x 10^3 sec^{-1}.

The rate constant for the reaction of ethane to CO and H_2, Equation 3.13 in the decomposition model, was estimated to be zero at 450°C, 500°C, and 550°C indicating the concentration of ethane has reached a pseudo steady state, and was not being further reacted to CO and H_2. Additionally, due to an estimated value of zero at 450°C and a higher estimated rate constant at 500°C than 550°C, the activation energy for the rate constant k_{10}, Equation 3.10, was determined by estimating the pre-exponential of the Arrhenius equation based on similar reactions, and minimizing the sum of the squares of the error between the estimated rate constants and the Arrhenius equation to determine the activation energy. The activation energy was estimated to be 157.3 kJ mol^{-1}.

Selected concentrations of liquid intermediates generated during xylose gasification by supercritical water versus reactor residence time are presented in Figure 3.6. The solid and dashed lines represent fits from the decomposition kinetic model. Major refractory liquid intermediates were acetic acid, propanoic acid, furfural, and glyceraldehyde. The measured concentration of the major refractory intermediates decreased with increasing residence times. Of the major liquid intermediates, acetic acid and propanoic acid had the highest predicted and measured concentration. Other modeled liquid products were xylose, maple lactone, and methyl formate. Methyl formate and xylose had a zero measured concentration for all conditions tested, indicating complete xylose conversion, and rapid conversion of methyl formate rapidly to acetic acid. The highest concentration of maple lactone was 0.17 mol m^{-3} at 450°C and 8.6 second residence time, and accounted for 1.0% of the total carbon in the feed. Although there is no proposed reaction pathway for the production of maple lactone from furfural, Williams and Onwudili (2005) proposed a reaction pathway for the formation of 3-methyly cyclopenten-2-one from 5-hydroxymethyl-furfural (5-HMF). It is likely that maple lactone is derived by a similar reaction pathway, and is a product of furfural and an unknown minor intermediate. In our proposed reaction mechanism furfural reacts with CH_4 to form maple

lactone. Although the reaction mechanism is likely more complicated, this simplified reaction pathway is sufficient to preserve the carbon balance.

The remainder of the unaccounted for minor intermediate products based on carbon in the liquid products was lumped into WSHS and accounted for up to 34% of the total carbon in the feed. The effect of residence time on the concentration of WSHS at 450°C, 500°C and 550°C is presented in Figure 3.6. Generally, the concentration of WSHS increased to a maximum, leveled off, and decreased with increasing residence time. The concentration of WSHS was greatest at 450°C and a 12 sec residence time, and decreased with increasing temperature. There was no WSHS at 650°C at the majority of residence times tested due to complete gasification of the feedstock. No carbon formation or reactor plugging was observed in any of the experiments, and thus was not integrated into either kinetic model.

The approach used to account for liquid phase intermediates in the gasification kinetic model was to assume that xylose was either dehydrated to furfural or reacted to WSHS. The term WSHS in this model accounted for all major and minor liquid intermediates other than furfural. Concentrations of WSHS and furfural as a function of residence time and temperatures are presented in Figure 3.7. The concentration of WSHS and furfural decreased with increasing residence time, and the rate both species reacted increased with reaction temperature. These results are indicative of an Arrhenius relationship between reaction temperature and reaction rate. The gasification kinetic model fit the data well except at a reaction temperature of 450°C when the model over predicted the concentration of WSHS. The over prediction was most likely due to constrained rate constant estimation, k_{21}, as a consequence of high CO concentration in the product gas unaccounted for by the thermodynamic equilibrium of the gas phase reactions.

3.6.2 Gas Phase Analysis

The gasification model will primarily be used to discuss the gas phase analysis; however results from both models will be presented and compared. Gas composition versus

residence time data for supercritical water gasification of 4.0 weight percent (0.28 molar) aqueous solution of xylose at 450°C, 500°C, 550°C, and 650°C are presented in Figure 3.8(A) for the decomposition kinetic model and Figure 8(B) for the gasification kinetic model. The solid and dashed lines represent model predictions. Major gas products at all conditions tested were H_2 and CO_2, and minor gas products were CH_4, CO, and C_2H_6. Small amounts (< 0.5%) of ethane and acetylene were identified but not quantified.

At 650°C, gas composition (62% ± 1.3% H_2, 33.7% ± 0.9% CO_2, 2.6% ± 0.6% CH_4, 1.6% ± 1.3% CO, 0.2% ± 0.07% C_2H_6) was independent of residence time. Both models predicted gas compositions similar to experimental results at this temperature. For reaction temperatures of 550°C and lower, the majority of the product gas comprised of CO_2 and H_2, however, the product gas contained significant amount of methane and CO. An increase in the concentration of CO was observed as reaction temperature and residence time were decreased. The high concentration of CO was not predicted by the decomposition or gasification kinetic models, and may affect the H_2 yield due to a lower than predicted CO conversion of the water gas shift reaction. Although the equilibrium constant for the water gas shift decreases as temperature decreases from 650°C to 450°C, the large excess of water in the feed drives the forward water gas shift reaction by the law of mass action. The highest predicted concentration of CO by the gasification model was 0.8 % at 650°C. Even though Ni and Cr rich alloys, such as Inconel and Hastelloy, drastically increase the reaction rate of the water gas shift [39], the higher than predicted concentration of CO at short residence times is likely due to non-equilibrium conversion of CO.

CH_4 in the product gas is produced from essentially two sources, gas phase reactions i.e. the methanation, and hydrogasification, and from reactions of organic liquid intermediates [40]. Since no coke or char formation was observed at any conditions tested, the hydrogasification reaction was not included in the reaction mechanism. At 650°C the concentration of CH_4 in the product gas was independent of residence time, However, at reaction temperatures between 450°C to 550°C, the concentration CH_4 increased with residence time and eventually approached a constant value between 4% –

7%. The gasification kinetic model predicts significant amounts of CH_4 and is in the product gas in good agreement with experimental results, whereas the decomposition kinetic model does not predict any CH_4. Since both models assume thermodynamic equilibrium the difference is attributed to non ideal interactions accounted for in the gasification kinetic model. The fugacity coefficients for all of the gas phase species deviated from unity. Previous studies on the thermodynamic analysis for the supercritical water gasification of glucose have also predicted significant amounts of methane at similar reaction conditions [38, 41].

The effect of reactor residence time on carbon gasification efficiency (CGE) and H_2 yield is presented in Figure 3.9. The dashed lines represent the decomposition kinetic model predictions and the solid lines represent the gasification kinetic model. In general carbon gasification efficiency increased with residence time and reaction temperature. CGE model predictions from both models fit the experimental data well. As expected the gasification kinetic model more accurately predicts CGE at higher reaction temperatures whereas the decomposition kinetic model better predicts CGE at lower temperatures where gasification is not dominant.

The hydrogen yield, defined as moles of H_2 generated per mole of xylose fed, increased with reaction temperature and residence time. At 650°C near stoichiometric H_2 yields for reforming, 8.9 ± 0.5 was achieved for fluid residence times of 0.9 seconds to 4.7 seconds. The H_2 yield based on xylose reforming is

$$C_5H_{10}O_5 + 5H_2O \rightarrow 5CO_2 + 10H_2 \qquad (56)$$

Theoretically it is possible to produce 10 moles of H_2 per mole of xylose reacted. H_2 model predictions from the gasification model tended to fit the experimental data well, whereas the decomposition kinetic model over predicted the H_2 yield as a result of under predicting the methane in the product gas. Hydrogen yields approaching 5 moles of H_2, the theoretical hydrogen yield based solely on the hydrogen contained in xylose, were reached at a reaction temperature of 500°C and a fluid average residence time of 25 seconds.

3.6.3 High Feed Concentration Analysis

The gasification kinetic model was used to predict gas composition and H_2 yield at 650°C, 250 bar, and 10.0 sec residence time from concentrated feed solutions. This model assumes that all the reactions are first order or pseudo first order, and the carbon gasification efficiency was 100% . The analysis is essentially used to investigate the effect of feed concentration on the thermodynamic equilibrium of the gas composition due to the water gas shift and methanation reactions.

Carbon gasification efficiency and H_2 yield are presented in Figure 3.10. The predicted H_2 yield decreased from 9.4 moles of H_2 produced per mole of xylose reacted with a 4.0 wt % feed solution concentration to 2.4 moles of H_2 produced per mole of xylose reacted with a 25 wt % feed solution concentration. The decrease in H_2 yield is due to changes in the equilibrium gas composition rather than incomplete CGE. Gas composition as a function of feed solution concentration is presented in Figure 3.10. As feed concentration increases, the concentration of CH_4 in the gas products increases. This is likely due to a decrease in the concentration of water as a result of water being consumed by the water gas shift reaction as well as an increase in the H_2 concentration relative to the concentration of water.

3.7 Conclusion

Two kinetic models that describe supercritical water gasification of xylose were proposed. Rate constants for both models were non-linearly estimated from product yield vs. residence time data. The decomposition model kinetically describes the how xylose is broken down to liquid intermediates, and is relevant to analysis aimed at optimization of low temperature supercritical water gasification of hemicellulose, or for production of chemicals from xylose. The gasification kinetic model assumes all gas phase reactions are in thermodynamic equilibrium and uses a simplified reaction mechanism to model gasification rates and gas composition. The gasification kinetic model is ideal for

optimizing supercritical water gasification of hemicellulose at conditions where gasification is dominant. Additionally, the gasification model is used to predict gas composition and H_2 yield as a function of feed concentration.

3.8 Acknowledgement

This research was supported by Bend Research, Inc., Bend, Oregon, and by the US Army under the Tactical Energy Systems program administered through the Oregon Nanoscience and Microtechnologies Breakthrough Institute.

3.9 Literature Cited

1. Saha B 2003 *Journal of Industrial Microbiology & Biotechnology* **30** 279-291
2. Mosier N, Wyman C, Dale B, Elander R, Lee Y, Holtzapple M, Ladisch M 2005 *Bioresource Technology* **96** 673-686
3. Hendriks A, Zeeman G 2009 *Bioresource Technology* **100** 10-18
4. Goodwin A, Rorrer G 2009 *Energy and Fuels* **23** 3818-3825
5. Agbogbo F K, Coward-Kelly G 2008 *Biotechnol Lett* **30** 1515-1524
6. Matsumura Y, Minowa T, Potic B, Kersten S, Prins W, van Swaaij W, Beld B, Elliott D, Neuenschwander G, Kruse A, Antal M 2005 *Biomass and Bioenergy* **29** 269-292
7. Calzavara Y, Joussot-Dubien C, Boissonnet G, Sarrade S 2005 *Energy Conversion and Management* **46** 615-631
8. Loppinet-Serani A, Aymonier C, Cansell F 2008 *ChemSusChem* **1** 486-503
9. Navarro R M, Sánchez-Sánchez M C, Alvarez-Galvan M C, del Valle F, Fierro J L G 2009 *Energy Environ* Sci **2** 35-54
10. Peterson A A, Vogel F, Lachance R P, Fröling M, Antal Jr M J, Tester J 2008 *Energy Environ Sci* **1** 32-65
11. Kruse A 2008 *Biofuels Bioproducts & Biorefining* **2** 415-437
12. Yoshida T, Matsumura Y *Ind Eng Chem* **40** 5469-5474
13. Goodwin A, Rorrer G 2008 *Ind Eng Chem* **47** 4106-4114
14. Holgate R H, Meyer J C, Tester J W 1995 *AICHE Journal* **41** 637-647
15. Hao X, Guo L, Mao X, Zhang X, Chen X 2003 *International Journal of Hydrogen Energy* **28** 55-64
16. Kersten S R A, Potic B, Prins W, Van Swaaij W P M 2006 *Ind Eng Chem Res* **45** 4169-4177
17. Yu D, Aihara M, Antal J A J 1993 *Energy and Fuels* **7** 574-577
18. Ehara K, Saka S 2002 *Cellulose* **9** 301-311
19. Resende F L P, Neff M E, Savage P 2007 *Energy and Fuels* **21** 3637-3643
20. Williams P, Onwudili J 2006 *Energy & Fuels* **20** 1259-1265

21. Matsumura Y, Yanachi S, Yoshida T 2006 *Ind Eng Chem Res* **45** 1875-1879

22. Yoshida T, Oshima Y, Matsumura Y 2004 *Biomass and Bioenergy* **26** 71-78

23. Ogihara Y, Smith R, Inomata H, Arai K 2005 *Cellulose* **12** 595 - 606

24. Lu Y J, Guo L J, Ji C, Zhang X, Hao X, Yan Q 2006 *International Journal of Hydrogen Energy* **31** 822-831

25. Yoshida T, Matsumura Y 2009 Ind Eng Chem Res **48** 8381-8386

26. Resende F, Savage P 2009 *Energy and Fuels* **23** 6213–6221

27. Yoshida T, Oshima Y 2004 *Ind Eng Chem Res* **43** 4097-4104

28. Watanabe M, Aizawa Y, Iida T, Levy C, Aida T M, Inomata H 2005 *Carbohydrate Research* **340** 1931-1939

29. Lee I G, Kim M S, Ihm S K 2002 *Ind Eng Chem Res* **41** 1182-1188

30. Kabyemela B M, Adschiri T, Malaluan R M, Arai K 1999 *Ind Eng Chem Res* **38** 2888-2895

31. Watanabe M, Aizawa Y, Iida T, Levy C, Aida T M, Inomata H 2005 *Carbohydrate Research* **340** 1931-1939

32. Williams P, Onwudili J 2005 *Ind Eng Chem Res* **44** 8739-8749

33. Kabyemela B M, Adschiri T, Malaluan R M, Arai K 1997 *Ind Eng Chem Res* **36** 1552-1558

34. Sinag A, Kruse A, Rathert J 2004 *Ind Eng Chem Res* **43** 502-508

35. Guo L, Lu Y, Zhang X, Ji C, Guan Y, Pei A 2007 *Catalysis Today* **129** 275-286

36. Qi J, Xiuyang L 2007 *Chin J Chem Eng* **15** 666-669

37. Sasaki M, Hayakawa T, Arai K, Adschiri T 2003 *The proceedings of the seventh international symposium on hydrothermal reactions* **2** 169-176

38. Tang H, Kitagawa K 2005 *Chemical Engineering Journal* **106** 261-267

39. Bustamante F, Enick R P, Killmeyer B H, Howard K S, Rothenberger Cugini AV, Morreale B D, Ciocco M V 2005 *AIChE Journal* **51** 1540-1454

40. Resende F, Fraley S, Berger M, Savage P 2008 *Energy and Fuels* **22** 1328-1334

41. Voll F A P, Rossi C C R S, Silva C, Guirardello R, Souza R O M A, Cabral V F, Cardozo-Filho L 2009 *International Journal of Hydrogen Energy* **34** 9737-9744

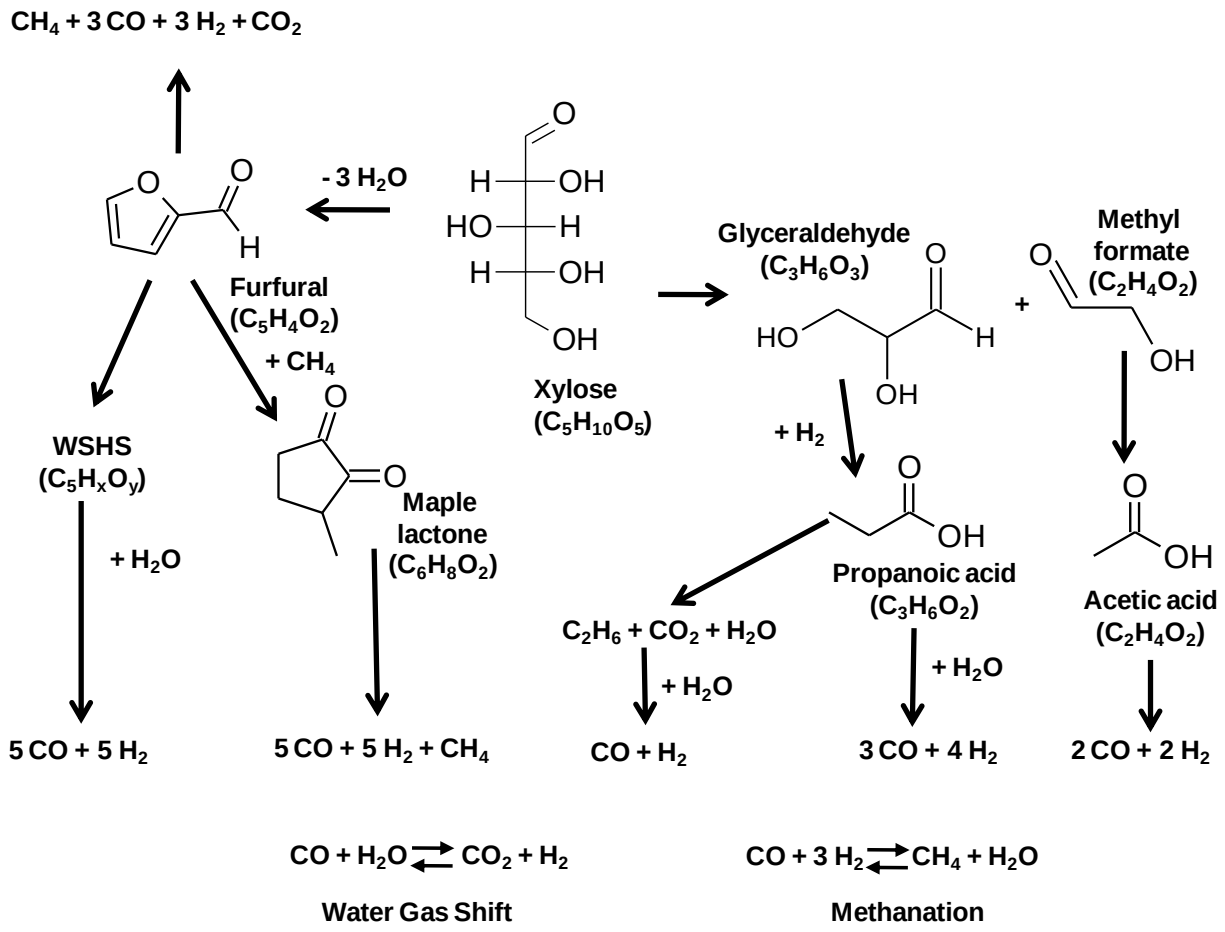

Figure 3.1. Proposed decomposition kinetic model reaction mechanism for gasification of xylose by supercritical water.

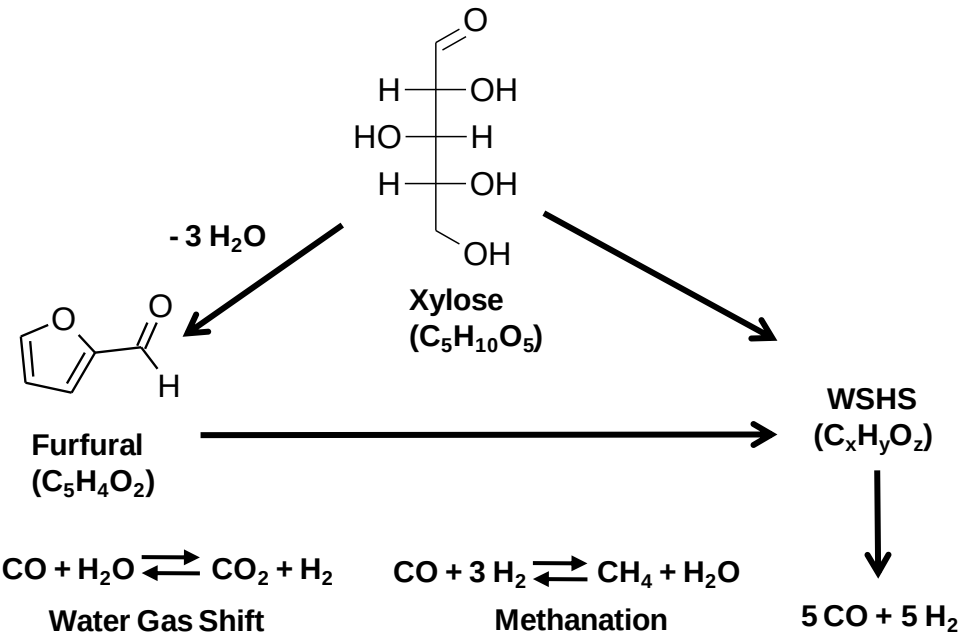

Figure 3.2. Proposed simplified gasification kinetic model reaction mechanism for gasification of xylose by supercritical water.

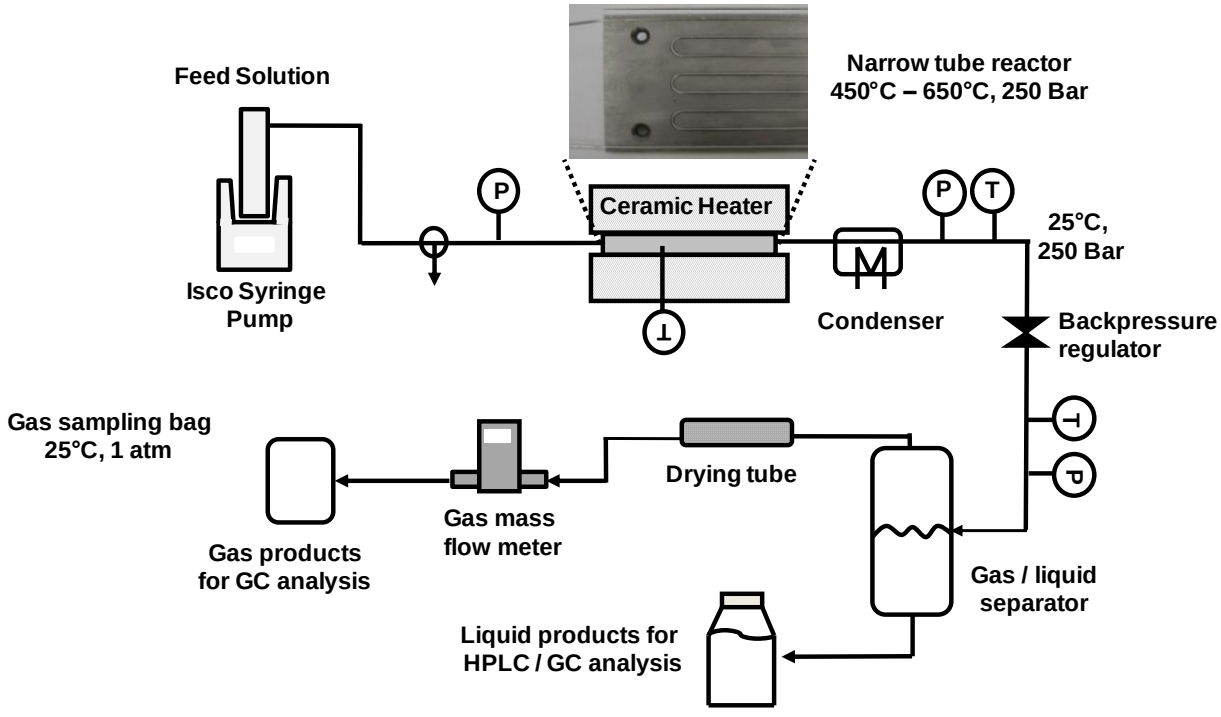

Figure 3.3. Continuous flow microtubular reactor test loop.

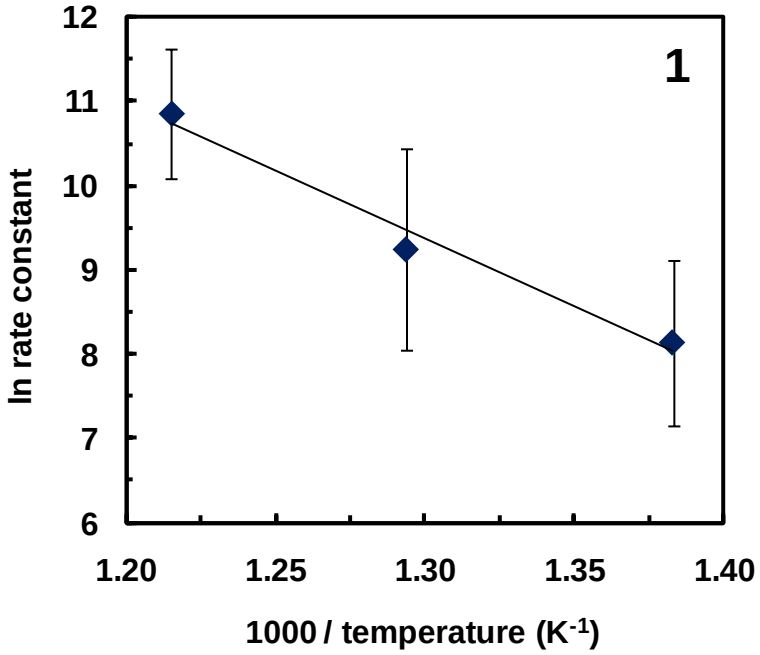
1
ln rate constant
12
11
10
9
8
7
6
1.20
1.25
1.30
1.35
1.40
1000 / temperature (K-1)

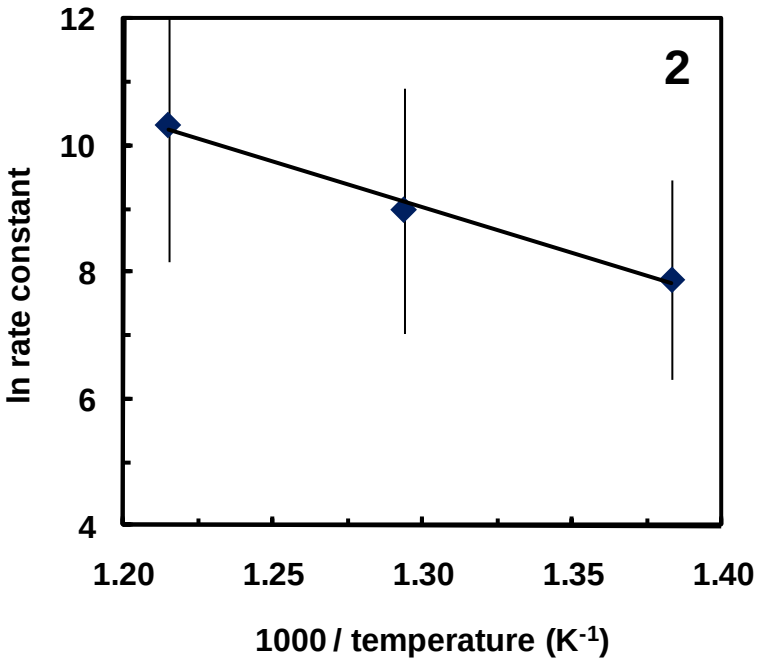
2
ln rate constant
12
10
8
6
4
1.20
1.25
1.30
1.35
1.40
1000 / temperature (K-1)

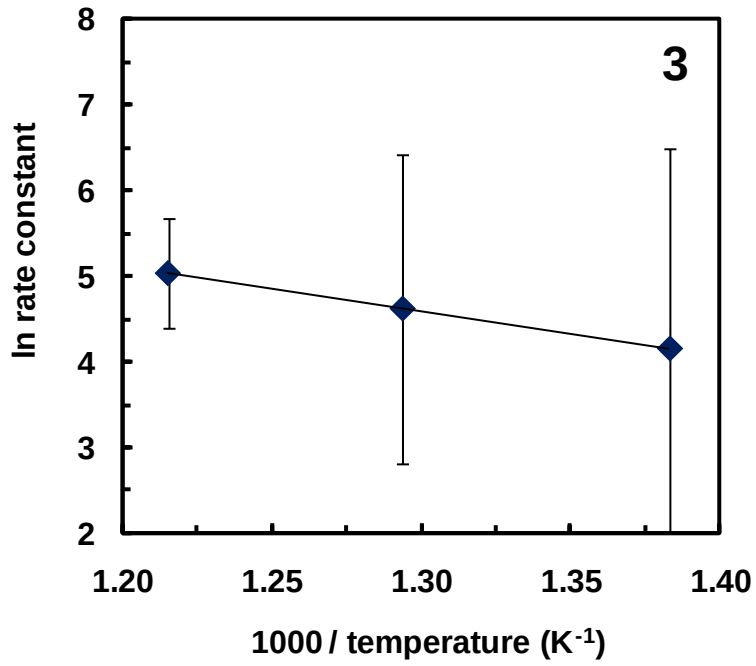
3
ln rate constant
8
7
6
5
4
3
2
1.20
1.25
1.30
1.35
1.40
1000 / temperature (K-1)

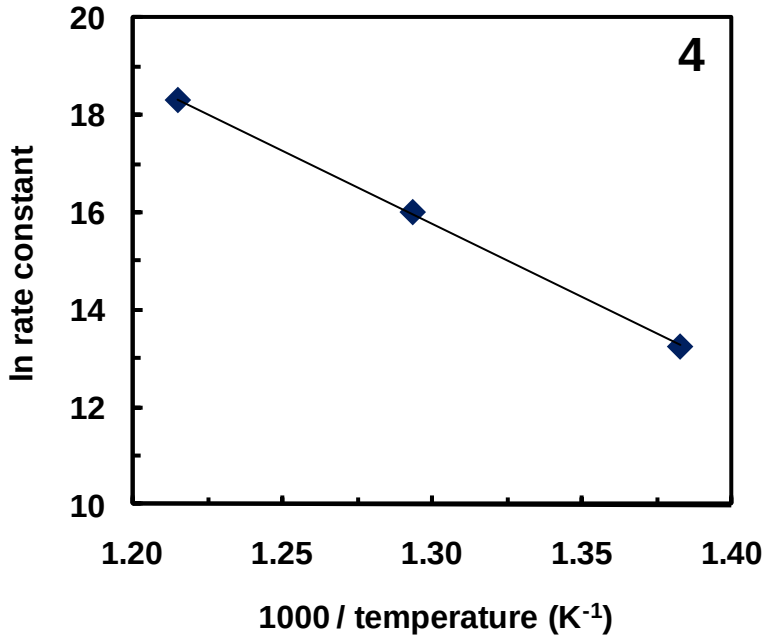
4
ln rate constant
20
18
16
14
12
10
1.20
1.25
1.30
1.35
1.40
1000 / temperature (K-1)

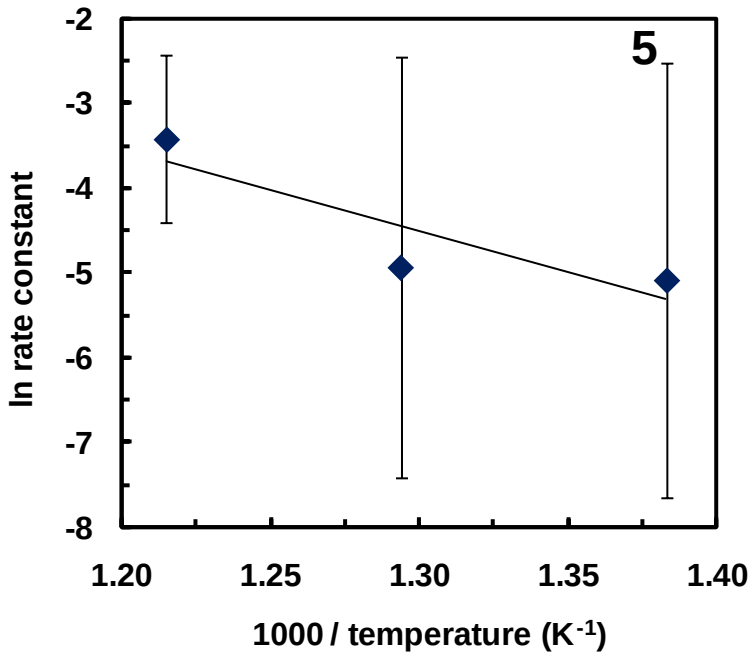
5
-2
-3
-4
-5
-6
-7
-8
ln rate constant
1.20
1.25
1.30
1.35
1.40
1000 / temperature (K-1)

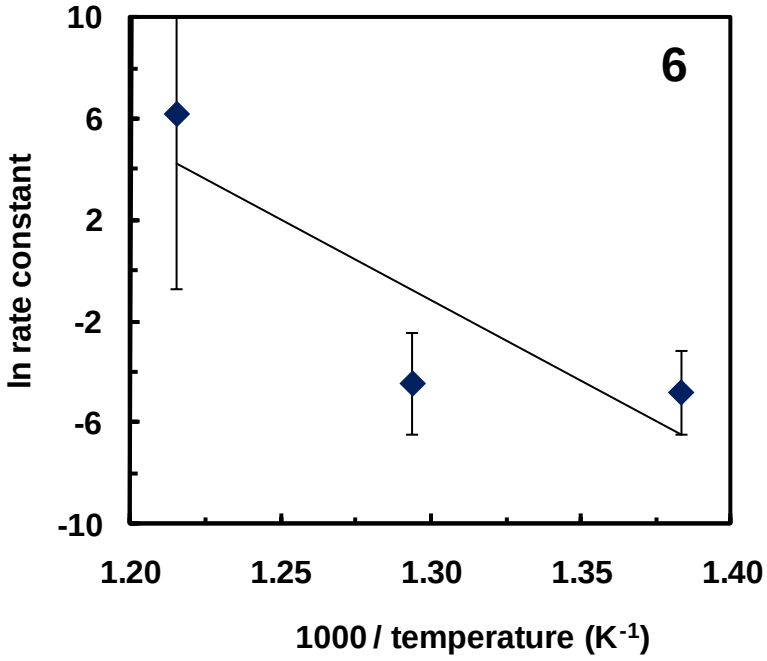
6
10
6
2
-2
-6
-10
ln rate constant
1.20
1.25
1.30
1.35
1.40
1000 / temperature (K-1)

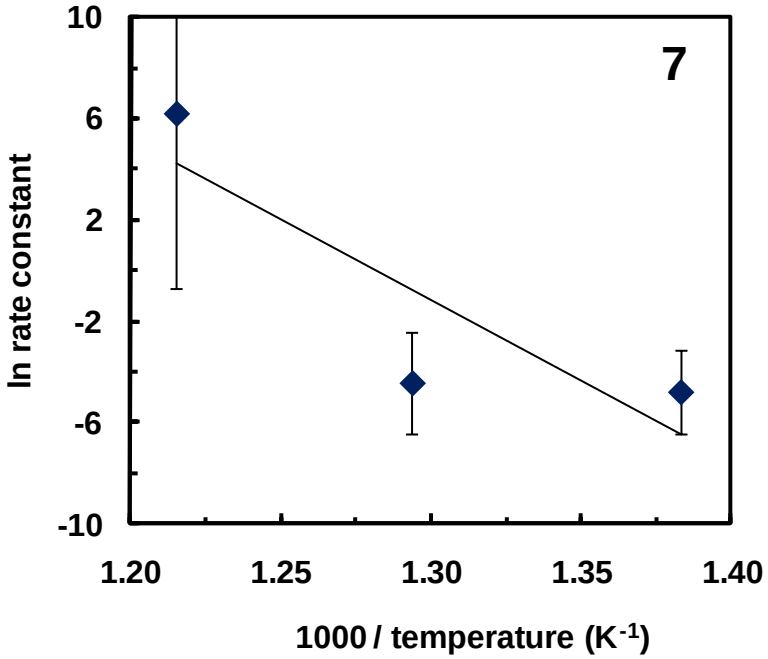
7
10
6
2
-2
-6
-10
ln rate constant
1.20
1.25
1.30
1.35
1.40
1000 / temperature (K-1)

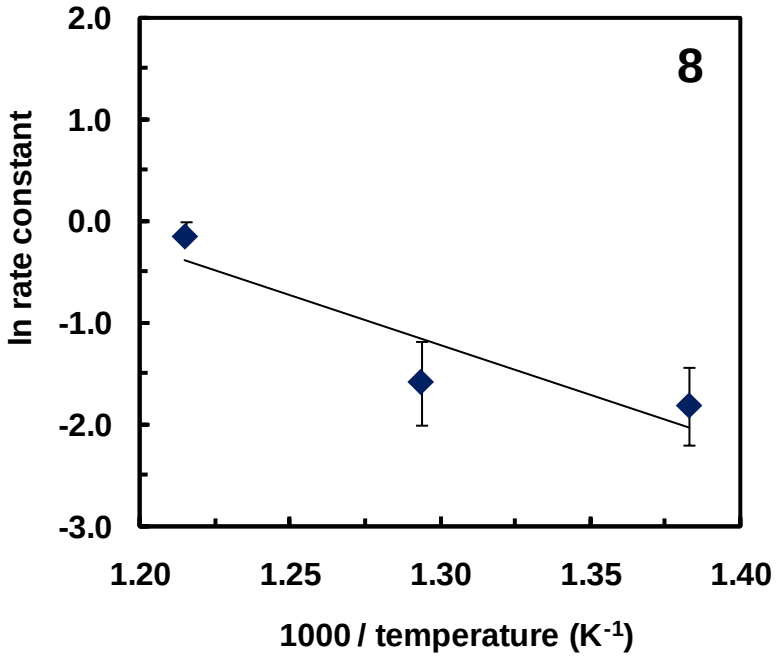
8
2.0
1.0
0.0
-1.0
-2.0
-3.0
ln rate constant
1.20
1.25
1.30
1.35
1.40
1000 / temperature (K-1)

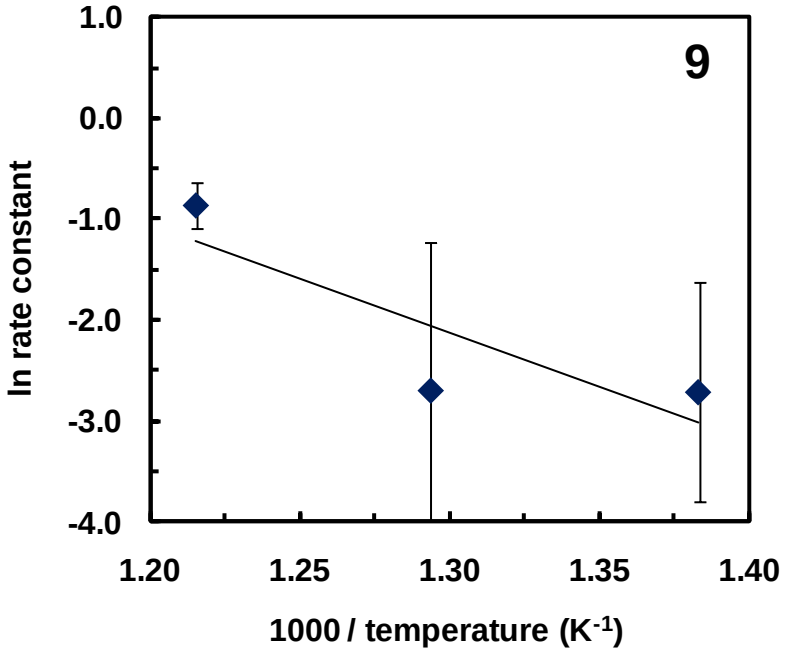
9
1.0
0.0
-1.0
-2.0
-3.0
-4.0
ln rate constant
1.20
1.25
1.30
1.35
1.40
1000 / temperature (K-1)

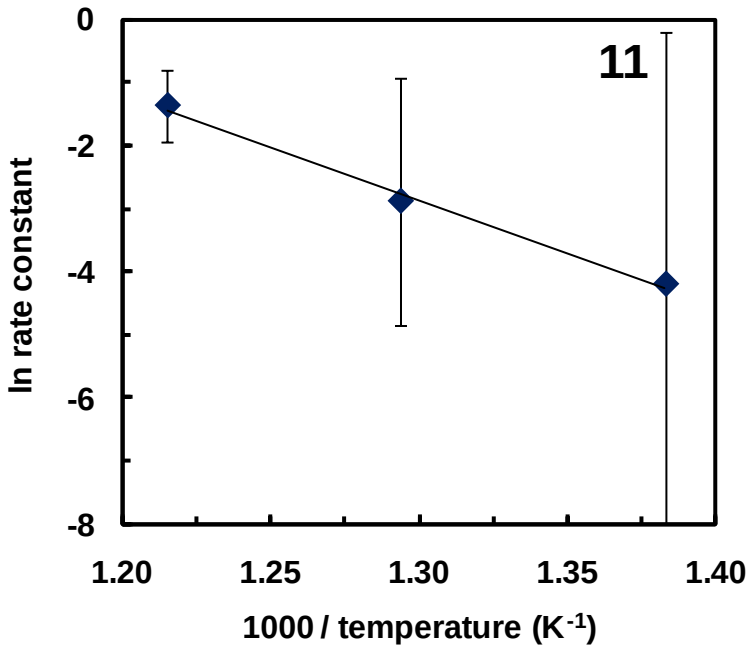
11
0
-2
-4
-6
-8
ln rate constant
1.20
1.25
1.30
1.35
1.40
1000 / temperature (K-1)

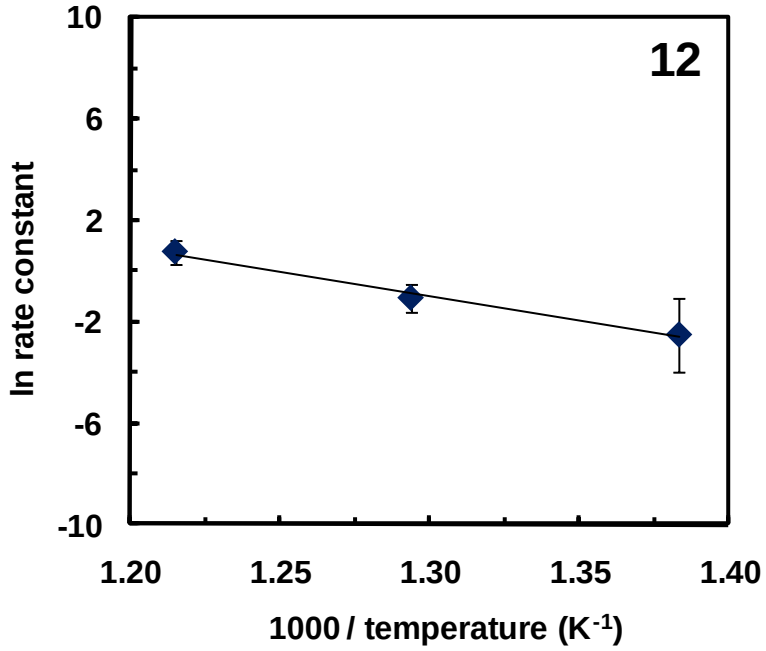

Figure 3.4(A). Arrhenius plots of estimated rate constants for the decomposition kinetic model. The number on the plot refers to the rate constant number in Equations 3.1 – 3.15.

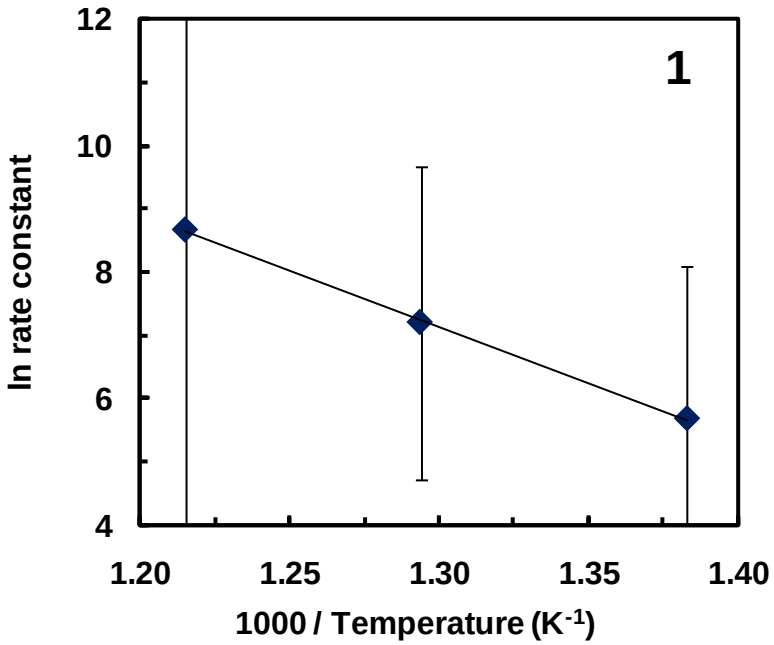

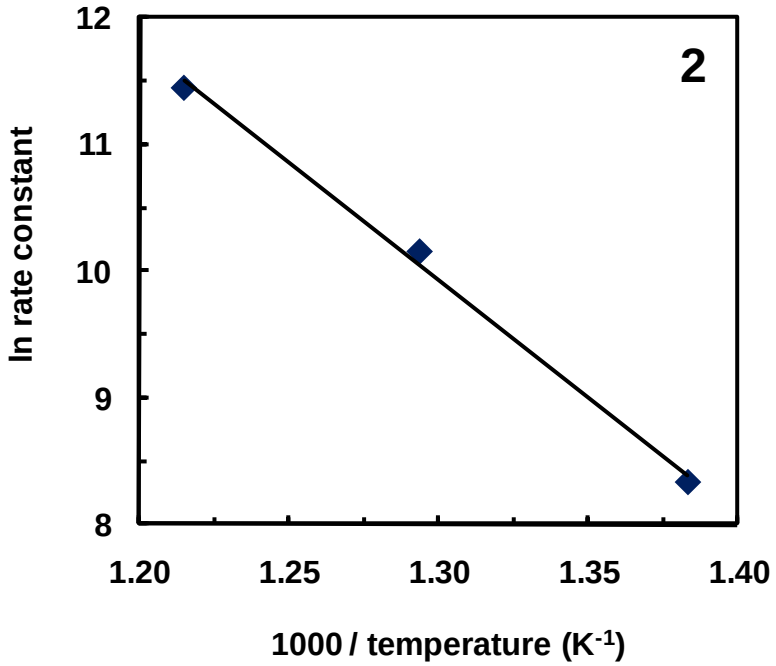
2
ln rate constant
12
11
10
9
8
1.20
1.25
1.30
1.35
1.40
1000 / temperature (K-1)

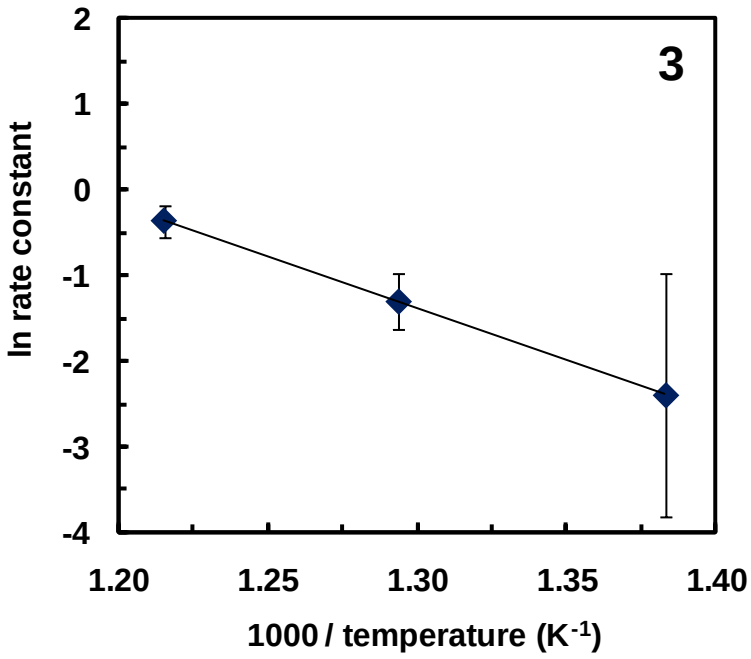
3
ln rate constant
2
1
0
-1
-2
-3
-4
1.20
1.25
1.30
1.35
1.40
1000 / temperature (K-1)

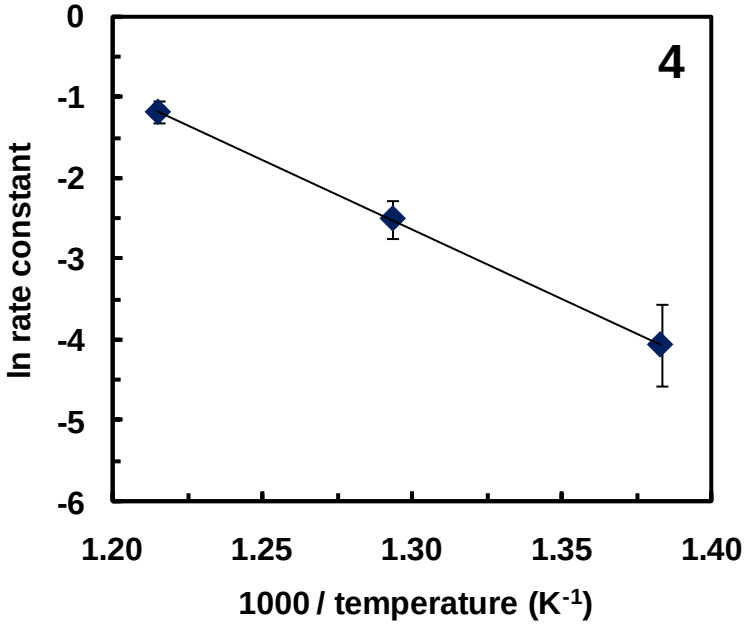

Figure 3.4(B). Arrhenius plots of estimated rate constants for the gasification kinetic model. The number on the plot refers to the rate constant number in Equations 3.29 – 3.32.

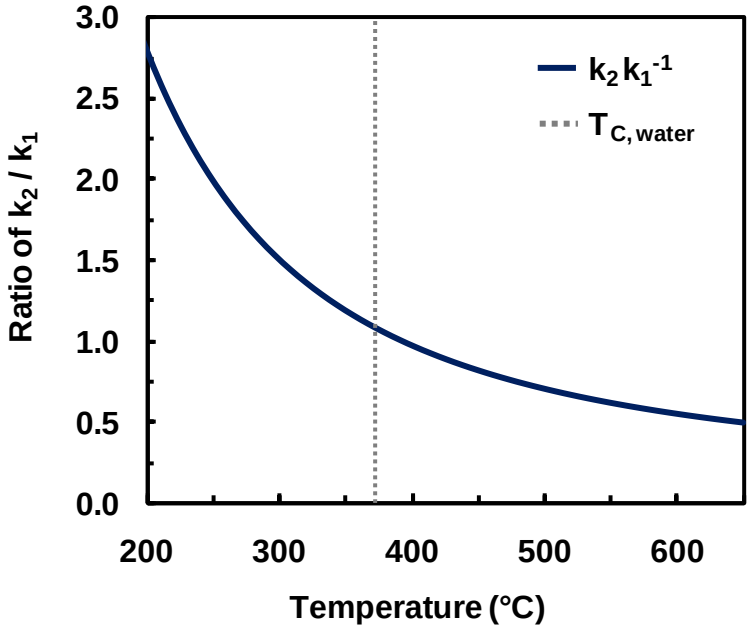

Figure 3.5. Ratio of rate constants k_1/ k_2 from the decomposition kinetic model. Estimated reaction rate k_1 is the decomposition of xylose to furfural, and k_2 is the decomposition of xylose to glyceraldehyde and methyl formate. The vertical dashed line represents the critical temperature of water.

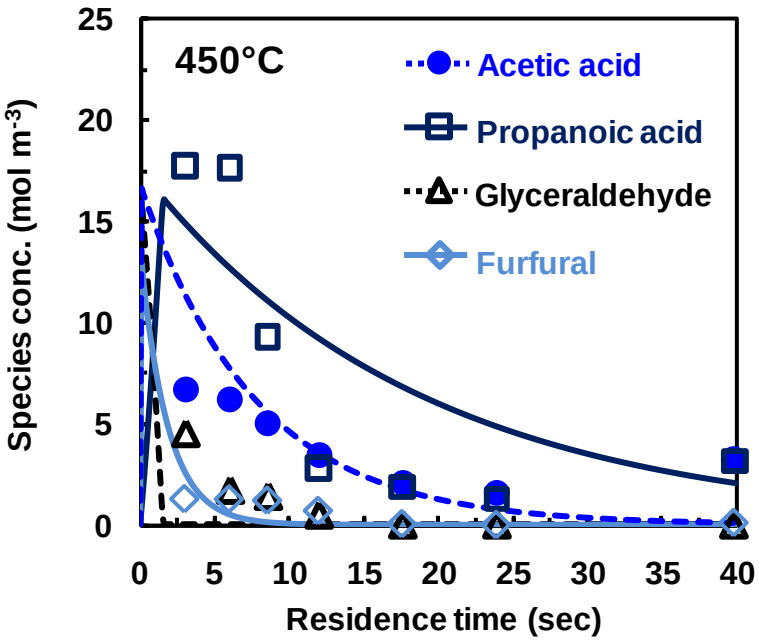
450°C
Acetic acid
Propanoic acid
Glyceraldehyde
Furfural
Species conc. (mol m-3)
Residence time (sec)
0
5
10
15
20
25
30
35
40

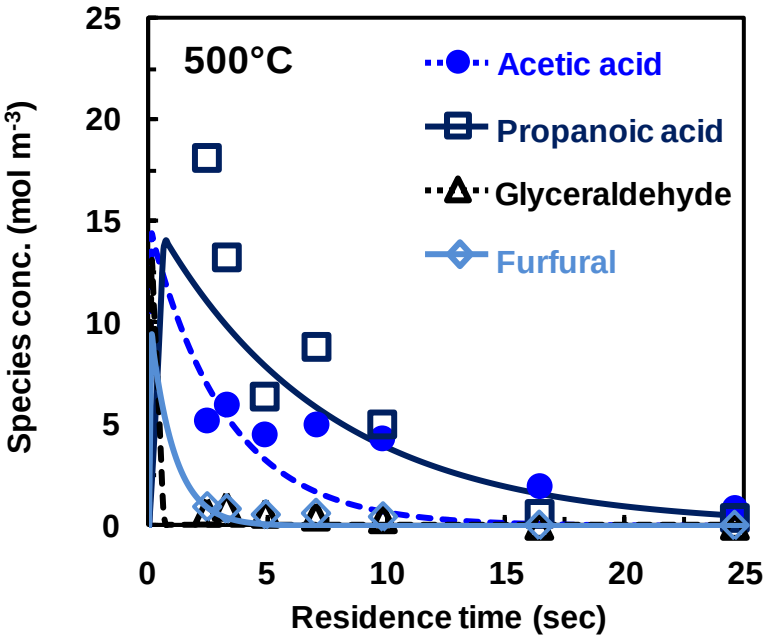
500°C
Acetic acid
Propanoic acid
Glyceraldehyde
Furfural
Species conc. (mol m-3)
Residence time (sec)
0
5
10
15
20
25

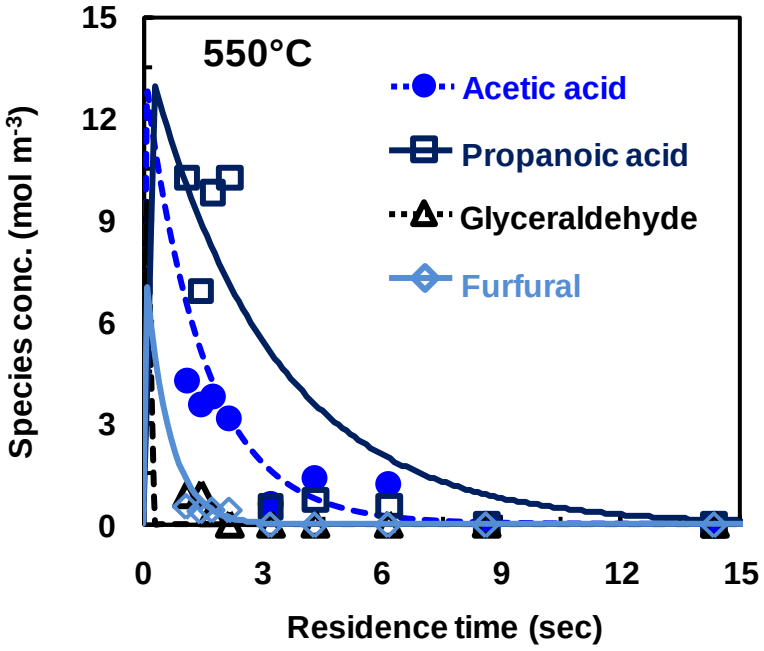

Figure 3.6. Liquid phase intermediate product formation from the supercritical water gasification of xylose (4.0 wt %, 277 mM) vs. residence time compared at 450°C, 500°C, and 550°C. The solid and dashed lines represent the non-linear least squares fit of the data to the decomposition kinetic model.

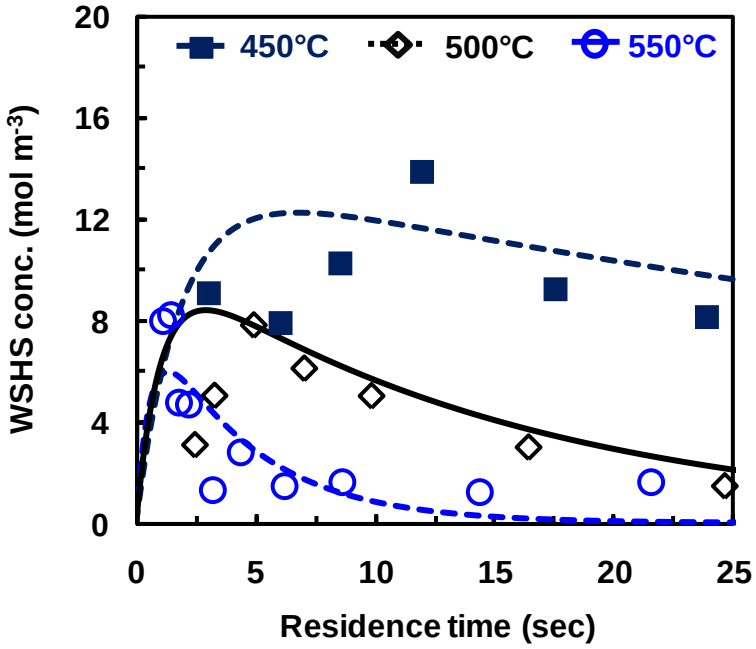

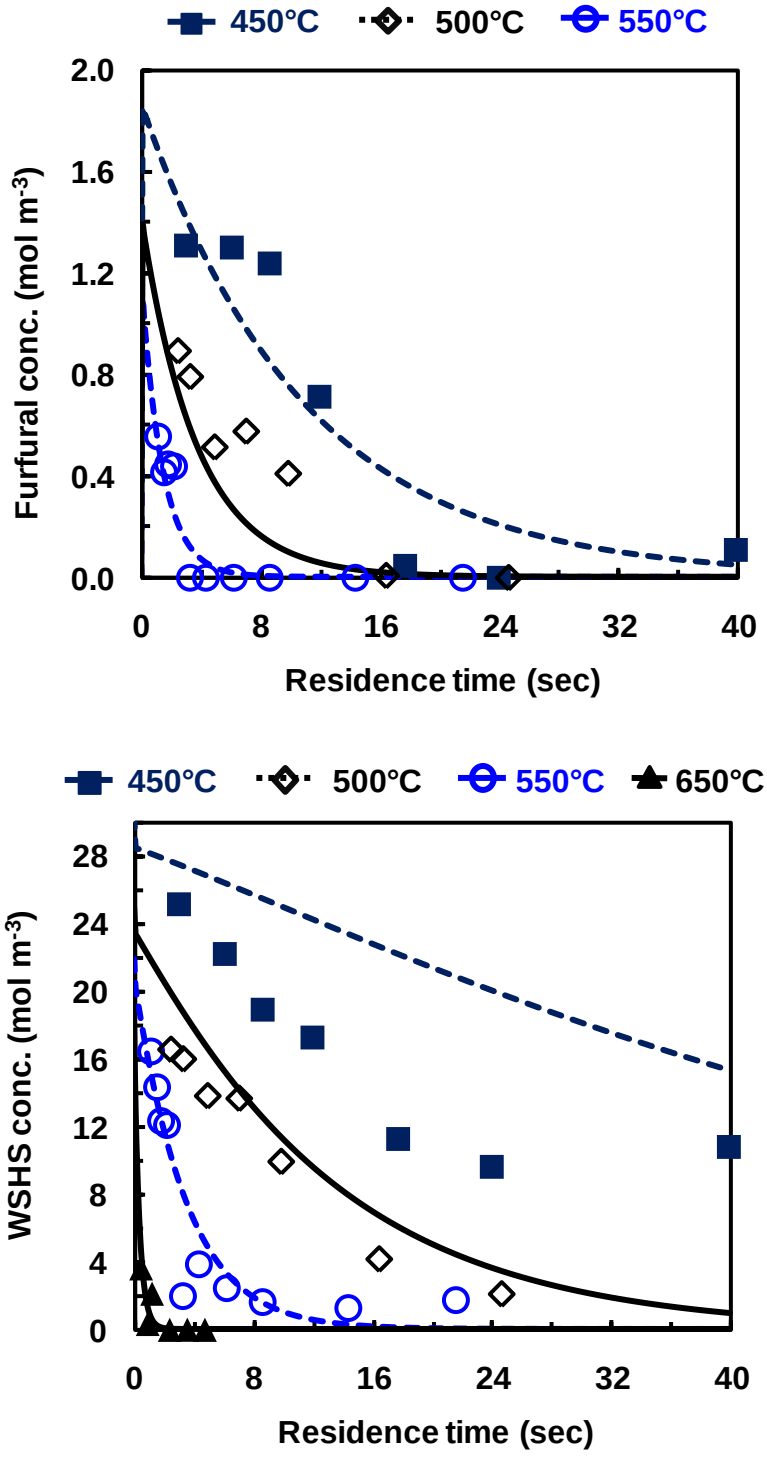

Figure 3.7. Liquid phase concentration of WSHS and furfural at 450°C, 500°C, 550°C, and 650°C. Liquid intermediate concentration is in M m^{-3} at reaction T and P. The solid and dashed lines represent the non-linear least squares fit of the data to the gasification kinetic model.

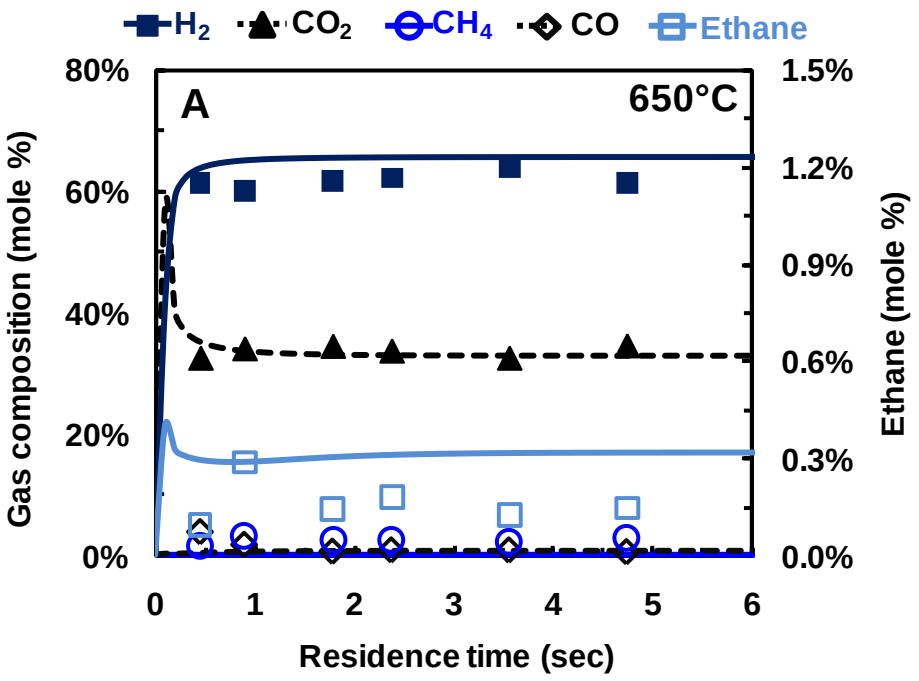
H2
CO2
CH4
CO
Ethane
A
650°C
Gas composition (mole %)
Ethane (mole %)
80%
60%
40%
20%
0%
1.5%
1.2%
0.9%
0.6%
0.3%
0.0%
0
1
2
3
4
5
6
Residence time (sec)

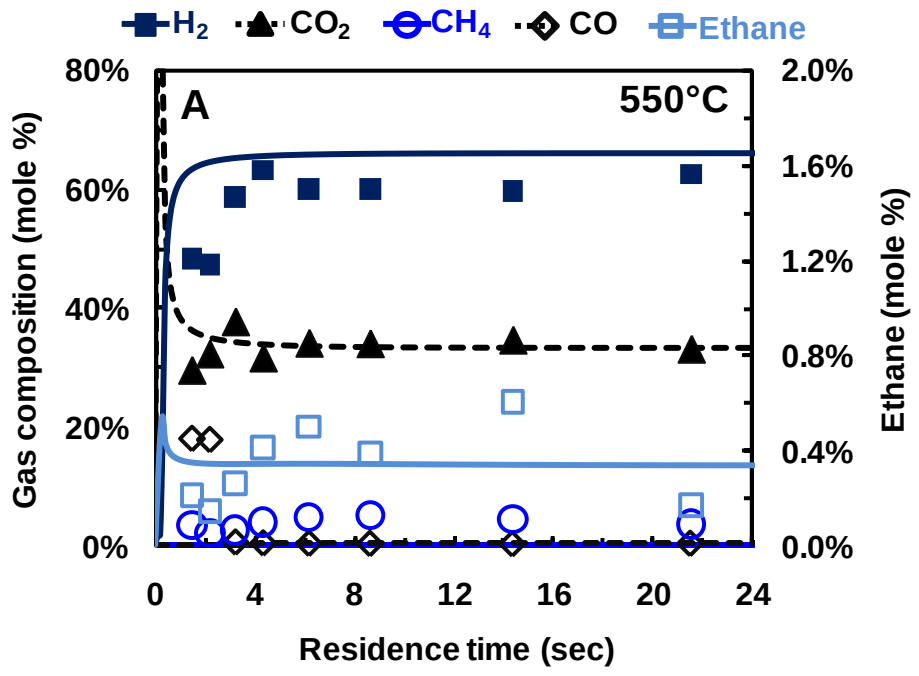
H2
CO2
CH4
CO
Ethane
A
550°C
Gas composition (mole %)
Ethane (mole %)
80%
60%
40%
20%
0%
2.0%
1.6%
1.2%
0.8%
0.4%
0.0%
0
4
8
12
16
20
24
Residence time (sec)

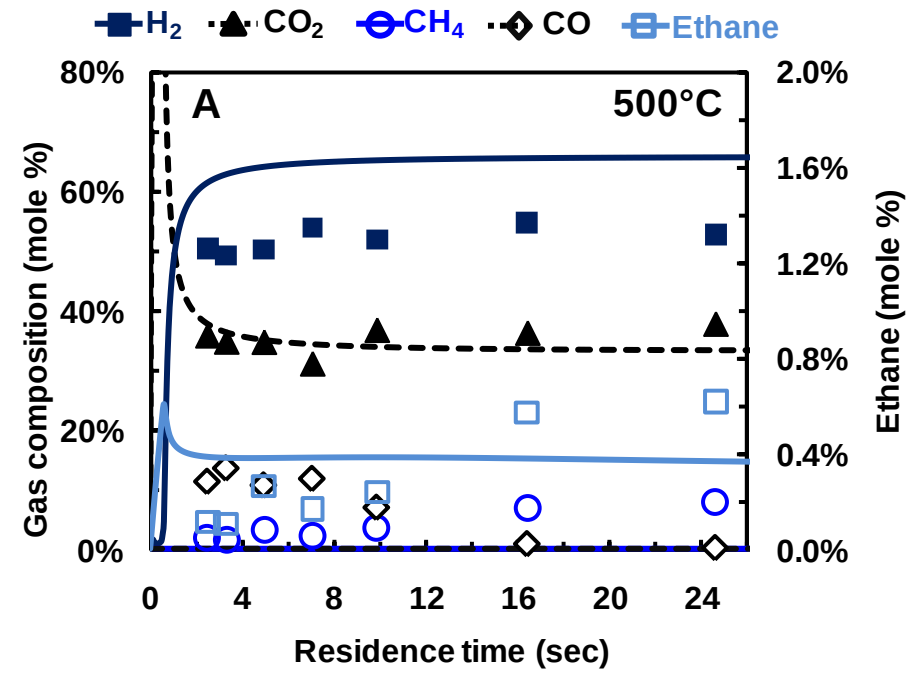
H2
CO2
CH4
CO
Ethane
A
500°C
Gas composition (mole %)
Ethane (mole %)
80%
60%
40%
20%
0%
2.0%
1.6%
1.2%
0.8%
0.4%
0.0%
0
4
8
12
16
20
24
Residence time (sec)

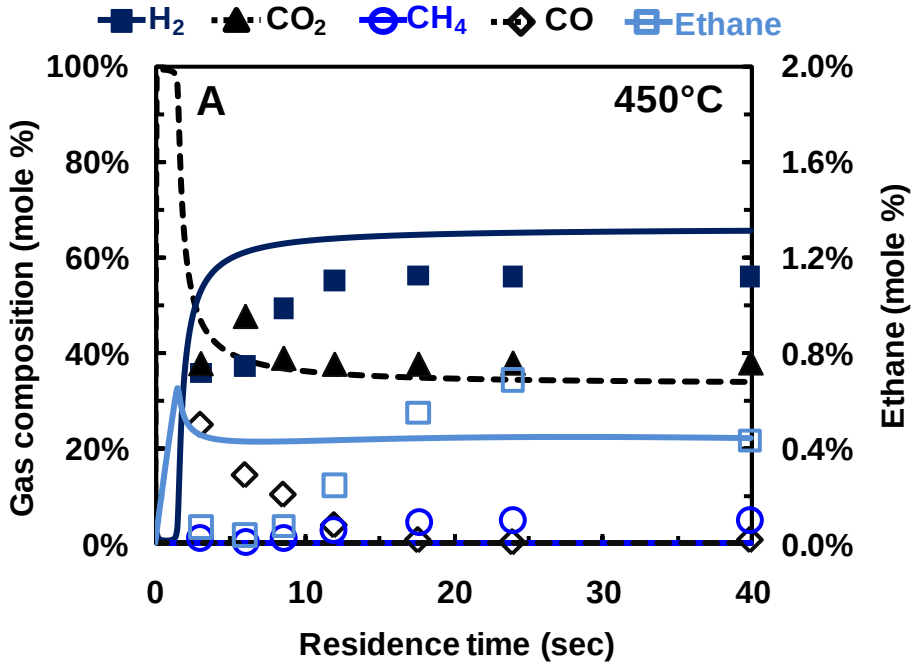
H2
CO2
CH4
CO
Ethane
A
450°C
Gas composition (mole %)
Ethane (mole %)
100%
80%
60%
40%
20%
0%
2.0%
1.6%
1.2%
0.8%
0.4%
0.0%
0
10
20
30
40
Residence time (sec)

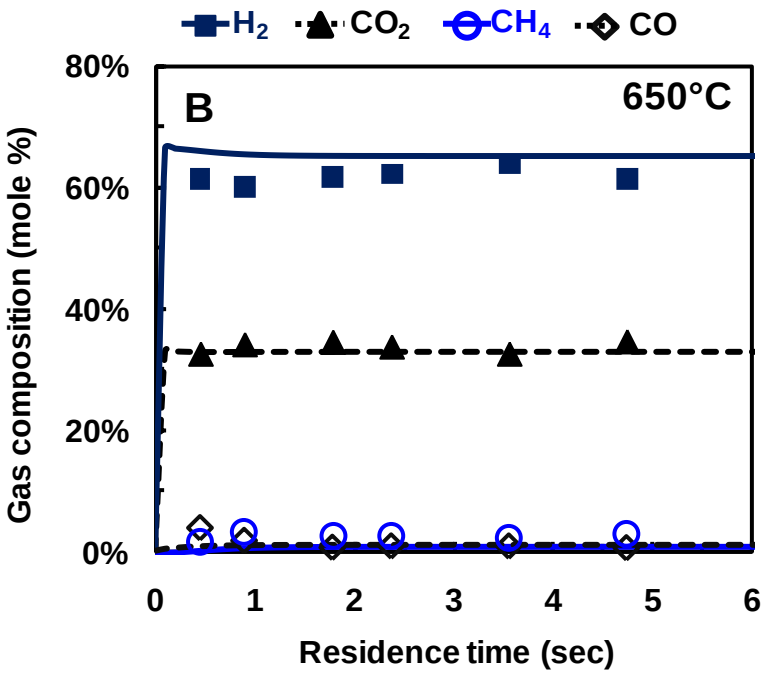
H2
CO2
CH4
CO
B
650°C
Gas composition (mole %)
80%
60%
40%
20%
0%
0
1
2
3
4
5
6
Residence time (sec)

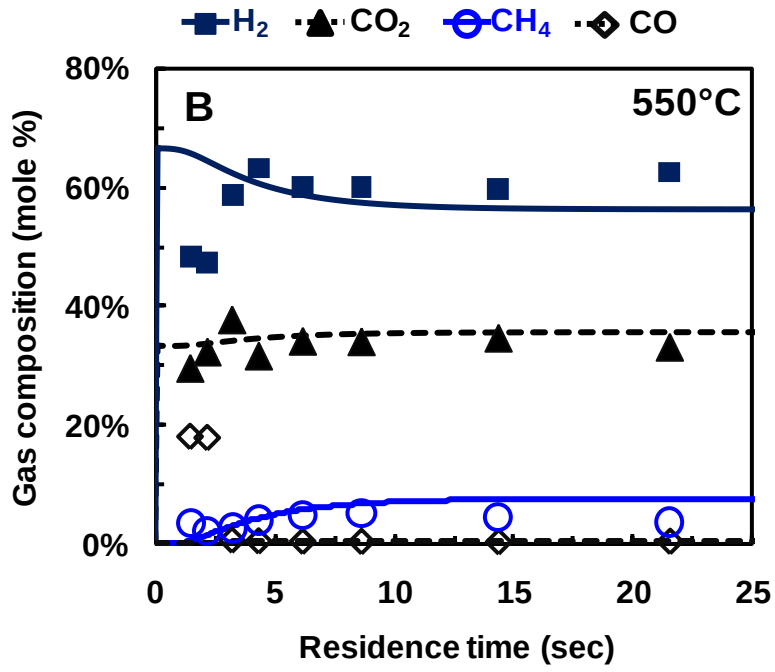
H2
CO2
CH4
CO
B
550°C
Gas composition (mole %)
80%
60%
40%
20%
0%
0
5
10
15
20
25
Residence time (sec)

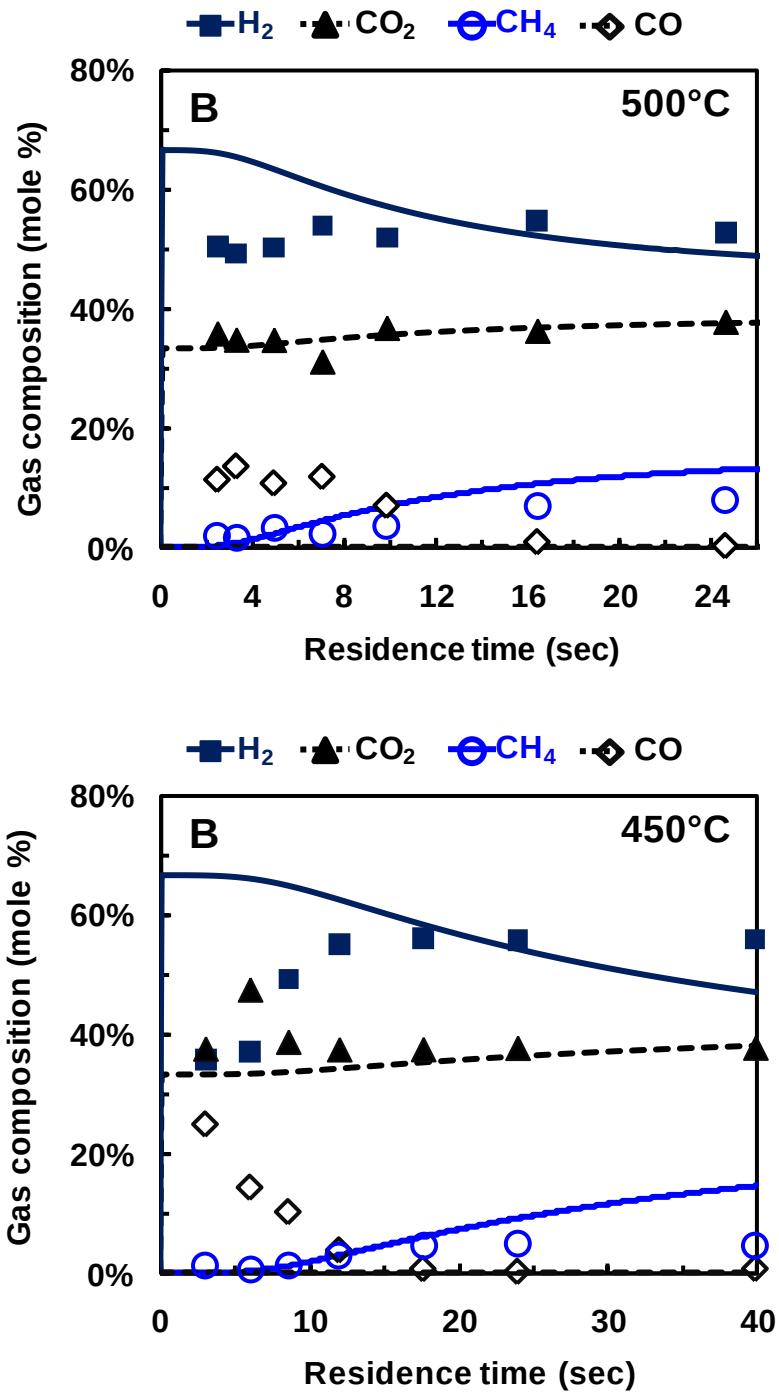

Figure 3.8. Gas product composition from the supercritical water gasification of xylose (4.0 wt %, 277 mM) vs. residence time compared at 450°C, 500°C, 550°C, and 650°C. The solid and dashed lines represent the non-linear least squares fit of the data to the (A) decomposition kinetic model and (B) gasification kinetic model.

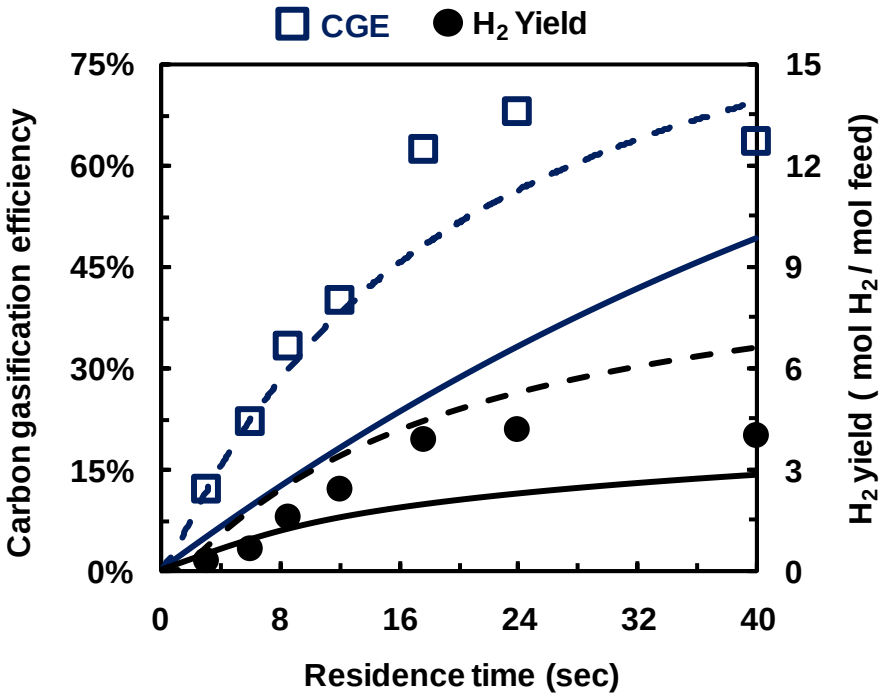
CGE
H2 Yield
75%
60%
45%
30%
15%
0%
Carbon gasification efficiency
15
12
9
6
3
0
H2 yield (mol H2 / mol feed)
0
8
16
24
32
40
Residence time (sec)

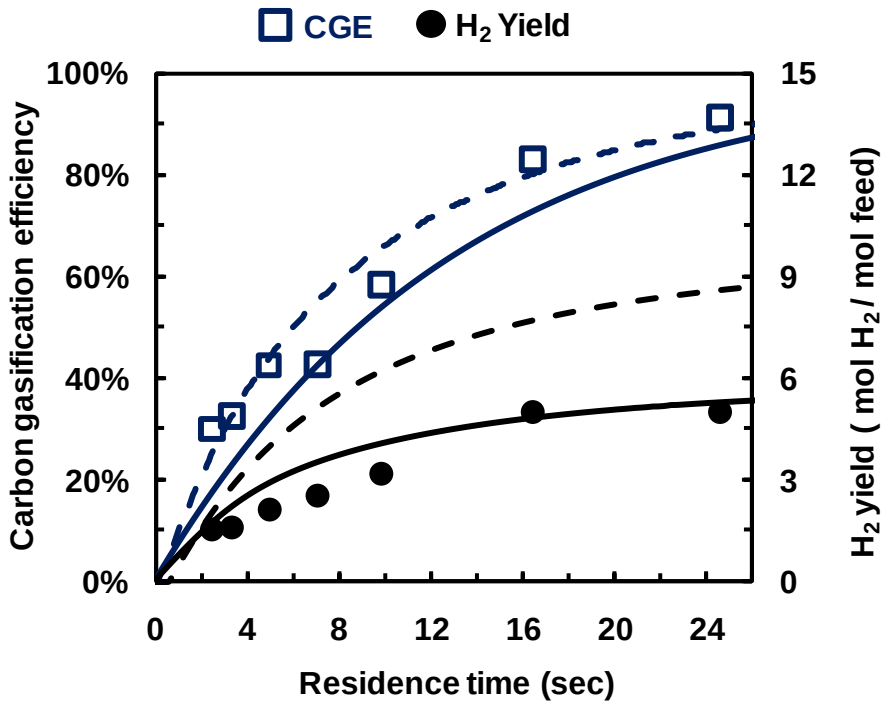
CGE
H2 Yield
100%
80%
60%
40%
20%
0%
Carbon gasification efficiency
15
12
9
6
3
0
H2 yield (mol H2 / mol feed)
0
4
8
12
16
20
24
Residence time (sec)

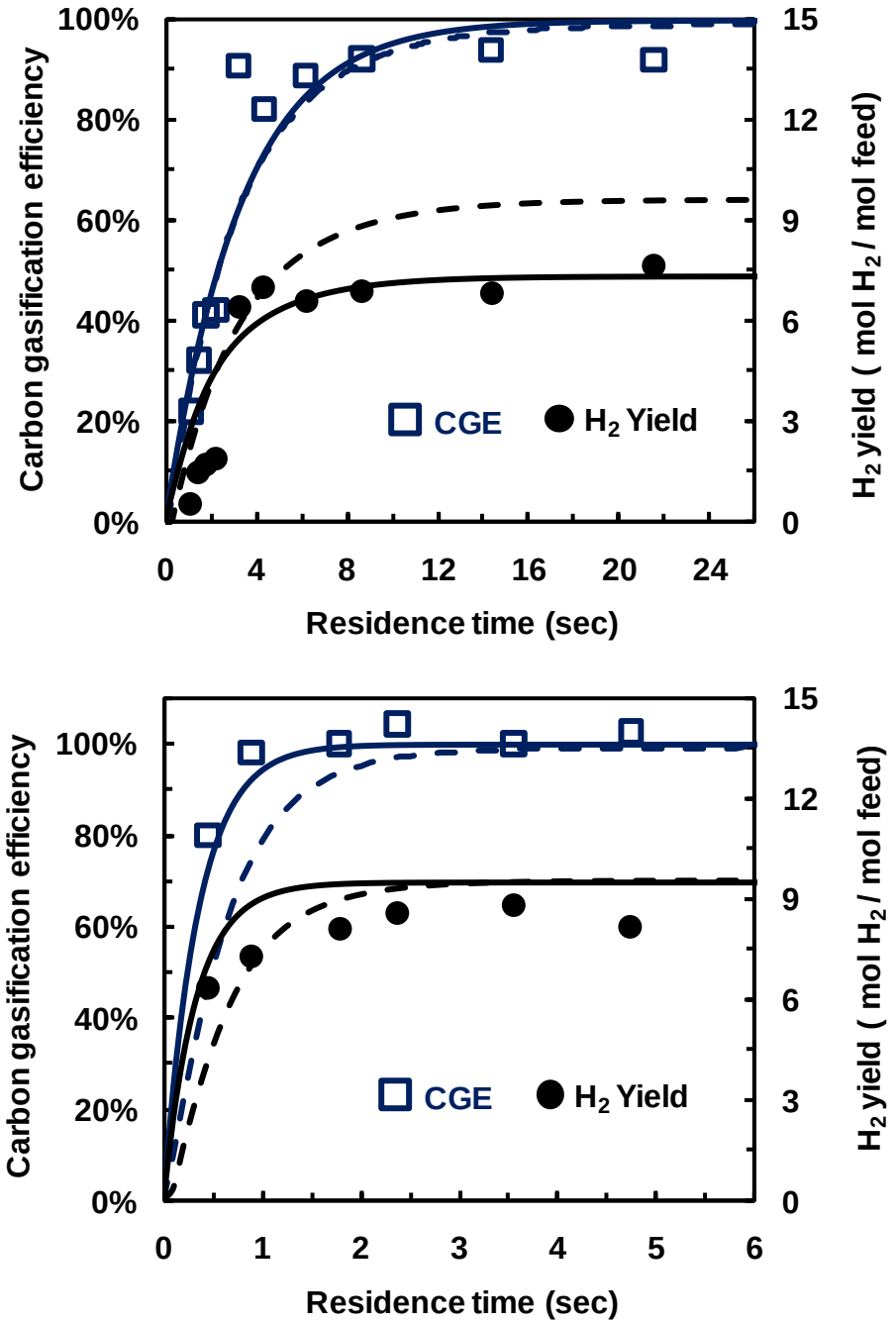

Figure 3.9. Carbon gasification efficiency and H_2 yield from the supercritical water gasification of xylose (4.0 wt %, 277 mM) vs. residence time compared at 450°C, 500°C, 550°C, and 650°C. The solid lines are fits from the gasification model and dashed lines are fits from the decomposition kinetic model.

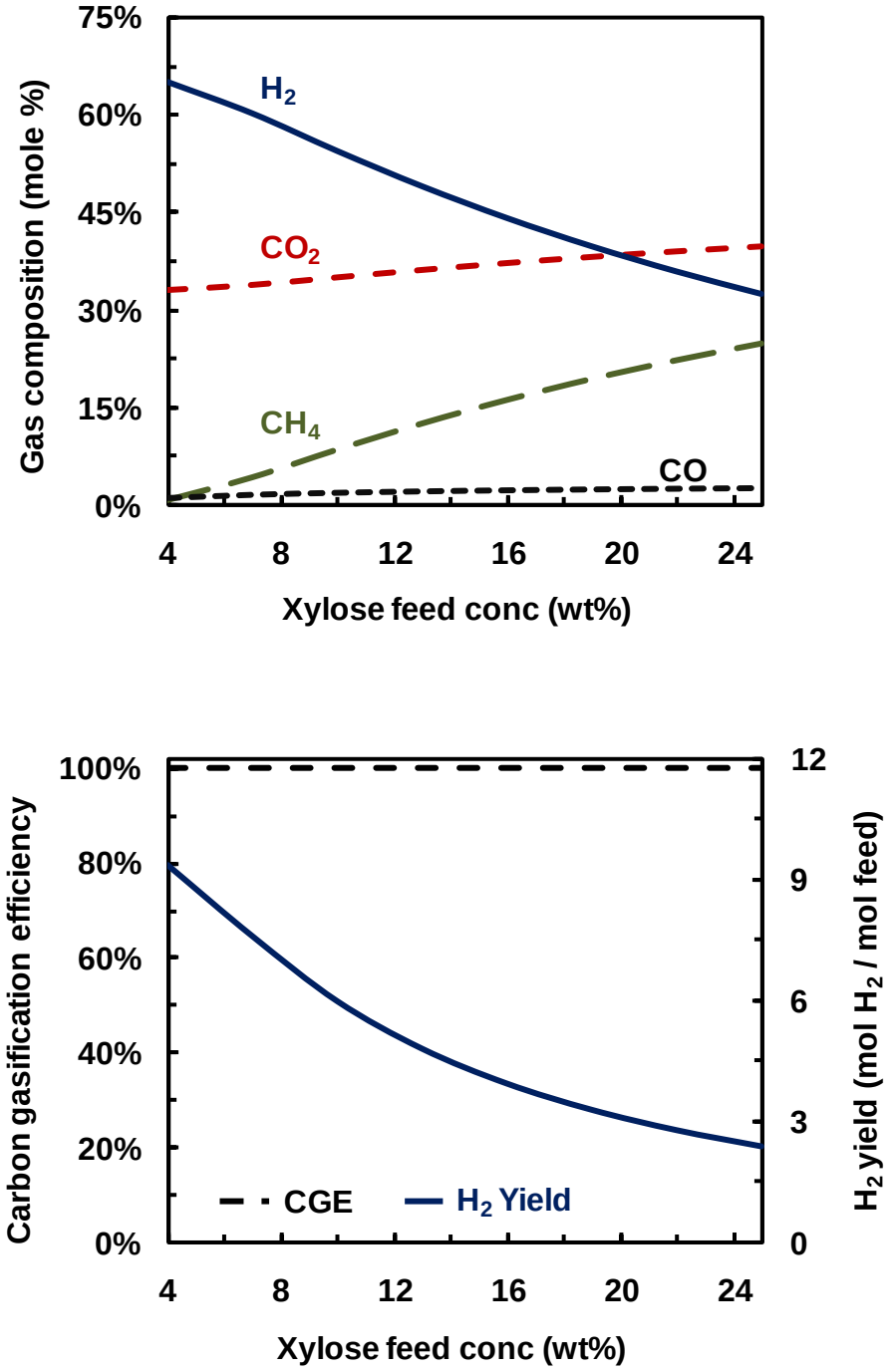

Figure 3.10. Predicted gas composition (A), carbon gasification efficiency, and H_2 yield (B) as a function of feed concentration. The predictions were from the gasification kinetic model at 650°C, 250 bar and a 10 second average fluid residence time.

Table 3.1. Summary of rate constant fitting parameters.

Decomposition kinetic model	
Number of differential equations	13
Number of measurements sets	13
Confidence level	95%
Initial step size	0.001
Gradient evaluation	2 sided difference
Termination tolerance	1.00E-09
Final residual estimate	1.00E-06
Error estimation	Sum of the squared residuals
Residence time range for fitted experimental data	3.0 - 24.0 sec (450°C) 2.5 - 16.4 sec (500°C) 1.1 - 8.6 sec (550°C)
Gasification kinetic model	
Number of differential equations	7
Number of measurements sets	7
Confidence level	95%
Initial step size	0.001
Gradient evaluation	2 sided difference
Termination tolerance	1.00E-09
Final residual estimate	1.00E-06
Error estimation	Sum of the squared residuals
Residence time range for fitted experimental data	3.0 - 40.0 sec (450°C) 2.5 - 24.6 sec (500°C) 1.1 - 21.5 sec (550°C)

Table 3.2. Summary of estimated kinetic parameters. *Due to an estimated rate constant of 0 sec^{-1} at 450°C, k_{10} was estimated by plotting the estimated rate constants at 500°C and 550°C vs. temperature and estimating an activation energy and pre-exponential.

Rate constant	Activation Energy (kj/mol)	error (±)	Pre-exponential (sec^{-1})	error (+)	error (-)
Decomposition kinetic model					
k_1	134.0	19.5	1.5E+13	3.1E+14	7.0E+11
k_2	120.1	11.1	1.2E+12	6.6E+12	2.1E+11
k_3	43.9	0.1	9.5E+04	9.7E+04	9.3E+04
k_4	250.7	3.8	7.5E+23	1.4E+24	4.2E+23
k_5	55.6	34.9	5.7E+03	1.3E+06	2.4E+01
k_6	532.4	313.7	4.4E+35	8.6E+56	2.3E+14
k_7	80.6	41.9	3.3E+03	2.3E+06	4.8E+00
k_8	81.5	37.6	1.0E+05	3.6E+07	2.9E+02
k_9	89.4	55.2	1.4E+05	7.9E+08	2.5E+01
k_{10}^*	157.3	N/A	1.0E+09	N/A	N/A
k_{11}	138.9	10.9	1.6E+08	8.5E+08	2.8E+07
k_{12}	161.7	16.7	3.5E+10	4.8E+11	2.6E+09
k_{13}	0.0	0.0	0.0E+00	0.0E+00	0.0E+00
Gasification kinetic model					
k_{18}	147.5	3.8	1.3E+13	2.4E+13	7.1E+12
k_{19}	154.7	9.4	6.6E+14	2.8E+15	1.5E+14
k_{20}	100.5	0.5	1.7E+06	1.8E+06	1.5E+06
k_{21}	142.7	1.5	3.5E+08	4.5E+08	2.8E+08

Chapter 4: Design and Fabrication of a Parallel Channel Hastelloy Microchannel Reactor for Supercritical Water Gasification of Biomass

4.1 Abstract

Due to high rates of heat transfer as a result of large surface area to volume ratios, microchannel reactors intensify endothermic supercritical water reforming reactions. A Hastelloy C-276 microchannel reactor based on a parallel processing architecture was designed and fabricated for supercritical water gasification of solubilized biomass. The reactor consists of 14 parallel 127 micron by 1000 micron by 46 cm channels that serpentine a total of 15 times through the device. Fabrication was accomplished by diffusion bonding a series of laser cut shims in between two header plates into a contiguous block. A pre-heater was integrated into the reactor to ensure temperature gradients at the entrance of the reactor, due to the fluid heating period, were isolated from subsequent channels. Due to the intricate nature of the microchannel reactors architecture, as well as the inability to directly evaluate the internal geometry of the reactor after diffusion bonding, the pressure drop and average residence time were measured to validate the reactors geometry.

Keywords: Microreactor; Microchannel; SCWG; Supercritical water; Biomass gasification; diffusion bonding;

4.2 Introduction

In the last decade, growing concerns about increased atmospheric CO_2 concentration and dwindling finite fossil fuel reserves have motivated a substantial volume of research in the field of alternative energy. Thermochemical conversion of biomass to fuels is a renewable, CO_2 neutral source of energy that may help sustain the world's energy supply [1-2]. Supercritical water reforming to H_2 is a promising technology for thermochemical biomass processing. Water in its supercritical state (any combination of temperature greater than 374°C and pressure greater than 220 bar) has been shown to completely gasify biomass to hydrogen rich gas with little or no byproduct formation. Recently there have been several reviews of supercritical water gasification of biomass [3-8]. Previous studies have shown that biomass gasification in supercritical water significantly benefits from enhanced heat transfer to the reacting fluid [9-10]. In particular, high rates of heat transfer minimize the fluid heating period and drive highly endothermic reactions that result in increased gas yields, decreased processing times, and the suppression of recalcitrant byproducts and coke precursor formation [11-13]. Furthermore, reactor walls comprised of a high nickel alloy, such as Hastelloy, have been shown to enhance supercritical water gasification of biomass by catalyzing biomass gasification reactions, suppressing coke formation and generating additional hydrogen through reforming [14-18]. High rates of heat transfer to the reacting fluid and large surface area to volume ratios make microchannel reactors an ideal platform to gasify biomass in supercritical water.

Microreactors gained popularity as a result of process intensification concepts and manufacturing methods derived from the electronic industry [19]. They offer several advantages relative to chemical processing in macroscopic continuous flow or batch reactors. Increased mass transfer rates can be used to facilitate diffusion limited processes such as multiphase and heterogeneous catalyzed reactions. High rates of heat transfer can facilitate reaction pathways often difficult to control in traditional flow reactors, including highly endothermic and exothermic reactions. More precise temperature control increases product selectivity, resulting in increased yields, and offers an alternative

approach to batch processing. In addition to process intensification, microreactors can be used for portable or integrated devices for decentralized chemical processing. This can be particularly useful for biomass processing due to high transportation costs as a result of the relatively low density and high water content of biomass compared to liquid fuels [20]. In regard to fuel processing, microreactor technology, including current and state of the art applications and fabrication techniques, has recently been reviewed [19, 21-24]. There are no reported current investigations that describe the design and fabrication of a microchannel reactor constructed from a nickel alloy to continuously gasify biomass above the critical temperature and pressure of water.

Although microreactor design is highly dependent on its desired application, the majority of scalable microreactor designs are based on parallel processing. The reacting fluid is split into several sub-streams at the reactor inlet, and recombined at the reactor outlet. Ideally, the physics in each microchannel will be identical. However, microreactor architecture, fabrication tolerances, and header or manifold design greatly affect the uniformity of flow distribution in the microchannels [25 - 29]. Two of the most widely used microreactor architectures are bifurcation and parallel channel. The bifurcating design is based on a single inlet channel that bifurcates several times through the reactor, whereas the parallel channel design is based on a inlet header channel that distributes the fluid to a series of parallel microchannels. In the absence of fabrication tolerances and sufficient channel length between branch points, the bifurcation architecture always produces equal flow distribution between microchannels [25]. However, the parallel channel architecture has a lower pressure drop, better heat transfer, smaller inlet and outlet header volumes, and flow distribution is less sensitive to fabrication tolerances [25, 28]. In addition to reactor architecture, microreactor manifold design is likely to have a significant impact on reactor transport properties. Parallel channel microreactor designs are typically optimized for flow uniformity by either varying the header channel hydraulic diameter to ensure a uniform pressure drop for each microchannel [25] or increase the header volume to decrease the header pressure drop relative to the microchannel pressure drop [30].

In the present study, we describe the design and fabrication of a parallel channel microreactor intended for supercritical water gasification of solubilized biomass. The reactor was constructed from Hastelloy C-276, a nickel alloy which intensifies supercritical water biomass gasification due to high catalytic activity in the reactor wall. The microreactor architecture uses a single plate manifold system to distribute the reacting fluid to 14 parallel microchannels that serpentine 15 times vertically through the device. Equal flow distribution in the channels was addressed by making the pressure drop through a microchannel much greater than the pressure drop through the distribution header and therefore minimizing the effect from stationary vortices that may form in the distribution channel. This was accomplished by making the channel much longer than the distribution channel by using a serpentine channel configuration similar to channel designs often used for water removal in fuel cells [31-38]. The reactor was fabricated by a combination of traditional milling, laser cutting, and diffusion bonding techniques. Due to the inability to directly visualize or measure the internal geometry in the microchannel reactor, macroscopic measurements including pressure drop and average fluid residence time were evaluated.

4.3 Reactor design and fabrication

4.3.1 Reactor Architecture

The Hastelloy C-276 microchannel reactor architecture is detailed in Figure 4.1. The reactor design is based on parallel processing by a split and recombine structure. The reacting fluid is distributed to a parallel array of 14 channels (1000 μm by 127 μm) though an inlet header (1000 μm by 750 μm). In each channel the fluid serpentines a total of 15 times vertically throughout the device before reaching the outlet header. The total length and volume of each channel from the inlet header to the outlet header is designed identical. A 1.0 cm integrated pre-heater in the first set of channels is designed to minimize a temperature drop in the reacting fluid for subsequent serpentine passes in each channel caused by a temperature gradient from heating the reacting fluid to the reaction temperature. The length of the first channel pass is 4.0 cm long and all channel passes are 3.0 cm long. The final microreactor design parameters are summarized in Table 4.1.

4.3.2 Reactor Fabrication

The microchannel reactor was fabricated by stacking, aligning, and diffusion bonding a series of Hastelloy C-276 shims in between two Hastelloy C-276 header plates. An exploded view of the reactor is presented in Figure 4.2. The square header plates are 5.0 cm on each side and 1.7 cm thick. A rectangular header channel, 1000 μm by 750 μm and 4.5 cm long, was cut into the inlet and outlet headers by traditional milling techniques. Five thermocouple wells were drilled 1.3 mm from the header channel wall. A detailed schematic of the top and bottom header plates is presented in Figure 4.3. These thermocouple measure the temperature down the header channel and provide a temperature gradient along the header. Two other thermocouple holes drilled into the inlet header block 1.0 cm into the opposite wall of the fluid entrance serve as the temperature controller thermocouples. The total inlet and outlet header volume is 0.03 cm^3, and accounts for 3.8% of the 0.9 cm^3 total reactor volume.

Two shim designs, channel shims and interlayer shims, Figure 4.4, were alternately stacked to create serpentine channel layers throughout the device. All of the shim stock was laser cut by Great Lakes Engineering, Maple Grove, Minnesota. Typical tolerance for their laser cutting process was ± 12.7 μm. The channel shims were 5.0 cm on each side and fabricated from 127 μm thick Hastelloy C-276 shim stock. A parallel array of 14 channels, 1000 μm wide by 127 μm high by 3.0 cm long were through cut into each shim. Each channel was chamfered at both ends with a radius of 500 μm. The integrated preheater channel shim has the same number of parallel channels as other channel shims, however the channels were 4.0 cm long, and the beginning of the channels were squared off to create a larger transition area for the fluid at the inlet header channel interface. Between each channel shim was an interlayer shim, which was 5.0 cm on each side and fabricated from 127 μm thick Hastelloy C-276 shim stock. Interlayer shims consisted of a parallel array of fourteen, 1000 μm diameter holes that were aligned with the ends of each channel in the previous channel shim. The interlayer shims served as the top and bottom plates for the channel shims, as well as a connection between two channel passes.

A repeat unit was made up of two channel shims and two interlayer shims. There are seven total repeat units in the reactor, not including the pre-heater channel shim. Each of the 14 channels is 46.2 cm long. Finally, all shims and headers had a 1.6 mm hole through cut in the corner for an alignment pin. The reactor was permanently bonded into one contiguous block by diffusion bonding.

4.3.3 Diffusion Bonding

Diffusion bonding is the process of solid state welding two faying surfaces by atomic inter-diffusion across the interface of the materials at elevated temperature and pressure. The temperature is usually 50% to 80% of the absolute melting point (T_m) of the material, and the pressure must be high enough to create localized deformation at the bonding interface, but low enough to prevent deformation of the macro features [25].

Due to small atomic distances necessary for bond formation between joining surfaces, careful surface preparation is necessary. Three variables were considered for header surface preparation, surface roughness, parallelism, and purity of the material surface. The headers were double disc grinded, lapped and polished to achieve desired surface properties. Header parallelism was measured on a Brown and Sharpe manual coordinate measurement machine, and header surface roughness measurements were performed on a Dektak^3 Vibraplane Model # 1281349 profilometer. Parallelism was less than 2.5 micron, and the average surface roughness, R_a, was less than 30 nm for each header. Channel and interlayer shims had an average surface roughness of R_a of 97.7 nm after laser cutting and cleaning. Diffusion bonding was less sensitive to shim surface roughness and parallelism due to a high level of material compliance during the bonding process as a result of the shim thickness (127 μm).

Impurities on the material surface may cause out-gassing, or may form surface oxides during the bonding process. As a result, a comprehensive cleaning process was used for each part being bonded. The headers, shims, and alignment pins were cleaned as follows: 15 minute sonication in 1.0 weight percent Liquinox, 15 minute sonication in deionized

distilled water, followed by 15 minute sonication in acetone. The parts were then etched with 5% by volume hydrofluoric acid 20% by volume nitric acid for 2.0 minutes, followed by sonication in deionized distilled water for 15 minutes, rinsed with acetone, and dried with nitrogen at 50°C. Surface roughness measurements indicated that etching did not substantially affect the surface roughness of the shims or headers. After cleaning, the shims and headers were stored in a vacuum desiccator until bonded. Although the reformation of surface oxides is very rapid for superalloys such as Hastelloy [26], the presence of surface oxides does not inhibit bonding, rather reduces the bonding kinetics [27].

A Thermal Systems diffusion hot press (model # HP30-4560) was used for diffusion bonding. Bonding conditions were first optimized by bonding sample shim stacks at conditions above and below the 1% and 2% 10 hour creep curves for Hastelloy C-276. The shim stacks were transversely cut, polished, and investigated for voids in the bond lines, as well as deformation of the channel features by scanning electron microscope (SEM). Optimized conditions were 1050°C bonding temperature with a 5°C min^{-1} temperature ramp, 10 MPa bonding pressure , and a dwell time of two hours. Bonding pressure was applied after the hot press reached temperature and released after the cycle time was complete. The base pressure inside the diffusion hot press was 10^{-7} Torr. An SEM image of a bond line between a sample shim stack and header bonded at the optimized conditions is presented in Figure 4.5. The images reveal little to no void fraction in the bond line, and indicate near complete bond formation between the shim and header. Bond lines for shim and header stacks bonded above the 10 hour 1% creep curve for Hastelloy C-276 showed little to no void fractions in the bonds, but suffered deformation of the macro features in the bonded pieces. Consequently, header and shim stacks bonded below the optimized conditions contained significant voids in their bond lines.

The reactor shims and headers were aligned with an internal stainless steel alignment pin and three external stainless steel alignment pins embedded into a graphite mold used to hold the reactor during bonding. A small amount of pressure, less than 1.0 MPa, was

applied to the graphite mold once placed in the diffusion hotpress to keep the structure aligned during the heating ramp. A photomicrograph of the bonded microchannel reactor is presented in Figure 4.6. After the reactor was bonded, Swagelok stainless steel 1/16 inch tube fittings (part #SS-100-6) were modified and TIG welded to the inlet and outlet ports of the reactor. Finally, the perimeter of the reactor was TIG welded to ensure no pin hole leaks.

The reactor was pressure tested by flowing 0.5 cm^3 min^{-1} of supercritical water at 650°C and 300 bar for five continuous days. This test also served to season the surface of the reactor wall given that the surface chemistry of nickel alloys is influenced by exposure to supercritical water [28-29].

4.4 Experimental

4.4.1 Pressure drop

Pressure readings were taken from pressure transducers located at the pump head and after a condenser located at the outlet of the reactor. Water was pumped to the reactor, at 25°C and 1.01 bar and 250 bar, by a Teledyne Isco 260D syringe pump operating at constant flow. Water was heated and maintained at the reaction temperature by two 375 W flat plate ceramic heaters (Thermcraft Inc., 29.5 cm x 7.93 cm x 2.06 cm with a Ni-Cr wire heating element) mounted to the top and bottom of the microchannel reactor. The reactor temperature was maintained by a PID controller with a Type J thermocouple inserted into the inlet header block of the microreactor. The reactor heating block was completely insulated with 3.8 cm thick Fibercraft board (Thermcraft, Inc.). The hot reactor effluent exiting the reactor was cooled to 20°C with a shell and tube heat exchanger using water as the coolant. The pressure was decreased from 250 bar to 1.03 bar by an adjustable precision back-pressure regulator (KHB1WOA6C2P6000, Swagelok Inc., stainless steel). The liquid feed flow rate to the reactor ranged from 1.0 ml/min to 33.7 ml/min at reactor temperature and pressure. The volumetric flowrate was estimated by the continuity equation.

4.4.2 Average Fluid Residence Time Measurement

A schematic for the average fluid residence time measurement is presented in Figure 4.7. A 2.0 µl aliquot of 35.0 mg ml^{-1} aqueous phenol tracer was injected into an aqueous feed stream, and monitored by time resolved UV adsorption before and after the microchannel reactor. Experiments were conducted at 25°C and ambient pressure. The working fluid was pumped by an Agilent series 1100 isocratic high performance liquid chromatography (HPLC) pump, and volumetric flowrates ranged between 1.0 ml min^{-1} and 5.0 ml min^{-1} at the pump. Phenol was injected by an Agilent 1100 high performance liquid chromatography auto sampler injector. The volume of the tracer injection could be accurately repeated and had a minimal effect on the steady state flow field in the reactor. The concentration of phenol was monitored at the inlet by a Waters 484 tunable absorbance detector at 272 nm and at the outlet by a Dionex VDM-2 variable wavelength detector at 272 nm. All data was collected at a rate of 5 Hz.

Two absorption curves were obtained for each experiment. Each point on the curves represents a fraction of the total tracer concentration at a specific residence time either at the inlet or outlet of the reactor. The experimental mean residence time, τ_{exp}, was calculated by

$$\tau_{\exp} = \frac{\int_0^\infty C(t)\,t\,dt}{\int_0^\infty C(t)\,dt} \cong \frac{\sum_i t_i C_i \Delta t_i}{\sum_i C_i \Delta t_i} \qquad (4.1)$$

where C_i is the concentration of the tracer, and t is time. The experimental mean residence time was defined as the time necessary for 50% of the tracer concentration to pass through the reactor. For precise residence time estimation, the time necessary for 50% of the tracer to pass the outlet detector was subtracted from the time it took 50% of the tracer to pass the inlet detector. Additionally, the mean residence time of control

experiments with no reactor in the test loop was subtracted from experiments with the reactor. The reactor was replaced with a zero dead volume HPLC connector.

4.5 Results and discussion

A parallel channel Hastelloy C-276 microchannel reactor for supercritical water gasification of biomass was designed and fabricated using scalable microfabrication techniques. After the microchannel reactor is diffusion bonded into a single contiguous block the reactor is essentially a "black box." Given that cutting open the reactor to directly measure the internal geometry would render the reactor unusable, an average fluid residence time based on tracer pulse measurement and pressure drop through the reactor, were measured to validate reactors internal geometry.

The pressure drop through the reactor was measured at 25°C and 1.01 bar with liquid water flowrates between 1.0 ml min^{-1} and 24.0 ml min^{-1}, and at 500°C and 250 bar with supercritical water flowrates between 2.8 ml min^{-1} and 28.1 ml min^{-1}. Pressure drops at both conditions, as a function of flowrate at the reactor conditions, are presented in Figure 4.8. The pressure drop at 25°C and 1.01 bar was linear as a function of flowrate, and had a y-intercept approaching zero, indicating the reactor had no catastrophic alignment issues due to partially or fully blocked flow in the channels. The pressure drop of the reactor, $dp\ dx^{-1}$, was modeled by the two dimensional analytical solution to the Navier Stokes equation for a rectangular channel assuming no slip boundary conditions

$$Q = \frac{4ba^3}{3\mu}\left(-\frac{dP}{dx}\right)\left(1 - \frac{192a}{\pi^5 b}\sum_{n=1,3,5}^{\infty}\frac{\tanh\left(\frac{n\pi b}{2a}\right)}{n^5}\right) \qquad (4.2)$$

where a is the half width of the channel, b is the half height of the channel, and μ(T,P) is the fluids dynamic viscosity. The calculated pressure drop through the headers was small compared to the channels and accounted for less than 1.0% of the total pressure drop

through the reactor. The calculated pressure drop is generally in good agreement with the experimental data at lower flowrates, but deviates from experimental data at higher flowrates. A reason for slightly higher experimental values is a slight misalignment of the interlayer shims causing a non-uniform flow distribution between the channels and resulting in smaller passages located between channel passes. Given that pressure drop is sensitive to any change in characteristic passage dimensions, or hydraulic diameter, a small misalignment could lead to a much larger pressure drop. In addition, machining tolerances may cause a non-uniform flow distribution, resulting in an increase in the pressure drop. Another explanation is simply that the channels were slightly compressed during diffusion bonding and are no longer 127 μm high. Leaving the channel height as a variable in Equation 4.2, and using least squares minimization to fit the model data to the experimental pressure drop data, the optimized value for the channel height is 119 μm, a 6 % difference. Lastly, the analytical model does not account for the pressure drop around the 180 degree turns between channel passes [39].

A second set of conditions under which the pressure drop was measured was 500°C and 250 bar. Pressure drop versus flowrate data are presented in Figure 4.8. At these conditions the fluid is supercritical and highly compressible. The resulting pressure drop as a function of flowrate was linear, and had a y-intercept greater than zero. The slope of the pressure drop at 500°C and 250 bar was less than the slope of the pressure drop at 25°C and 1.01 bar. Assuming a near uniform flow distribution, the decrease in the slope can be attributed to the decrease in viscosity of the fluid at from 0.89 cP at 25°C and 1.01 bar to 0.031 cP at 500°C and 250 bar. The non-zero intercept is most likely due to changes in the fluid density resulting from heating and cooling of the fluid. Modeling the pressure drop of supercritical water through the microchannel reactor was beyond the scope of this study due to several factors, such as unknown temperature gradients in the reactor inlet that may cause non-uniform flow distribution due to fluid density gradients. The magnitude and linear relationship between pressure drop and flowrate indicate that the reactor channels are aligned reasonably well and able to operate continuously within a range of flowrates and conditions representative of supercritical water gasification.

However, due to the architecture of the microchannel reactor, a more precise indication of the reactors performance is the average fluid residence time.

A tracer pulse residence time study was used to measure the mean fluid residence, τ_{exp}, time in the microchannel reactor by observing the time resolved concentration profile of an injected tracer at the inlet and outlet of the reactor. The volumetric flow rate was varied between 2.0 ml min^{-1} and 5.0 ml/min^{-1}, which corresponded to Reynolds numbers between 4.7 and 11.8. Ideally, these experiments would be conducted at supercritical water conditions, but due to the high reactivity of supercritical water as well as temperature and pressure limitations for the UV detectors, pulse tracer experiments were conducted at 25°C and 1.01 bar. Assuming a near uniform fluid distribution and Reynolds number in each channel, it is reasonable that the residence time distribution at ambient conditions will be similar to supercritical water conditions. The inverse of the experimental mean residence time at each flowrate was calculated directly from the discretized data and compared to the inverse of the calculated theoretical mean residence time, $\tau_{calc} = V_R / v$, in Figure 4.9. The calculated and experimental data are both linear and are in fairly good agreement with each other, which is indicative of a relatively equal flow distribution in the fourteen channels. A mal distribution in the channels, or even entire channel blockage, would result in significantly lower average residence times due to a reduction in the reactor volume. Assuming laminar flow, the small difference between the experimental and calculated values can be attributed to stagnant or vortex regions of flow in the reactor, most likely at the transition between serpentine passes and in the headers [40]. The presence of small stagnant regions would effectively decrease the overall reactor volume and account for the smaller measured average residence time. Analysis of dispersion in the microchannel reactor, and modeling of the fluid and heat transport properties in the microchannel reactor are beyond the scope of this study, but will be the subject of future studies.

4.6 Conclusion

A high temperature and pressure microchannel reactor for supercritical water gasification of solubilized biomass was designed and fabricated out of Hastelloy C-276 by a combination of laser cutting, traditional milling, and diffusion bonding techniques. The reactor architecture incorporates a parallel processing architecture to achieve a reactor volume of 0.9 cm^3. The microchannel reactor consists of fourteen, 127 μm by 1000 μm, parallel channels that serpentine a total 15 times through the reactor. Due to the inability to evaluate the reactors complex geometry and channel alignment after diffusion bonding, macroscopic measurements were used to evaluate the reactors geometry. The pressure drop through the reactor was sensible for continuous use at conditions above the critical temperature and pressure of water, and had a linear relationship with flowrate characteristic of laminar flow. The measured average fluid residence time was in agreement with the calculated mean residence time and indicated a uniform channel flow distribution.

4.7 Acknowledgement

This research was supported by Bend Research, Inc., Bend, Oregon, and by the US Army under the Tactical Energy Systems program administered through the Oregon Nanoscience and Microtechnologies Breakthrough Institute.

4.8 Literature cited

1. Petrou E C, and Pappis C P 2009 *Energy & Fuels* **23** 11055-1066
2. Hamelinck C N, and Faaij A P C 2006 *Energy Policy* **34** 3268-3283
3. Matsumura Y, Minowa T, Potic B, Kersten S, Prins W, van Swaaij W, Beld B, Elliott D, Neuenschwander G, Kruse A, and Antal Jr M J 2005 *Biomass and Bioenergy* **29** 269-92
4. Calzavara Y, Joussot-Dubien C, Boissonnet G, and Sarrade S 2005 *Energy Conversion and Management* **46** 615-31
5. Loppinet-Serani A, Aymonier C, and Cansell F 2008 *ChemSusChem* **1** 486-503
6. Navarro R M, Sánchez-Sánchez M C, Alvarez-Galvan M C, del Valle F, and Fierro J L G 2009 *Energy Environ Sci* **2** 35-54
7. Peterson A A, Vogel F, Lachance R P, Fröling M, Antal Jr M J, and Tester J 2008 *Energy Environ Sci* **1** 32-65
8. Kruse A 2008 *Biofuels Bioproducts & Biorefining* **2** 415-37
9. Goodwin A K, and Rorrer G L 2009 *Energy and Fuels* **23** 3818-25
10. Goodwin A K, Rorrer G L 2008 *Ind Eng Chem* **47** 4106-14
11. Lu YJ, Guo LJ, Ji C, Zhang X, Hao X, and Yan Q 2006 *International Journal of Hydrogen Energy* **31** 822-31
12. Watanabe M, Aizawa Y, Iida T, Levy C, Aida T M, and Inomata H 2005 *Carbohydrate Research* **340** 1931-39
13. Sinag A, Kruse A, and Rathert J 2004 *Ind Eng Chem Res* **43** 502-8
14. Resende F, Fraley S, Berger M, and Savage P 2008 *Energy and Fuels* **22** 1328-34
15. Resende, F L P and Savage P E 2010 *Ind Eng Chem* In press
16. Resende F L P, Neff M E, and Savage P E 2007 *Energy and Fuels* **21** 3637-43
17. Kersten S R A, Potic B, Prins W, and Van Swaaij W P M 2006 *Ind Eng Chem Res* **45** 4169-77
18. Antal J A J, Allen S G, Schulman D, and Xu X 2000 *Ind Eng Chem Res* **39** 4040-53
19. Holladay J D, Wang Y, and Jones E 2004 *Chem Rev* **104** 4767-90

20. Arai K, Smith R J, and Aida T M 2009 *Journal of Supercritical Fluids* **47** 628-36

21. Shah K, Ouyang X, and Besser R S 2005 *Chem Eng Technol* **28** 303-13

22. Hessler V, Loeb P, Loewe H, and Kolb G 2007 *Micro Instrumentation* **1** 85-129

23. Brandner J J 2008 *Microreactors in Organic Synthesis and Catalysis* **1** 1-17

24. Hessler V, Knobloch C, and Loewe H 2008 *Recent Patents on Chemical Engineering* **1** 1-16

25. Amador C, Gavriilidis A, and Angeli P 2004 *Che Eng J* **101** 379-90

26. Saber M, Commenge J M, Falk L 2010 *Chemical Engineering Science* **65** 372-379

27. Commenge J M, Falk L, Corriou J P, and Matlosz M 2002 *AICHE Journal* **48** 345-58

28. Escher W, Michel B, Poulikakos D 2009 *International Journal of Heat and Mass Transfer* **52** 1421-1430

29. Sotowa K I, Sugiyama S, Nakagawa K 2009 *Organic Process Research and Development* **13** 1026-1031

30. Bogojevic D, Sefiane K, Walton A J, Christy J R E, Cummins G, Lin H 2009 *Heat Transfer Engineering* **30** 1049-1057

31. Ha J W, Jang J H, Gil J H, Kim S 2008 *International Journal of Hydrogen Energy* **33** 2059-2063

32. Nam J H, Lee K, Sohn S, Kim C 2009 *Journal of Power Sources* **188** 14-23

33. Le A D, Zhou B, Shiu H, Lee C, Chang W 2010 *Journal of Power Sources* **195** 7302-7315

34. Wang X, Yan W, Duan Y, Weng F, Jung G, Lee C 2010 *Energy Conversion and Management* **51** 959-968

35. Wang X, Duan Y, Yan W, Peng X 2008 *Journal of Power Sources* **175** 397-407

36. Guilin H, Jianren F 2007 *Journal of Power Sources* **165** 171-184

37. Jeon D H, Greenway S, Shimpalee G S, Van Zee J W 2008 *International Journal of Hydrogen Energy* **33** 1052-1066

38. Nguyen P T, Berning T, Djilali N 2004 *Journal of Power Sources* **130** 149-157

39. Maharudrayya S, Jayanti S, Deshpande A P 2004 *Journal of Power Sources* **138** 1-13

40. Raju R, Roy S 2004 *Journal of Fluids Engineering* **126** 489-492

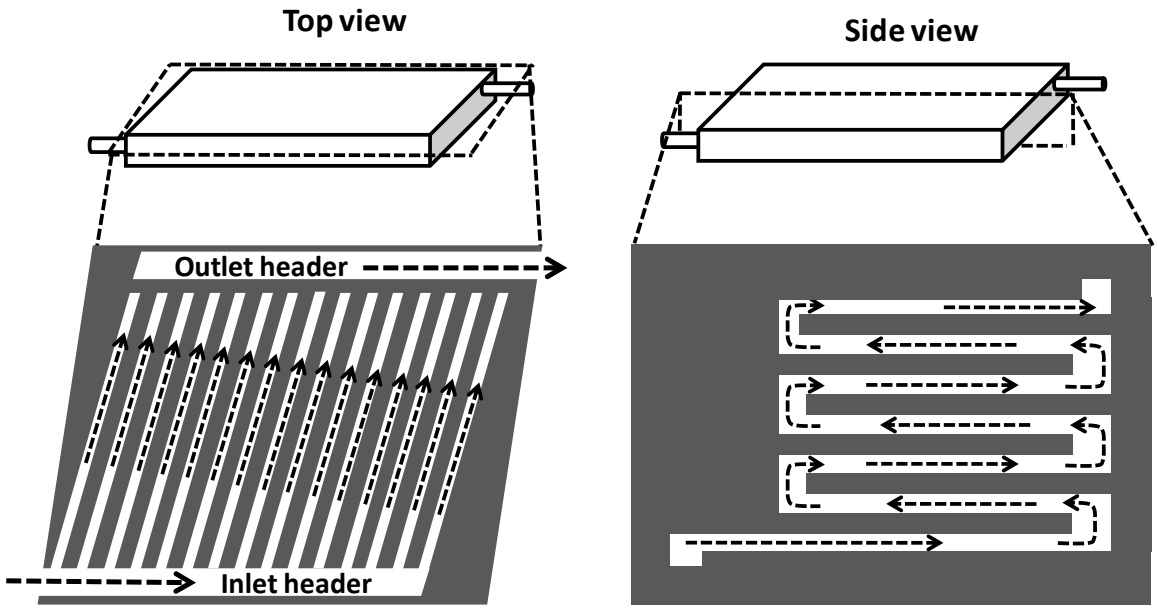

Figure 4.1. Microchannel reactor architecture: A) Parallel array of 14 channel (127 µm x 1000 µm). The fluid is distributed to the channels by the inlet header. B) Side view of a single serpentine channel (not to scale). The length of the integrated pre-heater (L_{Ph}) was 1 cm.

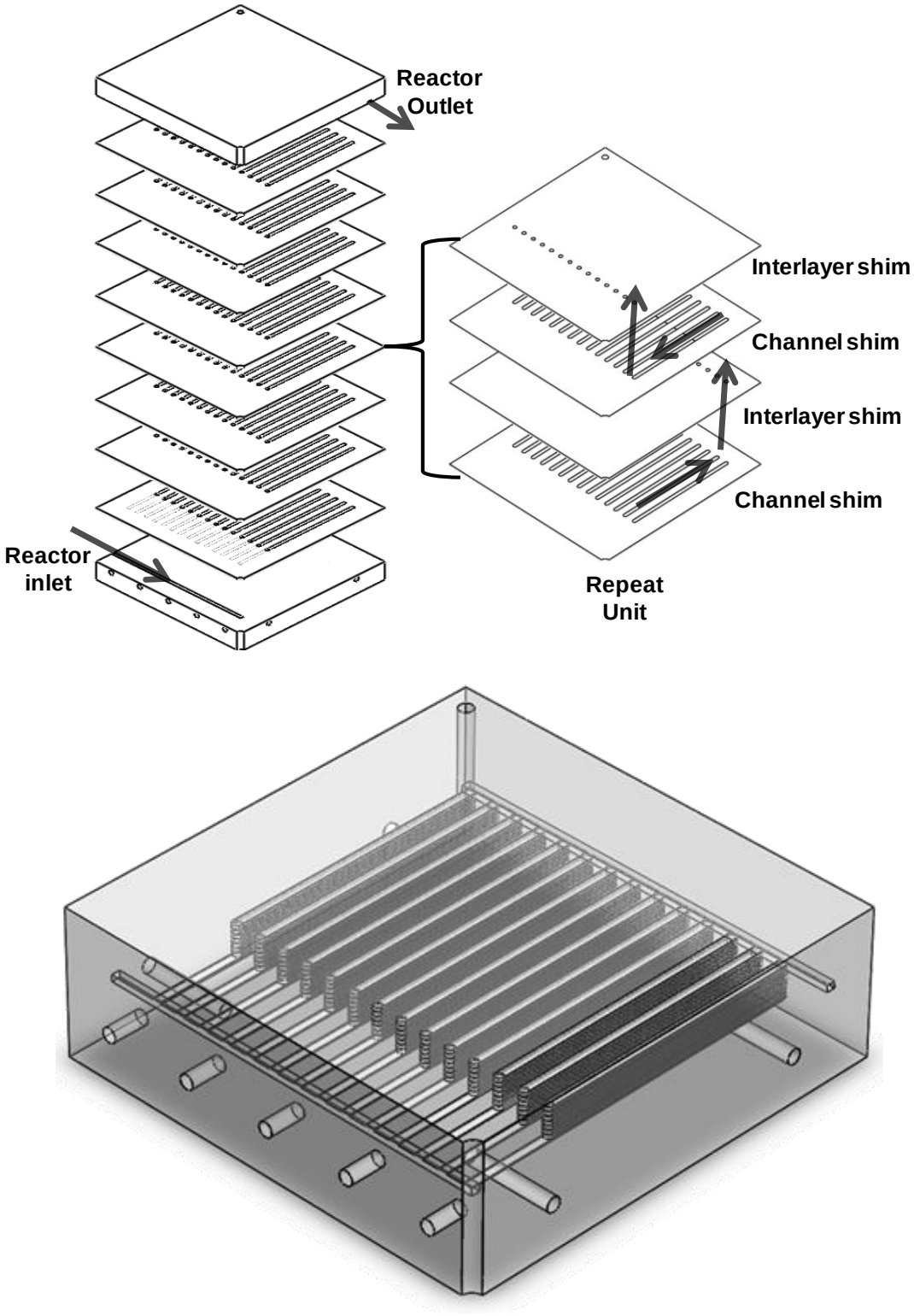

Figure 4.2. Exploded view of the microchannel reactor.

A)

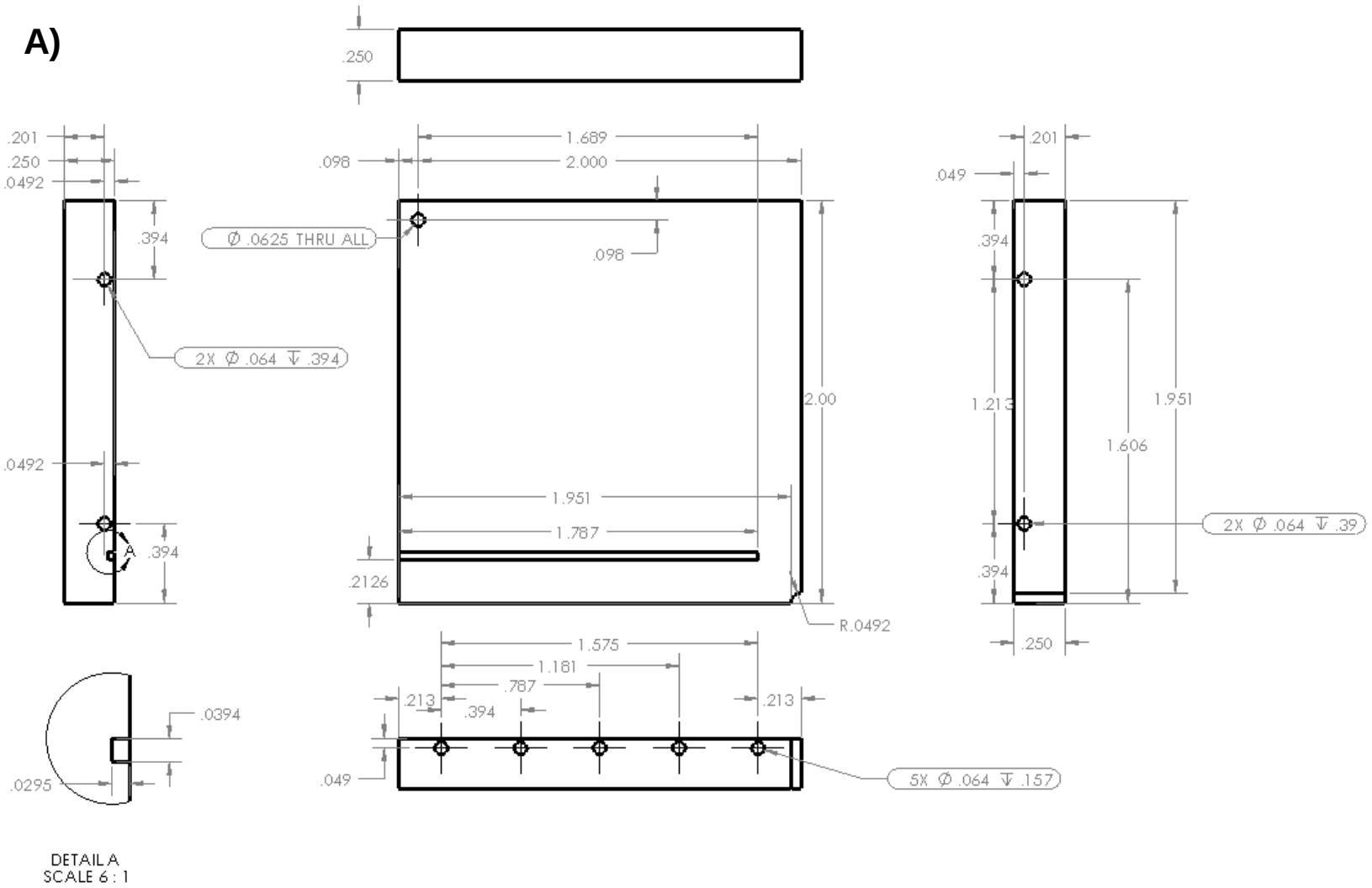

DETAIL A
SCALE 6 : 1

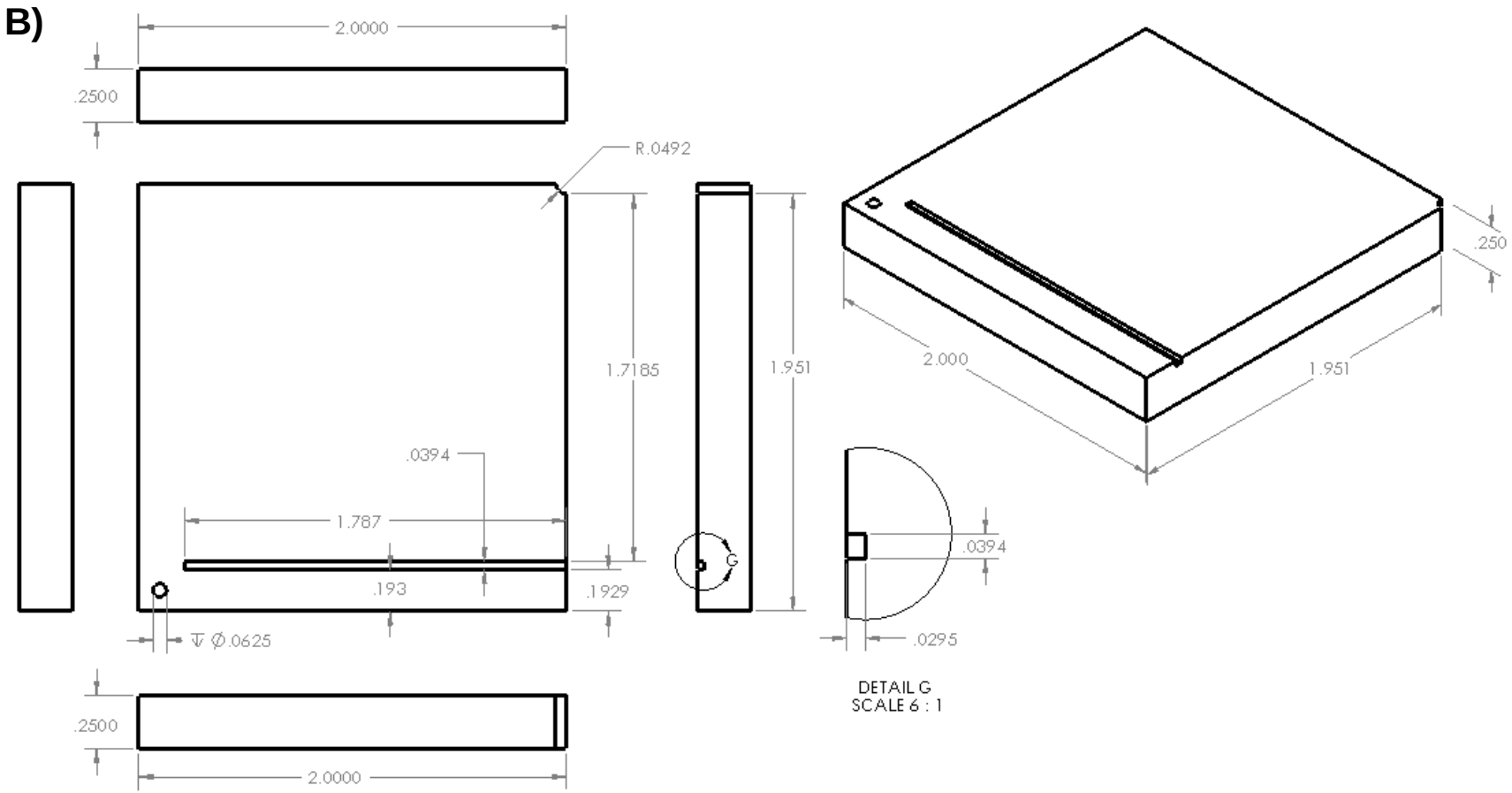

Figure 4.3. Detailed schematic drawings of the A) top and B) bottom headers.

A)

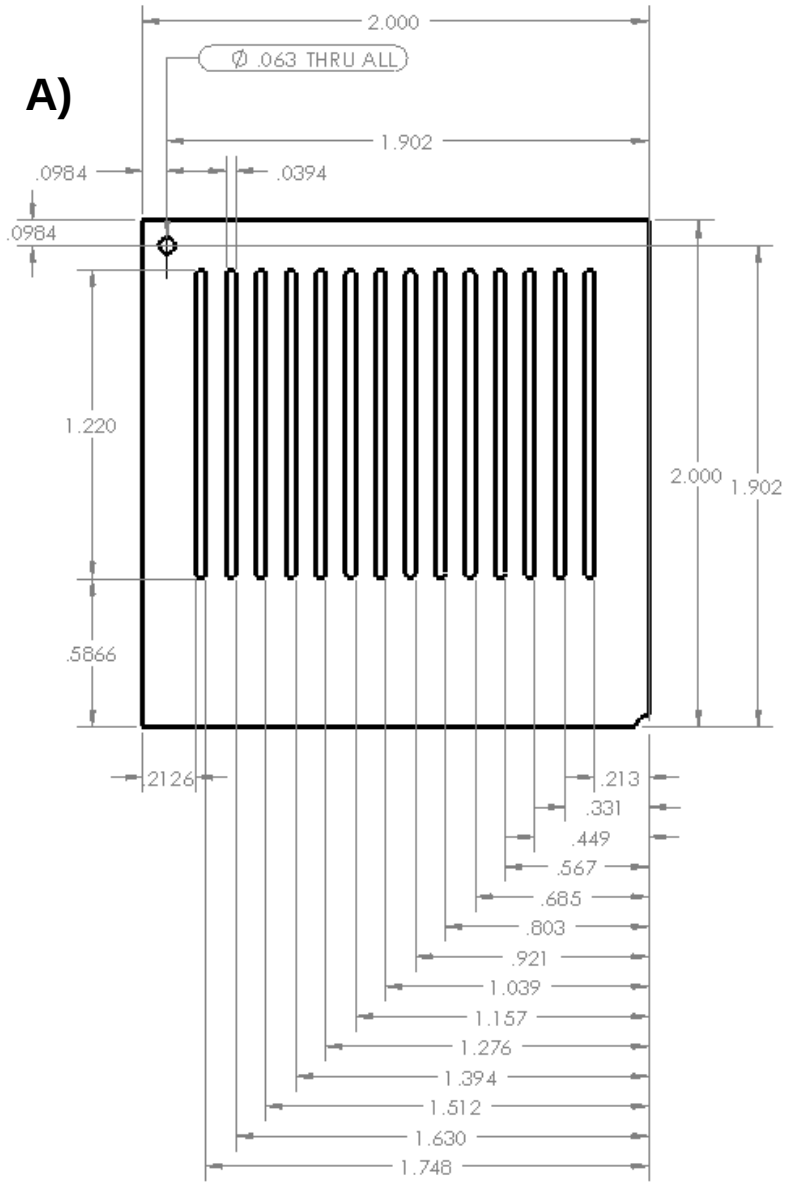
2.000
Ø .063 THRU ALL
1.902
.0984
.0394
.0984
1.220
2.000
1.902
.5866
.2126
.213
.331
.449
.567
.685
.803
.921
1.039
1.157
1.276
1.394
1.512
1.630
1.748

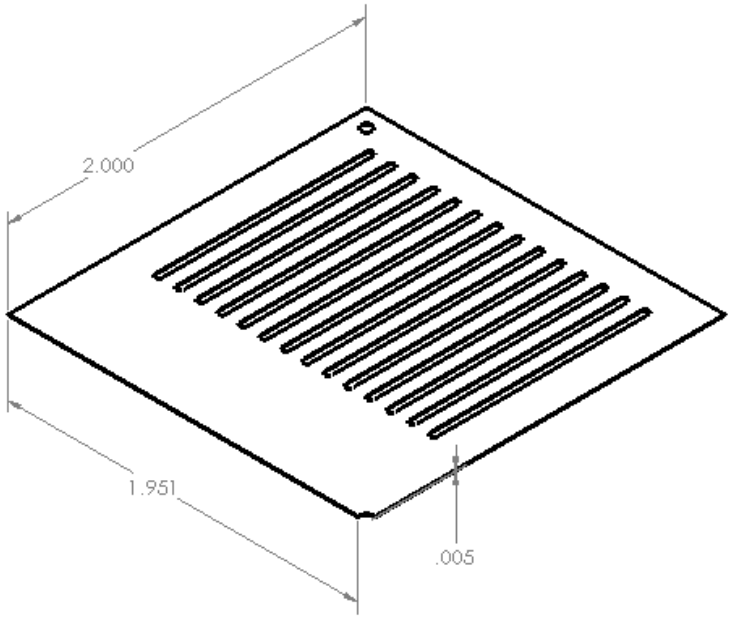
2.000
1.951
.005

B)

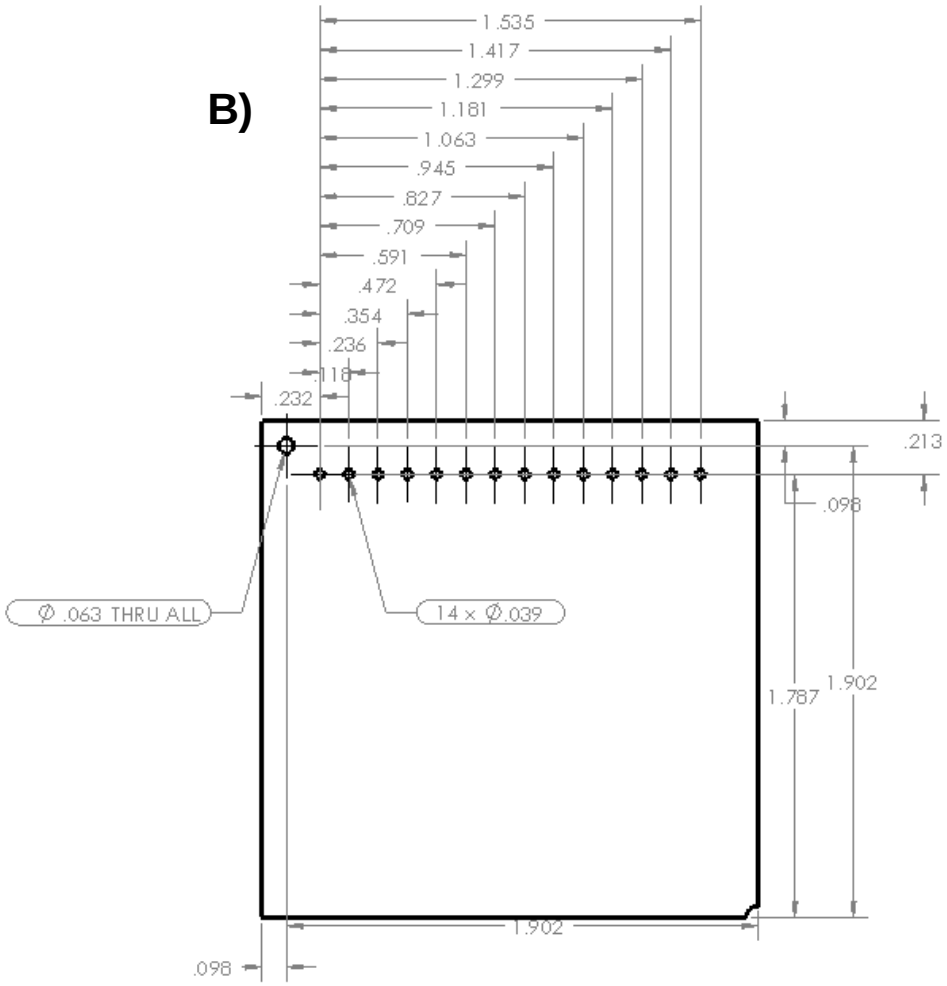
1.535
1.417
1.299
1.181
1.063
.945
.827
.709
.591
.472
.354
.236
.118
.232
.213
.098
Ø .063 THRU ALL
14 × Ø.039
1.787
1.902
1.902
.098

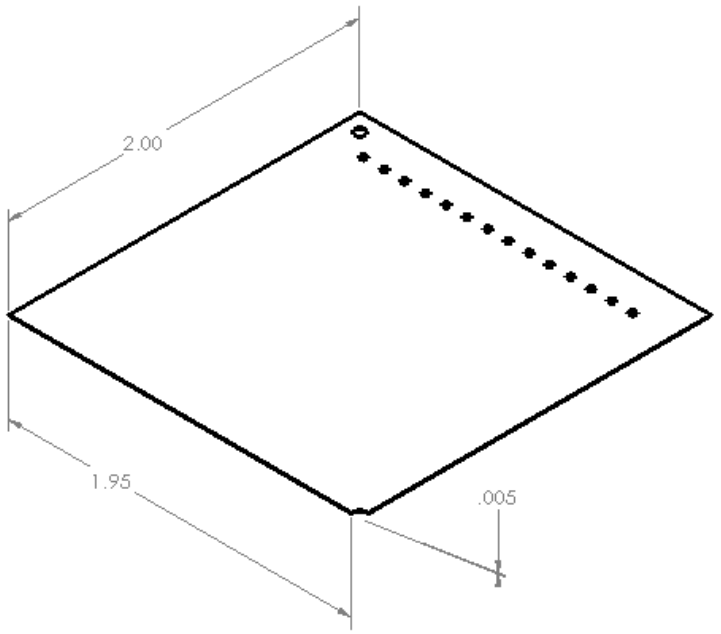
2.00
1.95
.005

C)

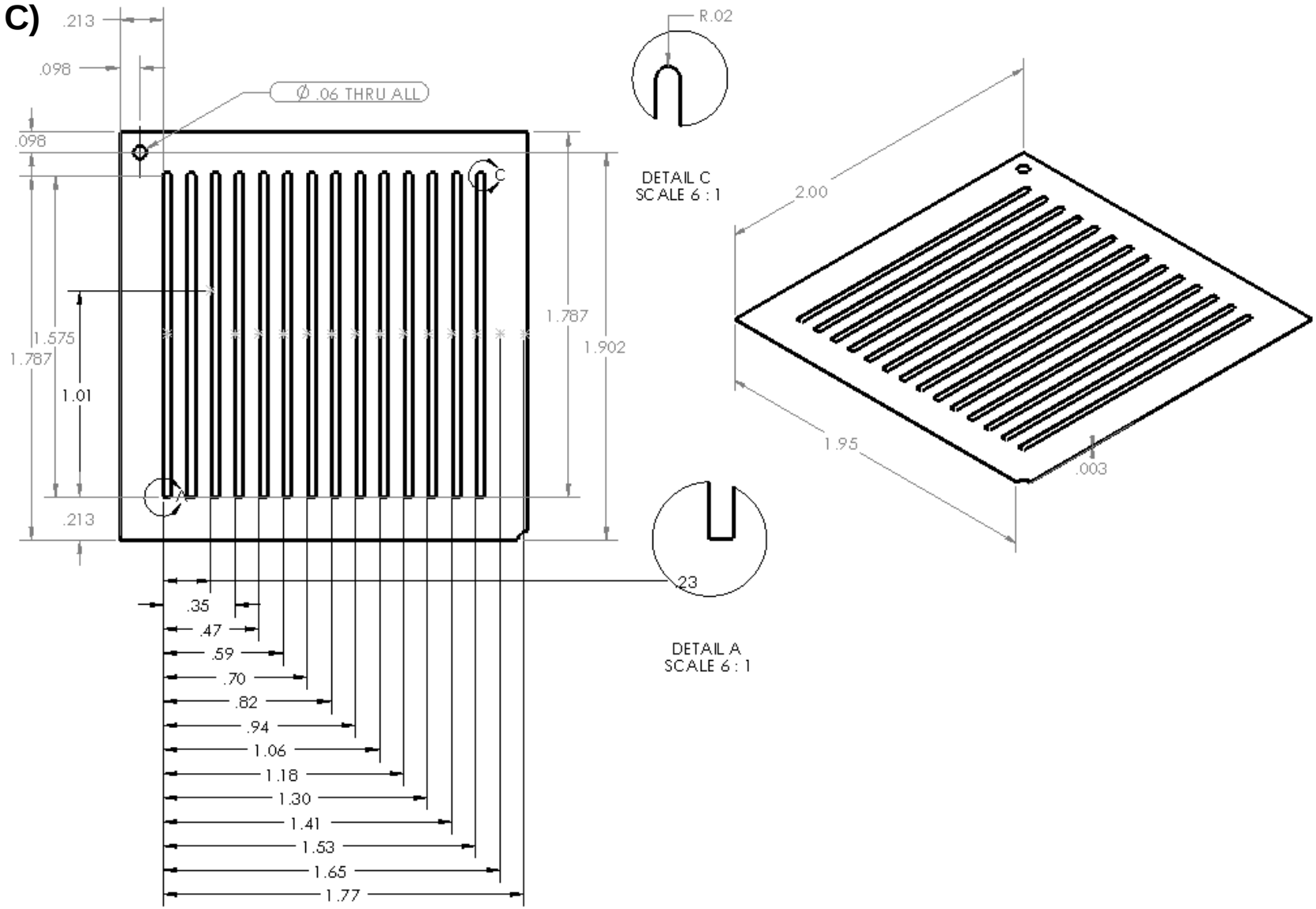
.213
.098
Ø .06 THRU ALL
.098
1.575
1.787
1.01
.213
1.787
1.902
C
R.02
DETAIL C
SCALE 6 : 1
2.00
1.95
.003
.23
DETAIL A
SCALE 6 : 1
.35
.47
.59
.70
.82
.94
1.06
1.18
1.30
1.41
1.53
1.65
1.77

C)

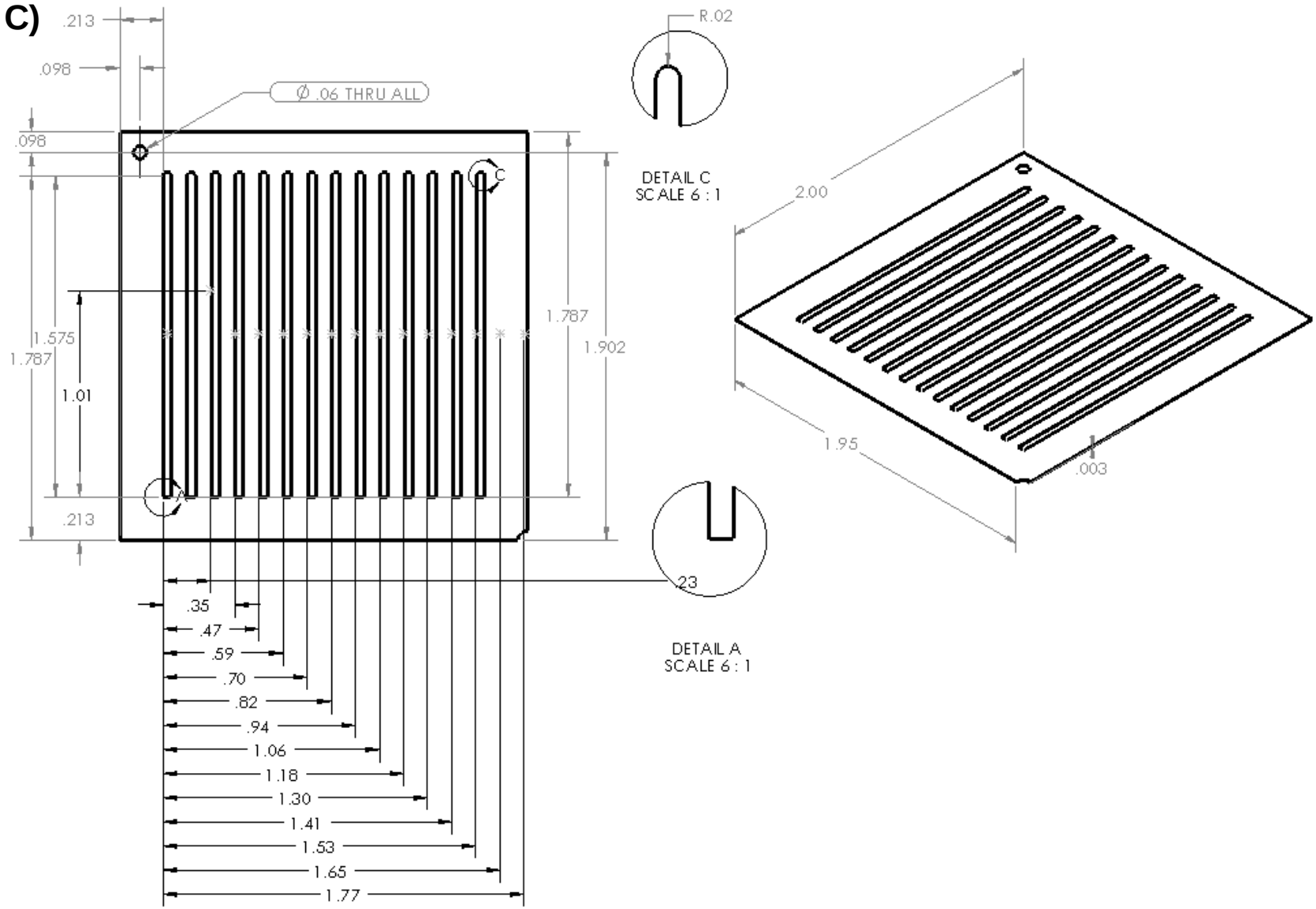
.213
.098
Ø .06 THRU ALL
.098
1.575
1.787
1.01
.213
1.787
1.902
C
R.02
DETAIL C
SCALE 6 : 1
2.00
1.95
.003
.23
DETAIL A
SCALE 6 : 1
.35
.47
.59
.70
.82
.94
1.06
1.18
1.30
1.41
1.53
1.65
1.77

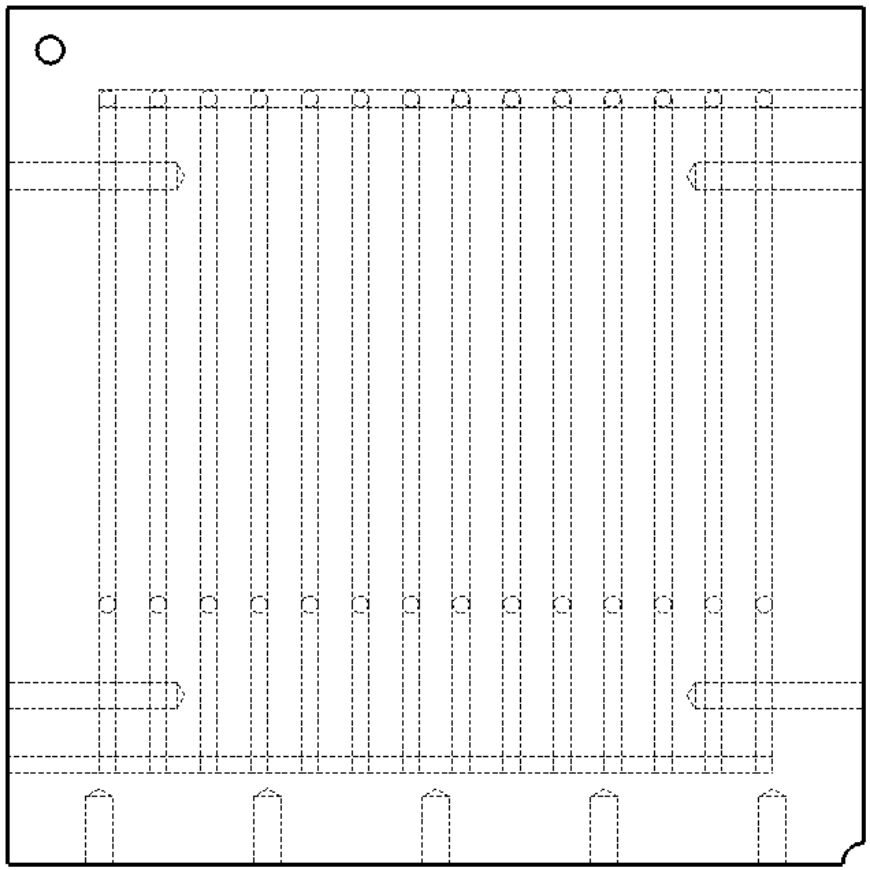

D)

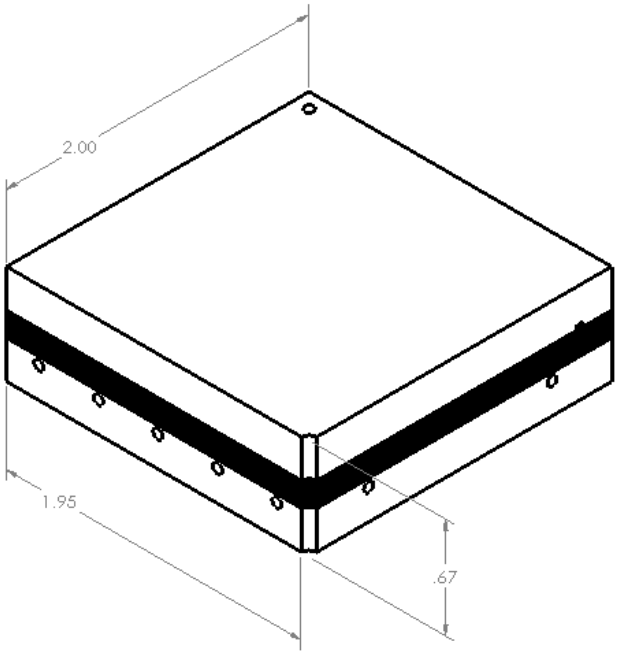

Figure 4.4. Detailed schematic drawings of the A) channel shim B) interlayer shim C) pre-heater shim and D) transparent top view and assembled view of the microchannel reactor.

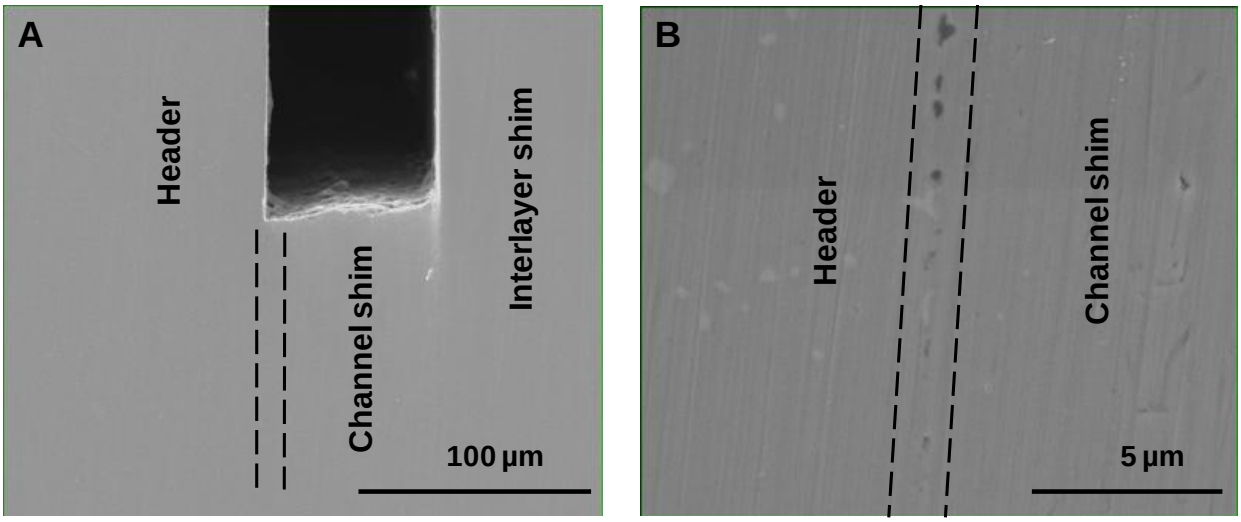

Figure 4.5. Sample shim bonding; A) SEM image of a bonded channel shim between a header plate and interlayer shim. The bond line is in between the dashed lines. B) Magnified SEM image the bond line in image A.

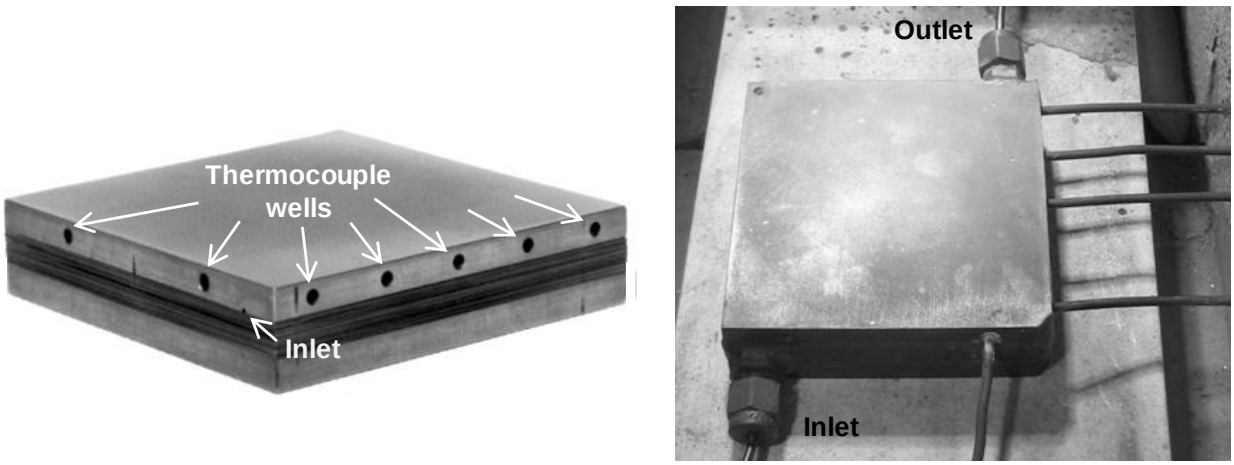

Figure 4.6. Diffusion bonded Hastelloy C-276 microchannel reactor.

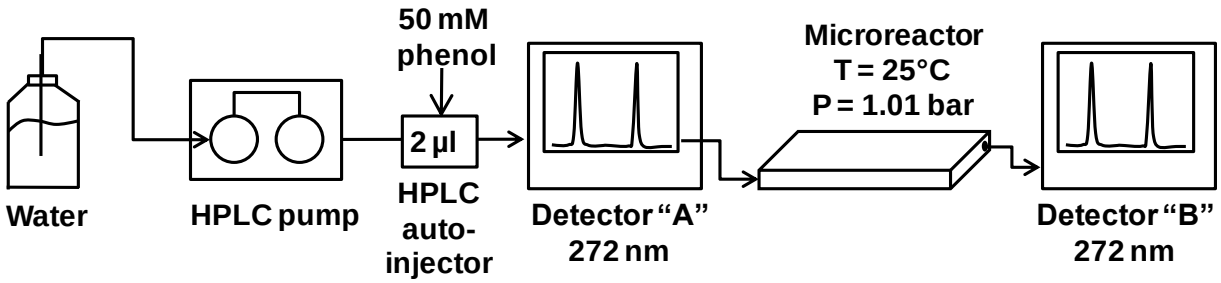

Figure 4.7. Schematic for pulse tracer residence time distribution experiment.

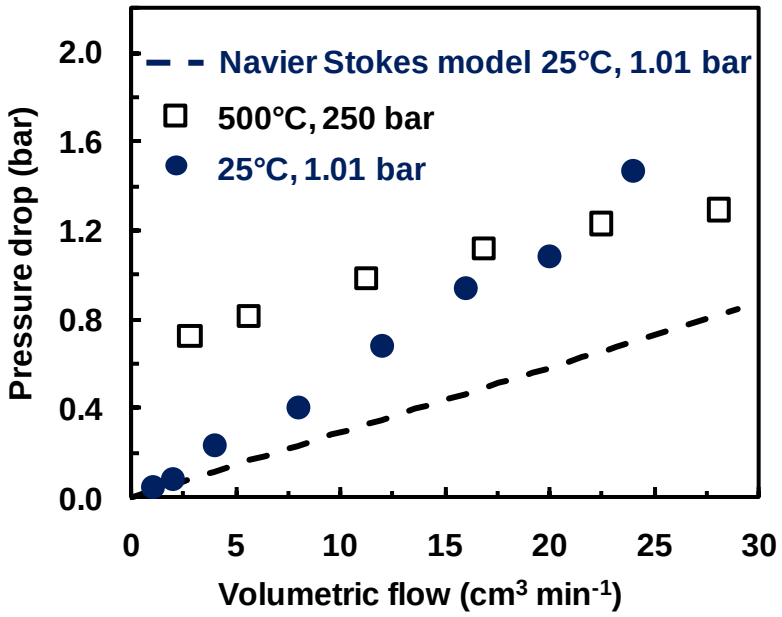

Figure 4.8. Pressure drop for the Hastelloy microchannel reactor at 25°C, 1.01 bar and 500°C, 250bar.

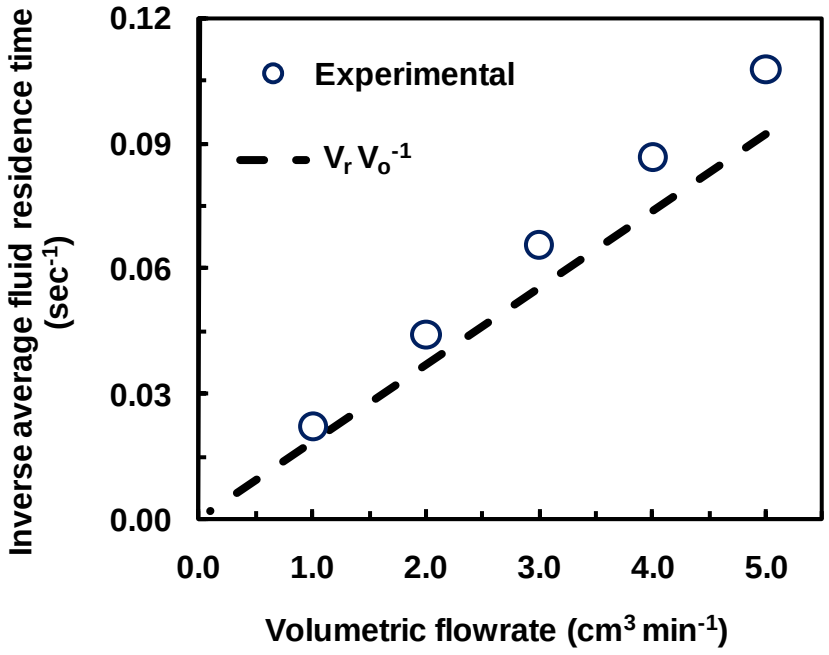

Figure 4.9. Calculated and experimental mean residence time comparison. Calculated mean residence time is based on volume of the reactor and volumetric flowrate of the feed solution.

Table 4.1. Design parameters for the Hastelloy microchannel reactor.

Overall dimensions	
Reactor width	5.0 cm
Reactor length	5.0 cm
Reactor height	1.7 cm
Reactor volume	0.9 cm^3
Channel dimensions	
Microchannel width	1000 μm
Microchannel height	127 μm
Channel hydraulic diameter	225 μm
Total length of each channel	46.2 cm
Length of integrated preheater	1.0 cm
Channels per shim	14
Number of channel shims	15
Number of interlayer shims	14
Single channel volume	0.06
Header Dimensions	
Header channel length	4.5 cm
Header channel width	0.100 cm
Header channel height	0.075 cm
Total header volume	0.034 cm^3

Chapter 5: Characterization of Residence Time Distribution in a Parallel Channel Microreactor

5.1 Abstract

Microchannel reactors offer a unique platform to gasify biomass to H_2 rich gas by supercritical water due to characteristic high rates of heat transfer needed to sustain highly endothermic biomass reforming reactions. However, for microreactors with complex architecture, the microchannel configuration may influence the hydrodynamics within the reactor, and therefore influence the product yield and selectivity of the reaction. In this study, the residence time distribution (RTD) for a supercritical water parallel channel microreactor is investigated experimentally and by computational fluid dynamics (CFD). The microreactor has 14 parallel microchannels (127 μm by 1000 μm) that serpentine 15 times vertically throughout the device. Experimental RTDs were determined by a tracer pulse study, where the outlet response was deconvolved from the inlet pulse using a one dimensional axial dispersion model. The microreactor RTD was approaching plug flow as characterized by its vessel dispersion number and its shape was influenced by Reynolds number. The RTD of a single channel configuration of the microchannel reactor was modeled by CFD and compared to experimental RTDs. Results from CFD simulations suggested that the RTD was sensitive to the Reynolds number and the binary diffusion coefficient of the tracer due to the hydrodynamics in the transition areas between serpentine microchannel passes. It was determined the reactor had a uniform channel flow distribution by comparing the RTDs for the single microchannel CFD model to experimental RTDs from the microchannel reactor.

5.2 Introduction

Microchannels substantially intensify chemical processing due to increased heat and mass transport properties as a result of high surface area to volume ratios. They have been integrated into several microstructure devices used in a wide variety of applications including micromixers, microreactors, MEMS devices, and microheat exchangers. Specifically, in regard to chemical reaction engineering, enhanced heat and mass transport properties allow for precise control of the reaction conditions, resulting in greater product selectivity and higher yields compared to chemical processing in traditional continuous flow tube reactors and higher throughput compared to chemical processing in batch reactors. In addition, the small size and footprint of microchannel reactors as well as small holdup volumes make them an ideal candidate for portable on demand synthesis or destruction of hazardous or toxic chemicals and materials. On site biomass processing, using microreactor technology, may substantially decrease high transportation costs as a result of the relative low density and high water content of biomass.

A microreactor target volume, for increased throughput, is often achieved through parallel processing. The inlet stream is split into numerous sub streams by a header or distribution channel within the microreactor and recombined at the reactor outlet. A critical goal for parallel processing microreactor design is to achieve identical conditions within each microchannel within the reactor. A microreactor with poorly distributed flow reduces possible benefits of enhanced control of transport properties, which can be achieved at the micron scale. Fundamentally, this can only happen if the fluid residence time distribution (RTD) in each of the microchannels is identical. The RTD describes the distribution of time it will take fluid elements to travel through the reactor, and enables accurate product yield predictions for first order chemical reactions and reasonable approximations for higher order reactions [3]. The type of microreactor architecture may have a significant effect on the fluid velocity distribution in each channel, and therefore directly affect the fluid RTD in the reactor. Microreactor architectures that uses bifurcating channels theoretically have a uniform channel flow distribution, however, the

flow distribution in microreactors designed around a parallel channel architecture are less sensitive to fabrication tolerances [1-2]. Parallel channel microreactors do not intrinsically have an "even RTD" based on the premise that equivalent channel volume correlates to an equal pressure drop in each channel due to the formation of stationary vortices in the distribution channel [20, 40]. However, equal flow distribution can be achieved by continuously changing the diameter of the distributing channel to ensure a uniform pressure drop through each microchannel, or alternatively, by increasing the pressure drop through each microchannel such that the pressure drop through the distribution channel is considerably less than the pressure drop through each microchannel [1, 4].

Residence time distribution can be directly measured by stepwise injecting a tracer pulse into the steady state flow field of a vessel and monitoring the tracer concentration at the outlet [17]. As the tracer moves through the reactor it is dispersed due to convection as a result of the viscous velocity profile that develops in laminar flow, molecular diffusion, and influenced by vortex or stagnant regions that may develop as a result of the structure geometry. Furthermore, for parallel processing microreactors, RTD is influenced by the uniformity of the velocity distribution in each microchannel. Although commonly used for macroscopic reactor characterization, residence time distribution also has been used to determine the extent of mixing in micromixers [7, 10, 18] and characterize the flow and channel flow distribution in parallel processing microstructured devices [1, 19]. Given that measuring the RTD of microstructured devices is sensitive to experimental method, new techniques have been developed to improve accuracy and repeatability of these measurements [6, 11]. However, these methods require custom fabricated microreactors with optical detection methods unsuitable for a non-transparent device. Alternatively, computational fluid dynamics (CFD) has been used in conjunction with experimental RTD to optimize mixing and flow distribution [1, 7, 10]. The use of CFD allows identification and isolation of features in a specific microstructure design that may influence the RTD.

In our previous work we integrated a parallel array of microchannels into a single device suitable for continuous operation at conditions above the critical temperature (374°C) and pressure (221 bar) of water. This was done by diffusion bonding a series of shims in between two header blocks that resulted in contiguous stainless steel or Hastelloy microchannel reactors [13, 15]. The narrow channels in the reactor provided high rates of heat transfer to the reacting fluid to drive highly endothermic biomass reforming reactions and minimize the reacting fluid heating period, resulting in a substantial enhancement for continuous biomass gasification by supercritical water [13-14]. Due to the complex reactor architecture and intricate fabrication process of these microchannel reactors, characterization of the flow field and RTD is necessary to assess and benchmark the reactors performance.

In this present study the affect of Reynolds number on RTD in a parallel channel Hastelloy microreactor designed for supercritical water gasification of biomass is investigated experimentally using water at standard conditions and with CFD by introducing a tracer pulse into the steady state flow field of the microreactor and recording its time dependant concentration at the reactors inlet and outlet. Since a perfect dirac δ function is not experimentally feasible, experimental RTDs were deconvolved from the measured inlet pulse by fitting the outlet response curve to a one dimensional axial dispersion model. The vessel dispersion number was determined from the deconvolved RTDs and the affect of Reynolds number on dispersion is discussed. The width and shape of the RTD provides insight into the reactors hydrodynamics and enables accurate product yield predictions. Since the microchannel reactor investigated uses parallel processing to achieve a desired reactor volume, and given that fabrication tolerances for microstructured devices may affect the physics in each of the parallel microchannels, the experimental RTD is compared to the RTD from a simulated CFD model of a single channel in the microreactor. Additionally, the CFD model is used to investigate how vortex regions that form in the transition areas between channel passes affect RTD for several Reynolds numbers.

5.3 Microchannel Reactor

The microreactor investigated is a parallel channel Hastelloy C-276 microreactor intended for continuous gasification of biomass by supercritical water. The reactor is designed to intensify biomass gasification in supercritical water by increasing the rate of heat transfer to the reacting fluid, driving endothermic biomass reforming reactions. A transparent three dimensional schematic of the reactor is presented in Figure 5.1. The reactor architecture and details about the reactor design and fabrication have been previously described [15]. The reactor features and dimensions are summarized in Table 5.1. Briefly, the reactor is comprised of 14 parallel channels that serpentine 15 times vertically through the reactor. A cross sectional view of a single channel is presented in Figure 5.2. The reacting fluid is distributed to each of the 14 channels by an inlet header and recombined at the exit of the reactor by an outlet header. The first channel pass is 4 cm long, and each subsequent channel pass is 3 cm long. The extra 1.0 cm in the first channel pass is designed to minimize a drop in the fluid temperature in later channel passes due to a temperature gradient caused by the fluid heating period. The average surface roughness (R_a) of the reactor walls was less than 100 nm.

5.4 Experimental

5.4.1 Residence Time Distribution from a Tracer Pulse Experiment

A schematic for the pulse tracer study is presented in Figure 5.3. A 2.0 µl aliquot of 35.0 mg ml^{-1} aqueous phenol solution was injected into an aqueous feed stream and monitored by time resolved UV absorption before and after the microchannel reactor. Experiments were conducted at 25°C and ambient pressure. The working fluid was pumped by an Agilent series 1100 isocratic high performance liquid chromatography (HPLC) pump and volumetric flowrates ranged between 1.0 cm^3 min^{-1} and 5.0 cm^3 min^{-1} at the pump. Assuming a uniform channel flow distribution, the microchannel volumetric flowrate range was 0.07 – 0.36 cm^3 min^{-1}. Phenol was injected by an Agilent 1100 high performance liquid chromatography auto sampler injector. The volume of the tracer

injection could be accurately repeated and had a minimal effect on the steady state flow field in the reactor. The concentration of phenol was monitored at the inlet by a Waters 484 tunable absorbance detector at 272 nm and at the outlet by a Dionex VDM-2 variable wavelength detector at 272 nm. All data was collected at a rate of 5 hertz. Experiments were determined to be highly reproducible by comparing the normalized inlet and outlet distributions for two tracer injections at the same conditions.

Two absorption curves were obtained for each experiment. Each point on the curves represents a fraction of the total tracer concentration at a specific residence time either at the inlet or outlet of the reactor. For modeling purposes it is convenient to represent the RTD curve such that the area under each curve is unity. To accomplish this, an exit age distribution, *E(t)*, was calculated solely from the absorption data by first calculating the area under the curve in its discrete form for the inlet and outlet absorption curves

$$A = \int_0^\infty C(t)dt \cong \sum_i C_i \Delta t_i = \frac{M}{v} \qquad (5.1)$$

where *A* is the area under the curve, *C* is the concentration of the tracer, *t* is the residence time, *M* is the units of tracer injected (moles), and *v* is the volumetric flow rate of the water. A normalized distribution, *E(t)*, curve was calculated in its discrete form $E(t) = Cv/M$. Given the input pulse into the microreactor is not a perfect Dirac δ function, the RTD of the microreactor cannot be directly calculated from the measured adsorption curve at the reactor outlet. A convolution integral is used to describe the coupled inlet and outlet responses.

$$E_{out}(t) = \int_0^t E_{in}(t - t')E_{dc}(t')dt' \qquad (5.2)$$

Where E_{out} is the normalized measured concentration at the reactor outlet, E_{in} is the normalized measured concentration at the inlet, and E_{dc} is the RTD. Numerous techniques have been applied to determine E_{dc} when E_{out} and E_{in} are measured, including transforming the data into the frequency domain [29 - 32] and direct parameter estimation in the time domain [33 - 35]. In this study, direct parameter estimation in the time domain

was used due to a substantial increase in the noise when the concentration data is transformed into the frequency domain and retransformed into the time domain. A transfer function given by the closed form solution of the plug flow axial dispersion model with open-open boundary conditions was used as a model for E_{dc}. The model is appropriate for laminar flow in long channels and assumes a dispersion coefficient, D, that represents the spreading of the tracer in the reactor. The dimensionless equation that describes the dispersion model is

$$\frac{\partial E}{\partial \theta} = \left(\frac{D}{uL}\right)\frac{\partial^2 E}{\partial z^2} - \frac{\partial E}{\partial z} \qquad (5.3)$$

where $z = (Ut + x)/L$ and $\theta = t/\tau$, L is the length of the channel, U is the average fluid velocity in the channel, and D is the dispersion coefficient. The dimensionless group (D/UL) is the vessel dispersion number and a measure of the extent of axial dispersion. Reactors with large vessel dispersion numbers simulate a mixed flow, and small vessel dispersion numbers indicate plug flow. The analytical solution of the axial dispersion model assuming a uniform velocity profile and open open boundary conditions is given by [36]

$$E_{dc}(t) = \sqrt{\frac{\left(UL/D\right)}{4\pi\tau_{av}t}}\exp\left[-\frac{\left(UL/D\right)\tau_{av}}{4t}\left(1-\frac{t}{\tau_{av}}\right)^2\right] \qquad (5.4)$$

where τ_{av} is the experimental mean residence time and is given in its discrete form by

$$\tau_{av} = \frac{\int_0^\infty C(t)\,t\,dt}{\int_0^\infty C(t)\,dt} \cong \frac{\sum_i t_i C_i \Delta t_i}{\sum_i C_i \Delta t_i} \qquad (5.5)$$

The experimental mean residence time was defined as the time necessary for 50% of the tracer to pass the outlet detector subtracted from the time it took 50% of the tracer to pass the inlet detector. Next, Equation 5.4 was substituted in Equation 5.2 and used to

calculate the outlet response, $E_{out,calc}$. A target function was used to relate $E_{out,calc}$ and $E_{out,exp}$

$$J(D) = \sum_{i=1}^{N} \left(E_{out,calc}(D) - E_{out,\exp} \right)^2 \qquad (5.6)$$

where N is the total number of measured concentration data. The vessel dispersion number, D, was used to fit the axial dispersion plug flow model to the experimental outlet responses. The optimal value for D was found by minimizing J in Equation 5.6. The experiment with the lowest minimized error, J, was normalized to one, and the error in the other experiments was scaled. Minimization was completed in MATLAB by the function *Fminsearch*.

Lastly, the experimental and simulated RTDs were characterized by the variance , σ_θ^2, in the dimensionless form and the skewness, s, of the distribution

$$\sigma^2 = \frac{\int_0^\infty \left(t - \tau_{av}\right)^2 E(t)\, dt}{\int_0^\infty E(t)\, dt} \cong \frac{\sum_i \left(t_i - \tau_{av}\right)^2 E_i\, \Delta t_i}{\sum_i E_i\, \Delta t_i} \qquad (5.7)$$

$$\sigma_\theta^2 = \frac{\sigma^2}{\tau_{av}^2} \qquad (5.8)$$

$$s = \frac{\int_0^\infty \left(t - \tau_{av}\right)^2 E(t)\, dt}{\sigma_\theta^{3/2}} \cong \frac{\sum_i \left(t_i - \tau_{av}\right)^2 E_i\, \Delta t_i}{\sigma_\theta^{3/2}} \qquad (5.9)$$

Given the error associated with deconvolving the experimental and simulated coupled inlet and outlet tracer pulses as described above, and in addition to the accuracy of the simulated experimental tracer inlet pulse in the CFD models, the variance and the skewness were calculated for the coupled residence time distributions, as well as deconvolved experimental residence time distributions for experimental data. This permits a direct comparison of the coupled experimental and modeled RTDs.

5.4.2 Computational Fluid Dynamic Model of Residence Time Distribution

Computational fluid dynamics was used to simulate RTD experiments in the microchannel reactor. These models provide insight into the shape of the RTD curve by examining the mixing and fluid dynamics in a single microchannel. Specifically, the hydrodynamics of the regions in between channel passes is investigated. The species transfer and fluid flow modeling was completed on Comsol Multiphysics 3.4 finite element modeling platform. The reactor geometry modeled is a two dimensional cross section of a single microchannel. The model geometry is presented in Figure 5.4. Additionally, two dimensional and three dimensional models of a section of a single channel were modeled to compare the approximation of a two dimensional versus a three dimensional geometry at a Reynolds number of 4 and 100. A three dimensional model of an entire single channel was computationally expensive and thus not feasible for this study. A binary diffusion coefficient for phenol in water at the experimental conditions was estimated 1.18×10^{-9} $m^2 s^{-1}$ by the Wilke-Chang correlation. A solution for the steady state flow field is computed prior to the injection of the tracer. The flow field was solved using the incompressible Navier Stokes equations for laminar fluid flow and was considered converged when the residuals were less than1×10^{-6}. Water at 25°C and ambient pressure was used as the working fluid. A no slip boundary condition was used for all wall boundaries. The inlet boundary was laminar inflow with a prescribed average velocity and the outlet boundary condition was a prescribed pressure of zero. After the steady state flow field converged, a time dependant solution of the convection and diffusion equation was solved. The boundary condition at the entrance of the reactor simulated a tracer pulse in laminar flow. The microchannel outlet boundary condition was convective flux. In order to make a direct comparison to the experimental data, the inlet tracer pulse in the CFD simulations was matched to the experimental inlet pulse at the same flow conditions by equation

$$C_{ph} = C_o \, e^{-\frac{(-t-t_{av})^2}{2\sigma_w^{\,2}}} \qquad (5.10)$$

where C_{ph} is the concentration of phenol with arbitrary units, C_o is the max concentration and is set to 1, t is the time in sec, t_{av} is the time when 50% of the tracer had been injected into the reactor, and σ_w is a peak width constant that was solved for minimizing the error between the calculated and experimental inlet concentration pulses using sum of the least squares method. Generally, the calculated inlet pulse matched the experimental pulse very well, therefore a direct comparison between the simulation and experimental data could be made, and avoided the use of a nonlinear step function in the CFD model. An integral balance at the inlet and outlet boundary was used to capture the tracer concentration as a function of time. All CFD simulations were run on a 64 bit HP xw4600 workstation with an Intel quad core processor at 2.4 GHz with 8 gigabytes of ram. Simulation solutions were determined to be grid independent by solving the steady state flow field with several mesh cases and comparing the velocity profile across the microchannel.

5.5 Results and Discussion

5.5.1 Vessel Dispersion number Versus Reynolds Number

Dispersion in a parallel channel Hastelloy microreactor was investigated experimentally and with CFD by determining the RTDs at several Reynolds numbers using a tracer pulse experiment. A two dimensional CFD model of a single microchannel is compared to experimental data to determine the uniformity of the fluid distribution in each of the reactors 14 microchannels and identify and characterize locations within the reactor where vortex or stagnant regions may occur.

The RTD in the Hastelloy microchannel reactor was measured by observing the time resolved concentration profile of an injected tracer at the inlet and outlet of the reactor. The volumetric flow rate was varied between 1.0 cm^3 min^{-1} and 5.0 cm^3 min^{-1}, which corresponded to Reynolds numbers between 2.4 and 12. Ideally, these experiments would be conducted at supercritical water conditions, but due to the high reactivity of supercritical water as well as temperature and pressure limitations for the UV absorption

detectors, tracer pulse experiments were conducted at 25°C and ambient pressure. Assuming a uniform fluid distribution in each microchannel, it is likely the RTD at the conditions considered by this study will be similar at supercritical water conditions. However, due to unknown temperature gradients in the reactor from the fluid heating period, endothermic biomass reforming reactions, and density gradient from biomass gasification, the possibility of a non-uniform flow distribution at reaction conditions that promote biomass gasification by supercritical water does not directly correlate to the current investigation. Nevertheless, this study provides insight into the reactors flow distribution and the flow profile at the conditions tested and is likely a good approximation for supercritical water conditions. A detailed process model for supercritical water gasification of biomass in the Hastelloy microreactor could be used to predict temperature gradients and flow distributions changes at reaction conditions, but is beyond the scope of this study.

In each experiment the input pulse into the microreactor was a sharp, narrow, and symmetric peak, characteristic of laminar flow. A representative inlet pulse outlet response for a flowrate of 3.0 ml min^{-1} is presented in Figure 5.5. The outlet response is asymmetric and wider compared to the inlet pulse indicating the tracer has spread while in the microreactor. Since the shape of the inlet peak is not a perfect dirac δ function, the shape of the outlet peak is coupled to the shape of the inlet peak and must be deconvolved to determine the inherent RTD. The deconvolved RTDs for Reynolds numbers ranging from 2.4 to 12 are presented in Figure 5.6. Each plot has three curves, the measured outlet tracer distribution, the calculated outlet tracer distribution based on Equation 5.4, and the deconvolved RTD. The experimental mean residence time, non-dimensional variance, and skewness are reported in Table 5.2 for the deconvolved and coupled RTDs. All of the measured outlet tracer distributions have a parabolic profile indicative of laminar flow. Measured outlet tracer distributions were generally in good agreement with calculated values from Equation 5.4, except at lower Reynolds numbers due to considerable tailing in the experiment RTDs. The skewness, which measures the asymmetry of a distribution, is used to quantify the extent of tailing for RTDs. An increase in the skewness for the coupled outlet response was observed with decreasing

Reynolds number, which resulted in increased error for the axial dispersion model fits. The normalized error between the calculated and measured outlet tracer distribution is presented in Figure 5.7. The error associated with fitting the measured outlet tracer distribution to the axial dispersion model was lowest for a Reynolds number of 12 and was normalized to 1.0. The fitting error for all other experiments was scaled. Assuming a uniform microchannel flow distribution, a reason for increased tailing at lower Reynolds numbers is due to a greater amount of tracer diffusion into vortex regions located between serpentine channel passes seen in Figure 5.4. For comparison, the RTD for laminar flow in a straight section of tube, neglecting surface roughness effects, will have a perfectly symmetrical RTD and the width of the peak will be determined by the length and diameter of the tube. The affect of Reynolds number on the hydrodynamics in the region between serpentine channel passes is discussed in further detail in the CFD modeling section.

The non dimensional vessel dispersion number, V_D, which characterizes the spread of the tracer throughout the reactor was estimated from the axial dispersion model fits. In the context of the microchannel reactor, the vessel dispersion number includes molecular diffusion, convection, and dispersion from the microchannel reactors architecture. Fitted vessel dispersion numbers versus Reynolds number are plotted in Figure 5.8. The vessel dispersion number for the microchannel reactor was independent of Reynolds number between 2.4 and 12 and averaged 0.013 ± 0.001. A RTD with a dispersion coefficient less than 0.01 is considered characteristic of plug flow [28], and therefore the RTD in the microchannel reactor is approaching plug flow for the conditions tested. Since the vessel dispersion number scales with velocity, $V_D = D/uL$, the dispersion coefficient in the microchannel reactor, D, must be increasing with Reynolds number. Given that the dispersion coefficient describes diffusion and mixing within the reactor, an increase in the dispersion coefficient, D, implies mixing within the microchannel reactor is influenced by Reynolds number. Alternatively, the uniformity of flow distribution may also affect the shape of the RTD, and is investigated by comparing the RTDs from a single microchannel CFD model to experimental results for the microchannel reactor.

5.5.2 CFD Simulation and Experimental Data Comparison

Computational fluid dynamics were used to model the steady state flow field through a single channel of the microreactor. After a steady state solution for the flow field was reached, a tracer pulse identical to the experimental inlet tracer pulse was injected into the entrance of the microchannel. The resulting outlet tracer pulse is directly compared to the experimental tracer pulse of the microchannel reactor.

Two dimensional CFD models were used to simulate tracer pulse experiments. The 2D models significantly decreased computation time, and are good approximation due to the large aspect ratio, 7.9, of the microchannels. Results from a 2D and 3D simulation that modeled a tracer pulse through a small section of a single microchannel are compared. The section includes one 180 degree turn, Figure 5.4, at Reynolds numbers of 4 and 100. The resulting RTDs are presented in Figure 5.9. In both cases the RTD from the 2D simulation closely matched the shape of the RTD from 3D models, however, the 2D simulation was a better approximation for a Reynolds number of 100. Additionally, the shape of the curves for the two cases was considerably different. At a Reynolds number of 4 substantial tailing is observed causing the distribution to appear similar to a combination of superimposed plug flow and mixed flow RTDs. For a Reynolds number of 100 only a small amount of tailing is observed and the RTD has a parabolic shape. Increased tailing in the RTD at lower Reynolds numbers is due to a change in the hydrodynamics in the transition area between serpentine channels passes. A contour plot showing the velocity field at the center of a channel for a Reynolds number of 100 and a stream line plot of the transition region between channel passes for Reynolds numbers of 4 and 100 are presented in Figure 5.10. At a Reynolds number of 4 there is a portion of the transition area that is recirculating at a much lower velocity compared to the bulk flow. Tracer molecules that end up in the recirculating region will spend a longer time in the transition area between channel passes and cause an increase in tailing. Additionally, as the Reynolds number decreases, the bulk fluid velocity decreases and the tracer spends a longer time in the transition region allowing a greater amount of the tracer to diffuse

into the recirculating region. A smaller amount of tailing for a Reynolds number of 100 is due to a greater amount of the tracer molecules taking the same path around the 180 degree turn in the transition area. At a Reynolds number of 4, two distinct regions in the channel transition area are observed, the bulk flow region and a recirculation region. At a Reynolds number of 100, the two distinct regions of flow observed at Reynolds number 4 have become less pronounced and greater mixing is observed.

Results from the single microchannel CFD simulations for Reynolds numbers 2.4, 7.1, and 12 are directly compared to experimental RTDs and presented in Figure 5.11. Given that the error associated with deconvolving the tracer outlet peak from the inlet pulse increased exponentially as Reynolds number decreased, simulating the trace pulse experiment in a CFD model provided a direct comparison of the outlet distribution between a single microchannel and the microchannel reactor. The simulated inlet tracer pulse fit the experimental pulse very well for each simulation and did not affect the RTD shape or time of the outlet response. The modeled RTD peaks had a parabolic profile similar to experimental RTDs and were within the same residence time range as the experimental RTD, however, greater tailing was observed in experimental RTDs. Residence time distribution characteristics from CFD simulations are presented in Table 5.2. Providing that only one channel is being modeled, the uniformity of the flow distribution can be removed as a variable and a relationship between Reynolds number and RTD for flow in a single microchannel can be established. As expected, the skewness of the distributions from the model simulations increased as Reynolds number decreased due to tailing from the change in hydrodynamics in the transition area between channels seen in Figure 5.10. The same trend was observed for experimental RTDs, however the skewness was greater.

It has been shown that an increase in the skewness is due to the hydrodynamics in the transition area between channel passes, however, there are several other factors that may have contributed to increased tailing in the experimental RTD. The CFD model does not account for the hydrodynamics in the reactor headers, which are approximately 3.7% of the total reactor volume. Although this is a small volume compared to the total

microchannel volume, stationary vortices in the microreactor header may affect the shape of the RTD [20, 40]. Additionally, CFD simulations were sensitive to the phenol water binary diffusion coefficient, $D_{1,2}$. The affect of the binary diffusion coefficient on RTD is presented in Figure 5.12. As the diffusion coefficient decreases the flow becomes dominated by convection and an increase in tailing is observed. For the lowest diffusion coefficient modeled, 1×10^{-10} m^2 sec^{-1}, the tail of the RTD approximates the RTD in a mixed flow reactor. Increasing the diffusion coefficient to 5×10^{-10} m^2 sec^{-1} resulted in a parabolic RTD, and increasing the diffusion coefficient greater than 5×10^{-10} m^2 sec^{-1} resulted in a narrower RTD. The variance of the RTD decreased as the diffusion coefficient was increased. Although an overestimated binary diffusion coefficient for phenol in water may account for the greater tailing in experimental RTDs, the effective diffusion coefficient is likely larger than the calculated value due to the effect of Taylor dispersion. In regard to supercritical water gasification, the binary diffusion coefficient of biomass derived molecules in supercritical water will likely be much larger than the phenol-water diffusion coefficient considered in this study, and therefore a narrow parabolic RTD would be expected. Lastly, the surface roughness of the microchannel walls may affect the shape of the RTD. The surface roughness, R_a, of the microchannel was measured to be 98 nm [15], and previous studies have shown that surface roughness may impact the velocity profile and pressure drop through the microchannel [37 - 39].

For the microchannel reactor investigated, the uniformity of the channel flow distribution was addressed in the reactor design by increasing the pressure drop through each microchannel relative to the pressure drop through the distribution header [15]. Although the microchannel flow distribution could not be directly measured, it was uniform and did not significantly alter the shape of the reactors RTD. The inverse average fluid residence time is plotted versus Reynolds number for the microreactor, a single microchannel, and the theoretical mean reactor residence time based on the reactor volume and inlet volumetric flowrate and presented in Figure 5.13. Experimental reactor residence times were in good agreement with residence times from the single microchannel CFD simulations indicating relatively uniform flow distribution in the microchannels. Although there is greater tailing in the experimental RTDs, the front parts of the

experimental and simulated coupled RTD match. Fronting would be expected if there was a poorly distributed flow in the microreactor. Average residence times for the CFD simulations and experiments were lower than the theoretical mean residence time as a result of stagnant regions in the transition areas located between serpentine channel passes.

5.6 Conclusion

In this study the RTD of a parallel channel Hastelloy microreactor intended for the gasification of biomass by supercritical water was investigated using a tracer pulse experiment and modeled using CFD. The serpentine configuration of the reactor channels is a unique way to integrate parallel microchannels into a compact microreactor that offers the benefits of enhanced transport properties characteristic of processing at the microscale, and the necessary reactor volume to conduct gasification experiments. Given the intricate reactor architecture, a RTD study was used characterize the dispersion and channel flow distribution in the reactor. Generally, the experimental RTD of the microchannel reactor had a parabolic shape characteristic of laminar flow, however, increased tailing was observed as a function of decreasing Reynolds number due to a change in the hydrodynamics located in the transition area between channel passes. A one dimensional axial dispersion model was used to model and deconvolve the outlet tracer response from the inlet tracer pulse. The vessel dispersion number, a parameter used to fit the experimental data to the model, indicated the microchannel reactor was approaching plug flow. Computational fluid dynamics simulation of a single microchannel as configured in the reactor, provided a relationship between the Reynolds number and the hydrodynamics in the transition area between channel passes, and gave insight into the sensitivity of the tracer diffusion coefficient on RTD. In addition, the flow distribution in the 14 parallel microchannels was determined to be uniform as a result of agreement between average modeled residence time of a single microchannel and experimental average residence time of the reactor.

5.7 Acknowledgement

This research was supported by Bend Research, Inc., Bend, Oregon, and by the US Army under the Tactical Energy Systems program administered through the Oregon Nanoscience and Microtechnologies Institute (ONAMI). COMSOL computational fluid dynamics modeling software was provided by ONAMI.

5.8 References

1. Amador C, Wenn D, Shaw J, Gavriilidis A, and Angeli P 2008 *Che Eng J* 135S S259-S269
2. Escher W, Michel B, Poulikakos D 2009 *International Journal of Heat and Mass Transfer* 52 1421-1430
3. Saber M, Commenge J M, Falk L 2010 *Chemical Engineering Science* 65 372-379
4. Commenge J M, Falk L, Corriou J P, and Matlosz M 2002 *AICHE Journal* 48 345-58
5. García-Serna J, García-Verdugo E, Hyde J R, Fraga-Dubreuil J, Yan C, Poliakoff M, and Cocero M J 2007 *J of Supercritical Fluids* 41 82-91
6. Trachsel F, Günther A, Khan S, and Jensen K F 2005 *Chemical Engineering Science* 60 5729-37
7. Adeosun J T, Lawal A 2010 *Chemical Engineering Science* 65 1865-1874
8. Heibel A K, Lebens P J M, Middelhoff J W, Kapteijn F, Moulijn J 2005 *AICHE Journal* **51** 121-132
9. Commenge J M, Obein T, Genin G, Framboisier X, Rode S, Schanen V, Pitiot P, Matlosz M 2006 *Chemical Engineering Science* **61** 597-604
10. Adeosun J T, Lawal A 2009 *Chemical Engineering Science* **64** 2422-2432
11. Lohse S, Kohnen B T, Janasek D, Dittrich P S, Franzke J, Agar, DW 2008 *Lab on a Chip* **8** 431-438
12. Hornung C H, Mackley, M R 2009 *Chemical Engineering Science* **64** 3889-3902
13. Goodwin A K, Rorrer G L 2008 *Ind Eng Chem* **47** 4106-14
14. Goodwin A K, Rorrer G L 2009 *Energy and Fuels* **23** 3818-25
15. Goodwin A K, Rorrer G L 2010 *Journal of Micromechanics and Microengineering* (In Progress Fabrication article)
16. Goodwin A K, Rorrer G L 2010 *Chemical Engineering Journal* accepted
17. Levenspiel O 1999 *Chemical Reaction Engineering* (New York, NY: John Wiley & Sons) p257
18. Bošković D, Loebbecke S 2008 *Chemical Engineering Journal* **135S** S138-S146
19. Hornung C H, Mackley M R, 2009 *Chemical Engineering Science* **64** 3889-3902

20. Amador C, Gavriilidis A, and Angeli P 2004 *Che Eng J* **101** 379-90

21. Viitanen P 1997 *Appl Radiat Isot* **48** 893-8

22. Fahim M A, and Wakao N 1982 *Che Eng J* **25** 1-8

23. García-Serna J, García-Verdugo E, Hyde J R, Fraga-Dubreuil J, Yan C, Poliakoff M, and Cocero M J 2007 *J of Supercritical Fluids* **41** 82-91

24. Martin A D 2000 *Che Eng Sci* **55** 5907-17

25. Michelsen M L 1972 *Che Eng J* **4** 171-9

26. Levenspeil O, and Smith W K 1957 *Chem Eng Sci* **6** 227

27. Commenge J M, Falk L, Corriou J P, and Matlosz M 2002 *AICHE Journal* **48** 345-58

28. Levenspiel O 1999 *Chemical Reaction Engineering* (New York, NY: John Wiley & Sons) p296

29. Navarro R M, Sánchez-Sánchez M C, Alvarez-Galvan M C, del Valle F, and Fierro J L G 2009 *Energy Environ Sci* **2** 35-54

30. Shah K, Ouyang X, and Besser R S 2005 *Chem Eng Technol* **28** 303-13

31. Hessler V, Loeb P, Loewe H, and Kolb G 2007 *Micro Instrumentation* **1** 85-129

32. Brandner J J 2008 *Microreactors in Organic Synthesis and Catalysis* **1** 1-17

33. Hessler V, Knobloch C, and Loewe H 2008 *Recent Patents on Chemical Engineering* **1** 1-16

34. Shirzadi A A, Assadi H, and Wallach E R 2001 *Surface and Interface Analysis* **31** 609-18

35. Shirzadi A A, and Wallach E R 2004 *Science and Technology of Welding and Joining* **9** 37-40

36. Cox M J, Kim M J, and Carpenter R W 2002 *Metallurgical and Materials Transactions A* **33A** 437-42

37. Kandlikar S G 2008 *Nanoscale and Microscale Thermophysical Engineering* **12** 61-82

38. Wang H, Wang Y 2007 *J Micromech Microeng* **17** 586-596

39. Ziarani A S, Mohamad A A 2008 *Nanoscale and Microscale Thermophysical Engineering* **12** 154-169

40. Knockmann N, Engler M, Haller D, Woias P 2005 *Heat Transfer Engineering* **26** 71-78

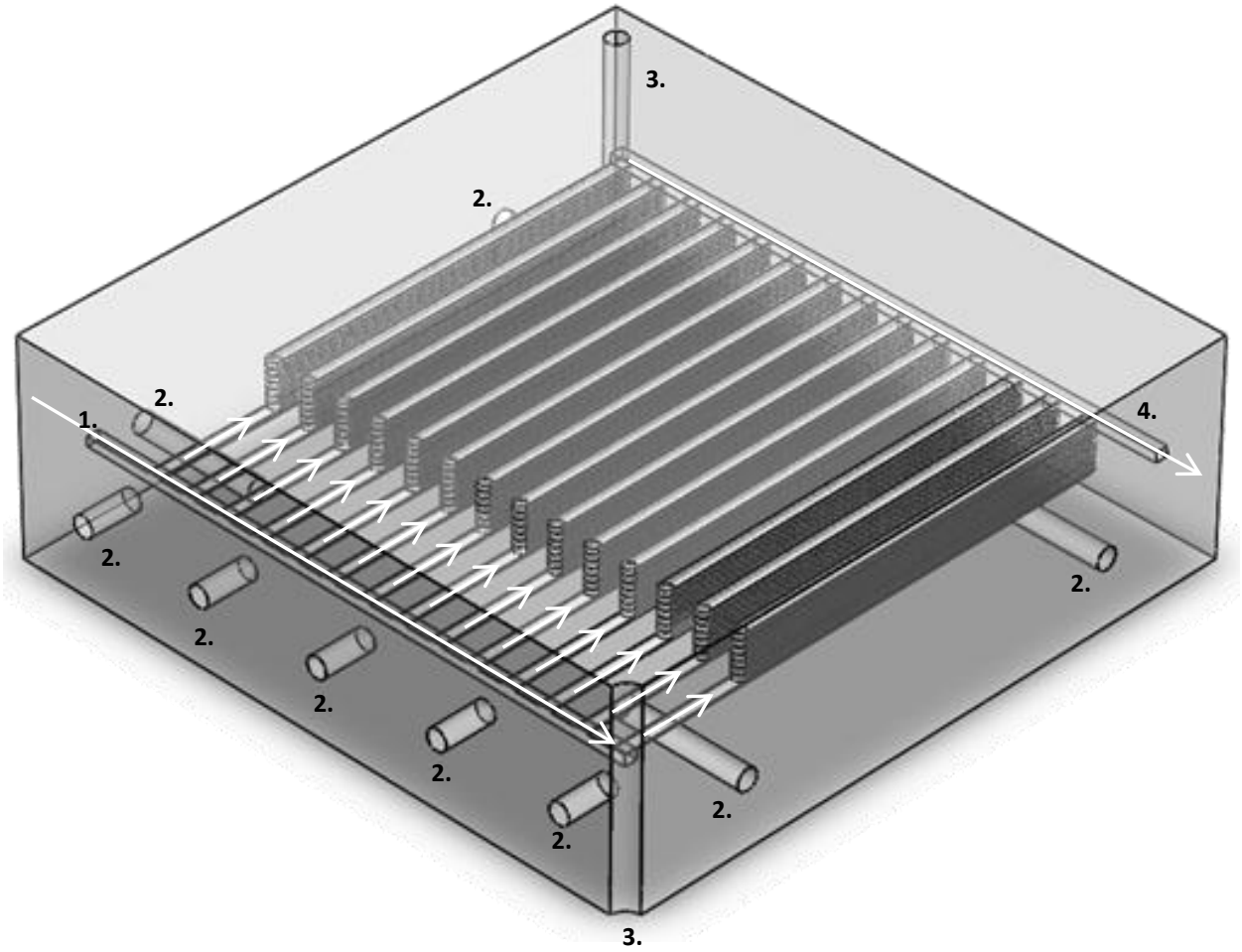

Figure 5.1. Transparent view of the Hastelloy C-276 Parallel channel microreactor. The arrows indicate the direction of flow. The microchannel reactor components are 1) inlet distribution header 2) thermowells 3) alignment pin holes used during fabrication 4) outlet header

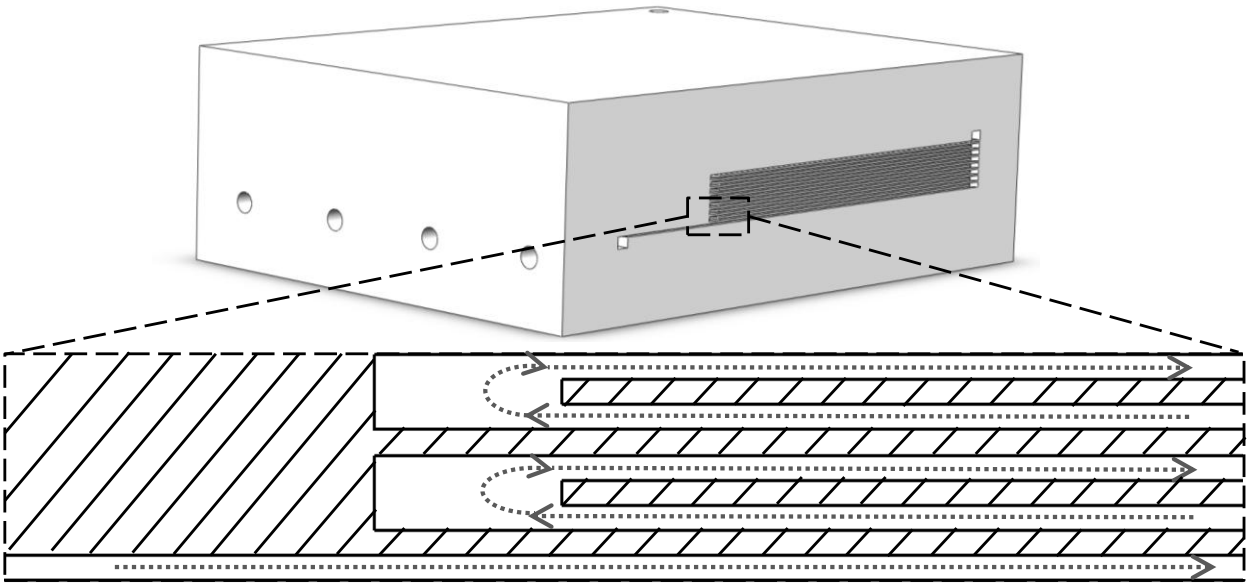

Figure 5.2. A cross sectional view of the microchannel reactor showing a single microchannel. The arrows indicate the direction of flow through the serpentine channels.

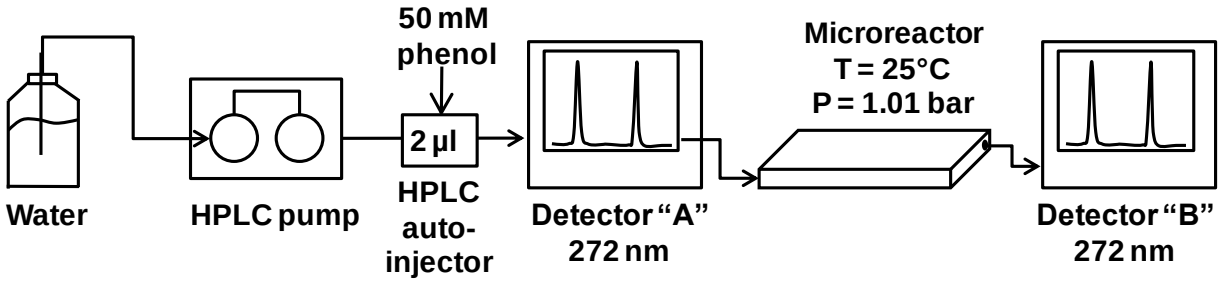

Figure 5.3. Schematic for tracer pulse residence time distribution experiment.

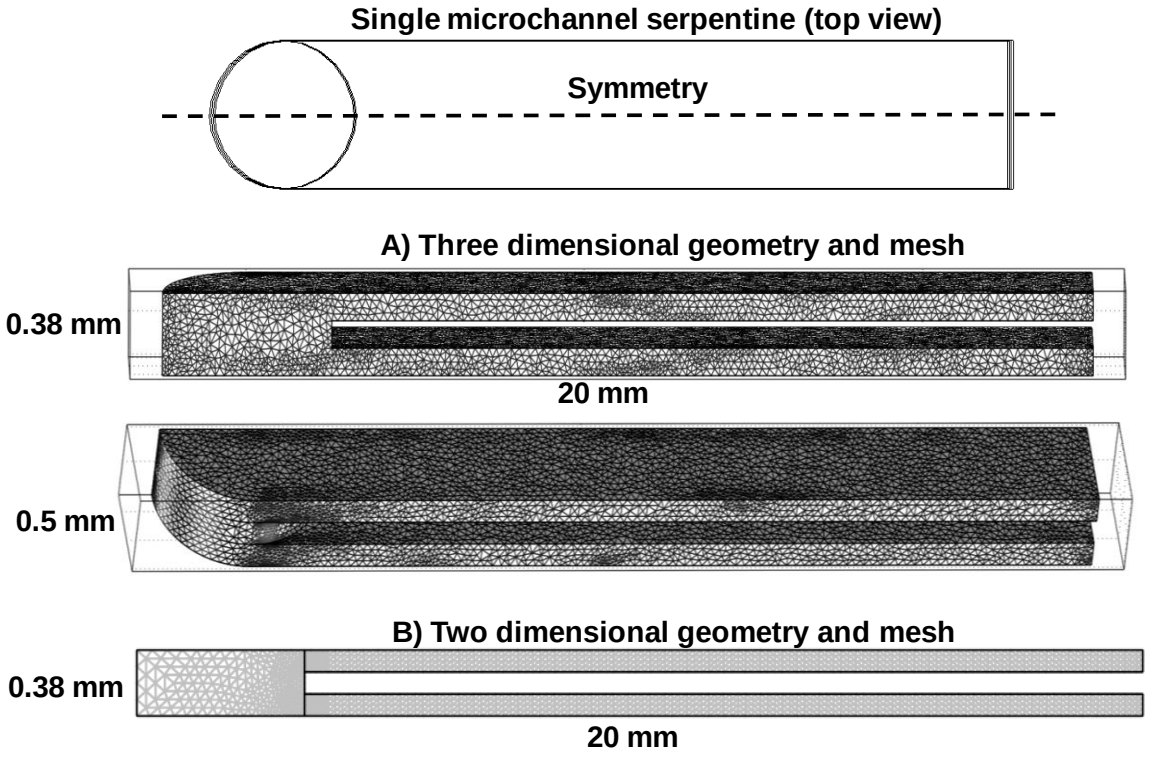

Figure 5.4. Two and three dimensional geometry and mesh for a section of a single microchannel. Half of the three dimensional channel was modeled as a result of symmetry.

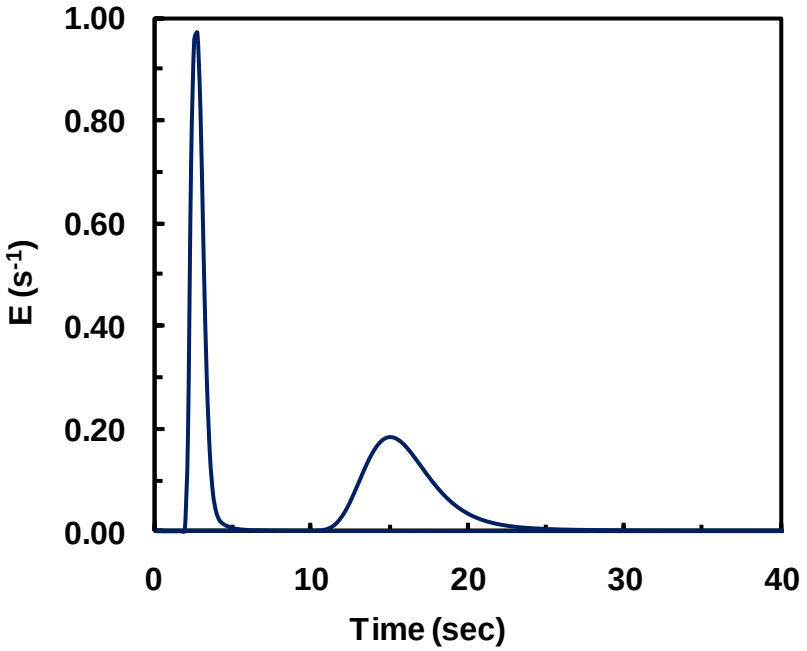

Figure 5.5. Normalized inlet tracer pulse and outlet response for a phenol in water at a volumetric flowrate of 4.0 ml min^{-1} in the Hastelloy microchannel reactor.

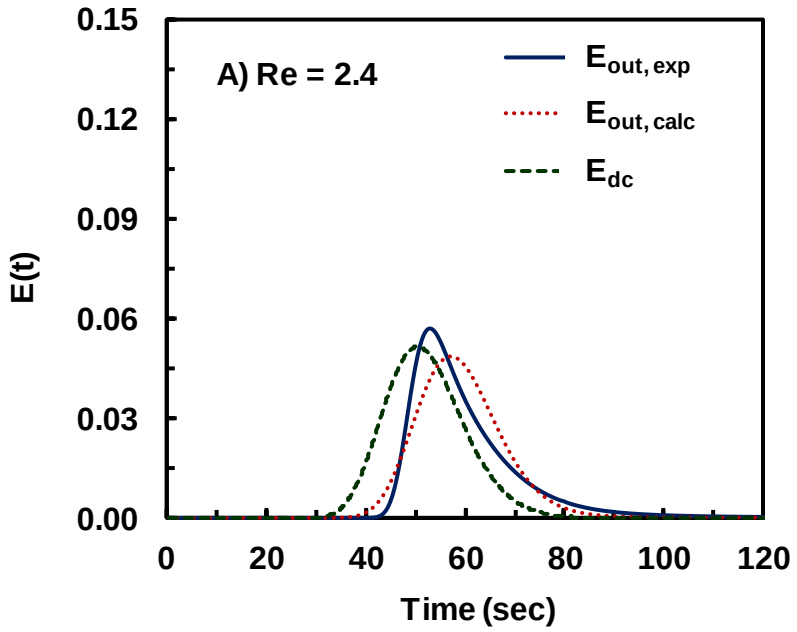

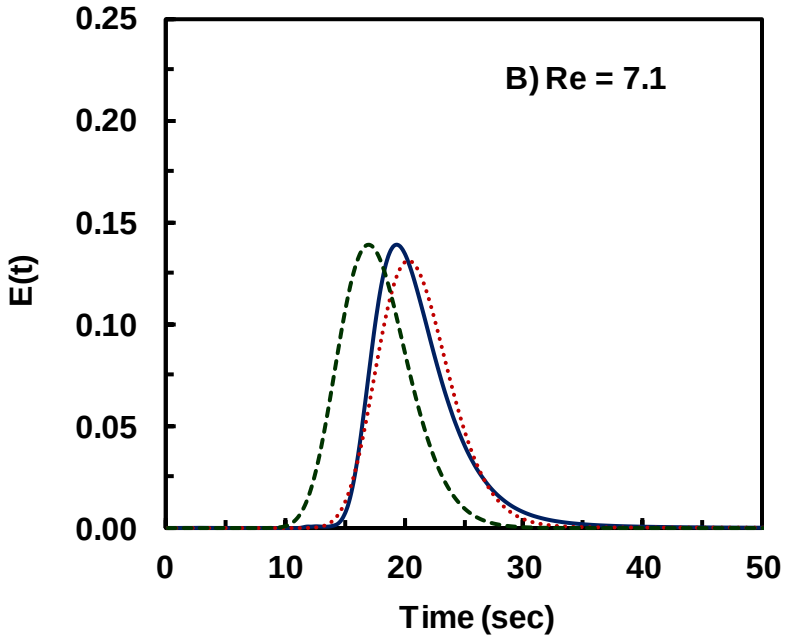
B) Re = 7.1
E(t)
0.25
0.20
0.15
0.10
0.05
0.00
0
10
20
30
40
50
Time (sec)

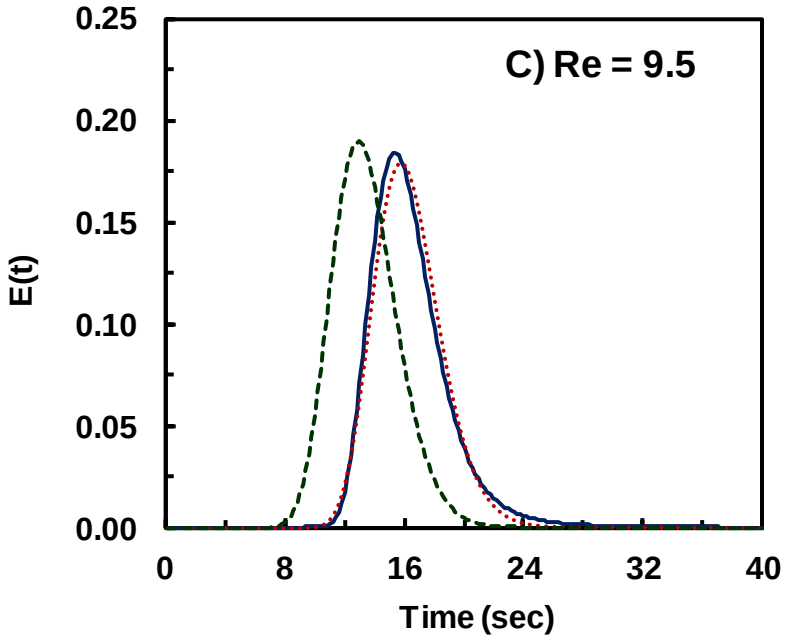
C) Re = 9.5
E(t)
0.25
0.20
0.15
0.10
0.05
0.00
0
8
16
24
32
40
Time (sec)

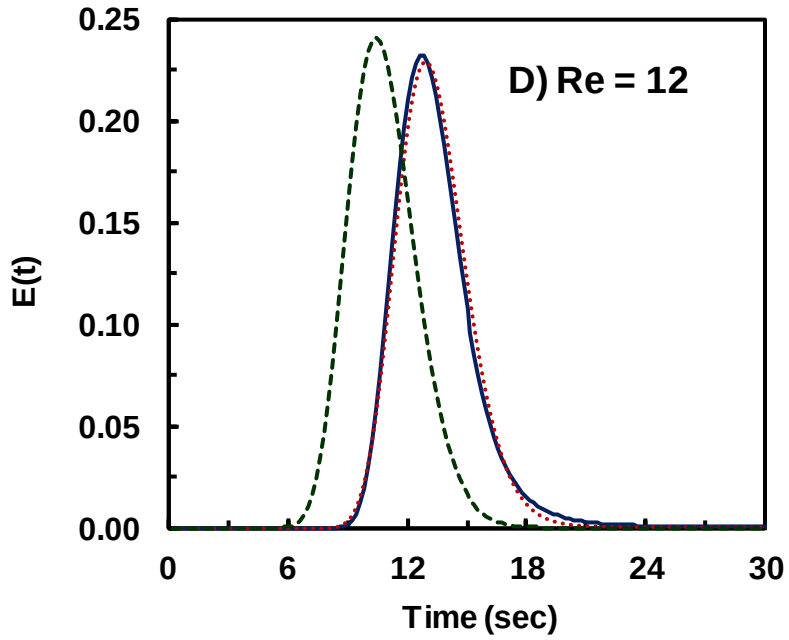

Figure 5.6. Residence time distribution axial dispersion model fits for the deconvolved inlet and outlet response data at Reynolds numbers A) Re 2.4, B) Re 7.1, C) Re 9.5, D) Re 12.

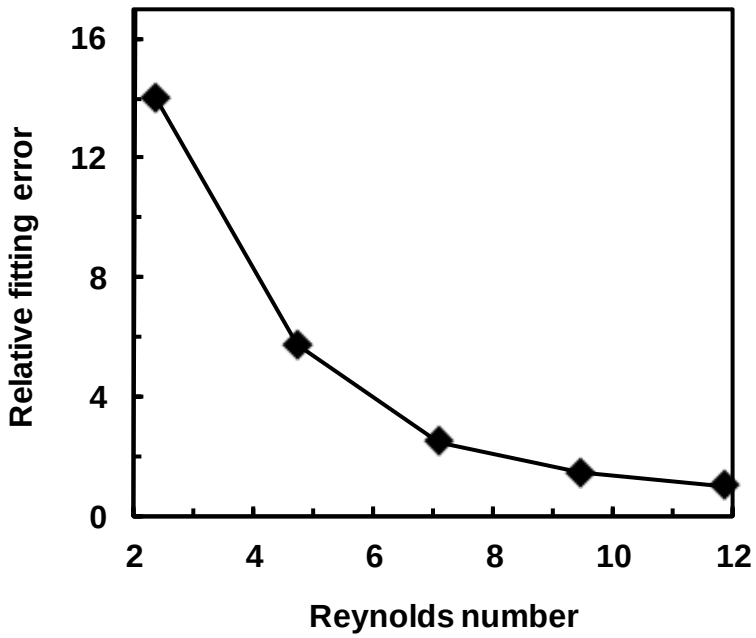

Figure 5.7. Error for the axial dispersion model fits of the deconvolved residence time distributions. The error for Re 12 was normalized to 1 and all other error was scaled.

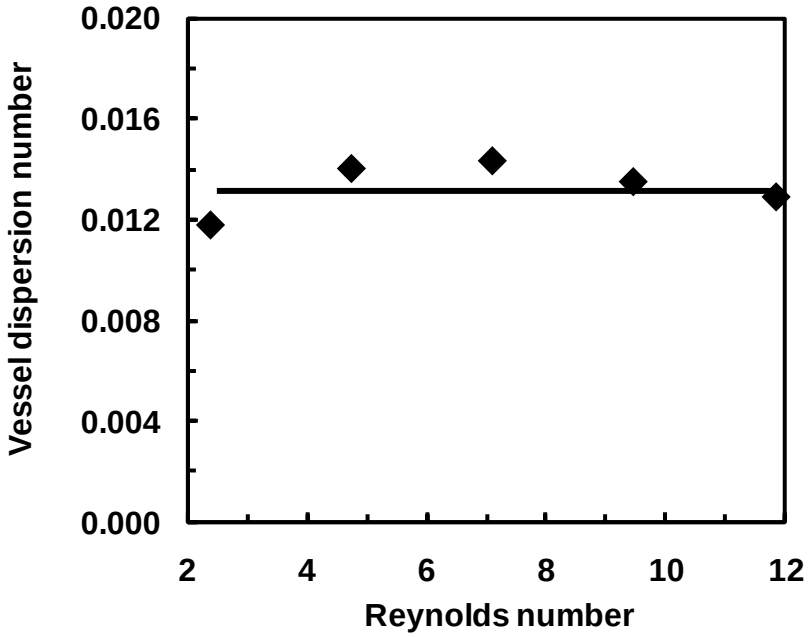

Figure 5.8. Vessel dispersion numbers verses Reynolds number.

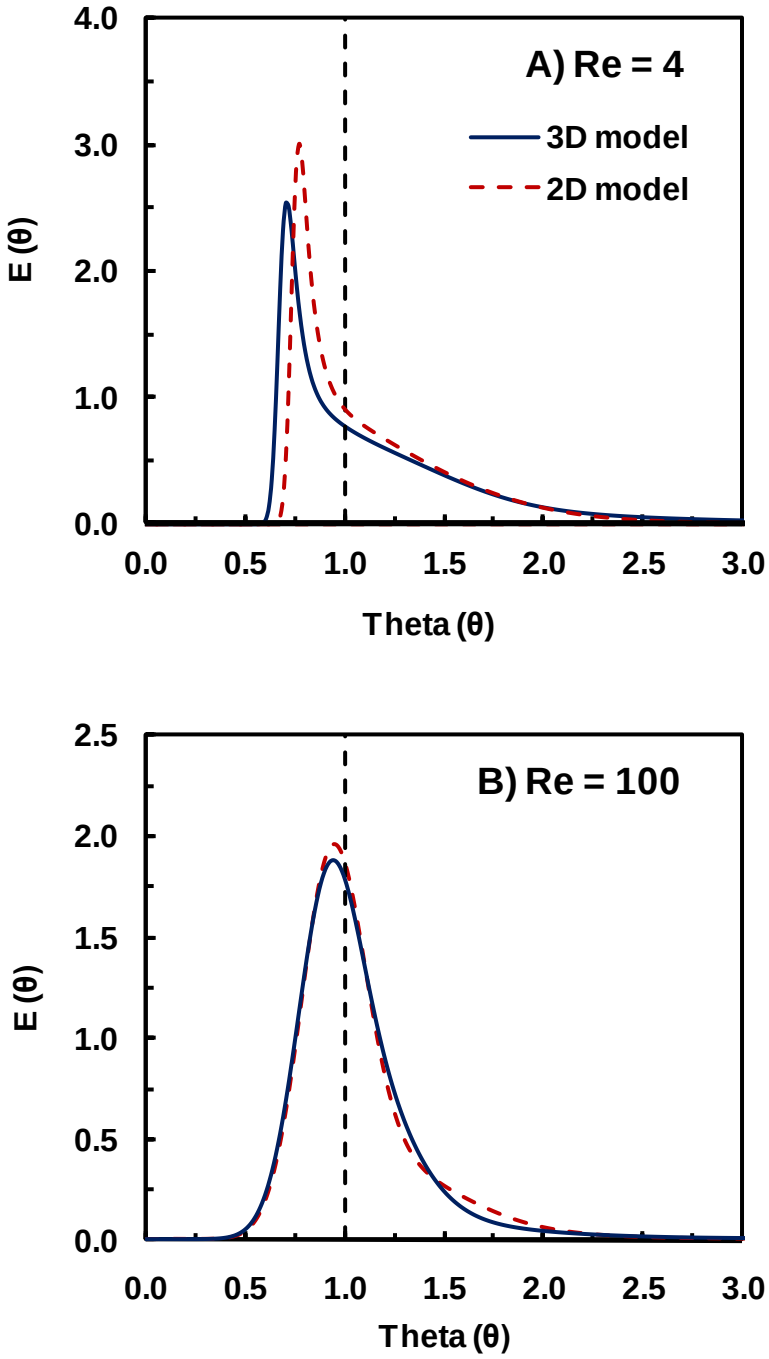

Figure 5.9. Comparison of 2D and 3D residence time distributions from a tracer pulse through a section of a single microchannel at a Reynolds number of A) Re 4 and B) Re100.

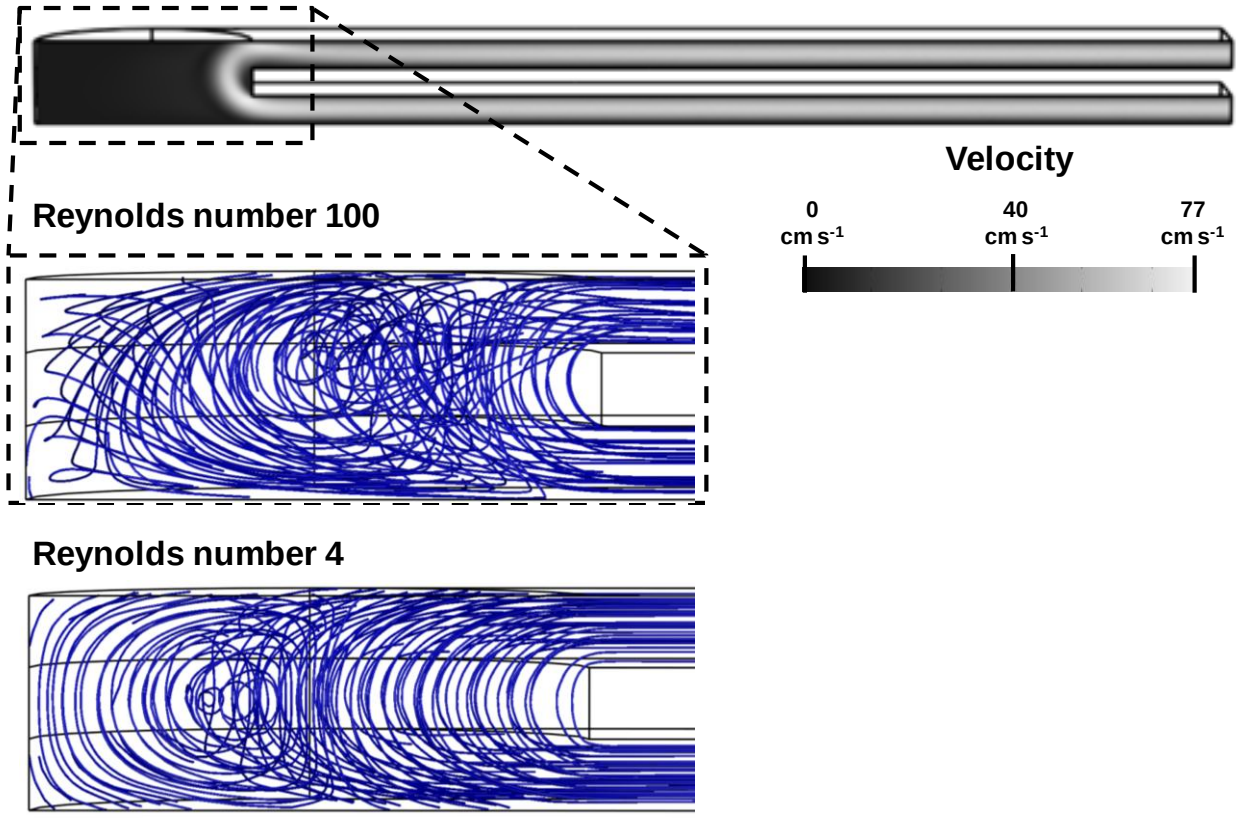

Figure 5.10. Velocity field plot at the center of a microchannel flowing around the transition area between two channel passes at a Re 100, and comparison of streamline plots at Re 4 and Re 100.

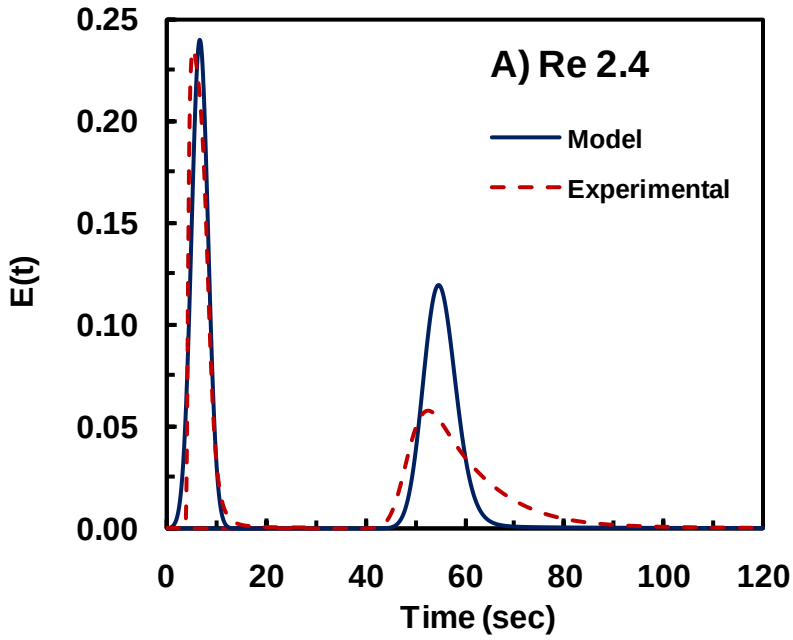
A) Re 2.4
Model
Experimental
E(t)
0.25
0.20
0.15
0.10
0.05
0.00
0
20
40
60
80
100
120
Time (sec)

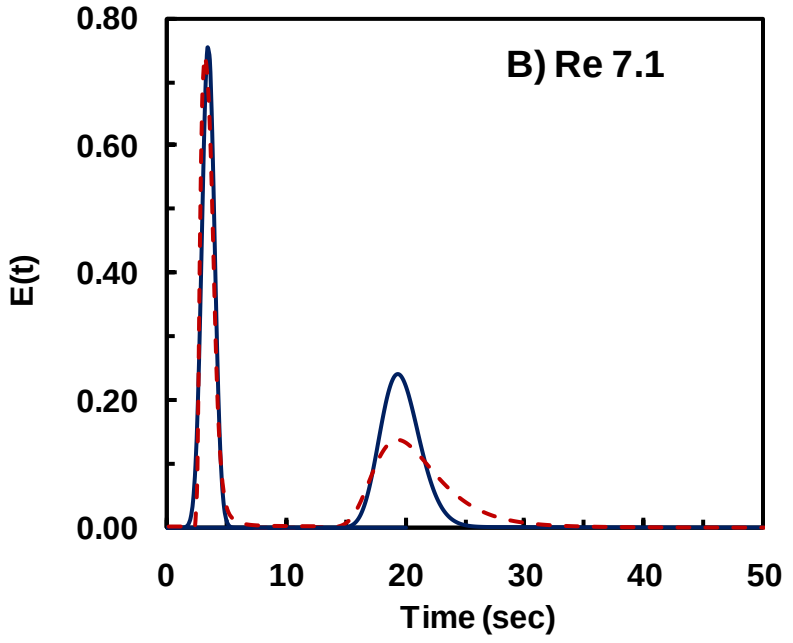
B) Re 7.1
E(t)
0.80
0.60
0.40
0.20
0.00
0
10
20
30
40
50
Time (sec)

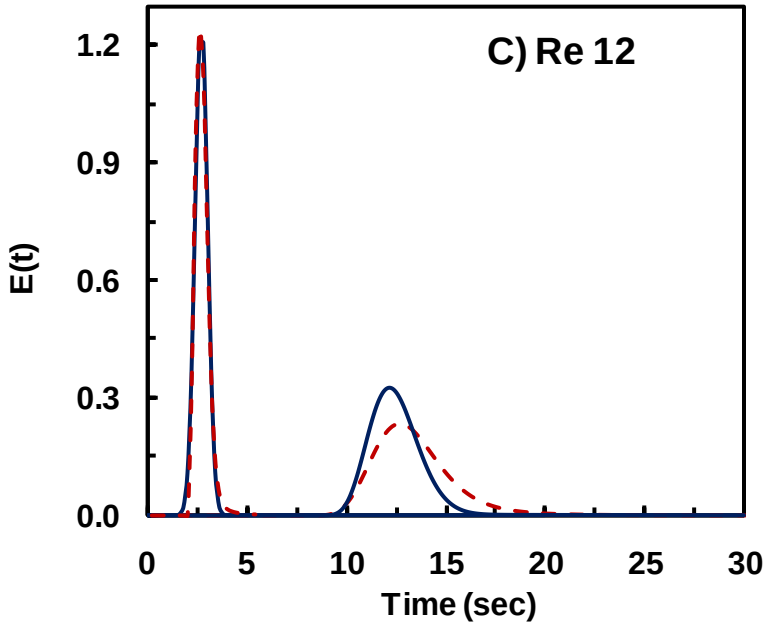

Figure 5.11. Comparison of single microchannel CFD simulations and experimental inlet tracer pulse and outlet residence time distributions at Reynolds numbers of A) 2.4, B) 7.1, and C) 12.

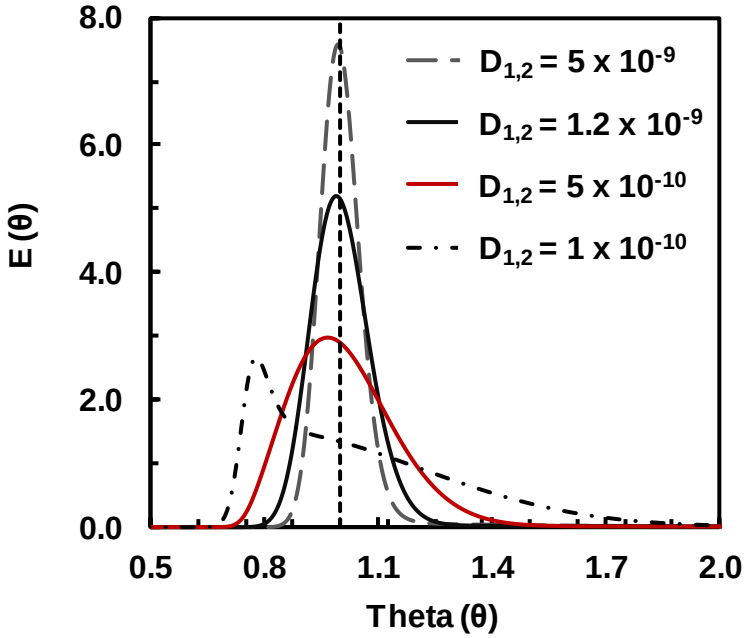

Figure 5.12. The affect of the binary diffusion coefficient on the residence time distribution in a single microchannel for a Reynolds number of 9.5. The units of the diffusion coefficient are in m^2 sec^{-1}.

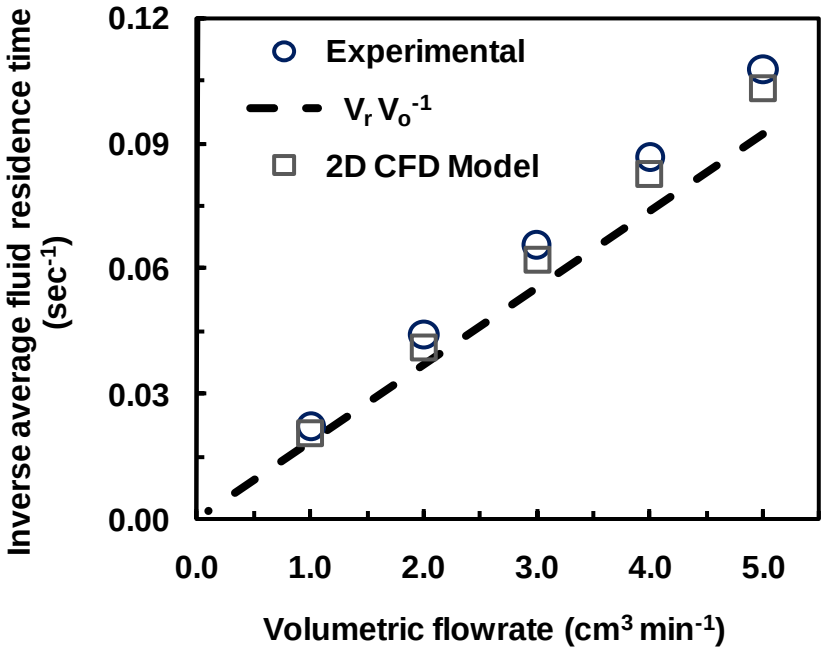

Figure 5.13. Theoretical mean residence time, average residence time for single channel CFD simulations, and experimental mean residence time comparison. Theoretical mean residence time is based on volume of the reactor and volumetric flowrate of the feed solution.

Table 5.1. Parallel channel microreactor dimensions

Overall dimensions	
reactor width	5.0 cm
reactor length	5.0 cm
reactor height	1.7 cm
reactor volume	0.9 cm3
Channel dimensions	
microchannel width	1000 µm
microchannel height	127 µm
microchannel hydraulic diameter	225 µm
total length of each channel	46.2 cm
number of microchannels	14
number serpentine layers	15
single microchannel volume	0.06
Header Dimensions	
header channel length	4.5 cm
header channel width	0.100 cm
header channel height	0.075 cm
total header volume	0.034 cm3

Table 5.2. Results from the experimental and CFD residence time distribution analysis at several Reynolds numbers.

Channel flowrate ($cm^3\ min^{-1}$)	Re number	Experimental					CFD Model		
		τ_{av} (sec)	σ^2_{θ}	s	$\sigma^2_{\theta dc}$	s_{dc}	τ_{av} (sec)	σ^2_{θ}	s
0.07	2.4	9.3	0.073	3.9	0.025	2.8	9.7	0.012	2.4
0.14	4.7	11.5	0.143	3.3	0.029	2.1	12.1	0.022	2.0
0.21	7.1	15.2	0.046	2.1	0.030	1.7	16.1	0.018	1.6
0.29	9.5	22.6	0.049	1.9	0.028	1.5	24.2	0.024	1.5
0.36	12	44.9	0.038	1.6	0.027	1.3	48.5	0.019	1.3

Chapter 6: Conversion of Xylose to Hydrogen-Rich Gas by Supercritical Water in a Hastelloy Microchannel Reactor

6.1 Abstract

Microchannel reactors offer high rates of heat transfer that intensify biomass gasification in supercritical water by sustaining the reaction temperature in the presence of endothermic reforming reactions and providing a rapid fluid heating period. Furthermore, the large surface area to volume ratio in microchannels enhances "unintentional" catalytic activity from the reactor wall for reactors comprised of nickel alloys such as Hastelloy. In this study, a parallel channel Hastelloy C-276 microreactor was used to gasify xylose, a hemicellulose model compound, at 650°C and 250 bar. The reactor consisted of 14 parallel microchannels (127µm by 1000 µm) integrated into a contiguous reactor block using scalable microfabrication techniques. The channels were configured in a serpentine structure that isolated the temperature gradient from fluid heating period from subsequent channel passes. Complete conversion of a 4.0 wt% aqueous xylose solution to H_2 rich gas was achieved in a 1.4 second average fluid residence time. Computational fluid dynamics were used to simulate xylose gasification experiments in the microchannel reactor and investigate temperature gradients due to the heat of reaction for xylose gasification. Additional simulations of the non-reacting flow were used to establish the effect of residence times less than 1.0 second on the average fluid temperature through the reactor. The results from this study suggest that the parallel channel Hastelloy microreactor offers a unique way to improve biomass gasification by supercritical water.

6.2 Introduction

Declining fossil fuel reserves and concerns about increasing atmospheric CO_2 concentration from the combustion of fossil fuels has motivated a considerable body of research in the field of alternative energy. Biomass is a renewable, CO_2 neutral and readily available potential feedstock that can be thermochemically converted to fuels and chemicals [1]. Candidate thermochemical conversion technologies include gasification, combustion, pyrolysis, and liquefaction. Unlike combustion, which typically focuses on heat generation by burning biomass in the presence of oxygen and pyrolysis which thermally decomposes biomass in the absence of oxygen to produce bio-oil, charcoal, and gas, gasification is focused on conversion of biomass to combustible gases by partial combustion with a controlled amount of oxidant. The product gas can be directly combusted for heat generation, fed to a PEM fuel cell for electricity generation, or used as a feedstock for the Fischer-Tropsch synthesis for the production of fuels and chemicals.

Due to its high reactivity and ability to solubilize non-polar compounds, supercritical water is an excellent platform for biomass gasification [2]. Since water plays the role of solvent and reactant, high moisture content biomass can be directly processed in supercritical water without energy intensive dewatering or drying pretreatment steps necessary for other thermochemical conversion technologies [1]. Furthermore, biomass gasification in supercritical water benefits from additional H_2 generation through reforming and produces a compressed product gas potentially low in CO. Recently there has been several review for biomass processing in supercritical water [3-15]. Two strategies for biomass gasification by supercritical water have emerged, a low temperature (350°C to 500°C) heterogeneous catalytic route that produces CH_4 as its major gas product, and a high temperature (500°C to 750°C) route that produces H_2 as its major gas product. Although catalysts designed for low temperature supercritical water gasification have shown potential to lower the activation energy for biomass gasification reactions and increase selectivity in the gas products, the stability of these catalyst systems need to be addressed for this technology to be implemented [16-21].

With regard to the high temperature route, biomass gasification by supercritical water can be substantially intensified by increasing the rate of heat transfer to the reacting fluid [22-26]. Previous kinetic studies for supercritical water gasification of glucose and xylose, biomass model compounds for cellulose and hemicellulose, suggest these biomass constituents rapidly decompose in near critical and supercritical water [27-32]. However, below the critical temperature of water, cellulose and hemicellulose sugars will dehydrate to furan type compounds, including 5-hydroxy-methyl-furfural and furfural, due to an ionic dominated reaction environment. Once above the critical temperature of water, cellulose and hemicellulose react via a retro-aldol condensation to organic acids due to a change in the reaction environment from ionic to free radical [33-34]. Given that furfurals are more recalcitrant to gasify compared to organic acids, a fast fluid heating period resulting from high rates of heat transfer will decrease the furfural concentration and therefore the time necessary to gasify biomass feedstocks. Furthermore, rapid heat transfer is needed to sustain the reaction temperature in the presence of highly endothermic biomass reforming reactions. For example when xylose is reformed to CO_2 and H_2, the enthalpy of reaction at 25°C and 1.01 bar based on water in the gas phase is 287 kJ mol^{-1}. In addition to rapid heat transfer, the chemical composition of the reactor material significantly influences gasification rates and product selectivity. Reactor walls comprised of a high nickel alloy, such as Hastelloy and Inconel, have been shown to catalyze biomass gasification reactions, suppress coke formation and generate additional hydrogen through reforming [10, 35-39]. Therefore, a high heat flux reactor fabricated from a nickel alloy will improve biomass gasification yields and increase H_2 product selectivity.

High rates of heat transfer and large surface area to volume ratios characteristic of micron sized reactor passages make microchannel reactors ideal for supercritical water gasification of biomass. In our previous work we integrated a series of parallel microchannels into a stainless steel microchannel reactor and reported a significant enhancement for the gasification of glucose [23]. Additionally, Hastelloy and stainless steel micron diameter tubular reactors were used to investigate the effect of intensified heat transfer on the co-gasification of xylose and phenol and estimate kinetics for the

gasification of xylose under intrinsic reaction conditions [22]. Specifically, we were able to completely gasify a 4.0 wt% aqueous solution of xylose to H_2 and CO_2 in less than a 1.0 second residence time [27]. Although the Hastelloy microtubular reactor demonstrated the greatest enhancement and H_2 selectivity for xylose gasification in supercritical water, the reactor is not scalable and therefore not feasible for continuous biomass gasification on a larger scale. Biomass gasification in the stainless steel microchannel reactor benefited from intensified heat transfer to the reacting fluid, but lacks the gasification enhancement from a high nickel concentration in the reactor wall.

The present study describes the gasification of xylose by supercritical water in a Hastelloy C-276 microchannel reactor at 650°C and 250 bar. The microreactor has a parallel array of 14 microchannels (127µm by 1000 µm) integrated into a single device and uses the concept of parallel processing to achieve a desired reactor volume. An integrated preheater in the reactor was designed to rapidly heat the reacting fluid up to the reaction temperature while isolating the temperature gradient caused by the fluid heating period from the serpentine microchannels. A two dimensional computational fluid dynamics model describing the heat and fluid transport properties in a single channel of the microreactor was solved with a kinetic model for xylose gasification by supercritical water. The CFD model is compared with experimental results, and suggests that the Hastelloy microchannel reactor offers a unique and novel way to intensify the supercritical water gasification of biomass.

6.3 Experimental

6.3.1 Microchannel reactor configuration and test loop

The microreactor investigated is a parallel channel Hastelloy C-276 microreactor designed for continuous gasification of biomass by supercritical water. A transparent three dimensional schematic of the reactor is presented in Figure 6.1. The reactor architecture and details about the reactor design and fabrication have been previously described [40]. The reactor features and dimensions are summarized in Table 6.1. Briefly,

the reactor is comprised of 14 parallel microchannels that serpentine 15 times vertically through the reactor. Each channel pass is 3.0 cm long with the exception of the first channel pass which is 4.0 cm long as a result of a 1.0 cm long integrated pre-heater designed to minimize a drop in the fluid temperature in subsequent channel passes due to a temperature gradient caused by the fluid heating period. A cross sectional view of a single channel is presented in Figure 6.2. The reacting fluid is distributed to each of the 14 channels by an inlet header and recombined at the exit of the reactor by an outlet header. The average surface roughness (R_a) of the reactor walls is less than 100 nm.

The continuous flow microreactor test loop is presented in Figure 6.3. All wetted parts, including thermocouples and pressure gauges, were constructed of 316 stainless steel. The microchannel reactor described in Figure 6.1 was sandwiched between two 375 W flat plate ceramic heaters. The heater block assembly was insulated by 3.8 cm thick Fibercraft board (Thermcraft, Inc.). Conduction from the ceramic heating plates to the upper and lower plates of the microchannel reactor was the primary mode of heat transfer. The reactor temperature was controlled by a PID controller with a type J thermocouple imbedded into the bottom plate of the microchannel reactor. A feed solution containing 4.0 wt % (41.7 g/L) α-D-xylose (Sigma-Aldrich X1500, >99% purity, CAS 58-86-6, mol wt 150.13) was fed to the reactor at 25°C and 250 bar with an ISCO Teledyne 260D syringe pump (266 mL capacity) operating at constant flow. All feed solutions were degassed by He gas sparging prior to use. The liquid feed flow rate to the reactor (25°C and 250 bar) was varied from 0.5 to 2.5 mL min^{-1} The reactor residence time (τ) was estimated by $\tau = V_R \rho(T,P) / v_o \rho_o$, where V_R is the reactor volume, v_o is the volumetric flow rate of the liquid feed solution at the reactor at inlet temperature T_o and system pressure P, ρ_o is the density of feed solution at T_o and P, and $\rho(T,P)$ is the fluid density at the set point reactor T and P. The hot effluent fluid exiting the reactor was cooled to 25°C with a shell-and-tube heat exchanger using water as the coolant. An adjustable precision back-pressure regulator (KHB1WOA6C2P6000, Swagelok, Inc., stainless steel) stepped down the pressure from 250 to 1.01 bar. The liquid products were collected in the gas-liquid separator. The gas products were dried in-line, metered with a mass flow-meter (Omega, Inc. FMA 1800 series, 0-200 sccm, and 0-1000 sccm,

aluminum/brass body), and then collected into a 2.0 L Tedlar gas collection bag. The volumetric flow rate obtained from the mass flow-meter reading was corrected for the gas composition.

6.3.2 Analytical Procedures

Procedures for the analysis of condensed liquid phase products by high performance liquid chromatography (HPLC) were described previously [27]. Gas products were quantitatively analyzed by an online SRI multiple gas analyzer #1 gas chromatograph (GC) equipped with a thermal conductivity detector for H_2 analysis, and a FID detector with a methanizer for CO, CH_4, CO_2, C_2H_2, C_2H_4, and C_2H_6 analysis. The gas mixture was separated on two columns, a 2-meter Molecular Sieve 13X and a 2-meter Silica Gel. The GC oven temperature was held at 40°C for 3 min., then ramped to 135°C at a rate of 16°C/min, and held at 135°C for 2.67 min. A standard gas injection volume of 250 µl was injected three times for all gas samples. The concentration of the gas species was reported as an average of three injections. Gas products were identified by retention time and quantified by external calibration against a standard gas mixture (Alltech Associates Inc., gas standard #19792). Calibration was performed with three 100 µL standard gas injections.

6.3.3 Computational fluid dynamics (CFD) modeling and simulation

Computational fluid dynamics was used to simulate xylose gasification by supercritical water in a single channel of the Hastelloy microchannel reactor. Finite volume CFD simulations were performed on Fluent version 6.3.26 operated in the double precision mode and interfaced with Gambit version 2.4.6. Model simulations were run on a HP-XW4300 workstation using a Linux operating system equipped with a Pentium 4 processor and 8 gigabytes of RAM. The reactor geometry modeled consists of a two dimensional cross section of a single microchannel, and is presented in Figure 6.2. The two dimensional model geometry is a good approximation due to the high channel aspect

ratio of 7.9 [41]. The thermo-physical properties of water at 650°C and 250 bar were used to approximate the properties of the working fluid and are presented in Table 6.2 along with the thermo-physical properties of Hastelloy C-276 [42]. The density of the reacting fluid was held constant, and therefore the model did not account for density changes due to a change in the reacting fluid temperature or density changes as a result of gas generation. A generic binary diffusion coefficient of 1×10^{-8} m^2 sec^{-1} was used for each species in the reacting mixture. The fluid flow was modeled by the Navier Stokes equations for laminar flow. The mass flowrate at the channel inlet boundary ranged from 2.2 to 10.8 kg hr^{-1}(Fluent assumes a 1.0 m channel width for two dimensional models). A prescribed pressure of 250 bar was used for the reactor outlet boundary condition, and a no slip boundary condition was used to describe the velocity at the channel walls. For the general heat equation, a prescribed temperature of 650°C was used as a boundary condition at the top and bottom of the reactor where the heater contacts the reactor wall, and insulation or zero heat flux boundary condition was used on the sides of the reactor. A prescribed fluid temperature of 25°C was used at the microchannel entrance, and a zero heat flux boundary condition was used at the microchannel outlet. The kinetic model reaction mechanism for xylose gasification by supercritical water is presented in Figure 6.4. The kinetic model was previously developed to predict gas yields for supercritical water gasification of xylose at reaction conditions where gasification is dominant [27] and is appropriate for the conditions considered by this study. All of the liquid phase decomposition reactions are pseudo first order and the temperature dependence of the rate constants was described by the Arrhenius equation. Specifically, in the kinetic model, xylose is dehydrated to furfural or reacted to water soluble humic substance (WSHS), a general term that encompasses all of the liquid decomposition products from xylose and other liquid intermediates. In the kinetic model furfural is further decomposed to WSHS, which is stoichiometrically gasified to CO and H_2. The water gas shift and methanation reactions are assumed to be in thermodynamic equilibrium at the temperature of the reacting fluid in the reactor. The temperature dependence on the equilibrium constant for the water gas shift and methanation reactions was calculated by the Van't Hoft equation. Fugacity of the gas phase species was used to account for non-ideal behavior at 250 bar,

and was based on the Peng Robinson equation of state for the pure gas species and did not account for mixing interactions in the reacting fluid. Standard heats of reactions were calculated by Hess's law at the reacting fluid temperature and 1.01 bar. Thermodynamic properties of WSHS were calculated based on the products of the following equation

$$C_5H_{10}O_5\left(Xy\right) \rightarrow C_2H_4O_2\left(AA\right) + C_2H_4O_2\left(PA\right) + H_2O \qquad (6.1)$$

Although WSHS consists of many more liquid intermediate compounds, major liquid decomposition products were acetic acid and propionic acid [27], and likely are a good approximation of the thermodynamic properties of the bulk term.

A structured quadrahedral mesh was used to discritize the area inside of the microchannel, and an unstructured quadrahedral mesh was used to discritize the reactor block. A mesh containing 930,000 nodes was found adequate for a mesh independent solution. This conclusion was reached by refining the mesh based on gradients of pressure and temperature, resolving the problem and comparing solutions. The Fluent pressure based solver was used to solve the fluid flow, energy equation, and species transport equations in the microchannel reactor. The SIMPLE algorithm was used for pressure velocity coupling and a second order upwind discritization scheme was used for species equations, momentum, and energy. The standard discritization scheme was used for the pressure and the "Green-Gauss Node based gradient option" was chosen for the gradient option. Default under relaxation factors were found to be sufficient for all variables. Simulations were solved by initially solving the steady state fluid flow and energy equations, commonly referred to as the "cold flow solution". The residuals were less than 1 $x10^{-6}$, therefore the case was considered converged when the pressure, monitored at the inlet, reached an asymptote and no longer changed with each iteration. Once a steady state cold flow solution was reached the species transport, using the laminar finite rate model and stiff chemistry option, was solved using the unsteady state solver and a fixed time step of 1 x 10^{-5} sec. The concentration of H_2 and WSHS were monitored at the microchannel outlet and the simulation was considered converged when the concentration of these species had reached an asymptote and no longer changed with

each time step. The difference in the mass flux at the inlet and outlet was less than 1 x 10^{-13} kg s^{-1} for all simulations.

6.4 Results

6.4.1 Effect of residence time on gas yield

Supercritical water gasification of xylose in the microchannel reactor resulted in H_2 rich gas and a clear aqueous liquid phase. The reaction conditions considered by this study are described in Table 6.3. No coking or char was observed for any of the reaction conditions tested. The effect of residence time on the percentage of recovered carbon in the gas, also referred to as the carbon gasification efficiency (CGE) is compared to CFD simulations and presented in Figure 6.5A. The experimental and predicted CGE was independent of residence time between 1.4 and 7.1 seconds and average values are reported in Table 6.4. CFD simulation results were in good agreement with experimental values and indicated near complete gasification of the feed substrate within experimental error. Although experimental residence times did not go below 1.4 seconds, CFD simulations predicted a sharp decrease in the CGE for residence times less than 1.4 second due to incomplete gasification of the feed substrate. An organic acids and residual sugars analysis completed on the liquid products revealed no detectable intermediates for all conditions tested. Measured and predicted liquid intermediate concentration versus residence time is presented in Figure 6.5B. Although, no liquid intermediates were detected for xylose gasification experiments, CFD simulations predicted a sharp increase in furfural and WSHS concentrations below a 1.4 second residence time.

The effect of residence time on the H_2 yield, defined as the moles of H_2 generated per mole of xylose fed, for xylose gasification is presented in Figure 6.5A. The theoretical H_2 yield for xylose gasification based on the concentration of hydrogen in the feed stock is 5, and based on reforming is 10. The excess 5 moles of H_2 generated from reforming are liberated from water, a result of the water gas shift reaction. The experimental H_2 yield was independent of residence time, and averaged 8.9 ± 1.0 moles of H_2 generated per

mole of xylose fed. The H_2 yield was less than the theoretical yield for reforming due to the presence of CH_4 and CO in the product gas. For the range of experimental residence times tested, the H_2 yield based on CFD simulations was 9.7 ± 0.2 moles of H_2 generated per mole of xylose reacted. For residence times less than 1.0 second, CFD simulations predicted a substantial decrease in the H_2 yield due to incomplete gasification of the feed substrate given that the gas phase reaction are in thermodynamic equilibrium.

6.4.2 Effect of residence time on gas composition

Major gas products for the gasification of xylose in the microchannel reactor consisted of H_2 and CO_2, and minor gas products included CO, CH_4, C_2H_6. The effect of residence time on gas composition for xylose gasification is presented in Figure 6.5C. Experimental and predicted gas composition was generally in good agreement and independent of residence time ranging from 1.4 to 7.1 seconds. However, one notable difference between CFD predictions and experimental values was the concentration of CH_4 in the product gas. Based on equilibrium values for the water gas shift and methanation reactions, an average CH_4 concentration of 0.1% ± 0.0% was predicted, whereas the average CH_4 concentration observed over the range of residence times tested was much higher at 3.9% ± 0.6%. For residence times less than 1.0 second, CFD simulations predicted a similar gas composition as longer residence times with the exception of a sharp increase in the CO concentration, up to 5.3 % for a 0.7 second residence time. Although C_2H_6 was measured in the product gas, the kinetic model did not include a pathway for ethane formation, and was therefore not reported in Table 6.4.

6.4.3 CFD simulation: microchannel temperature profile during xylose gasification

Since biomass gasification reaction rates and equilibrium gas composition are sensitive to the reaction temperature [22, 43-48], CFD simulations were used gain insight into temperature gradients that exist in the reactor. The temperature profile through the reactor is dependent on the fluid Reynolds number and the feed concentration due to

endothermic nature of biomass gasification reactions. To address the effect of heat of reaction from xylose gasification on the temperature of the reacting fluid, the temperature profile through a single microchannel was simulated with and without reactions at a 1.4 and 7.1 second residence time. The temperature profile through the microchannel was calculated on a streamline which was released at the center of the entrance of the channel. A sample plot showing the microchannel geometry and the streamline through the microchannel for a 1.4 second residence time is presented in Figure 6.6. The streamline was located at the center of the channel, or the part of the flow with the highest velocity. A plot showing the fluid velocity on the streamline for 1.4 and 7.1 second residence times is presented in Figure 6.7. The vertical lines in the Figure represent the 15 serpentine channel passes in each microchannel. In both cases a decrease in the fluid velocity is observed when the fluid goes around the 180 degree turn between serpentine channel passes, and the effect becomes more pronounced at shorter residence times. A velocity vector plot also presented in Figure 6.7 shows the flow field for xylose gasification for a 1.4 second residence time. From the velocity vector plot it is apparent that an eddy and a small vortex forms in the transition area between channel passes. It is important to note that the Reynolds number has a considerable effect on the flow field in between channel passes and therefore has an effect on the fluid residence time distribution however this is beyond the scope of this study.

The non-reacting or “cold flow” streamline temperature profile through the microchannel is compared with the reacting flow and presented in Figure 6.8. For a 7.1 second residence time, the temperature of the reacting fluid rapidly increases from 25°C past the critical temperature of water within the first 200 μm of the first channel pass. Once past the critical temperature of water xylose dehydration to furfural is no longer favored due to a change in reaction environment from ionic to free radical. At the end of the first channel pass the temperature of the fluid fluctuates about 10°C between subsequent channel passes. Generally, a decrease in the reaction temperature is predicted when the fluid is flowing in the direction of the microchannel entrance due to the temperature gradient from the fluid heating period. The microchannel temperature profile is similar for the cold flow and reacting flow, however a slight drop in the fluids temperature, less

than 1.2°C, is observed in the first 7 channel passes due to the heat of reaction from WSHS being gasified to CO and H_2. After which the temperature of the cold flow and reacting flow are similar due to complete gasification of the feed substrate. For a 1.4 second residence time the fluid temperature rapidly increases to a maximum of 646°C by the end of the first channel, but decreases to 618°C by the end of the second channel. The lowest average channel pass temperature was predicted for channel passes located at the middle of the reactor since the location of these channels are furthest from the reactor heaters. By comparing the cold flow and reacting flow streamline temperatures for a 1.4 second residence time it is evident that endothermic xylose gasification reactions has a greater effect on the temperature of the reacting fluid compared to longer residence times, however a maximum temperature drop in the reacting fluid of only 9.6°C was predicted compared to the cold flow. In addition, the average streamline temperature through the microchannel was 632°C for the cold flow and 626°C for the reacting flow, and therefore it is unlikely that the temperature difference will substantially affect the gas yield or H_2 selectivity for xylose gasification.

6.4.4 CFD simulation: liquid intermediate formation

To get a better idea how residence time and reaction temperature may affect liquid and gas production formation in the microchannel reactor, streamline concentrations of WSHS, furfural, CO_2, and H_2 for a 1.4 and 7.1 second residence time were calculated and are presented in Figure 6.9. Given that xylose is completely reacted in 3 mm of the first channel for a residence time of 1.4 seconds, the concentration of WSHS and furfural were used to represent liquid intermediates in the reacting flow. The maximum concentration for WSHS and furfural were similar for both residence times, however, for a residence time of 7.1 seconds, furfural was completely reacted to WSHS by the first 10 cm (3 channel passes) of the microchannel and WSHS was completely gasified to CO and H_2 in 20 cm (7 channel passes) of the microchannel. In comparison, for a 1.4 second average fluid residence time a small concentration of WSHS was predicted at the reactor outlet. This is contrary to our experimental results which no liquid intermediates were measured

at the outlet as seen in Figure 6.5B. It should be noted that the average predicted concentration of WSHS at the outlet will be lower than the streamline value given that the streamlines velocity is near the maximum velocity of the fluid, and not an average velocity. A streamline with a lower velocity will have a longer residence time and therefore the concentration of WSHS will be less. For an average residence time of 7.1 seconds, the streamline concentrations of CO_2 and H_2 increase for the first 15 cm of the microchannel until they reach an asymptote indicating all of the liquid intermediates have been gasified. Small fluctuations in the H_2 and CO_2 concentrations on the asymptote are due to changes in the equilibrium of the water gas shift and methanation reactions from the fluctuating reaction temperature. At an average fluid residence time of 1.4 seconds, the concentration of H_2 and CO_2 increase throughout the entire length of the microchannel, and are approaching the species concentration asymptotes predicted for a 7.1 second residence time.

6.4.5 CFD simulation of non reacting flow for less than 1.0 second residence time

Considering previous CFD simulations within the experimental average fluid residence time range considered by this study, it is evident that fluid velocity has a greater effect on the reacting fluid temperature than endothermic xylose reforming reactions. Therefore, CFD simulations were used to determine the effect of residence times less than one second on the streamline temperature of the cold flow, and is presented in Figure 6.9 for residence times ranging from 0.2 to 1.0 seconds. Temperature fluctuations between channel passes were similar for residence times between 0.5 and 1.0 seconds, however the effect of decreasing the residence time was a lower overall average streamline temperature through the length of the channel. The lowest average streamline temperature of 474°C was for predicted for a 0.2 second residence time.

6.5 Discussion

This article describes the continuous gasification of xylose by supercritical water in a novel parallel channel Hastelloy microreactor at conditions where gasification is dominant. The reactor is designed to intensify biomass gasification by providing high rates of heat transfer to the reacting fluid in order to minimize the fluid heating period and drive endothermic biomass reforming reactions. The reactor contains 14 parallel microchannels integrated into a single device constructed from Hastelloy C-276. Computational fluid dynamics were used to simulate the fluid, heat, and mass transport properties in a single microchannel, and aided in understanding the effect of residence time on temperature gradients in the reactor.

Reforming xylose to H_2 rich gas in the microchannel reactor benefited from high rates of heat transfer to the reacting fluid provided by the microchannel reactor. It is well established that increasing the rate of heat transfer during supercritical water biomass gasification increases gasification efficiency [25-26, 49]. In our previous work we exploited this concept and by gasifying xylose in a Hastelloy microtubular reactor at conditions where gasification is dominant [22, 27]. The reactor configuration provided sufficient heat transfer necessary for isothermal gasification of xylose at fast residence times, and resulted in complete gasification of a 4.0 wt% xylose solution to H_2 rich gas in less than 1.0 second residence time. In this study a Hastelloy microchannel reactor was used in place of the microtubular reactor. The microchannel reactor offers two significant advantages over the microtubular reactor. First, the microchannel reactor is fabricated using scalable microfabrication techniques. Depending on the desired reactor volume, complete channels and channel layers can be added to the existing device to increase the reactor volume. Since the physics in the individual microchannels stay the same, the device performance is will not be appreciably affected by scaling up the reactor volume. Two technical issues associated with microreactor scale up for this particular design are the formation of temperature gradients in the vertical direction of the reactor with the addition of channel passes and equal microchannel flow distribution with the addition of complete microchannels. Temperature gradients in the vertical direction from increasing

the number of shims and therefore channel passes can be addressed by integrating internal heaters into the shim stack section of the reactor. Combustion microchannels that internally combusts a portion of the gas products to sustain the reaction temperature have been previously integrated into microreactors for catalytic steam reforming of methane to self sustain the reaction temperature [50-51]. The uniformity of the flow distribution between microchannels becomes an issue when as the number of microchannels increases, but can be addressed by header design [52-53].

The second advantage the microchannel reactor has over the microtubular reactor is enhanced heat transfer as a result of a higher surface area to volume ratio. Although CFD simulations predict small temperature gradients between microchannel passes for the range of experimental residence times considered by this study, seen in Figure 6.8, the rate of heat transfer to fluid is greater compared to the 762 μm diameter Hastelloy microtube reactor used in our previous study. For example, the heat transfer coefficient, *h*, for supercritical water at 650°C and 250 bar in the microchannel reactor was 2691 W m^{-2} K^{-1} at a Reynolds number of 87, which corresponded to a average fluid residence time of 2.4 seconds. Based on the same residence time and reaction conditions, the heat transfer coefficient in the Hastelloy microtubular reactor was 528 W m^{-2} K^{-1} at a Reynolds number of 1130, a five-fold greater heat transfer coefficient in the microchannel reactor [23].

In addition to intensified heat transfer, biomass gasification in the microchannel reactor benefits from enhanced catalytic activity due to a large surface area to volume ratio and the presence of iron and nickel in the reactor walls. The microchannel reactor used in this study was fabricated from Hastelloy C-276, a nickel alloy that contains nominally 50% to 60% nickel, 15% chromium, 16% molybdenum, and 4 to 7% iron. When exposed to supercritical water nickel alloys such as Hastelloy C-276, develops an outer oxide layer at the surface consisting of nickel oxide and an inner layer rich in chromium, oxygen, and nickel clusters [54-55]. It has been shown that the exposed nickel on the surface of the reactor wall substantially increases gas yields for supercritical water gasification of cellulose and lignin by promoting the water gas shift reaction, methanation reaction, and

liquid intermediate decomposition reactions [10, 35-38]. Additionally, increasing the catalyst surface area to biomass weight ratio has been shown to improve gasification yields and H_2 selectivity for cellulose gasification [39]. Therefore, in regard to xylose gasification in the microchannel reactor, the low concentration of CO in the product gas (less than 1.0%) and a H_2 yield approaching the theoretical limit for reforming xylose was attributed to enhanced promotion of the water gas shift and methanation reactions from the high concentration of nickel exposed on the surface of the reactor walls and high surface area to volume ratio in the microchannel reactor.

The results from xylose gasification by supercritical water in the microchannel reactor was the complete gasification of a 4.0 wt% solution of xylose within a 1.4 second residence time with no observable coke formation. Furthermore, for the range of residence times tested, a H_2 yield of 8.9 ± 1.0 moles of H_2 generated per mole of xylose fed was obtained. Aside from our previous studies in the microtube reactor, there do not appear to be any reported investigations that non-catalytically gasify hemicellulose by supercritical water at conditions that promote gasification. The microchannel reactor offers considerable improvement compared to previous catalytic studies that obtained a H_2 yield of less than one, and a carbon recovery in the gas of less than 70% for xylan gasification just above the critical temperature of water [56-57]. Furthermore, the timescale for complete gasification of xylose in the microchannel reactor was on the scale of seconds compared to a 20 minute reaction time used by the previous catalytic studies. It is likely that complete xylose gasification could be achieved at a lower average fluid residence time in the microreactor, however, CFD simulations of the non reacting flow corresponding to residence times less than one second, seen in Figure 6.10, indicate a substantial drop in the average reaction temperature due to the temperature gradient from heating the reacting fluid to 650°C from 25°C at the entrance of the reactor. Although the fluid temperature at the entrance of the microchannel was set to 25°C in the CFD model simulations, the actual fluid temperature at the channel entrance in the reactor will be higher due to the heating period during the residence time in the reactor header, which make up approximately 3.7% of the total residence time in the microchannel reactor. Additionally, the channel entrance temperature will be affected by the fluid velocity and

position of the channel down the length of the header. Since the reactor is a contiguous block and there is no way to measure the fluid temperature at a specific channel inlet, and a CFD model of the entire reactor block would be computationally expensive and therefore not feasible, a 25°C boundary condition was implemented. Nevertheless, the trend observed from CFD simulations provides insight into the microchannel temperature profile at high flowrates. Given the micron size of the reactor channels, the device is sensitive to coke formation that may plug the reactor, and therefore was not operated at these conditions.

6.6 Conclusion

In conclusion, xylose was continuously gasified to H_2 rich gas by supercritical water in a novel Hastelloy microchannel reactor. A large surface area to volume ratio in the reactor provided high rates of heat transfer and intensified catalytic activity from nickel in the reactor wall which resulted in complete gasification of 4.0 wt% aqueous solution of xylose in a 1.4 second residence time. Major gas products consisted of CO_2 and H_2, and an average H_2 yield of 8.9 moles of H_2 generated per mole of xylose fed was obtained. Results from CFD simulations suggest there is little effect on the reaction temperature due to endothermic xylose gasification reactions, rather the reacting fluid temperature is sensitive to the average fluid residence time due to the temperature gradient from the fluid heating period.

6.7 Acknowledgements

This research was supported by Bend Research, Inc., Bend, Oregon, and by the US Army under the Tactical Energy Systems program administered through the Oregon Nanoscience and Microtechnologies Institute (ONAMI). Computational fluid dynamics modeling software and workstation was provided by ONAMI.

TOC measurements were provided by the Cooperative Chemical Analytical Laboratory established by memorandum of understanding no. PNW-82-187 between the U.S. Forest Service Pacific Northwest Research Station and the Department of Forest Ecosystems and Society, Oregon State University.

6.8 Literature cited

1. Zhang L, Xu C, Champagne P 2010 *Energy Conservation and Management* **51** 969-982
2. Loppinet-Serani A, Aymonier C, and Cansell F 2009 *J Chem Technol Biotechnol* **85** 583-589
3. Demirbas A 2010 *Energy Sources Part A* **32** 1342-1354
4. Matsumura Y, Minowa T, Potic B, Kersten S, Prins W, van Swaaij W, Beld B, Elliott D, Neuenschwander G, Kruse A, and Antal Jr M J 2005 *Biomass and Bioenergy* **29** 269-92
5. Calzavara Y, Joussot-Dubien C, Boissonnet G, and Sarrade S 2005 *Energy Conversion and Management* **46** 615-31
6. Loppinet-Serani A, Aymonier C, and Cansell F 2008 *ChemSusChem* **1** 486-503
7. Navarro R M, Sánchez-Sánchez M C, Alvarez-Galvan M C, del Valle F, and Fierro J L G 2009 *Energy Environ Sci* **2** 35-54
8. Peterson A A, Vogel F, Lachance R P, Fröling M, Antal Jr M J, and Tester J 2008 *Energy Environ Sci* **1** 32-65
9. Kruse A 2008 *Biofuels Bioproducts & Biorefining* **2** 415-37
10. Guo Y, Wang S Z, Xu D H, Gong Y M, Ma H H, Tang X Y 2010 *Renewable and Sustainable Energy Reviews* **14** 334-343
11. Kruse A, Vogel H 2008 *Chem Eng Technol* **31** 1241-1245
12. Savage P E 2009 *Journal of Supercritical Fluids* **47** 407-414
13. Vogel F 2009 *Handbook of Green Chemistry: Green Calalysis* vol 2, ed P T Anastas and R H Crabtree (Germany: Wiley-VCH Verlag GmbH & Co KGaA) pp 281-324
14. Ding Z Y, Frisch M A, Li L, Gloyna E F 1996 *Ind Eng Chem Res* **35** 3257-3279
15. Savage P E 2000 *Catalysis Today* **62** 167-173
16. Byrd A J, Gupta, R B 2010 *Applied Catalysis A: General* **381** 177-182
17. Furusawa T, Sato T, Saito M, Ishiyama Y, Sato M, Itoh N, Suzuki N 2007 *Applied Catalysis A: General* **327** 300-310
18. Osada M, Sato O, Arai K, Shirai M 2006 *Energy & Fuels* **20** 2337-2343
19. Tomita K, Oshima Y 2004 *Ind Eng Chem Res* **43** 7740-7743

20. Yu J, Savage P E 2001 *Applied Catalysis B: Environmental* **31** 123-132

21. Aki S N V K, Ding Z, Abraham M A 1996 *AICHE Journal* **42** 1995-2004

22. Goodwin A K, and Rorrer G L 2009 *Energy and Fuels* **23** 3818-25

23. Goodwin A K, Rorrer G L 2008 *Ind Eng Chem* **47** 4106-14

24. Lu YJ, Guo LJ, Ji C, Zhang X, Hao X, and Yan Q 2006 *International Journal of Hydrogen Energy* **31** 822-31

25. Watanabe M, Aizawa Y, Iida T, Levy C, Aida T M, and Inomata H 2005 *Carbohydrate Research* **340** 1931-39

26. Sinag A, Kruse A, and Rathert J 2004 *Ind Eng Chem Res* **43** 502-8

27. Goodwin A K, Rorrer G L 2010 *Chemical Engineering Journal* accepted

28. Matsumura Y, Yanachi S, Yoshida T 2006 *Ind Eng Chem Res* **45** 1875-1879

29. Lee I, Kim M, Ihm S 2002 *Ind Eng Chem Res* **41** 1182-1188

30. Kabyemela B M, Adschiri T, Malaluan R M, Arai K 1999 *Ind Eng Chem Res* **38** 2888-2895

31. Kabyemela B M, Adschiri T, Malaluan R M, Arai K 1997 *Ind Eng Chem Res* **36** 1552-1558

32. Qi J, Xiuyang L 2007 *Chin J Chem Eng* **15** 666-669.

33. Watanabe M, Aizawa Y, Iida T, Levy C, Aida T M, Inomata H 2005 *Carbohydrate Research* **340** 1931-1939

34. Sasaki M, Hayakawa T, Arai K, Adschiri T 2003 *Hydrothermal reactions and techniques; the proceedings of the seventh international symposium on hydrothermal reactions* **2** 169-176

35. Kersten S R A, Potic B, Prins W, and Van Swaaij W P M 2006 *Ind Eng Chem Res* **45** 4169-77

36. Antal J A J, Allen S G, Schulman D, and Xu X 2000 *Ind Eng Chem Res* **39** 4040-53

37. Yu D, Aihara M, Antal J A J 1993 *Energy and Fuels* **7** 574-577

38. DiLeo G J, Neff M E, Savage P E 2007 *Energy and Fuels* **21** 2340-2345

39. Resende F L P, Savage P E 2010 *Ind Eng Chem Res* **49** 2694-2700

40. Goodwin A K, Rorrer G L 2010 In preparation

41. Goodwin A K, Rorrer G L 2010 In preparation

42. Davis J R 2000 *ASM Specialty Handbook: Nickel, Cobalt and Their Alloys* (ASM International) p 45

43. Resende F, Fraley S, Berger M, and Savage P 2008 *Energy and Fuels* **22** 1328-34

44. Resende, F L P and Savage P E 2010 *Ind Eng Chem* In press

45. Resende F L P, Neff M E, and Savage P E 2007 *Energy and Fuels* **21** 3637-43

46. Lu Y, Guo L, Zhang X, Yan Q 2007 *Chemical Engineering Journal* **131** 233-244

47. Tang H, Kitagawa K 2005 *Chemical Engineering Journal* **106** 261-267

48. Yan Q, Guo L, Lu Y 2006 *Energy Conservation and Management* **47** 1515-1528

49. Matsumura Y, Harada M, Nagata K, Kikuchi Y 2006 *Chem Eng Comm* **193** 649-659

50. Cremmers C, Pelz A, Stimming U, Haas-Santo K, Goerke O, Pfeifer P Schubert K 2007 *Fuel Cells* **7** 91-98

51. Stefanidis G D, Vlachos D G, Kaisare N S, Kaisare N S, Maestri M 2009 *AIChE Journal* **55** 180-191

52. Mettler M S, Stefanidis G D, Vlachos D G 2010 *Ind Eng Chem Res* In Press

53. Saber M, Commenge J M, Falk L 2010 *Chemical Engineering Science* **65** 372-379

54. Zhang Q, Tang R, Yin K, Luo X, Zhang L 2009 *Corrosion Science* **51** 2090-2097

55. Boukis N, Habicht W, Franz G, Dinjus E 2003 *Materials and Corrosion* **54** 326-330

56. Yoshida T, Matsumura, Y 2001 *Ind Eng Chem Res* **40** 5469-5474

57. Guo L J, Lu Y J, Zhang X M, Ji C M, Guan Y, Pei A X 2007 *Catalysis Today* **129** 275-286

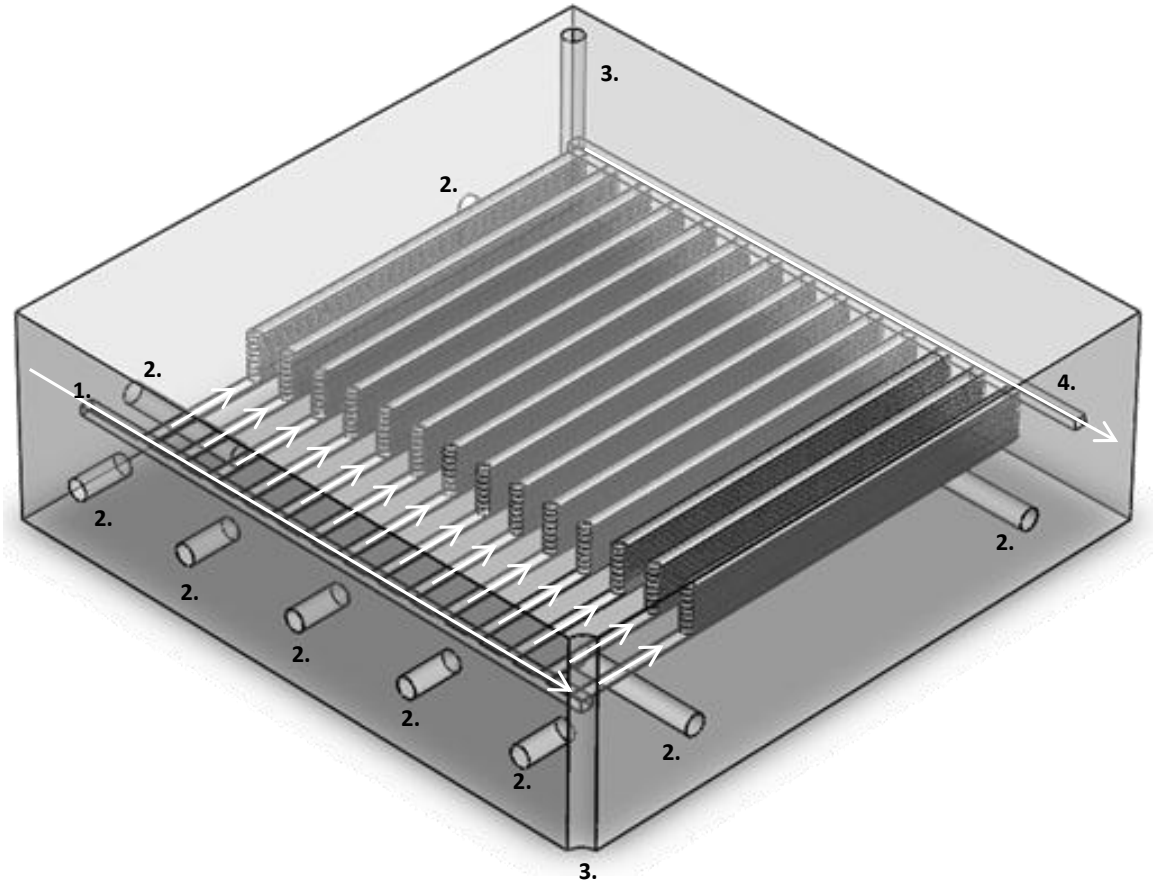

Figure 6.1. Transparent view of the Hastelloy C-276 Parallel channel microreactor. The arrows indicate the direction of flow. The microchannel reactor components are 1) inlet distribution header 2) thermowells 3) alignment pin holes used during fabrication 4) outlet header

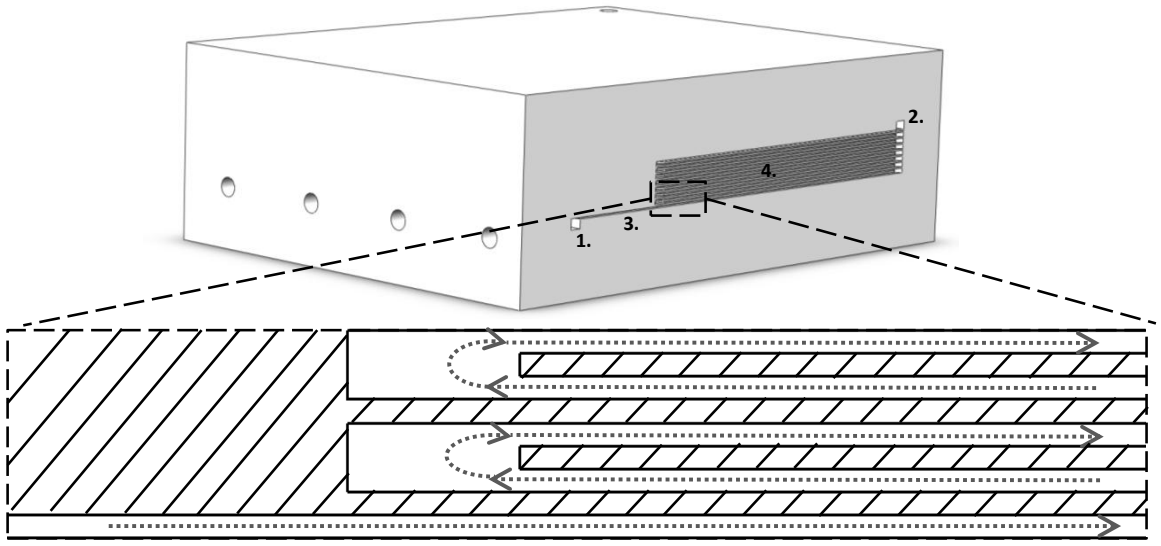

Figure 6.2. Cross section view of a single channel in the Hastelloy C-276 Parallel channel microreactor. The arrows indicate the direction of flow. The microchannel reactor components are 1) inlet header 2) outlet header 3) integrated pre-heater 4) microchannel segment that serpentines 15 times vertically.

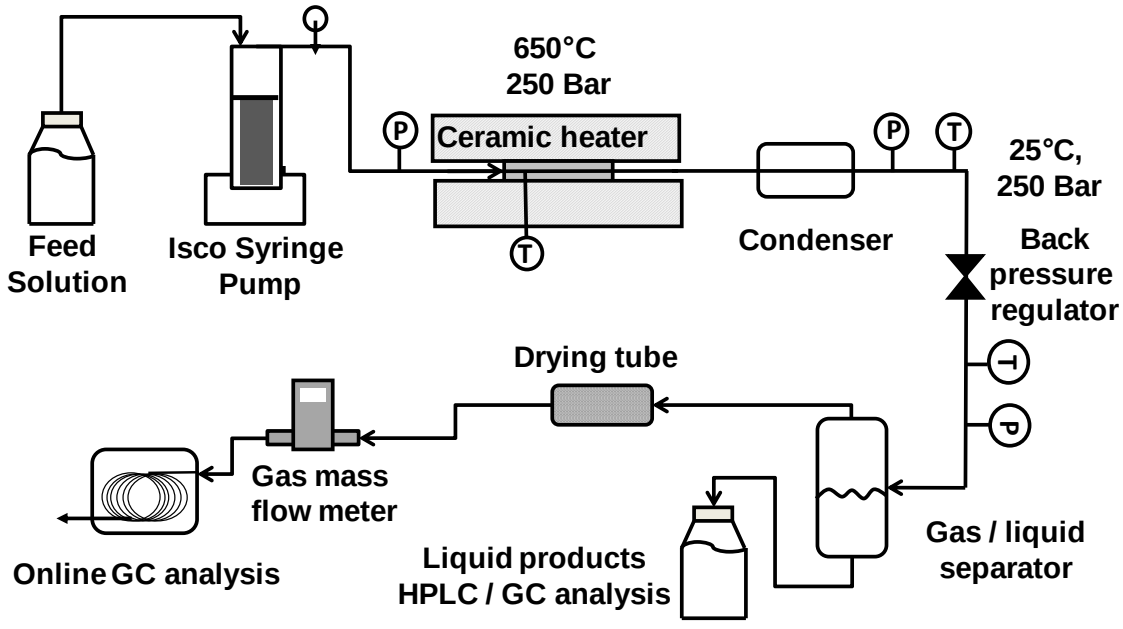

Figure 6.3. Microchannel reactor test loop.

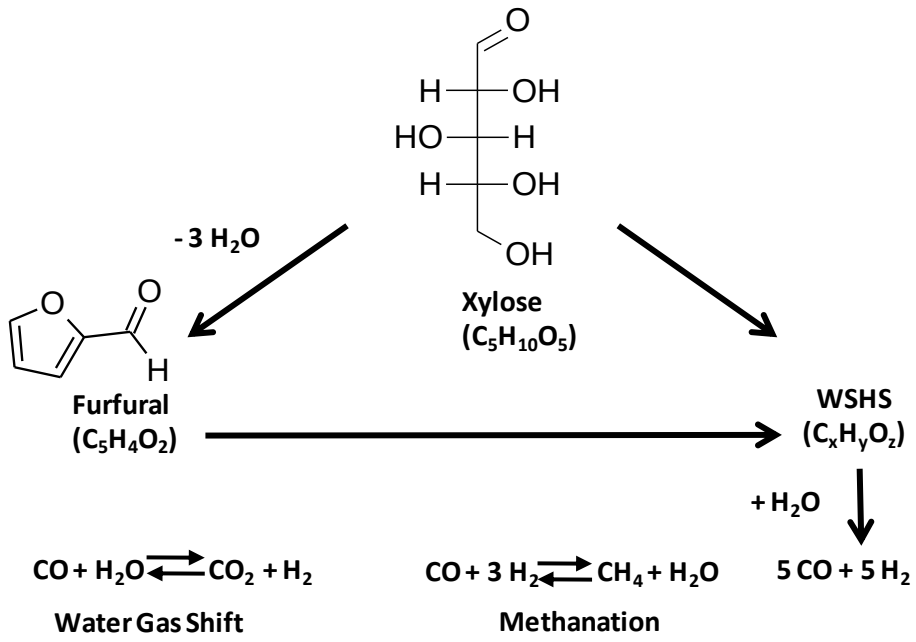

Figure 6.4. Reaction mechanism for xylose gasification by supercritical water.

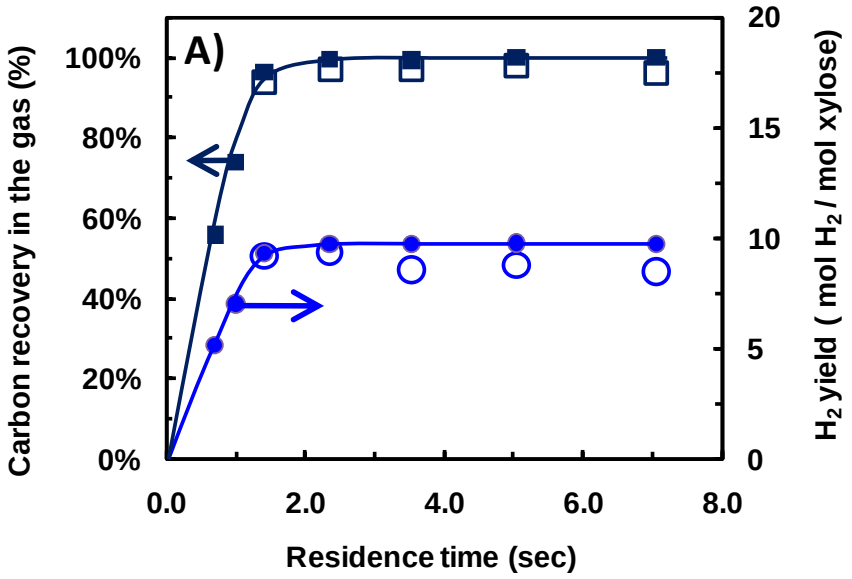

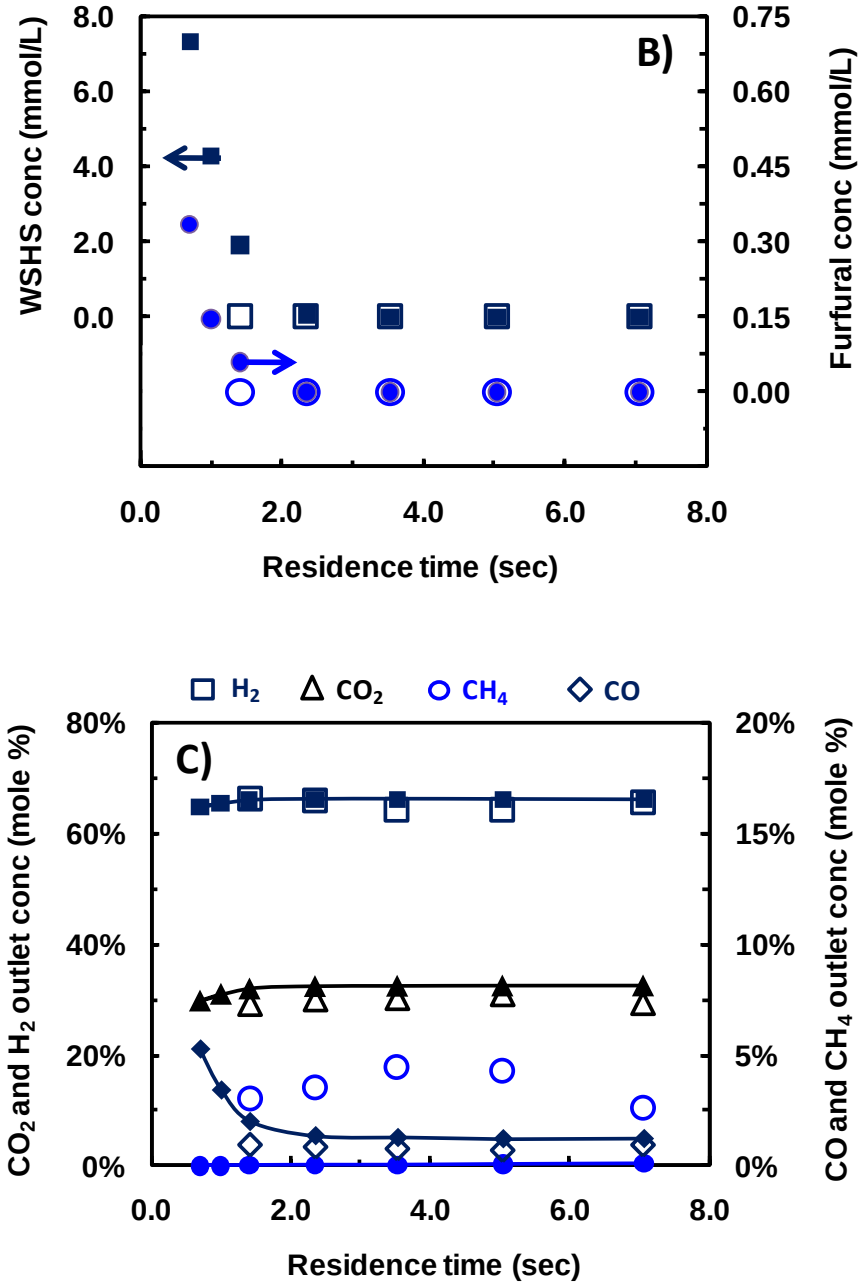

Figure 6.5. Gas and liquid products composition and yield versus residence time for xylose gasification at 650°C and 250 bar in the microchannel reactor; A) Carbon recovery in gas and H_2 yield; B) liquid intermediate concentration; C) gas composition. The filled in markers are predictions from CFD simulations and the outline markers are experimental results.

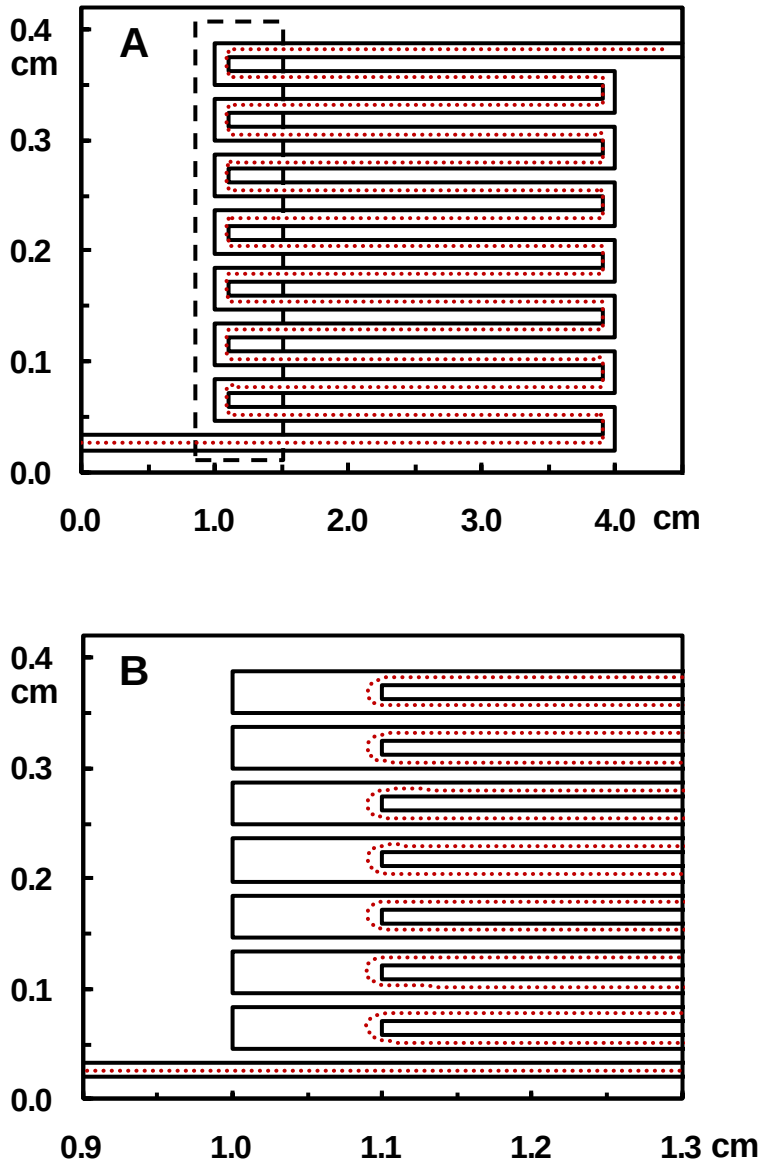

Figure 6.6. Streamline plot through the microchannel reactor for a 1.4 second residence time and a reactor temperature of 650°C and pressure of 250 bar. The streamline represents the path taken by a massless particle released from the center of the reactor inlet. Plots of the process variables for this residence time are plotted on this streamline. A) entire channel, not to scale; B) Dashed rectangular section in Figure A; drawn to scale.

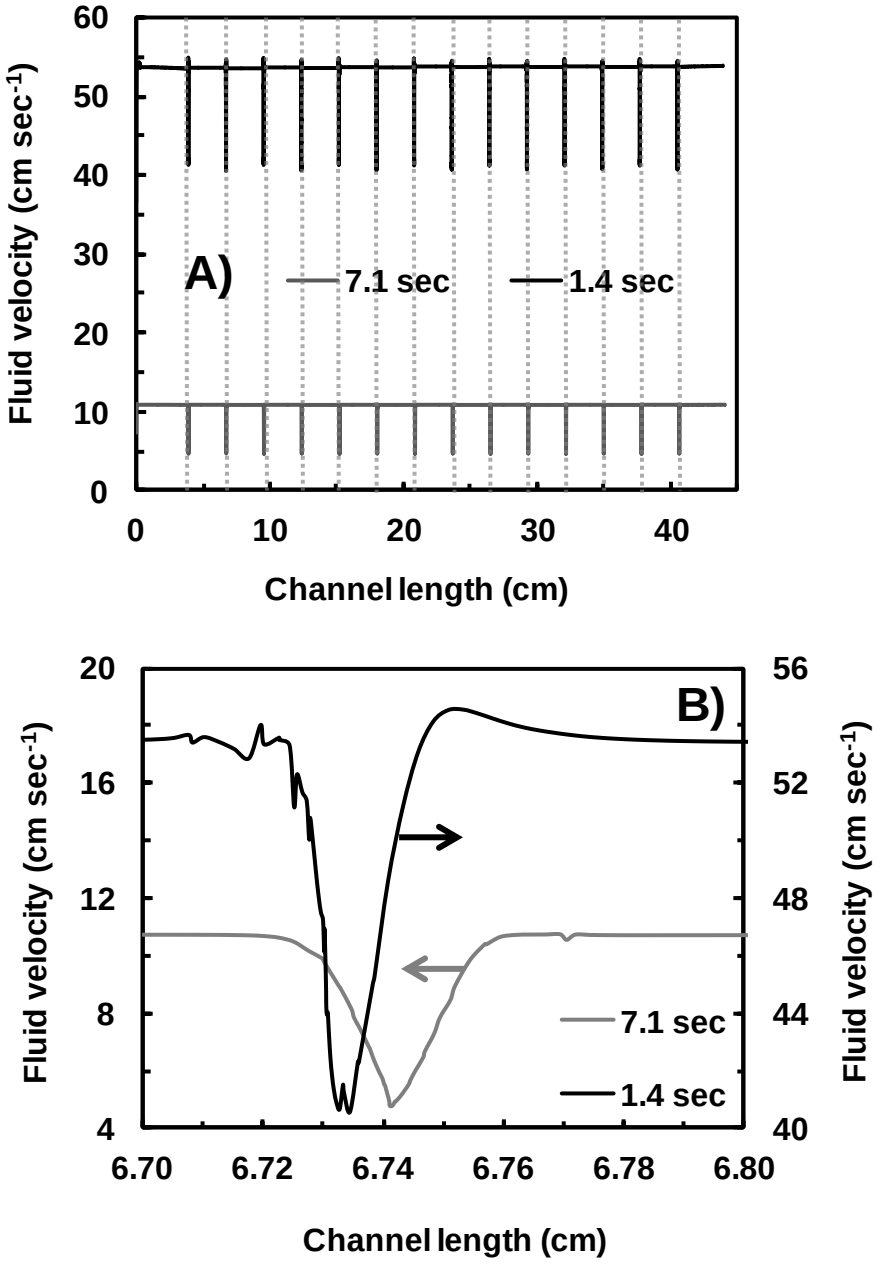
A)
7.1 sec
1.4 sec
Fluid velocity (cm sec-1)
Channel length (cm)
0
10
20
30
40
50
60
B)
7.1 sec
1.4 sec
Fluid velocity (cm sec-1)
Fluid velocity (cm sec-1)
Channel length (cm)
4
8
12
16
20
40
44
48
52
56
6.70
6.72
6.74
6.76
6.78
6.80

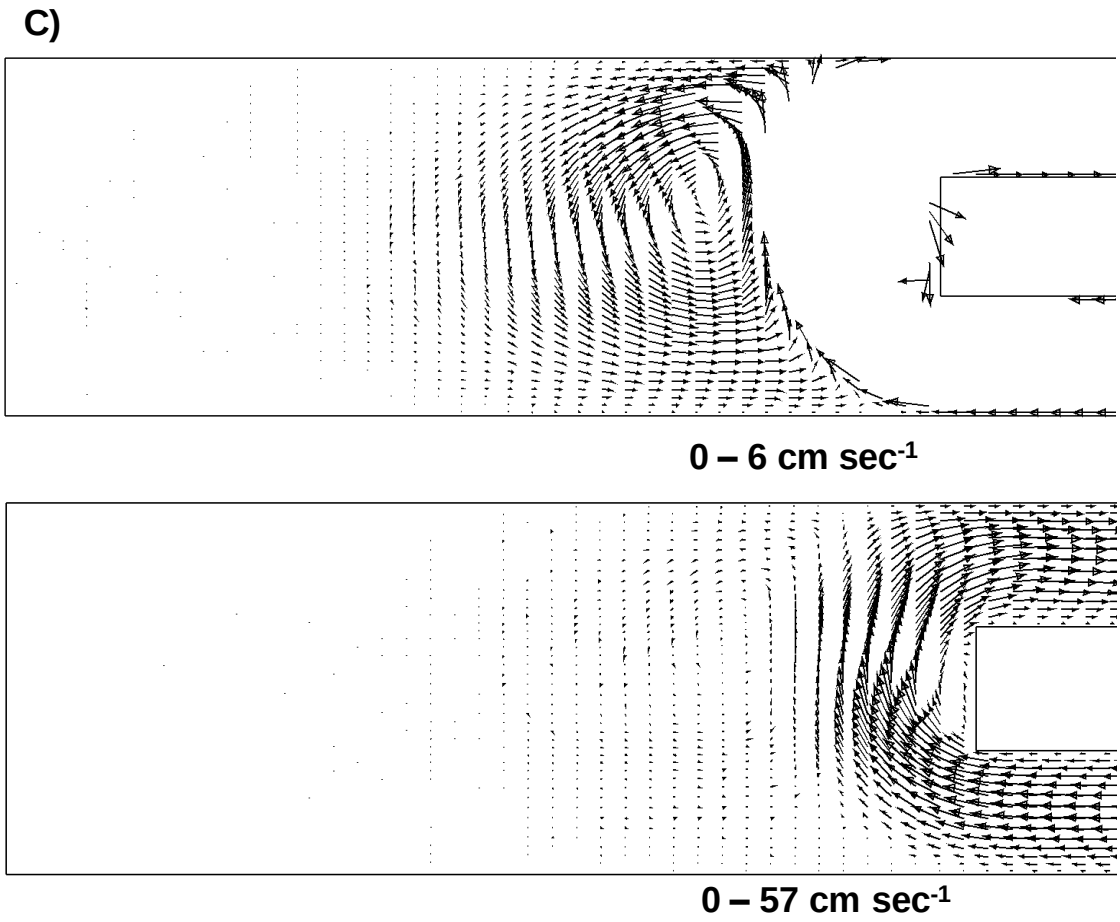

Figure 6.7. Streamline velocity profile through the reactor at for xylose gasification at 650°C and 250 bar. A) is the velocity through the entire microchannel, B) is the velocity profile around the 180 degree turn between serpentine layers, and C) is a velocity vector plot for the region in between serpentine layers for 1.4 second residence time. The velocity vector plot is represented at two different velocity scales for the same residence time.

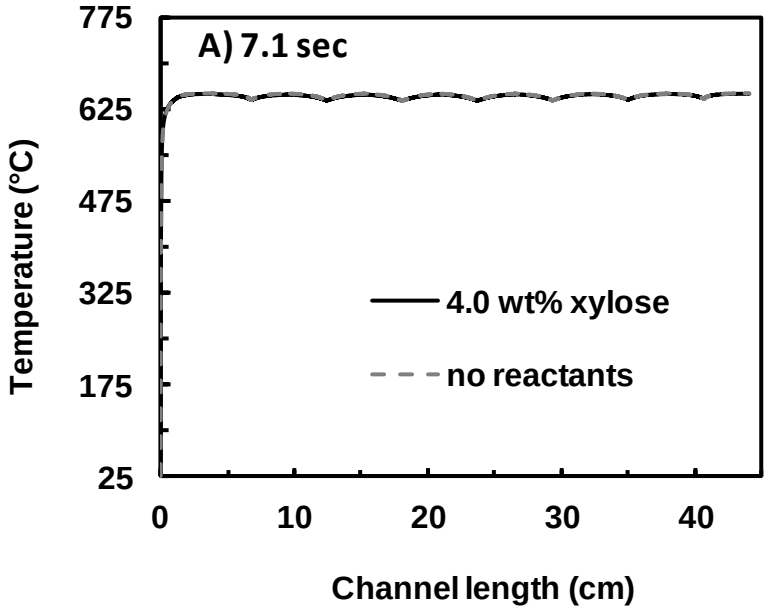
A) 7.1 sec
775
625
475
325
175
25
Temperature (°C)
4.0 wt% xylose
no reactants
0
10
20
30
40
Channel length (cm)

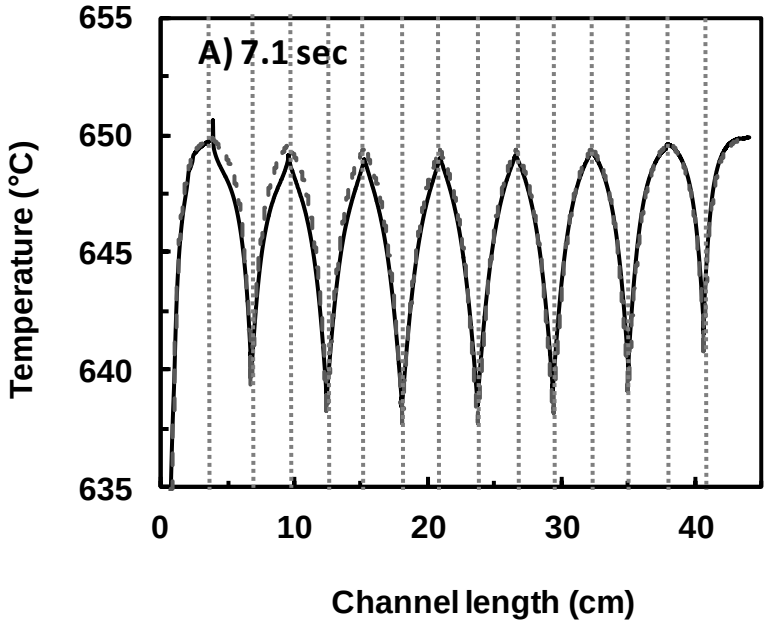
A) 7.1 sec
655
650
645
640
635
Temperature (°C)
0
10
20
30
40
Channel length (cm)

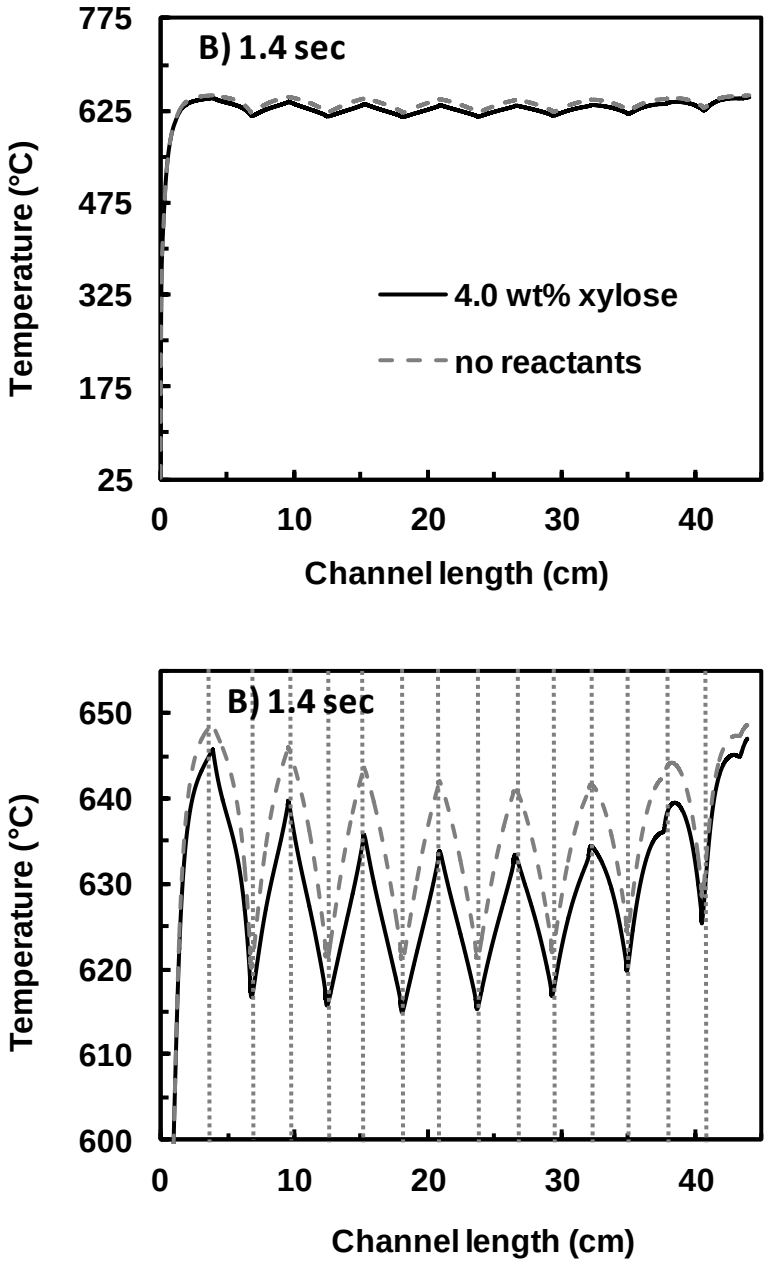

Figure 6.8. Streamline temperature profile through the reactor at a reactor temperature of 650°C and pressure of 250 bar. A) 7.1 second residence time; B) 1.4 second residence time. The temperature prediction for xylose gasification was based on a 4.0 wt% feed solution. The area between vertical dotted lines corresponds to the 15 serpentine channel passes in a single microchannel.

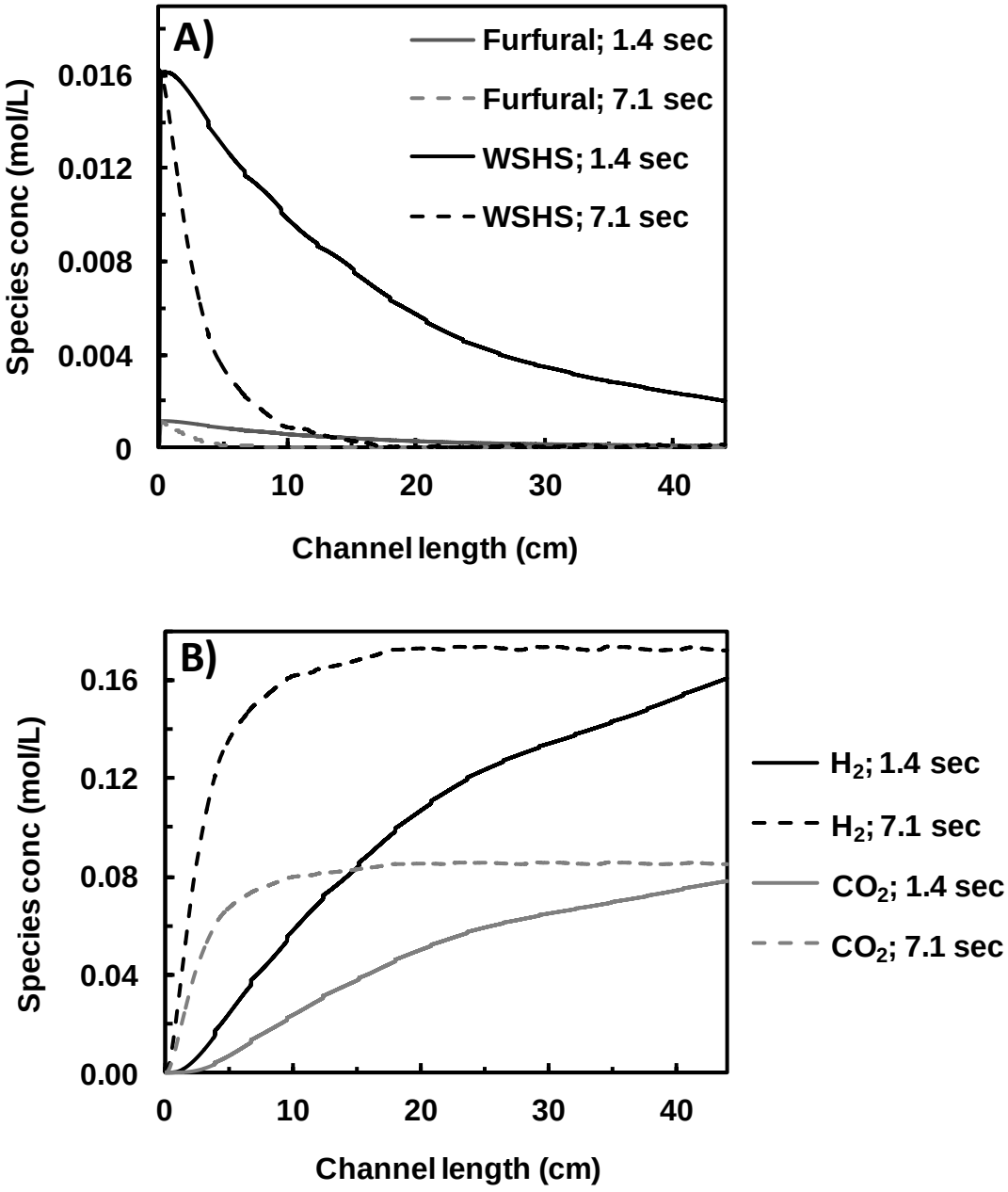

Figure 6.9. Streamline concentrations for A) liquid decomposition products and B) gas products from CFD simulations for gasification of 4.0 wt% xylose at 650°C and 250.

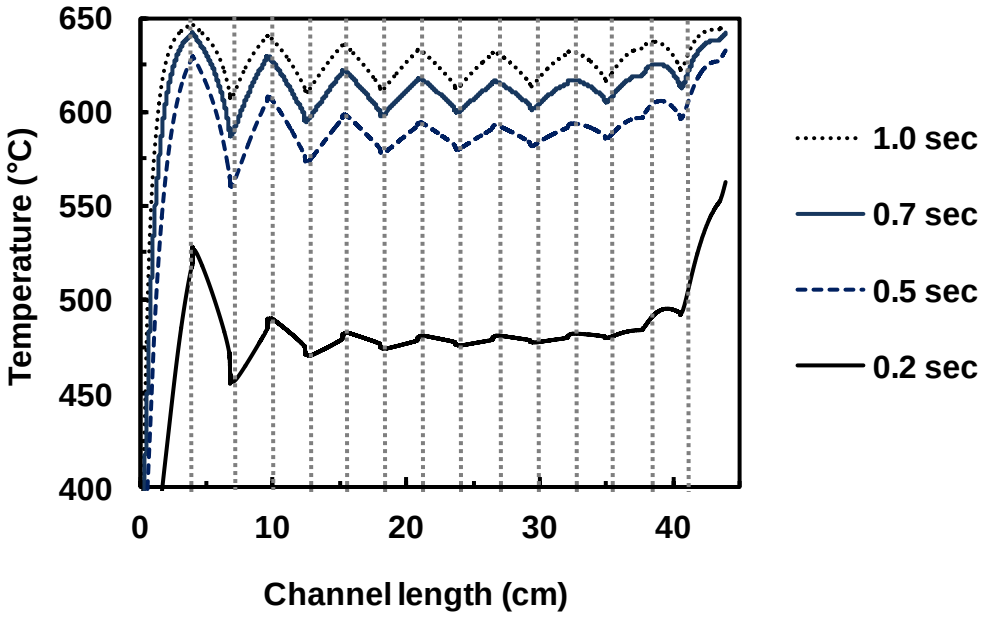

Figure 6.10. Comparison of cold flow streamline temperatures through the microchannel at a reactor temperature of 650°C and pressure of 250 bar at sub 1.0 second residence times.

Table 6.1. Parallel channel Hastelloy microreactor dimensions.

Overall dimensions	
reactor width	5.0 cm
reactor length	5.0 cm
reactor height	1.7 cm
reactor volume	0.9 cm3
Channel dimensions	
microchannel width	1000 µm
microchannel height	127 µm
microchannel hydraulic diameter	225 µm
total length of each channel	46.2 cm
number of microchannels	14
number serpentine layers	15
single microchannel volume	0.06
Header Dimensions	
header channel length	4.5 cm
header channel width	0.100 cm
header channel height	0.075 cm
total header volume	0.034 cm3

Table 6.2. Thermo-physical properties for Hastelloy C-276 and working fluid used for CFD simulations.

	pressure (bar)	temperature range (°C)	density ($g\ cm^{-3}$)	thermal conductivity ($w\ m^{-1}\ K^{-1}$)	heat capacity ($J\ kg^{-1}\ K^{-1}$)	viscosity (cP)
reacting fluid	250	25 - 650	0.065	0.11 - 0.62	2819	0.036
Hastelloy C-276	1.0	25 - 650	8.89	9.4 - 20.9	427	

Table 6.3. Reactor condition considered by this study.

	experiments (xylose gasification)	model (xylose gasification)	model (no reactions)
Temperature (°C)	650	650	650
Pressure (bar)	250	250	250
Feed concentration (wt%)	4.0	4.0	0.0
Fluid residence time (sec)	1.4 - 7.1	0.7 - 7.1	0.2 - 1.0

Table 6.4. Gas composition, carbon recovery in the gas, and H_2 yield for gasification of xylose and xylan at 650°C and 250 bar.

	CGE (%)	H_2 (mole %)	CO_2 (mole %)	CH_4 (mole %)	CO (mole %)	C_2H_6 (mole %)
Xylose	96 ± 1.6	65.0 ± 1.1	30.0 ± 0.7	3.9 ± 0.6	0.8 ± 0.1	0.3 ±0.1
Xylose (model)	99 ± 1.6	66.1 ± 0.1	32.4 ± 0.2	0.1 ± 0.0	1.4 ± 0.3	

Chapter 7: Comprehensive Conclusion

In this study, the continuous gasification of solubilized biomass constituents by supercritical water was substantially intensified using microreactor technology. The large surface area to volume ratio characteristic of micron sized passages provided high rates of heat transfer to the reacting fluid unattainable by traditional continuous flow tube reactors. The high heat transfer rate was used to sustain the reaction temperature during endothermic supercritical water biomass gasification reactions, and resulted in complete biomass gasification for very short residence times. Furthermore, enhanced heat transfer resulted in a rapid fluid heating period which virtually eliminated the formation of coke and reduced the formation of refractory liquid intermediates typically produced during continuous biomass gasification. Two continuous flow microreactor configurations were used in this study.

The first reactor configuration was a microtubular reactor used to gasify xylose, phenol, and xylose / phenol mixtures under continuous flow conditions at short residence times. Xylose and phenol were used as biomass constituent model compounds for hemicellulose and lignin respectively. Complete xylose gasification based on carbon was achieved in less than 1.0 second residence time at 650ºC and 250 bar in a 762 µm diameter Hastelloy microtube reactor. Complete conversion of phenol was achieved at 750°C, 250 bar and a 7.4 second residence time in a 508 µm diameter stainless steel reactor. It was concluded that when phenol and xylose were co-gasified the rapid gasification of xylose to H_2 and CO_2 increased the gasification rate of phenol by hydrogenation of the phenol.

A first order rate constant for phenol conversion in supercritical water at 700°C – 750°C and 250 bar was estimated for experiments in the stainless steel microtube reactor. A detailed reaction mechanism and two kinetic models were developed for xylose gasification in the Hastelloy microtube reactor. The first model, the decomposition kinetic model, describes how xylose is broken down to liquid intermediates in supercritical water, and is relevant to analysis aimed at optimization of low temperature supercritical water gasification of hemicellulose, or for production of commodity

chemicals from xylose. The second model, the gasification kinetic model, uses a simplified reaction mechanism to model gasification rates and gas composition ideal for optimizing supercritical water gasification of hemicellulose at conditions where gasification is dominant.

The second microreactor configuration studied was a parallel channel Hastelloy microreactor. The reactor consisted of 14 serpentine parallel rectangular microchannels (1000μm by 127 μm) integrated into a single contiguous reactor block by diffusion bonding a series of shims between two header plates. The pressure drop through the reactor was used to validate the reactors internal geometry and a residence time distribution study was used to characterize the flow in the reactor. By comparing experimental residence time distribution of the entire microchannel reactor to residence time distributions from computational fluid dynamics model simulations of a single microchannel configuration it was concluded that the flow profile through the reactor was approaching plug flow and there was a uniform flow distribution between the 14 parallel microchannels. Furthermore, the effect of Reynolds number and diffusion coefficient on the residence time distribution in the microchannel reactor was established.

A 4.0 wt% aqueous solution of xylose was continuously and completely gasified to H_2 and CO_2 in the parallel channel Hastelloy microreactor within a 1.4 second residence time. Rapid heat transfer and enhanced catalytic activity from high nickel content in the microreactor wall increased the rate of biomass gasification and promoted the water gas shift and methanation reactions which resulted in a H_2 yield of 8.9 moles of H_2 produced per mole of xylose reacted. Results from CFD simulations of xylose gasification in the parallel channel microreactor suggest there is little effect on the reaction temperature from endothermic biomass reforming reactions, rather the reacting fluid temperature is sensitive to the average fluid residence time below 1.0 second due to a temperature gradient from the fluid heating period.

A potential area of future work for continued research on biomass gasification by supercritical water in a microchannel reactor should include an investigation on the effect of biomass feed concentration on gasification yield and H_2 selectivity. Although

increasing the feed concentration theoretically produces more gas per mass of feed and therefore improves the overall energy efficiency of the process, previous studies in continuous flow reactors that used aqueous feed solutions containing greater than 10 wt% biomass observed an increase in coke formation and poor gasification efficiency. This result is likely due to insufficient heat transfer to the reacting fluid. As the feed concentration is increased higher rates of heat transfer are necessary to sustain the reaction temperature due to greater heat loss from endothermic biomass reforming reactions. With regard to cellulose and hemicellulose, without sufficient heat transfer, a greater amount of furfural and other recalcitrant intermediates are produced. Not only are some of these intermediates known coke precursors, they are also difficult to gasify and thus require a longer reaction time for complete gasification. It is likely that high rates of heat transfer characteristic of microchannels will be able to sustain the reaction temperature for concentrated feed solutions and establish an intrinsic relationship between feed concentration and gasification efficiency. Initial high feed concentration studies in the microtube reactor have been completed for glucose and are discussed in Appendix 2.

Another potential area of future work for continuation of this research is a next generation microchannel reactor. The supercritical water microchannel reactor should include two key upgrades from the current microchannel reactor described in Chapter 4. The first upgrade is an integrated microchannel combustor that would provide heat for biomass reforming reactions by combusting a portion of the product gas. This concept makes the process self sustaining and has been previously demonstrated for steam reforming of methanol in microchannel reactors. Combustion channels could be integrated into the existing microchannel reactor design by modifying the interlayer shim design or by adding a new shim design intermittent within the repeating structure of the existing reactor shim stack design. A fuel mixture of H_2 and CH_4 from the product gas can easily be separated from water and CO_2 at the reaction pressure and ambient temperature in a high pressure gas liquid separator. The second modification to the existing microchannel reactor design would be to modify the transition area between channel passes. Results from CFD model simulations, detailed in Chapters 5 and 6,

predict the formation of stationary vortices and stagnant regions in the transition area between channel passes. Decreasing this area by modifying the passage on the interlayer shims will help to minimize these hydrodynamic effects and result in a more symmetrical and narrow residence time distribution.

APPENDIX

Appendix 1: Hastelloy C-276 Supercritical Water Gasification Microchannel Reactor Fabrication: Diffusion Bonding Study for Hastelloy C-276

A1.1 Abstract

Microchannel reactor technology is an attractive platform to intensify supercritical water gasification biomass. As a consequence of the harsh reaction environment a microchannel reactor designed for supercritical water gasification must be able to continuously operate at temperatures greater than 600°C and a pressure of 250 bar. One way to fabricate such a reactor is by diffusion bonding a series of shims between two header plates. The result is a contagious reactor block with a complex network of internal microchannels. Additionally, Fabrication of the reactor from a high content nickel alloy, such as Hastelloy C-276, substantially intensifies biomass gasification reactions and the water gas shift reaction due to its high catalytic activity and the large surface area to volume ratios characteristic of microchannel reactors. An investigation to determine optimal diffusion bonding conditions for Hastelloy C-276 was completed. A series of sample shim stacks were diffusion bonded at several conditions above and below the 1% 10 hour Hastelloy C-276 creep curve. Metallurgy was used to investigate the bond lines for voids, and the macro features were investigated for deformation. Optimal bonding conditions are recommended.

A1.2 Introduction

Microreactors provide numerous advantages compared to traditional flow through reactors. Enhanced convective heat and mass transfer combined with short transport distances increase product yields for chemical reactions due to enhanced reaction kinetics. Additionally, microreactors can facilitate reaction pathways often difficult to control in traditional flow through reactors, including highly endothermic and exothermic reactions. More precise temperature control may increase product selectivity and offers an alternative approach to batch processing. At its infancy, chemical processing in microreactors typically was limited to sub millimeter inner diameter tubes, and was widely used to determine intrinsic kinetics for heterogeneous catalytic systems. However, thrusts towards the miniaturization of electronics led to innovative manufacturing techniques that allowed for novel three dimensional micron sized complex geometries to be realized and applied to chemical engineering operations for process intensification. Current state of the art manufacturing techniques and microchannel devices have been reviewed [1-3]. Typical, microchannel devices are designed with a split and recombine configuration to achieve a desired reactor volume. The feed stream is split into a series of identical parallel channels. The reactor effluent is then recombined at the reactor outlet header. Since the physics is theoretically the same in each channel, the number of parallel channels is used to scale the process. It is generally accepted that compared to traditional scale up, numbering up channels in a microchannel device is more straight forward.

There are many fabrication techniques used for split and recombine microchannel reactors, however, materials and thus fabrication techniques are limited for the fabrication of high temperature and high pressure reactors. Conditions for supercritical water gasification of biomass, where gasification is dominate, are temperatures greater than 600°C and a pressure of 250 bar. In this regard the reactor material must be able to withstand stresses imparted from the reacting fluid over the lifetime of the reactor. Nickel alloys, such as Hastelloy C-276, not only offer excellent heat resistance for high temperature chemical processing, they have better corrosion resistance compared to stainless steel and other metals suitable for this application. In addition the high nickel

content in the reactor wall catalyzes supercritical water decomposition reactions as well as the water gas shift reaction [4-5]. The fabrication techniques used by Goodwin and Rorrer [10] to construct a stainless steel supercritical water microchannel reactor offer a simple and straight forward approach for reactor design, however there is need for a study that optimizes diffusion bonding conditions for Hastelloy C-276.

Diffusion bonding is the process of solid state welding two faying surfaces by atomic inter-diffusion across the interface of the materials at elevated temperature and pressure. Specifically, when two surfaces are in close enough proximity, there will be inter-diffusion of atoms across the interface of the two surfaces. Several mechanisms have been proposed for solid state bond formation [6]. The bonding temperature is usually 50% to 80% of the absolute melting point (T_m) of the material, and the bonding pressure must be high enough to create localized deformation at the interface, but low enough to prevent deformation of the macro features [7]. The processes usually take place under an inert atmosphere or ultra high vacuum as a result of the high reactivity of oxygen at bonding temperatures. For typical high temperature and low pressure or high pressure and low to moderate temperature chemical processes in a diffusion bonded microreactor reactor an incomplete or partial diffusion bond will typically not significantly affect the performance of the reactor, assuming the reactor perimeter is hermetically sealed. However, for a process like supercritical water gasification where the stresses imparted on the reactor from the process conditions are close to the yield strength of the material, a complete bond as close to the strength of the original material is necessary.

In this study, a series of temperatures and pressures were investigated for diffusion bonding Hastelloy-C276 shim stacks. Specifically, Hastelloy C-276 coupons were bonded to a stack of 76 µm thick Hastelloy C-276 shims, that when bonded, created two parallel rows of 28 microchannels. The bonded shim stack was investigated for voids in bond lines as well as deformation of macro features.

A1.3 Materials and Methods

Hastelloy C-276 bar stock (127 cm by 7.6 cm by 0.64 cm) was purchased from High Temp Metals, Inc. Sylmar, Ca., and was cut into three 5 cm by 5 cm by 0.64 cm pieces. Each coupon was double disc grinded until 2.5 μm parallel and the bonding surface lapped to a surface roughness of no more than 200 nm R_a by Petersen Precision Engineering, LLC, Redwood City, Ca.. The bonding surfaces of the Hastelloy coupons were polished to a surface roughness less than 100 nm R_a on a Leco 805800 polisher with Buetler Metadi 1.0 μm diamond polish. Surface roughness measurements were performed on a Dektak^3 Vibraplane Model # 1281349 surface analyzer, and surface parallelism measurements were performed on a Brown and Sharpe manual coordinate measurement machine.

76 μm Hastelloy C-276 shim stock was purchased from ESPI Metals, Ashland Or. All of the shim stock was laser cut by Great Lakes Engineering, Maple Grove, Minnesota. Typical tolerance for their laser cutting process was ± 12.7 μm. The shims were fabricated into channel shims and interlayer shims, and are presented in Figure A1.1. Channel shims were 5 cm by 5 cm and had 28 parallel channels 76 μm by 500 μm by 4 cm through cut into each shim. Interlayer shims were 5 cm by 5 cm and had a series of 28 500 μm diameter holes through cut at either end. The interlayer shims served as the top and bottom plates for the channel shims, and the holes in the interlayer shim served as an interconnect between channel passes. After the shims were laser cut, they were mechanically de-burred by hand with 600 grit sand paper. The surfaces of the shims were not machined further due to a high level of compliance resulting from the thickness of the shim.

The shims and coupons were cleaned by the following procedure: sonication in 1.0 weight percent Liquinox for 15 minutes, followed by sonication in deionized distilled water for 15 minutes, followed by sonication for 15 minutes in acetone. The parts were then etched with a solution of 5% by volume hydrofluoric acid and 20% by volume nitric acid for 2.0 minutes, followed by sonication in deionized distilled water for 15 minutes,

rinsed with acetone, and dried with nitrogen at 50°C. After cleaning, the shims and coupons were stored in a vacuum desiccator until bonded. Although the reformation of surface oxides is very rapid for superalloys such as Hastelloy [8], the presence of surface oxides does not inhibit bonding, rather reduces the bonding kinetics [9]. Furthermore nickel oxides typically present on the surface of Hastelloy C-276 readily dissolve into the bulk materials at bonding conditions [6].

After the shims were cleaned, they were stacked together in preparation for bonding. A representative shim stack is presented in Figure A1.1. Each shim stack contained one coupon, two interlayer shims, and two channel shims. The coupon served as a model for the header of the device. The final bonded block included 2 channel passes and a header plate. The shims were placed in between two graphite blocks, and aligned by three external stainless steel alignment pins that created an "L" shape on the inside edge of the graphite fixture. Although the use of an alignment pin inside the structure being bonded is recommended, this study was focused primarily on bond line formation and did not investigate alignment precision.

A Thermal Systems diffusion hot press was used for diffusion bonding. A small amount of pressure, less than 1.0 MPa, was applied to the graphite mold once placed in the diffusion hotpress. After the pressure inside the diffusion hotpress was below 10^{-4} Torr, the thermal cycle was started. The temperature was ramped at 5.0°C min^{-1} until the set point temperature was reached. At this point the desired pressure was applied to the shim stack for a two hour dwell time. The shim stack was cooled at a rate of 2.0°C min^{-1}.

Metallurgy was performed by cutting a representative cross section of the bonded shim stack with a Buehler isomet 11-180 diamond saw. A representative schematic showing the location of the cut cross section and the location of the investigated bond line is presented in Figure A1.2. The inner surface of the cross section was wet sanded on a Leco VP-50 grinder for 15 minutes per sand paper grit at 400 rpm. The sand paper grit used in chronological order was 240 followed by 400 followed by 600. Finally, the

surface of the piece was polished on a Leco 805800 polisher with Buetler Metadi 1.0 μm diamond polish at 500 rpm. The bond line was investigated by a FEI Quanta 600 FEG scanning electron microscope.

A1.4 Results and Discussion

Sample shim stacks were bonded at several conditions to determine optimal diffusion bonding conditions for Hastelloy C-276. Temperature was the main process variable investigated, however, pressure was also varied slightly to accommodate a higher temperature and stay below the 10 hour 1.0% creep curve for Hastelloy C-276. A plot showing the 1.0%, 2.0%, and 5.0% 10 hour creep curves for Hastelloy C-276 as well as bonding conditions for this study are presented in Figure A1.3. Bonding conditions were kept below the 1.0% creep curve for Hastelloy C-276 due to deformation of macro features in previously bonded microchannel reactors bonded above the 1.0% creep curve. Cross sectional images of microchannel reactors bonded at conditions above the 1.0% creep curve are presented in Figure A1.5. Only slight deformation of the macro features can be observed for the reactor bonded at 1050°C and 18.2 MPa, however, the microchannel reactor bonded at 1050°C and 25 MPa shows significant channel deformation that ultimately led to catastrophic failure of the device. Even small channel deformation may decrease channel volume and influence flow distribution in parallel processing microchannel reactors. It is necessary to determine bonding conditions that minimize deformation of the macro features and promote complete bonding.

An ideal bond between two faying surfaces will have no evidence of a bond line and contain no void areas. Many hypothesis exist for a diffusion bonding mechanism, however, it is generally accepted that diffusion bonding proceeds by the following steps, assuming the surfaces are in close enough contact; the oxide layer, or any other surface film is reacted or diffused into the bulk material, plastic deformation of the surfaces brings individual atoms on each surface close enough to interact; the atoms diffuse into empty space that essentially makes up the bond line; followed by recrystallization of the

atoms [6]. Assuming no voids in the bond line, the bonded material is as strong as the bulk material of the unbounded piece [9].

SEM images of a cross section of the bonded shim stacks at three bonding conditions are presented in Figure A1.4. The SEMs are focused on bond lines near the channels between the Hastelloy coupon and the first channel shim. Generally, this area had the greatest concentration of voids in the bonding interface compared to bond lines between shims. A reason for this is the edges of the channel shim are de-burred mechanically, possibly leading to uneven parallelism around the perimeter of the channels. It is necessary to try and minimize any voids caused by de-burring as they will affect the reactor channel volume and thus the flow distribution in the parallel channels. Never the less, shims bonded at 900°C and 15 MPa, Figure A1.4A, had significant voids in the bond lines at all SEM resolutions. At a magnification of 16000x, one can conclude that the shim coupon interface is only partially bonded. If the temperature or pressure of the bonding conditions does not cause plastic deformation at the surface of the interface, bonds will only form at the individual asperities. The resulting bond will be weak compared to the bulk material, and failure at the bond is likely. If the local pressure at the asperities is greater than the yield strength, the surface will plastically deform, crush the asperities, and maximize the amount of surface area brought together within atomic distances. At bonding condition of 1000°C and 15 MPa, Figure A1.4 B, bonding was vastly improved compared to previous conditions; however there were still significant voids present in the bond lines. At 1000x magnification there appears to be very little if any bond line at the interface, however at 16000x significant voids are observed. Unlike previous shim stack bonded at 950°C and 15 MPa, the voids were not continuous throughout the bond line. In order to increase bonding completeness the bonding temperature was increased to 1050°C. However, due to constraints from the 10 hour 1.0% Hastelloy C-276 creep curve, the pressure was lowered to 10 MPa. The resulting bond formation can be observed in Figure A1.4C. There is no observable bond line in the SEMs taken at 1000x and 2000x. When magnified to 16000x, a few very small voids on the order of nanometers are observed, however, the majority of the bond line is invisible, indicating a near homogeneous bond was formed.

A1.5 Conclusion

This study determined optimal diffusion bonding conditions for a Hastelloy C-276 shim stack. Temperature and pressure were varied at several conditions below the 1.0% 10 hour creep curve for Hastelloy C-276. A bonding temperature of 1050°C and bonding pressure of 10 MPa was found to be optimal for bond formation with no macro feature deformation. Previous microreactors bonded at 1050°C and pressures greater than 10 MPa suffered from severe microchannel deformation, and sample shim stack bonded at temperatures lower than 1050°C showed significant voids in the bond lines.

A1.6 Literature Cited

1. Holladay J, Wang Y, Jones E 2004 *Chem Rev* **104** 4767-4790
2. Jensen K, F 2001 *Chem Eng Sci* **56** 293-303
3. Wang Y, Holladay J 2005 *Microreactor Technology and Process Intensification* Oxford University Press
4. Antal J A J, Allen S G, Schulman D, Xu X 2000 *Ind. Eng Chem Res* **39** 4040-4053
5. Kersten S R A, Potic B, Prins W, Van Swaaij W P M 2006 *Ind Eng Chem Res* **45** 4169-4177
6. Kazakov N F 1985 *Diffusion Bonding of Materials* Pergamon Press
7. Shirzadi A A, Assadi H, Wallach E R 2001 *Surface and Interface Analysis* **31** 609-618
8. Shirzadi A A, Wallach E R 2004 *Science and Technology of Welding and Joining* **9** 37-40
9. Cox M J, Kim M J, Carpenter R W 2002 *Metallurgical and Materials Transactions A* 33A 437-442
10. Goodwin A K, Rorrer G L 2008 *Ind Eng Chem* **47** 4106-14

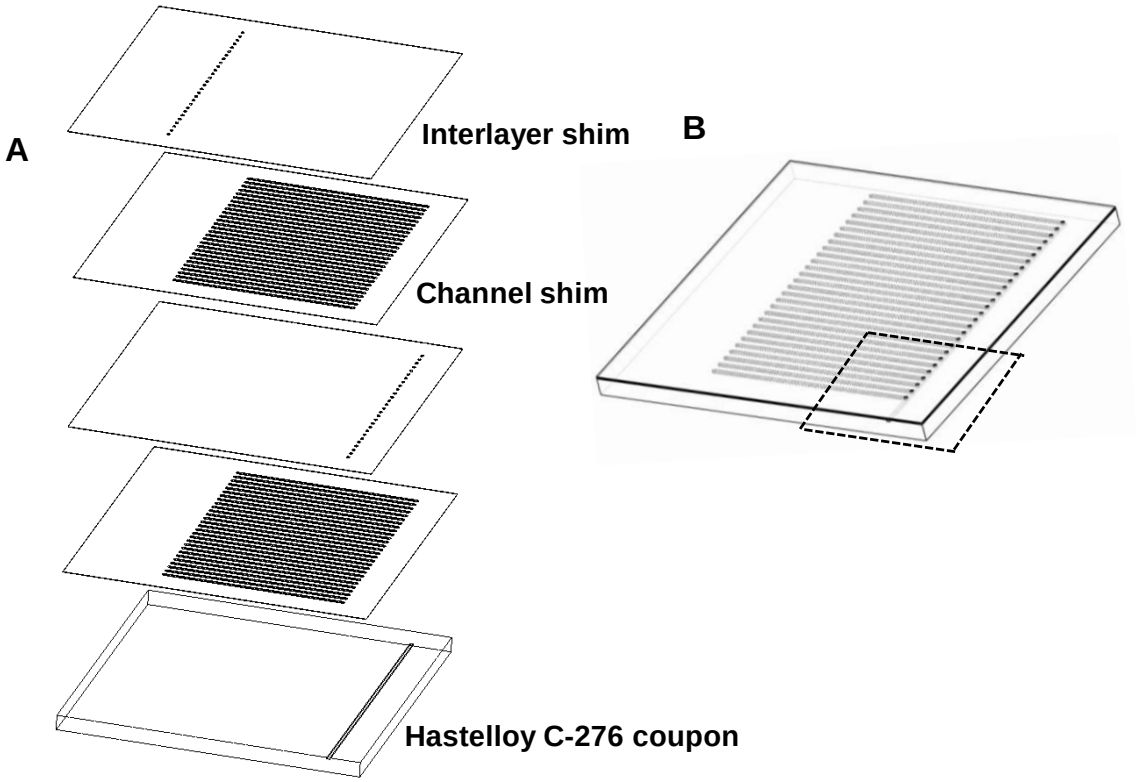

Figure A1.1. A) Expanded view of sample Hastelloy C-276 shim stack. Each stack contains one header coupon, two channel shims and two interlayer shims. B) Representative bonded shim stack. The dashed line represents the cross section used for bond analysis.

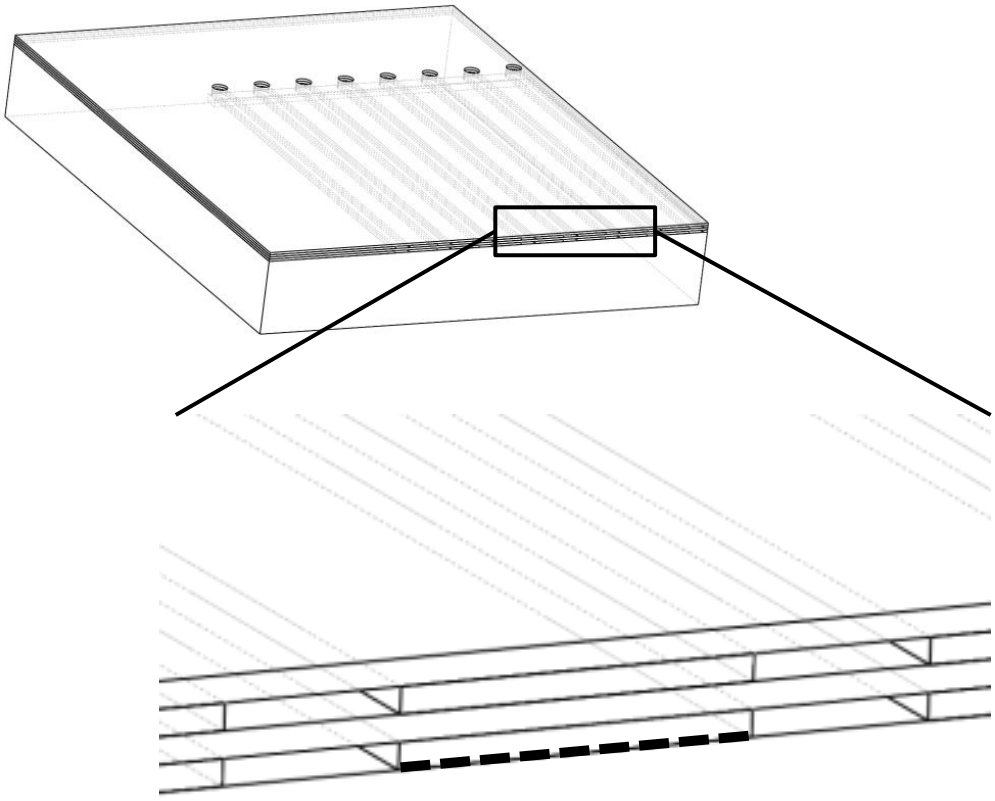

Figure A1.2. Expanded view of a sample cross sectional area from a bonded shim stack used for bond line analysis. The dashed line represents the investigated bond line.

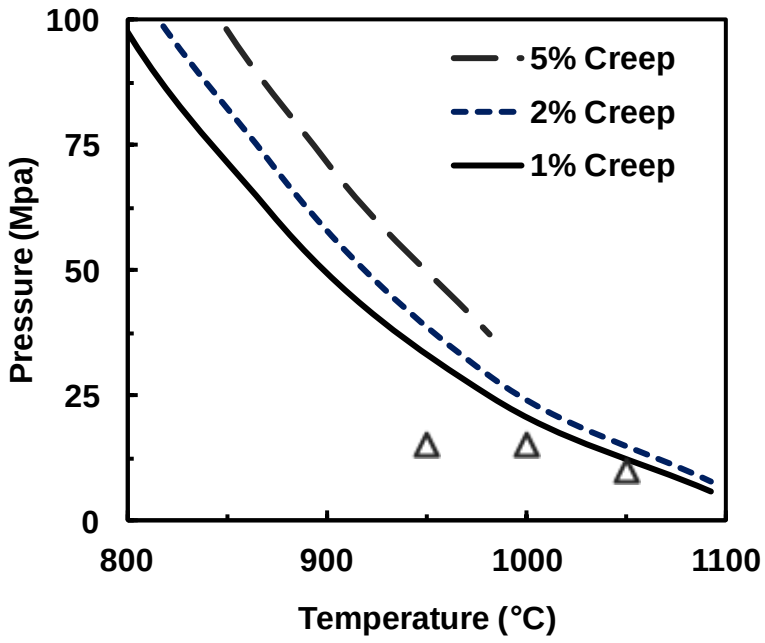

Figure A1.3. Ten hour 1.0%, 2.0%, and 5.0% creep curves for Hastelloy C-276 and bonding conditions for the three sample shim stacks, 950°C and 15 MPa, 1000°C and 15 MPa, 1050°C and 10 MPa.

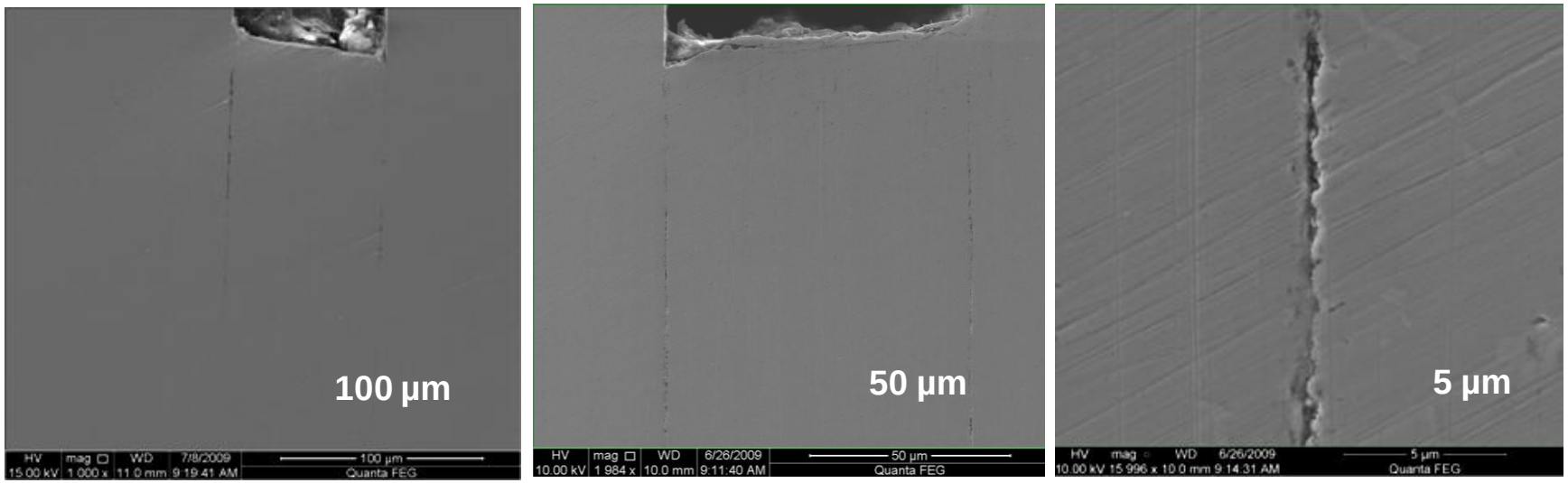

Figure A1.4A. SEM images of a sample bond line in a shim stack bonded at 950°C and 15 MPa.

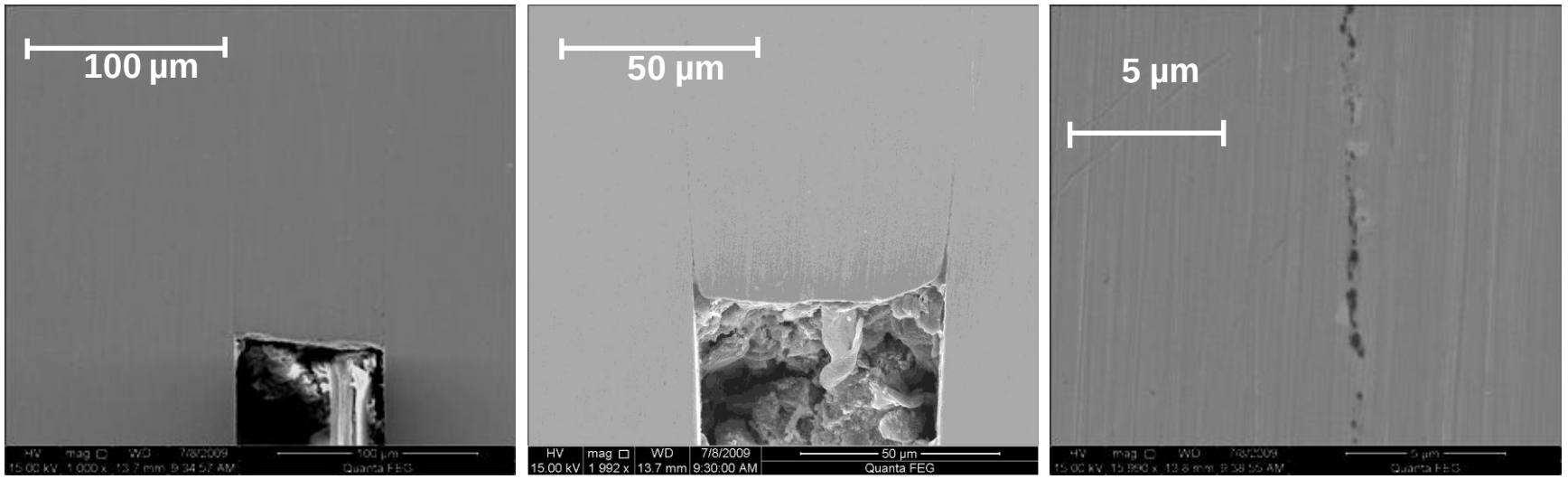

Figure A1.4B. SEM images of a sample bond line in a shim stack bonded at 1000°C and 15 MPa.

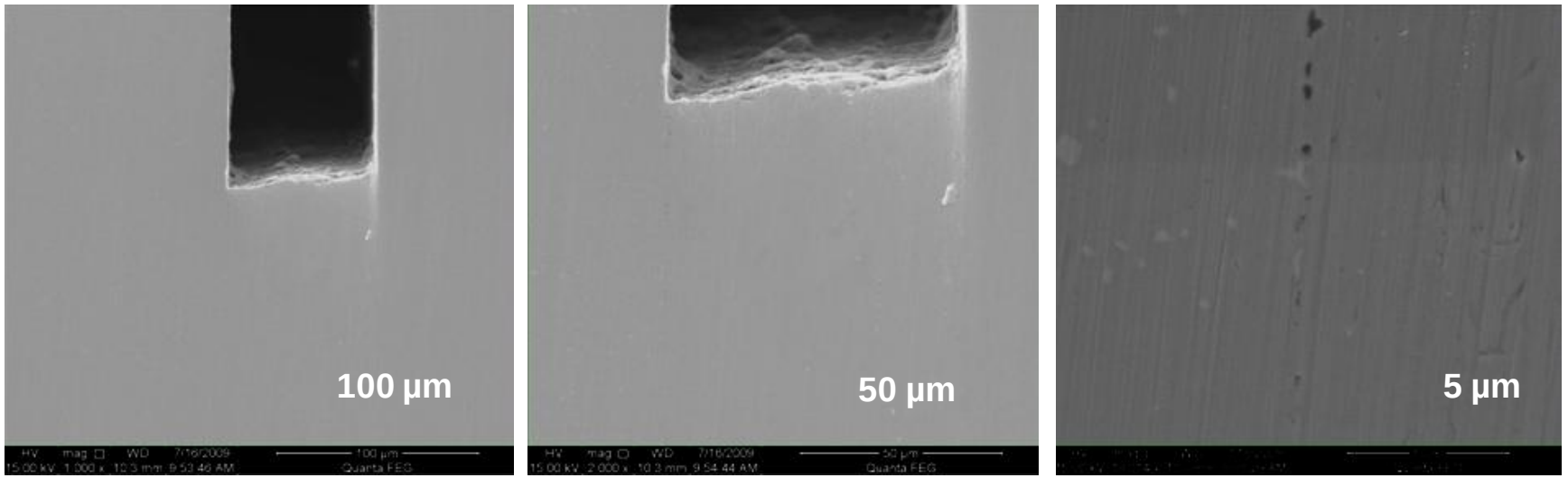

Figure A1.4C. SEM images of a sample bond line in a shim stack bonded at 1050°C and 10 MPa.

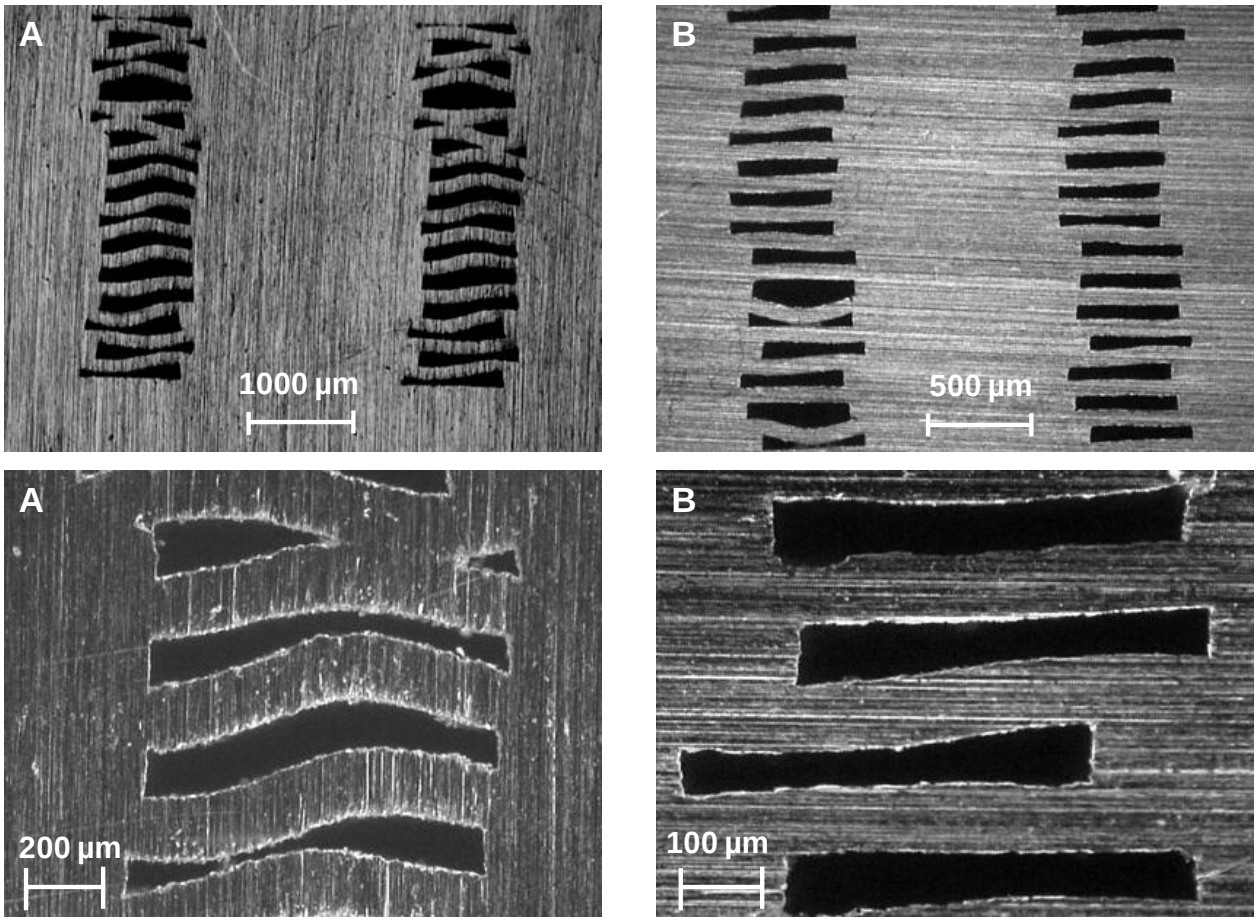

Figure A1.5. Previously bonded cross sections of Hastelloy C-276 microchannel reactors. A) Reactor was bonded at 1050°C and 25 MPa. The channels are 1000 µm by 127 µm. B) Reactor was bonded at 1050°C and 18.2 MPa. The channels are 500 µm by 76 µm.

Appendix 2: Supercritical Water Gasification of Biomass Constituents: Miscellaneous Experiments

A2.1 The effect of feed concentration on the gasification of glucose

Glucose, a model compound for cellulose and starch, was gasified by supercritical water at 750°C and 250 bar and a 6.0 second average fluid residence time. The effect of feed concentration (2.0 wt% to 25.0 wt %) on gas yield and H_2 selectivity was investigated. Glucose was readily soluble for all feed concentrations considered by this study.

The 762 μm diameter Hastelloy microtube reactor and reactor test loop used in this study was previously described in Chapter 2.31. Analytical procedures for gas product identification and quantification in addition to liquid product identification and quantification have previously been described Chapter 2.3.2.

Glucose gasification by supercritical water in the Hastelloy microtube reactor resulted in H_2 rich gas and a clear liquid effluent for all conditions tested. The effect of feed concentration on gas composition is presented in Figure A2.1. The gas products were comprised of mostly H_2 and CO_2 and minor gas products included CH_4 and CO. In general the feed concentration had little effect on the resulting gas composition. However, an increase in the CH_4 and CO concentrations and a small decrease in the H_2 concentration were observed for feed concentrations over 20 wt%. The low CO and CH_4 concentration in the gas for low feed concentrations is due to the high concentration of water in the feed driving the water gas shift and methanation reactions by the law of mass action. As the glucose feed concentration is increased the relative concentration of water to gas decreases from the greater amount of gas being produced and the large amount of water needed for reforming

$$C_6H_{12}O_6 + 6\,H_2O \longrightarrow 6\,CO_2 + 12\,H_2 \qquad \text{(A2.1)}$$

where 6 moles of water are consumed for every mole of glucose reacted. The lower water concentration in the reacting fluid has an effect on the equilibrium concentrations for the

water gas shift and methanation reactions. An increase in the concentration of CH_4 and CO is expected since the water gas shift and methanation reactions are no longer dominated by mass action from the excessive amount of water in the reacting fluid.

The effect of glucose feed concentration on the carbon gasification efficiency (CGE), defined as the amount of carbon in the feed recovered in the gas products, is presented in Figure A2.2. Complete CGE was achieved for feed concentration between 2.0 wt% and 10.0 wt%. The CGE decreased for feed concentrations greater than 10 wt%. The lowest CGE measured was 83% for 25 wt% glucose feed solution. Although a decrease in the CGE was observed for glucose feed concentrations 17.5 wt% and higher, no intermediates were measured in the liquid products for any of the glucose concentrations tested. However, an increase in the pressure drop through the reactor was observed over time for a feed concentration of 20 wt% and higher, indicating the possibility of coke formation which would also account for the missing carbon in the gas. The effect of feed concentration on H_2 yield followed a similar trend as the CGE and is presented in Figure A2.2. For feed concentrations of 10 wt% and less a H_2 yield of 9 moles of H_2 per mole of glucose reacted is achieved. For feed concentrations greater than 10 wt% a decrease in the H_2 yield is observed with increasing feed concentration. This is due to a change in the equilibrium of the water gas shift and methanation reactions, as discussed earlier, and possible coke formation that contains H_2.

This study has shown that glucose feed solutions up to 25 wt% can be continuously gasified to H_2 and CO_2 by supercritical water in a Hastelloy microtube reactor. Two issues that need to be considered when gasifying biomass with a high feed concentration are thermodynamic constraints in relation to the product gas composition and coke formation. High rates of heat transfer have been shown to decreases coke formation and sustain the reaction temperature in the presence of endothermic biomass reforming reactions. However, as the feed concentration increases the effect of the highly endothermic biomass reforming reactions are likely to affect the reaction temperature which may promote the formation of coke. Heat transfer to the reacting fluid is likely the

limiting factor to eliminate coke formation during continuous gasification of high concentration biomass feed streams by supercritical water.

A2.2 The gasification of xylan from beechwood in the parallel channel Hastelloy microreactor

A 2.0 wt% aqueous suspension of xylan from Beechwood was continuously gasified by supercritical water in the parallel channel Hastelloy microreactor at 650°C and 250 bar. The microchannel reactor and test loop has been previously described in Chapter 4. Xylan is a biomass model compound for hemicellulose and was purchased from Sigma Aldrich, CAS number 9014-63-5. Xylan from beechwood is a dull yellow crystalline powder, and was only slightly soluble in water and therefore the feed was prepared as a 2.0 wt% xylan suspension in water. The yellow cloudy suspension was homogeneous and no precipitation was observed after 24 hours. The feed was pumped to the reactor at a feed rate of 0.5 cm^3 min^{-1} which corresponded to a 7.1 second average fluid residence time in the reactor based on the reactor temperature and pressure. Analytical procedures for gas product identification and quantification have previously been described in Chapter 6.3.2. Due to the complex chemical structure of xylan and the possibility for numerous decomposition intermediates, a total organic carbon (TOC) measurement was used to measure the residual carbon in the liquid products. The carbon gasification efficiency was then calculated by a mass balance. TOC measurements were performed on a Shimadzu TOC-VCSH Combustion Analyzer using the standard method APHA 5310 B [1].

Xylan gasification by supercritical water in the Hastelloy microchannel reactor resulted in H_2 rich gas and a clear liquid effluent. A picture of the feed suspension and liquid products are presented in Figure A2.3. An increase of 10 bar in the pressure drop through the reactor was observed after a 2.0 hour on stream time which indicated the possibility of coke formation. The resulting gas composition consisted of 65.8% H_2, 30.4 % CO_2, 2.7% CH_4, 0.5% CO, and 0.5% C_2H_6, and is compared to the gas composition from the supercritical water gasification of a 4.0 wt% aqueous solution of xylose at the same reaction conditions in Figure A2.4. The gas composition for xylose and xylan gasification was similar, and therefore xylan hydrolysis and the heterogeneous chemical structure of xylan from real biomass had little effect on the H_2 selectivity in the product gas compared

to the gasification xylose. TOC measurements indicated no residual carbon in the liquid products indicating a 100% CGE. Although the carbon mass balance does not account for coke formation which may slightly decrease the CGE. This study has shown that the parallel channel Hastelloy microreactor has the potential to gasify hemicellulose from real biomass and to gasify homogeneous biomass suspensions.

Literature Cited

1. APHA 2005 *Standard Methods for the Examination of Water and Wastewater; 21st Edition* (American Public Health Association: Washington, DC)

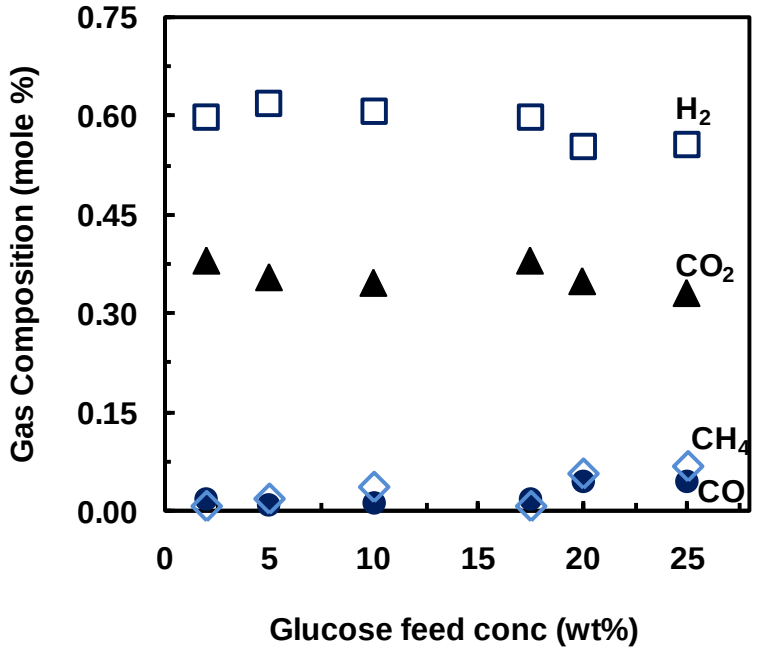

Figure A2.1. Gas composition from the supercritical water gasification of glucose in the 762 µm diameter Hastelloy micro tube reactor versus feed concentration at 650°C and 250 bar.

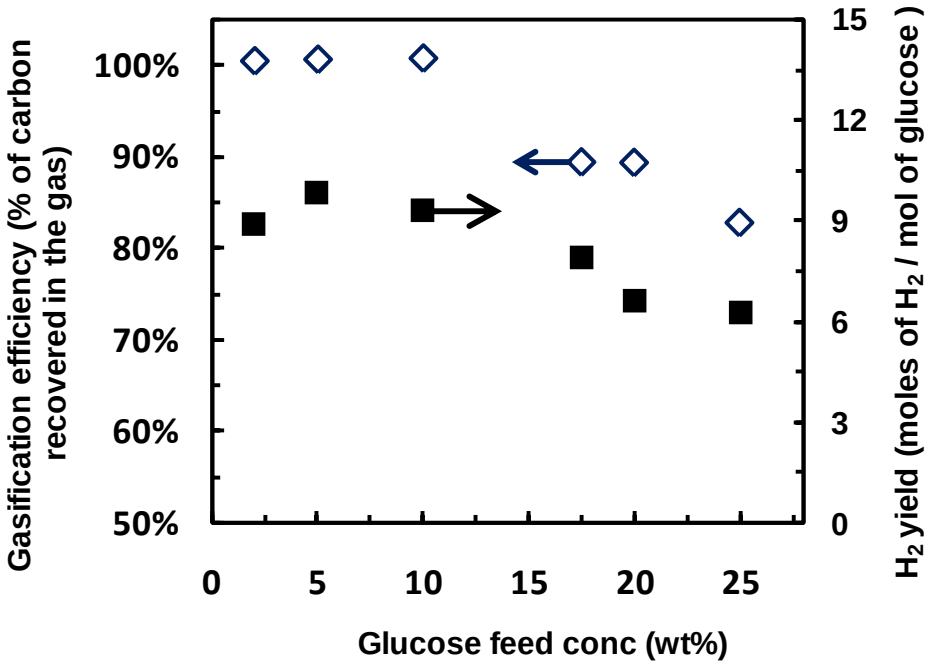

Figure A2.2. Carbon gasification efficiency and H_2 yield from the supercritical water gasification of glucose in the 762 µm diameter Hastelloy micro tube reactor versus feed concentration at 650°C and 250 bar.

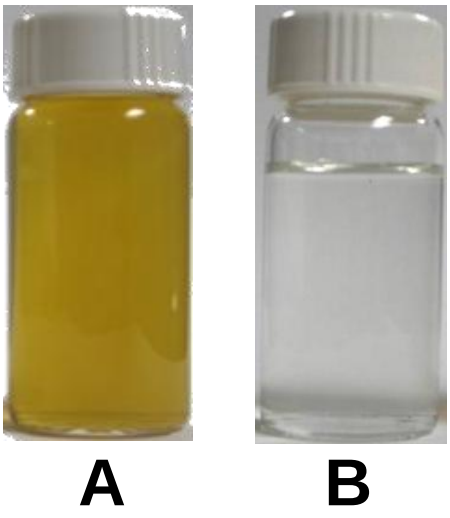

Figure A2.3. A) 2.0 wt% xylan from beechwood feed suspension. B) Liquid products from the supercritical water gasification of a 2.0 wt% xylan suspension in the parallel channel Hastelloy microreactor at 650 ºC and 250 bar.

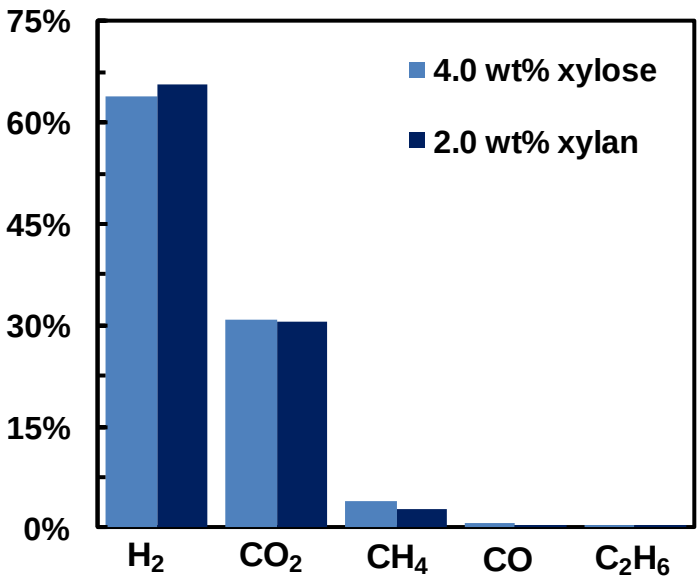

Figure A2.4. Gas composition from the supercritical water gasification of 2.0 wt% xylan suspension and a 4.0 wt% xylose solution in the parallel channel Hastelloy microreactor at 650°C and 250 bar.

Appendix 3: Supercritical Water Gasification Test Loop

Microchannel reactor test loop

The microchannel reactor test loop used is presented in Figures A3.1 – A3.3. The feed is delivered to the reactor by an Isco 260D high pressure syringe pump operated in constant flow or constant pressure mode. A schematic of the pump setup is presented in Figure A3.1. A series of check valves (Swagelok 4C2 series) located on the side of the pump enables the pump to automatically refill the syringe barrel while keeping the rest of the system at reaction pressure. The seals in the check valves need to be replaced periodically and a check valve rebuild kit can be ordered through Swagelok. The pump can be set to manual refill or automatic refill when the fluid in the barrel reaches a set volume. When the pump refills it creates a partial vacuum in the barrel which draws the fluid from the feed bottle through a 5 µm stainless steel filter and into the pump. The stainless steel inline filter (Swagelok 2TF series) periodically needs to be cleaned in concentrated nitric acid. The feed should be prepared in a 1.0 L Kimax bottle with the modified cap seen in Figure A3.1. A Swagelok high pressure three way ball valve located on the side of the pump can be used to bypass the reactor and directly pump the feed into the sink as waste.

The reactor is placed in a stainless steel furnace insulated with 1.5 inches of Thermcraft high temperature insulation and a layer of 3/16 inch Millboard high temperature insulation. A picture of the furnace can be seen in Figure A3.2. There are two temperature ceramic heaters located in the furnace. The heaters are 11.6 inches by 3.1 inches PH ceramic flat plat heaters from Thermcraft Inc. They were constructed from 80-20 nickel-chrome wire helically wound and placed in a grooved ceramic holder. Each heater used 115 volts of AC, and 375 watts of power. The leads from the heaters go through the reactor wall and into a ceramic terminal located at the front of the reactor. Although the heater leads are wrapped in ceramic beads, the lead itself must not be touching the side of the metal reactor where the lead comes through the reactor wall. If the lead touches the metal when the controller is active a short will trip the fuse in the temperature controller, which will need to be replaced. The temperature of the reactor is controlled by an Omega Instruments CN9422-C2 1/16 DIN temperature controller with a

P.I.D. control strategy connected to a 10 amp solid state relay. A 1/16 inch type k thermocouple is used as the primary temperature reading for the controller. Several other thermocouples in the reactor are used to take temperature measurements and are connected to an IOtech data logger. The threads in any Swagelok connections made inside the reactor must be coated with liquid stainless steel to keep the parts from seizing.

After the reactor furnace a counter current shell and tube condenser seen in Figure A3.2 is used to quench the reaction and condense the reactor effluent. Water is used as the cooling fluid in the shell side of the condenser. The flow rate of the water is adjusted at the spigot located in the hood. A temperature and pressure measurement of the fluid is taken after the condenser. A type K thermocouple is used for the temperature measurement and is connected to a thermocouple reader located above the reactor seen in Figure A3.2. An Omega PX series pressure transducer (0 – 5000 psi) is connected to the IOtech data logger and used to measure the system pressure after the condenser. Ideally, all the thermocouples, pressure transducer, and gas mass flow meters would be connected to the data logger, however due to a limited number of inputs some of the thermocouples are connected to the thermocouple reader located above the reactor test loop.

A Swagelok KHB series back pressure regulator (0 – 5000 psi) is used to regulate the reaction pressure and can be seen in Figure A3.2. In regard to biomass gasification, the reactor effluent (25°C and 250 bar) enters the back pressure regulator as three phase flow which causes periodic gas spikes due to a build up and release of CO_2 in the back pressure regulator. The gas spikes are an artifact of the low mass flow rate through the back pressure regulator and they can be suppressed by applying a small amount of pressure (~10 psi) on the outlet of the back pressure regulator by adjusting the fine metering needle valve located after the gas liquid separator. The back pressure should not exceed 50 psi as this is the pressure limit for the gas liquid separator. The back pressure can be monitored by the pressure gauge (0 - 100 psi) located after the back pressure regulator and before the gas liquid separator. The pressure on the outlet of the back pressure regulator will not eliminate the gas spikes, but it will cause them to occur more frequently and be less pronounced. The two way ball valve located after the back

pressure regulator is used to isolate parts of the reactor during leak testing and therefore is left open during gasification experiments.

After the fluid pressure is stepped down, the gas and liquid in the reactor effluent are separated by a gas liquid separator seen in Figure A3.3. The gas liquid separator is fabricated from a Kimax bottle and modified Kimax bottle top. Kimax bottles ranging in volume from 50 to 500 ml can be used to collect the liquid products. As previously mentioned the fine metering needle valve located after the gas liquid separator is used to apply approximately 10 psi back pressure the outlet of the back pressure regulator by restricting the gas flow.

Given that the gas phase products contain a small amount of residual water vapor that can artificially inflate the gas mass flow rate, a drying tube filled with Drierite water sorbent is located after the gas liquid separator seen in Figure A3.3 and used eliminate water in the gas stream. The Drierite sorbent in the drying tube should be changed when a color change in the sorbent from blue to pink is observed. After the gas products are dried the gas mass flow rate is measured by a series of Omega FMA series gas mass flow meters seen in Figure A3.3. The two flow meters are in series to accurately measure the gas flow rate during and between gas spikes. There are several gas mass flow meters available in the lab ranging from 0 – 20 SCCM up to 0 – 1000 SCCM. The pressure in the gas mass flow meters should never exceed 25 psi.

The gas composition is identified by an online SRI multiple gas analyzer #1 GC equipped with a thermal conductivity detector for H_2 analysis, and a FID detector with a methanizer for CO, CH_4, CO_2, C_2H_2, C_2H_4, and C_2H_6 analysis. The gas mixture is separated on two columns, a 2-meter Molecular Sieve 13X and a 2-meter Silica Gel. The GC oven temperature was held at 40°C for 3 min., then ramped to 135°C at a rate of 16°C/min, and held at 135°C for 2.67 min.

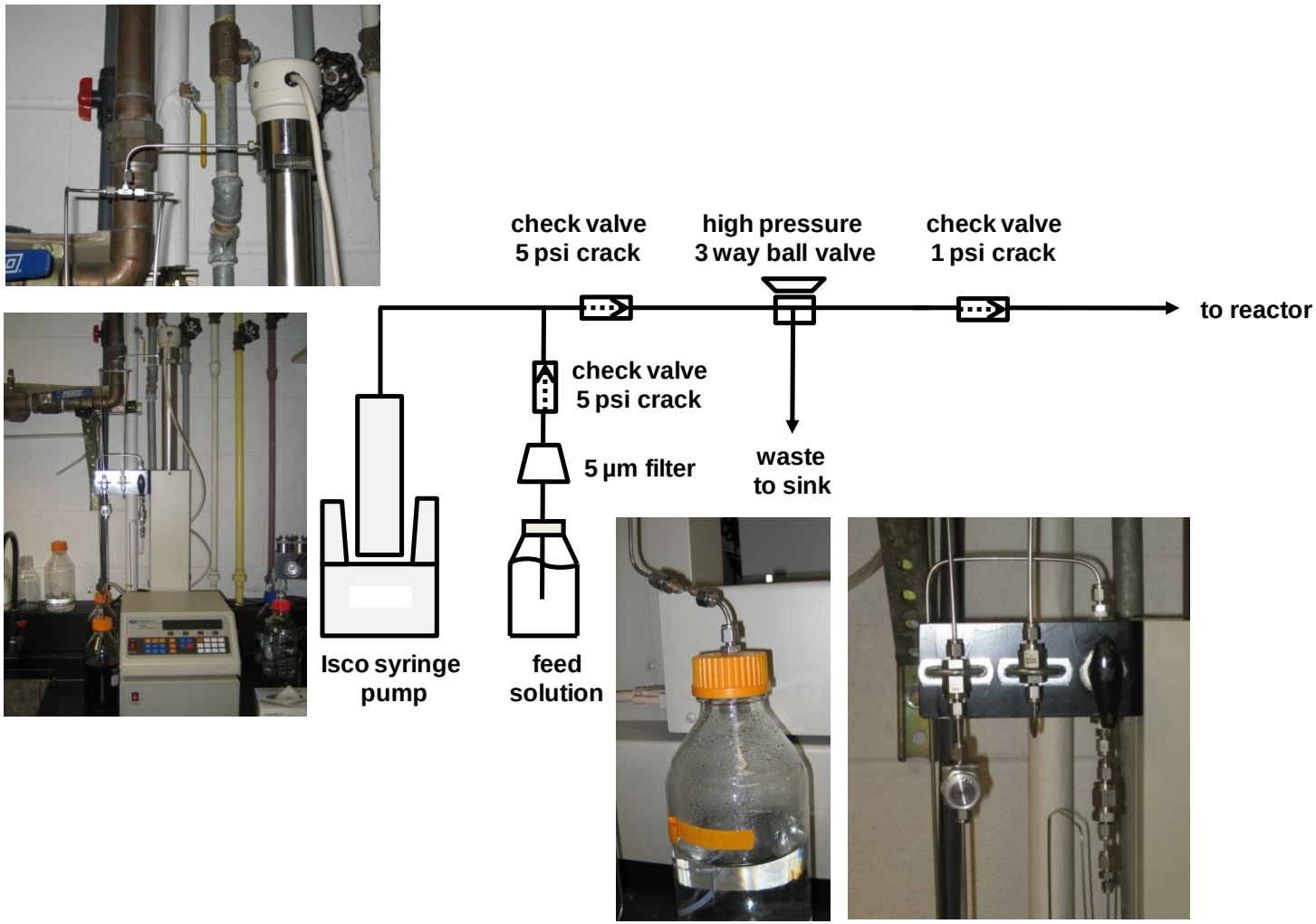

Figure A3.1 Detailed schematic of the supercritical water gasification test loop.

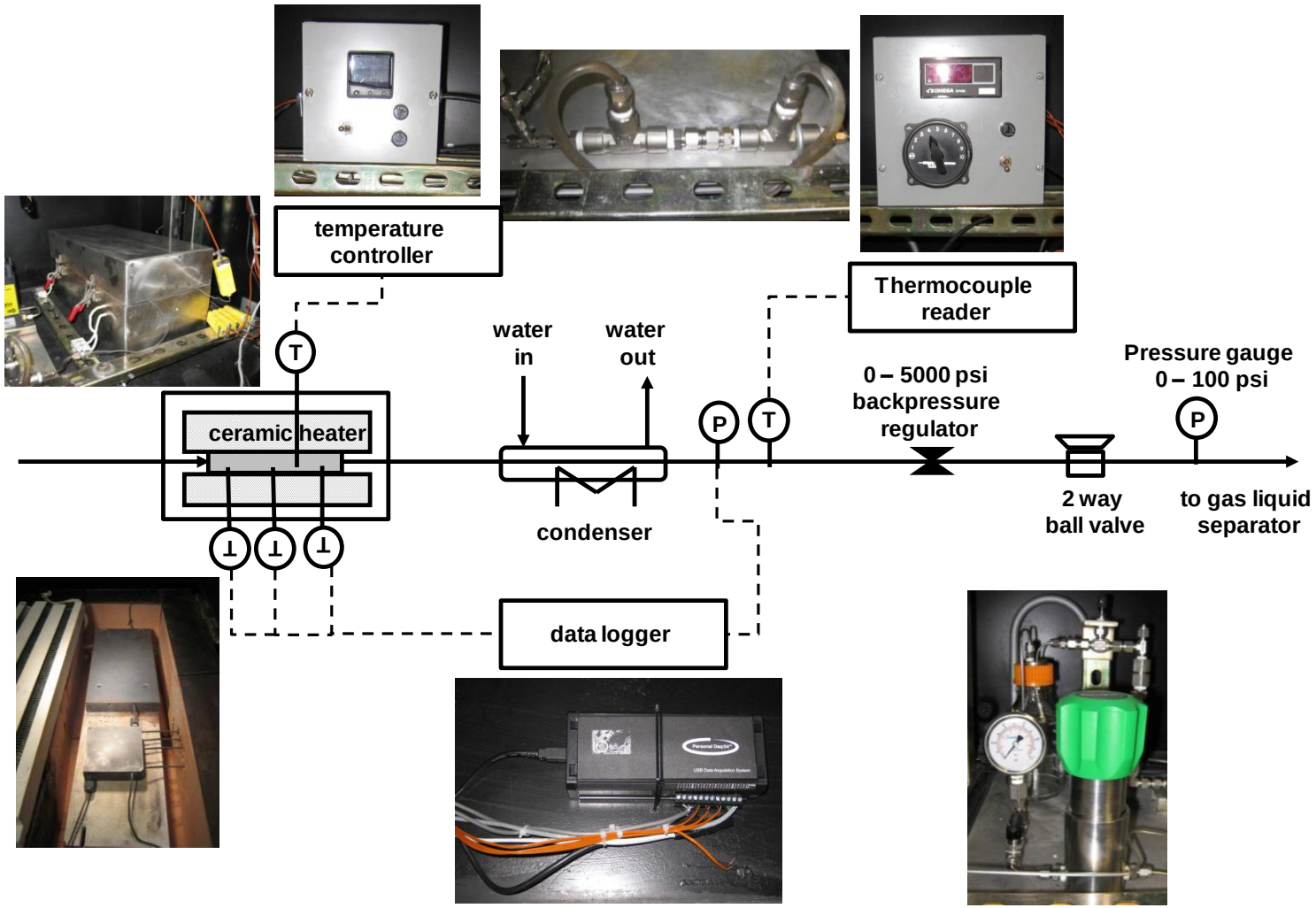

Figure A3.2 Detailed schematic of the supercritical water gasification test loop.

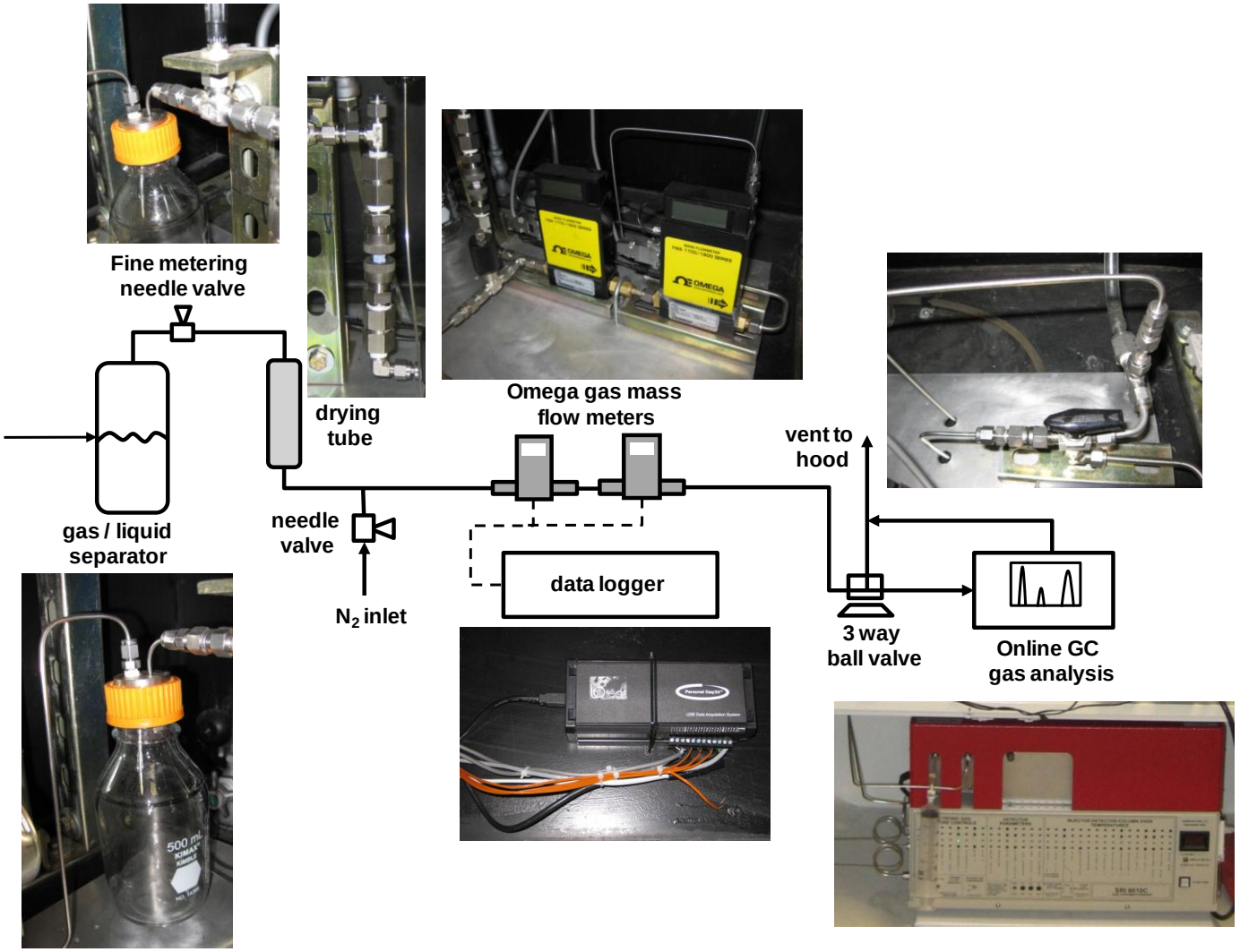

Figure A3.3 Detailed schematic of the supercritical water gasification test loop.